Conceptual Design and Technical Risk Analysis of Quiet Commercial Aircraft Using Physics-Based Noise Analysis Methods

A Thesis
Presented to
The Academic Faculty

by

Erik D. Olson

In Partial Fulfillment
of the Requirements for the Degree
Doctor of Philosophy

School of Aerospace Engineering
Georgia Institute of Technology
August 2006

Conceptual Design and Technical Risk Analysis of Quiet Commercial Aircraft Using Physics-Based Noise Analysis Methods

Approved by:

Dr. Dimitri Mavris, Advisor
School of Aerospace Engineering
Georgia Institute of Technology

Dr. Daniel Schrage
School of Aerospace Engineering
Georgia Institute of Technology

Dr. Lakshmi Sankar
School of Aerospace Engineering
Georgia Institute of Technology

Mr. Philip Gliebe
Acoustics Section
General Electric Aircraft Engines

Dr. Joe Posey
Langley Research Center
National Aeronautics and Space Administration

Date Approved: May 18, 2006

ACKNOWLEDGEMENTS

First and foremost, I wish to thank my parents, Lloyd and Debbie, for bringing me up in an environment where the pursuit of knowledge and achievement of personal excellence were always fostered and encouraged. You have always been my role models and without your love and support I would have achieved much less in life.

Thanks to my adviser, Dr. Dimitri Mavris, who convinced me after three quarters of graduate study that I had set my goals too low. Without your persistent but gentle prodding, I would have fallen one step short of the ultimate prize and would always have regretted it. Thank you also to my thesis committee, Dr. Daniel Schrage, Dr. Lakshmi Sankar, Dr. Joe Posey, and Mr. Philip Gliebe, for taking the time to read this thesis and to provide very valuable feedback.

I wish to thank Bob Biedron, Rodrick Chima, Theodore Katsanis, Thomas Lavelle, Eric McFarland and the staff of the Commercial Technology Office at NASA-Glenn Research Center for their help in obtaining the analysis codes used in this study, and to Edmane Envia and Abbas Khavaran for providing the data used in the validation studies. I also wish to thank the three branch heads I had from the very beginning of my graduate studies through the completion of my research—Samuel Dollyhigh, Robert McKinley and William Kimmel—without whose support and encouragement this undertaking would not have been possible. Thanks to those in ASDL who encouraged me along the way, gave me advice, and ultimately went above and beyond the call of duty to help me meet all those last minute deadlines, especially Dani, Michelle, Jimmy, Lexie and Cara.

Finally, thanks to my beloved wife, Janice, for making many more sacrifices than she should have needed to and always stubbornly supporting my desire to finish this degree, even when my own desire was flagging. I would not have reached this point without you.

TABLE OF CONTENTS

LIST OF TABLES

LIST OF FIGURES

NOMENCLATURE

$\vec{a}$	Gust magnitude
A	Constant
A	Quadrupole noise source strength
A	Coefficient for blade thickness equation
AVDR	Fan rotor stream tube area contraction ratio
b	Response surface equation coefficient
$\mathbf{b}$	Coefficients vector
B	Coefficient for blade thickness equation
B	Constant
B	Number of fan rotor blades
c	Rotor or stator blade chord
c	Speed of sound
C	Coefficient for blade thickness equation
C	Tone correction factor, PNdB
C_D	Drag coefficient
$C_{D,0}$	Drag coefficient at zero lift
C_L	Lift coefficient
$C_{L,0}$	Lift coefficient at zero angle of attack
$C_{L,\alpha}$	Lift-curve slope
$\overline{C}$	Modified convection factor
C_1, C_2, C_3, C_4, C_5, C_6, C_7, C_8	Empirical coefficients
D	Coefficient for blade thickness equation
D	D criterion

D	Fan or nozzle diameter, ft
D_eq	Nozzle equivalent diameter, ft
D_R	Rotor diffusion ratio
D_S	Stator diffusion ratio
f	Blade camber surface function
f	Frequency, Hz
f_b	Fan rotor blade passing frequency, Hz
f_C	Third-octave band center frequency, Hz
f_L	Third-octave band lower frequency, Hz
f_U	Third-octave band upper frequency, Hz
F	Objective function
F_b	Amount by which the tone exceeds the the surrounding bands
F_{shock}	Shock pressure loss factor
F_2	Normal force per unit span
g	Limit-state function
G	Response function
h	Altitude, ft
H	Fourier transform
I	Acoustic intensity
j	Iteration index
J_m	Bessel function of the first kind of order m
k	Index for discrete noise measurements
k	Turbulence intensity
$\vec{k}$	Wave number vector
K_1	Linear coefficient of drag polar equation
K_2	Quadratic coefficient of drag polar equation
l	Characteristic turbulent eddy size
L_A	A-weighted sound pressure level, dBA
L_{DN}	Day-night noise level, dBA

L_{eq}	Equivalent sound level, dBA
L_{EPN}	Effective perceived noise level, EPNdB
L_p	Sound pressure level, dB
$L_p^{''}$	Background sound pressure level, dB
$L_{\mathcal{P}}$	Sound power level, dB
L_{OA}	Overall sound pressure level, dB
L_{PN}	Perceived noise level, PNdB
L_{PNT}	Tone-corrected perceived noise level, PNdB
L_0,L_1,L_2	Constants for perceived noisiness calculation, dB
m	Circumferential mode number
m	Slope of a line
$\dot{m}$	Mass flow rate
M	Mach number
M_c	Convection Mach number
M_{le}	Rotor leading-edge relative Mach number
M_j	Mach number at jet exit plane
M_s	Mach number relative to rotor or stator
M_R	Rotor exit relative Mach number
M_S	Stator inlet Mach number
M_0,M_1	Constants for perceived noisiness calculation
n	Number of streamlines
n	Radial model number
n	Iteration index
n	Perceived noisiness, noy
$\hat{n}$	Unit normal vector
N	Total perceived noisiness, noy
p	Mean pressure
p_r	Fan total pressure ratio
$p_{r,des}$	Design fan rotor total pressure rise

$p_{r,i}$	Total pressure ratio on the i^{th} streamline
p_{ref}	Reference pressure
p'	Acoustic pressure
$\overline{p}$	Rotor relative total pressure
$P(r)$	Radial component of duct mode solution
$\mathcal{P}$	Sound power
$\mathcal{P}_{ref}$	Reference sound power
q	Harmonic of fan blade passing frequency
r	Radius
r_h	Annular duct inner radius
r_t	Annular duct outer radius
R	Fan stage reaction
R	Gas constant for air
R	Radius, ft
R	Response value
R	Source to observer distance, ft
s	Integral multiplier
s	Fan blade centerline distance, normalized by blade chord
S	Grid stretching factor
t	Time, sec
t	Blade thickness normal to camber line
T	Temperature
T	Normalizing time constant, sec
T_{ij}	Lighthill Acoustic Analogy instantaneous applied stress tensor
u'	Turbulent velocity fluctuation
u_∞	Incident gust velocity
U	Mean flow velocity
U_f	Mean velocity at the fan face
v'	Acoustic velocity

V	Number of fan stator vanes
V	Velocity, ft/sec
V_m	Meridional velocity
V_2	Aircraft velocity at the obstacle after critical engine failure, kt
V_θ^*	Prescribed circumferential velocity distribution, ft/sec
W_A	A-weighting factor
x	Distance from brake release, ft
x	Generic design variable
$\overline{x}$	Normalized value of design variable
$\vec{x}$	Observer location
x_1,x_2,x_3	Cartesian components of observer location vector
X	Axial distance, ft
$\mathbf{X}$	Design matrix
$\mathbf{Y}$	Response vector
$\vec{y}$	Noise source location
$\vec{y}$	Coordinate system fixed to stator
Y_m	Bessel function of the second kind of order m
z	Axial coordinate, ft
z_{shock}	Axial shock location relative to blade chord
α	Angle of attack, deg
α_c	Empirical constant
β_c	Empirical constant
γ	Ratio of specific heats
δ_{ij}	Delta function
ϵ	Turbulence dissipation rate
θ	Circumferential coordinate
κ	Wave number function
μ	Mean value of probability distribution
ρ	Density

ρ'	Acoustic density
σ	Standard deviation of probability distribution
τ	Retarded time, sec
τ	Shear stress
ϕ	Velocity potential
Φ_s	Grid stretching parameter
ψ	Test function
ω	Radial frequency
ω_0	Characteristic frequency
Ω	Fan rotational speed
Ω_V	Velocity relaxation factor
Ω_E	Error correction relaxation factor

Subscripts

av	Average value
b	Third-octave band index
l	Value on the left end point of a spline
le	Value near the fan blade leading edge
m	Quantity for circumferential mode m
mn	Quantity for circumferential mode m and radial mode n
min	Minimum value
max	Maximum value
noz	Value at the nozzle exit
r	Radial component
r	Value on the right end point of a spline
rms	Root-mean-square value
te	Value near the fan blade trailing edge
z	Axial component
θ	Circumferential component
1	Value at beginning of integration period

1	Components parallel to blade chord
2	Value at end of integration period
2	Component normal to blade chord
3	Component in the radial direction
90%	90% confidence value
∞	Freestream conditions

Abbreviations

ANOPP	Aircraft Noise Prediction Program
BPF	Blade-passing frequency, Hz
BPR	Bypass ratio
CAA	Computational aeroacoustics
CCD	Central-composite design
CFD	Computational fluid dynamics
DNL	Day-night noise level, dBA
DOE	Design of Experiments
EPNL	Effective perceived noise level, EPNdB
FAR	Federal Aviation Regulations
FLOPS	Flight Optimization System
FORM	First-order reliability methods
FPA	First-principles analysis
FPR	Fan pressure ratio
HPCPR	High-pressure compressor pressure ratio
HSCT	High-speed civil transport
ICAO	International Civil Aviation Organization
IPCPR	Intermediate-pressure compressor pressure ratio
MPI	Message Passing Interface
MPT	Multiple pure tones
NASA	National Aeronautics and Space Administration
NEPCOMP	Navy Engine Performance Computer Program

NN	Neural network
NPR	Nozzle pressure ratio
OASPL	Overall sound pressure level, dB
OPR	Overall pressure ratio
PDF	Probability density function
PNL	Perceived noise level, PNdB
PNLT	Tone-corrected perceived noise level, PNdB
PVM	Parallel Virtual Machine
PWL	Sound power level, dB
RMS	Root-mean-square
RPM	Revolutions per minute
RSE	Response-surface equation
RSM	Response-surface Methodology
RVC3D	Rotor Viscous 3-dimensional computer program
SDT	Source Diagnostic Test
SFC	Specific fuel consumption, lbm/hr/lbf
SORM	Second-order reliability methods
SPL	Sound pressure level, dB
SST	Shear-stress transport
TFaNS	Tone Fan Noise System
UCAV	Uninhabited combat air vehicle

SUMMARY

With the rapid growth in air travel which is expected in the coming decades, the noise produced by aircraft will continue to be an important consideration in their design. Amid intense competition, aircraft and engine manufacturers are typically required to guarantee that their products will not exceed given noise levels, even at early stages in the design process when considerable uncertainty still exists in how the final product will perform. Prior experience has shown that the noise level of any signal source can be reduced by a few decibels through conventional design alternatives, but achieving additional reductions requires a significantly larger level of effort in terms of research and cost and an increasingly interdisciplinary effort. The use of physics-based analysis tools earlier in the design process, instead of the traditional empirical methods, can improve the process by making the analysis applicable to newer, revolutionary designs and by offering the ability to directly assess the benefits of new technologies. Unfortunately, the greater computational time required by physics-based analysis has tended to make it impractical for use in conceptual design studies where many rapid computations are required and where design knowledge is limited. In this research program, an approach was developed which allows for design studies of commercial aircraft using physics-based noise analysis methods while retaining the ability to perform the rapid tradeoff and risk analysis studies needed at the conceptual design stage.

Using a diverse collection of computer programs, an integrated analysis process was assembled for calculating the engine cycle performance and takeoff and landing performance, and for predicting the community noise levels of an aircraft using physics-based analysis for the fan rotor-stator interaction tones and jet mixing noise and empirical methods for the other sources. Additional intermediate methods were included to define the detailed engine duct geometry and fan rotor blade geometry that were required by the higher-fidelity noise analysis methods. The physics-based portions of the noise analysis were validated using scale-model experimental results. The new analysis process was used to assess the

performance and noise of the baseline aircraft, a 300-passenger, twin-engine commercial transport aircraft powered by two high-bypass ratio turbofan engines.

The analysis process was then used in combination with Design of Experiments to create response surface equations (RSEs) for the engine and aircraft performance metrics, geometric constraints and takeoff and landing noise levels. In addition, Monte Carlo analysis was used to assess the expected variability of the metrics under the influence of uncertainty, and to determine how the variability is affected by the choice of engine cycle. Finally, the RSEs were used to conduct a series of proof-of-concept design studies: an examination of the compromises in engine cycle design that are needed to achieve lower noise levels, including a quantification of the resulting performance penalty; an assessment of the noise benefits of swept fan stators as a function of the engine cycle to which they are applied and calculation of the optimum sweep angle for any engine design point; a robust design study examining how the engine performance-versus-noise tradeoffs change when uncertainties in engine component efficiencies, operating environment and modelling errors are taken into account; and a final robust design study examining whether the engine cycle design point can be shifted to make the engine more robust relative to the type of aircraft it is used to power.

This study found that the greatest technical challenge in implementing physics-based analysis at earlier design stages resulted from an order-of-magnitude increase in the detail of the geometry definition required by the higher-fidelity analysis methods. Additional layers of preliminary geometric design methods were required in the analysis process to provide this detail, greatly increasing the computational requirements. The use of wrappers, automated data interfaces, and autonomous geometry definition and grid generation was vital for making the process practical to use. The use of RSEs to approximate the outputs from the analysis process, while sacrificing some of the accuracy which can theoretically be gained by using higher-fidelity methods, had the advantage of greatly increasing the utility of the analysis process. The use of a domain-spanning approximation technique such as response surface methodology, in particular, allowed for visualization of design tradeoffs encompassing the entire design space. When used in combination with Monte

Carlo analysis, it was possible to assess the influence of the design variables on the risk of meeting performance goals and design constraints, and to demonstrate how risk can be mitigated by the choice of design variable values and how the required margins of safety change for different engine cycles.

CHAPTER I

INTRODUCTION

In the near future, worldwide demand for air travel is expected to grow by an average of about 4 percent per year, so that by 2040 the demand is expected to be about four times as great as today[13]. Although today's aircraft are 20 dB quieter than the first jet-powered airplanes, earlier dramatic improvements in noise levels have gradually given way to smaller improvements, so that the trend of lower noise with time in recent years has approached a slope of zero. In the absence of further noise reduction technology, total noise exposure will begin to increase due to the projected growth in air traffic and in the number of people living in the vicinity of airports. If noise reduction does not continue, noise restrictions at the international, national and local levels could severely constrain the capacity of the global aviation system to meet the growing demand[97][139]. A recent survey found that the majority of European airports are already subject to direct noise-related constraints on capacity, and the percentage is expected to increase significantly in the near future[127].

Prior experience has shown that the noise level of any signal source can be reduced by a few decibels through conventional design alternatives, but achieving additional reductions requires a significantly larger level of effort in terms of research and cost and an increasingly interdisciplinary effort[128]. According to Willshire and Stephens,

> As more progress is made in reducing aircraft noise it becomes increasingly more difficult to make additional significant reductions. It also becomes necessary to greatly improve the accuracy in predicting the fundamental dependencies of the many noise sources on the various aircraft. The advances in today's high speed computing power in terms of both speed and storage has now made possible new approaches to noise prediction. . . . A key to future success will be a systems approach in which multiple noise sources are considered simultaneously giving equal weight to other engineering disciplines[139].

Thus, it will become necessary to focus not just on the reduction of individual noise sources,

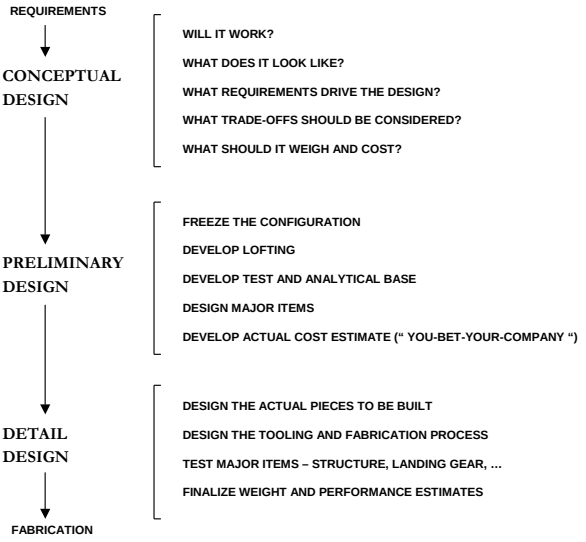

Figure 1: Three phases of aircraft design[113].

but on a *concurrent* approach which examines the interaction of multiple engineering disciplines at earlier stages in the design process.

1.1 Concurrent design

To understand how a concurrent approach can improve the aircraft design process, consider the typical process as shown in Figure 1. Aircraft design is traditionally broken into three major phases: conceptual, preliminary, and detail[113]. Conceptual design usually begins with a set of design requirements, which are either explicitly stated by the prospective costumer or are based on projections of what future customers may need; sometimes the design will begin as an innovative idea rather than as a response to a set of requirements. During conceptual design, the aircraft's configuration arrangement is decided and its size, weight and performance are estimated. Although some changes occur during preliminary design, major changes are ordinarily confined to the conceptual phase.

Preliminary design begins when the major revisions are complete, and only minor revisions can be expected to occur in the configuration arrangement. During preliminary design, specialists conduct design and analysis of structures, landing gear and control systems, and detailed analysis and testing is initiated in propulsion, aerodynamics and structures. The objective of the preliminary design phase is to establish confidence that the airplane can be

built on time and at the estimated cost before the detail design begins.

Finally, detail design involves the design of the actual pieces of the aircraft which are to be fabricated. Also, production designers determine how the aircraft will be fabricated, and may make minor changes to the design to make the pieces easier to manufacture. The testing effort increases, and is carried out on actual prototype structural components. Flight system control laws are tested on detailed working models, and flight simulators are developed and tested by test pilots for both the company and the customer. The detail design ends with fabrication of the aircraft.

The solid curves in Figure 2 show the typical growth of design knowledge, design freedom, and committed cost for a complex system over time, from the earliest stages of design and development to product release. At the beginning of the conceptual design, nothing is known about the design, no costs have been committed because no decisions have been made regarding the nature of the final design, and the designer has complete freedom to make any design choices. However, due to the time and budget constraints on the design and development process, the number of possible configurations must be reduced substantially before preliminary analysis methods can be employed. During the conceptual design phase the freedom rapidly decreases and the committed cost rapidly increases as early decisions are made about the design, because these early choices quickly lock the design into a limited set of possible outcomes. At this stage in the process, however, knowledge about the design is still quite limited since the decisions are typically made based on very simplified, empirically-based analysis methods or back-of-the-envelope calculations. As a result, very important decisions are made based on limited knowledge of the design and simple analysis.

The goal of concurrent design is to shift the knowledge, cost, and freedom curves as shown by the arrows in Figure 2. Adopting a multidisciplinary analysis environment and improving the fidelity of analysis in the early stages of the design process results in a more rapid increase in design knowledge than in the traditional design process. Additionally, by limiting the number of choices made about the design until more knowledge can be obtained, the design freedom can be retained for a greater portion of the process so that the greatest drop-off occurs at the later stages. As result of these changes, the committed cost is kept

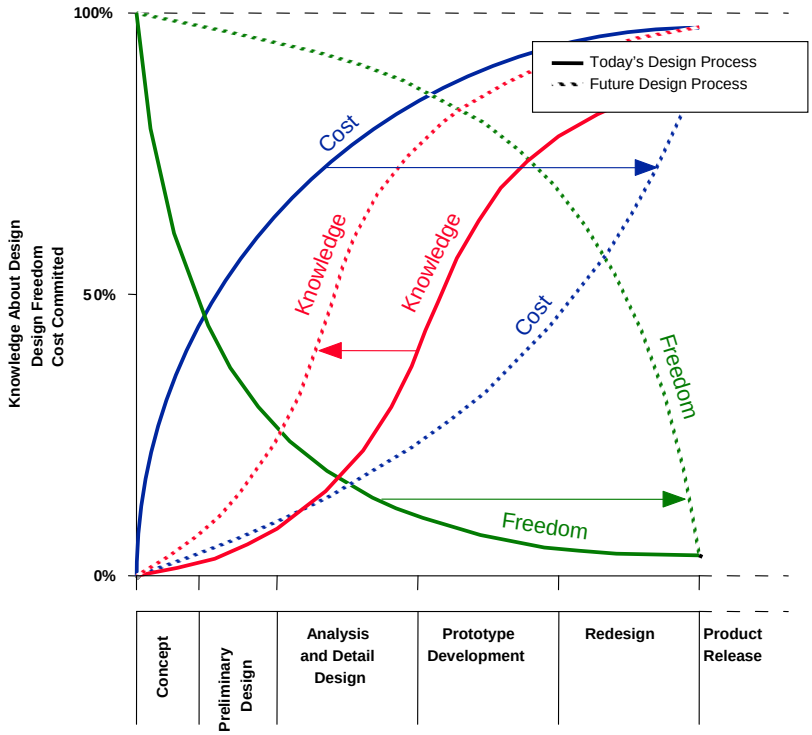

Figure 2: Evolution of design knowledge, design freedom, and cost committed during the design and development process[89].

low until the bulk of the decisions are made, later in the process.

1.2 First-principles noise analysis

As mentioned previously, one way of accelerating the acquisition of design knowledge is by using higher-fidelity analysis earlier in the design process. During a traditional conceptual design study, however, the limited information about the engine geometry and flow fields usually necessitates the use of empirical methods to predict the acoustic characteristics of the design. These methods typically give predicted noise levels as a function of the general engine geometry—such as cross-sectional areas of components and blade and vane counts—as well as the component inlet and exhaust mean flow and thermodynamic information, and the aircraft flight condition. Detailed information about blade design and nozzle geometry usually are not necessary or desired. The empirical methods are quick to execute so that rapid evaluation of many different designs is possible.

Unfortunately, empirical noise prediction methods can be extremely limited due to the

reliance on measured noise levels for model and full-scale engines. The database which makes up the empirical curve fits may be outdated in terms of the technology level and design methods, and since the prediction methods likely do not correlate noise levels with any new technology, it is usually impossible to evaluate the effects of brand new technologies directly. Instead, correction or "fudge" factors must be applied to the predicted noise levels using a limited set of fresh experimental results. During subsequent design studies, these correction factors must often be extrapolated to conditions for which experimental results are not available, calling into question the validity of the results. For these reasons, any empirical database can quickly become unsuitable for examining revolutionary design concepts.

On the other hand, analysis methods based on physical laws, i.e. first principles, are always applicable to any design problem—at least in theory—because the laws of physics always apply. In practice, first-principles analysis (FPA) methods are usually limited by the assumptions which are needed to make the problem tractable; nevertheless, FPA is usually applicable to a larger design space and tends to be more accurate for designs outside the database of the available empirical methods. Additionally, FPA tends to give better trends outside the empirical database because it is not subject to extrapolation errors like empirical analysis, and can give a better assessment of the effects of variables which are not included in the empirical equations.

Another very important advantage of FPA is the ability to make a more direct and thorough analysis of new technologies by direct simulation rather than correction factors. If the technology can be modelled directly and its effects captured by the physics of the problem, the benefits of the technology can be assessed not only for the geometry and operating conditions for which experimental data are available, but also for other designs and at other conditions. Direct assessment ensures that the effects of design changes and operating conditions on the technology benefits can be accurately assessed so that the design can be optimized concurrently with the new technology.

The drawback to using FPA is that the analysis is by necessity much more complex than can typically be afforded early in the design process. Since the physics of the problem is dependent upon the detailed geometry of the engine, FPA requires a much more thorough

definition of the engine geometry and internal flow field than is usually available for a conceptual design. Physics-based computer programs require a much greater execution time, making it impossible to perform the large numbers of analyses required in numerical optimization. Often the problem setup itself is complex, involving preliminary flow field solutions and grid generation and refinement before the acoustic analysis can be performed. Such programs also tend to be less robust and more likely to produce discontinuous trends, which also make their use in optimization difficult.

The benefits and drawbacks of using FPA earlier in design cycle have been acknowledged for some time, and previous research exists which focuses on techniques for overcoming the barriers to its use. In general, this research has focused on the implementation of approximation techniques to develop highly-efficient surrogate models for the high-fidelity analysis methods; these surrogate models can then be used to provide rapid functional evaluations during design optimization. In the literature, the most commonly used approximation method is response-surface methodology, which seeks to create a response-surface equation (RSE) relating the value of an output to the values of design variables; the RSE is an algebraic function, usually polynomial, and thus can be evaluated very rapidly. The RSEs are created using linear regression of a matrix of runs. Another common method is artificial neural networks (ANN), which use a network of simple processing units called artificial neurons to create an approximation using a set of points to "train" the neurons.

During the 1990's, NASA's High-Speed Research Program focused much technology development and systems analysis research toward solving the technical, environmental and economic challenges of designing and building a high-speed civil transport (HSCT) aircraft. Since the HSCT was a revolutionary aircraft configuration for which empirical databases for aerodynamic, structural, and other disciplinary characteristics were not suitable, much emphasis was placed on using FPA methods of various fidelity levels to analyze the vehicle concepts. The increased emphasis on FPA and rapid improvements in computing speed served to vitalize research into new concurrent design paradigms using FPA at an earlier stage.

Chen and Varadarajan[17] used an HSCT as a test application to study the relative

benefits of response-surface methodology and artificial neural networks as approximation methods. Using a previously-existing multidisciplinary model for an HSCT, metamodels were created for the aircraft lift-to-drag ratio, takeoff field length and nitrous-oxides emissions as a function of several system-level and wing planform variables; RSEs and ANNs were created using run matrices of 531 points, and the relative benefits of each technique were assessed in terms of both accuracy and effectiveness for used in optimization. Patnaik et al [107][108] also used an HSCT model to compare RSM and ANN approximations. Using both techniques, metamodels were created for the vehicle gross weight, takeoff and landing performance constraints, jet velocity and compressor discharge temperature using a common matrix of 412 test points, and the performance of RSM and ANN were compared for cases where the design variable ranges were kept narrow or allowed to be much wider.

Several studies were conducted using RSM as a method for creating metamodels for an HSCT using simple FPA methods for a single discipline. Giunta et al conducted aerodynamic analysis an HSCT using a combination of vortex-lattice induced drag analysis, volumetric wave-drag analysis, and a Mach-box type method for supersonic drag-due-to-lift[50]. The aerodynamic analysis results were used in mission analysis of the aircraft, and an RSE was created relating the takeoff gross weight to a reduced set of four wing planform variables using a run matrix of 157 points. The RSE was then used in a design optimization study to find the best wing planform for minimum gross weight. Crisafulli et al developed RSEs for the aircraft pitch-up characteristics using two-dimensional potential-flow aerodynamic analysis[29]. Balabanov et al created RSEs for wing bending material weight using thousands of coarse finite-element analyses to form a quadratic RSE and hundreds of refined finite-element analyses to form a linear RSE for the fine-grid correction[5]. Along the same lines, Kaufman et al [70] used a finite-element structural analysis and optimization method to create a wing bending material weight RSE using a design matrix of 1025 points.

Although most research into the application of approximation methods in conceptual design has focused on the HSCT, some studies have been conducted for additional test problems. Scharl and Mavris [119] used ANNs to approximate the individual outputs of a

vortex-lattice aerodynamic analysis, engine performance tables and empirical weight equations to provide the necessary quantities from the individual disciplines for analyzing the stability and control characteristics of a subsonic transport. The run matrix for the aerodynamic analysis method consisted of 3400 runs. Jeon et al [66] used low-fidelity analysis for aerodynamic characteristics and empirical methods to estimate the component weights of an uninhabited combat air vehicle (UCAV) concept. RSEs were created for the individual disciplines, the overall system was integrated using a collaborative optimization framework, and the gross weight of the vehicle was minimized, subject to design constraints, using a genetic algorithm. In this study, the RSEs were combined with Kriging, which is another approximation technique, to increase the confidence of the approximations. Kodiyalam, Lin and Wujek [78] used RSM to demonstrate optimization with metamodels for two demonstration cases: a cantilevered beam modelled with simple analytical methods, and a oil tanker ship conceptual design analyzed with low-fidelity methods. Engelund et al [38] analyzed the aerodynamic characteristics of a reusable launch vehicle using a combination of slender body theory, source and vortex panel distributions, empirical viscous and wave drag estimating techniques, hypersonic empirical impact pressure methods and approximate boundary layer relations. Three-dimensional solid models of the vehicle were created from simple parametric geometry variables such as fineness ratio. RSEs were created relating the vehicle dry weight to five geometric parameters using a matrix of 27 runs, and an optimizer was used to find the geometry for minimum dry weight subject to several constraints. Along the same lines, Unal et al [136] used the same combination of analysis methods to create RSEs relating the dry weight of a dual-fuel, single-stage-to-orbit launch vehicle to the thrust/weight ratio, transition Mach number, liquid hydrogen flow percentage, and nozzle expansion ratio. As before, the RSEs were used to find the optimum combination of design variable values for minimum dry weight.

These studies described above helped to develop and refine techniques for using approximation methods to enable higher-fidelity analysis methods, to compare different approximation techniques to judge the relative benefits of each and to develop rules for when the

different methods are appropriate to use, and to conduct proof-of-concept studies demonstrating the practical application of the methodologies developed. However, the disciplinary analysis methods used in these studies could only be described as mostly low-fidelity. While the computational times for these methods were higher than empirical or simple analytical methods, they were still sufficiently low to not seriously challenge their use in large design matrices. In many of these studies it was still possible to use design matrices of hundreds of points in creating the approximation models. In addition, the methods did not require overly complex geometry definition that could not be generated using a short list of parametric geometry variables, such as fuselage fineness ratio, wing area, leading-edge sweep, thickness-to-chord ratios, etc.

In a smaller subset of studies, true medium- to high-fidelity analysis methods have been used. While the basic principles behind the use of approximation methods can be laid out and demonstrated using lower-fidelity analysis methods, it is more useful to demonstrate the concepts for true high-fidelity analysis processes because there are additional technical issues that must be worked out relating to detailed geometry definition, modelling complexity issues, etc.

In one earlier study, Knill et al [76] calculated the cruise drag of an HSCT wing-body using Euler analysis, and combined the results with linear theory for the additional wave drag of the nacelles and empennage for the total drag. RSEs were created relating a number of parametric airfoil, wing planform and fuselage geometry variables, and were used to find the optimum design for minimum takeoff gross weight. A key to the efficiency of the analysis was that the three-dimensional geometric representation of the vehicle could be automatically generated from the input design variable values, making it possible to quickly generate the computational grid for each Euler analysis. Full linear theory results were used to pre-screen the design space to decide which variables were expected to be important when the full Euler analysis was run, and to find an approximately optimal configuration so that the ranges on the design variables could be kept smaller.

Kale, Joshi and Pant [68] used axisymmetric CFD analysis to calculate the drag coefficient of aerostats, with are aerodynamically-shaped, lighter-than-air objects tethered to

the ground. The aerostat envelope was represented by a body of revolution with a cross-sectional shape determined by six parameters. RSEs were created for the drag coefficient as a function of the geometry parameters in a number of different Reynolds number regimes, using axisymmetric viscous CFD analysis. The RSEs were presented as an alternative to empirical relations which could subsequently be used in multidisciplinary optimization applications to replace the need to call expense CFD calculations.

Finally, Poteet and Blosser [111] implemented a design of experiments approach using high-fidelity computational hypervelocity impact simulations to determine the most effective place to add mass to a metallic thermal protection system of a reusable launch system to improve hypervelocity impact protection.

These studies were conducted using true high-fidelity analysis methods and demonstrated the appropriate use of approximation methods to facilitate their use in design optimization studies. Several factors limit the extension of the lessons learned from these studies to any general design problem, however: first, the high-fidelity analysis methods were limited to single disciplinary analysis method, and not to a complex analysis process involving multiple interrelated disciplines; and second, in each study the generation of a geometric representation of the design was relatively straightforward due to the simplicity of the geometry—e.g., axisymmetric or two-dimensional—or due to the availability of rapid geometric optimization tools.

Despite the existence of these previous studies, there remain additional technical issues to be worked out before FPA can be implemented in a general sense for any type of conceptual design. A revolutionary engine or aircraft concept would likely require FPA for multiple disciplines having complex interrelationships. In addition, definition of the design geometry with detail sufficient for the use of high-fidelity methods, and the consequent generation of suitable computational grids, cannot always be done in an automated fashion and may require complex sub-optimization to arrive at an appropriate optimized geometry. Many of the techniques demonstrated in the studies cited previously would not be feasible if the execution times for the disciplinary analysis techniques were increased from a few minutes to a few hours, or even several days. For these reasons, it is clear that further research is

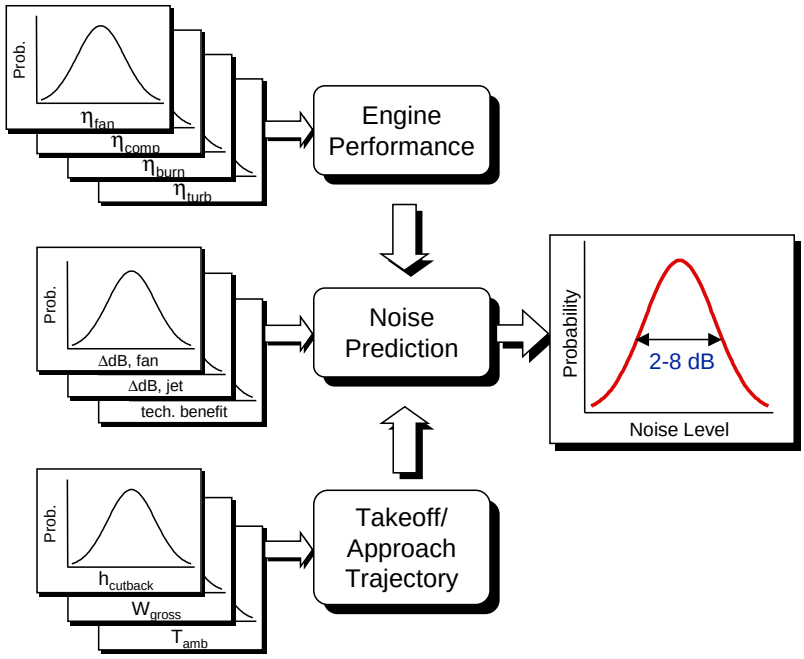

Figure 3: Contribution of individual sources of uncertainty to overall noise risk.

required before the concurrent design paradigm shift can be fully realized for any system.

1.3 Noise guarantees

In the preceding discussions of this chapter and in the previous studies cited to this point, it has been inherently assumed that the analysis methods used in the assessment of a design concept will predict the correct values for the aerodynamics, weight, impact tolerance, etc. of a conceptual-level system. Unfortunately, it is impossible to predict perfectly the measured noise levels of a future aircraft due to inherent uncertainties that are always present prior to actual tests on a full-scale system. There are uncertainties in the mission requirements, including the size and performance of the aircraft if the aircraft and engine are being designed concurrently; uncertainty caused by the infusion of new technologies; and uncertainty due to limited model fidelity in the engine cycle performance, flight performance and noise prediction methods. When the sources of uncertainty are rolled up, they lead to a total uncertainty in the certification noise levels which typically corresponds to a standard deviation of 1 to 4 EPNdB at the preliminary design stage[61] (Figure 3).

A difficult issue facing the designer is the increasing expectations by prospective customers that the purchase of a new aircraft or gas turbine engine will backed by guarantees on fuel efficiency, reliability, weight, and emissions and noise. An airframe manufacturer is typically required to guarantee to a customer that its aircraft will not exceed maximum allowable community, interior, and ramp noise levels. In addition, an airline may request or demand compliance with restrictions at specific airports at which the airline plans to operate the airplane. These guarantees are often a very important factor in competition among airplane and engine manufacturers[61].

For a completely new airplane design with new engines, a decision on airplane go-ahead and customer guarantees usually must be made at early design stages when the uncertainties are high. To account for the uncertainty in the final noise levels, the aircraft must be designed from the start so that the nominal noise prediction is sufficiently below the guarantee levels to reduce the design risk to an acceptable level. Since reductions in noise levels carry an associated economic penalty, the aircraft will typically be unduly penalized since there is a high probability that the operational noise level ultimately falls below the targeted level. The more accurate the prediction of the aircraft's weight, performance and environmental impact, the smaller the economic penalty that must be designed into the system. Increased fidelity in noise analysis early in the design process could reduce the modelling uncertainty, allowing for smaller initial margins for the same design risk. This would help reduce the economic penalty required to meet the guaranteed noise levels since the probability of falling significantly below the target would be reduced.

Risk can be defined as uncertainty in the ability to achieve mission and operational requirements, schedule or cost goals during design and development[18]. Sources of risk can be grouped into four categories:

1. Technology risk, which is caused by uncertainty in the projected benefits of new technologies due to limited previous demonstration of their functional performance and the need for unique fabrication and test facilities.

2. Mission and operational risk, which may be caused by complex or poorly-defined

mission requirements or requirements for greater reliability or maintainability than previously achieved.

3. Risk due to dependence on outside factors such as the need to make significant changes to support facilities and equipment.

4. Programmatic risk due to uncertainty in estimating and planning program schedules and cost and the possibility that technology setbacks could impact the schedule and cost.

In this study, the emphasis is placed on assessment of *technical* risk, which is the uncertainty in the performance of a new system or its components, and may include risk in the feasibility of a design concept[27][120].

To properly assess the risk of failing to meet the design constraints or performance and noise targets, it is necessary to accurately predict the probability distributions for each of the design metrics using *probabilistic methods*. Much past research has worked to create the foundations for probabilistic analysis in engineering design, and for developing methods by which the design of an aerospace system can be conducted in a manner which accounts for the inherent uncertainties. DeLaurentis and Mavris[33] described a robust design methodology which uses approximation methods, such as RSM, in a manner similar to the deterministic studies seen previously in Section 1.2; in this case, however, instead of approximations for deterministic outputs, probabilistic analysis is used to find the probability distribution of the output and the approximations are created for the varying confidence levels from the distribution. The methodology was demonstrated using a robust design study for an HSCT to maximize robustness in the vehicle's affordability while meeting stability, handling quality, and control authority constraints at critical points in the flight envelope.

Mavris, Macsotai and Roth [91] demonstrated these concepts by creating probabilistic RSEs for a commercial transport engine. RSEs were created relating the failure probabilities of design range and engine design constraints to several engine cycle design parameters, and the engine cycle design was optimized to minimize the probability of failure subject to the probabilistic constraints.

Mahadevan and Smith [85] investigated techniques for probabilistic analysis and optimization in the multidisciplinary design of aerospace systems. The optimization problem was demonstrated by minimizing a cost-related objective—vehicle empty weight—subject to a risk-based constraint—-the probability of failing to satisfy a pitching-moment condition. The study also made use of RSEs to relate the empty weight to the vehicle geometry parameters, and a first-order reliability calculation method was used to assess the risk of exceeding the pitch-up constraint.

Mavris and Hayden [90] used vortex lattice potential flow analysis for wing aerodynamic loading, combined with an equivalent laminated plate analytical method to compute the weight of the structural components of an HSCT wing. RSEs were created for the optimized wing structural weight as a function of parametric planform geometry variables, and the RSEs were used in mission analysis calculations to replace empirical wing weight equations. A probabilistic assessment of the vehicle's gross weight was performed using deterministic wing, horizontal tail and vertical tail planform geometry and engine design variables rather than uncertain variables. By assigning uniform distributions to the design variables and performing probabilistic analysis as if they were uncertain variables, the study gave an initial estimate of the proportion of the design space in which the design was feasible.

Bozkaya et al [12] demonstrated that probabilistic analysis can be used even for a higher-fidelity analysis process. In their study, aa variable-fidelity analysis process for solid rocket motors was created by combining quasi one-dimensional analysis of ballistic performance with finite-element analysis of nozzle stress levels. RSEs were created relating the required nozzle performance parameters and structural reliability of the nozzle to uncertainty due to finite manufacturing tolerances and variations in propellant properties, structural material properties and operating conditions. The RSEs were then used to provide analysis results during a Monte Carlo analysis to calculate the probability of the nozzle failing to meet its performance requirements and the probability of structural failure of the nozzle case.

Finally, Garzon and Darmofal [44] demonstrated techniques for robust design optimization using FPA. They used a fast-executing blade-to-blade Euler flow analysis coupled with

a boundary layer analysis method to analyze a transonic compressor blade section. Probabilistic analysis was conducted for the nominal compressor geometry to determine the baseline performance distribution, using three different probabilistic analysis methods for comparison: direct Monte Carlo analysis, Monte Carlo analysis combined with RSEs, and Gaussian quadrature. RSEs were created relating the mean and standard deviation of each performance parameter to the incidence and deviation angles and the blade relative thickness. Finally, optimization was performed to find the best values for the incidence angle, deviation angle and blade thickness to minimize the mean total pressure loss while maintaining a minimum mean flow turning angle.

These previous studies developed a variety of methods for assessing the effects of uncertainty on the variability of performance measures and constraints for aerospace systems, and demonstrated techniques for handling the large numbers of functional analyses required to calculate probability distributions and failure probabilities. Like the studies in the previous section, however, the applicability of these techniques to highly-complex systems with analysis processes that may require days to execute is not clear. Further research is required to demonstrate that the combination of probabilistic analysis, robust design techniques, and very complex FPA processes can indeed be used in the conceptual design phase and to demonstrate that these concepts can be extended to any type of system.

1.4 Goal and motivation

As outlined in the previous sections, using first-principles noise analysis earlier in design and development of a new aircraft or engine could benefit the process by accelerating the acquisition of design knowledge and reducing the uncertainty in the noise levels of the final design. This research was motivated by the fact that, due to the complexity of acoustic analysis, true physics-based noise analysis normally cannot be carried out until detailed geometry and flow field information is available. At the conceptual stage, the only available recourse for analyzing new concepts has been either through the use of empirical curve fit equations or experimental results for designs with similar features. While often providing accurate results for engine and aircraft designs which are similar to previous designs, these

methods are inadequate for analyzing new concepts which are significantly different than their predecessors.

The fundamental goal for this research was to develop a methodology for the conceptual design and risk analysis of quiet commercial aircraft using noise analyses which are based on first principles. Techniques were sought out which make it practical to incorporate higher-fidelity noise analysis into early design stages, thus improving the knowledge which can be gained about the design, while still retaining the flexibility to examine many different combinations of design variables so as not to limit the design freedom. In addition, methods were used for estimating the variance in the overall noise levels due to the presence of underlying uncertainty, and for examining the effect of design variables on the overall noise risk.

1.5 Research questions and hypotheses

To achieve the goal of this research and bridge the gap between the traditional empirically-based conceptual design methodology and a new process incorporating first-principles analysis, it was necessary to answer three research questions:

1. How can greater accuracy and applicability of noise analysis be incorporated into the conceptual design process while retaining the ability to rapidly evaluate a large array of designs?

2. How do inherent uncertainties affect the variations in the certification and operational noise levels of an aircraft concept?

3. Can the design risk associated with meeting a noise goal be contained through careful design choices at the conceptual level?

Question 1 highlights issues which have previously been roadblocks to the use of physics-based analysis earlier in the design process, while Questions 2 and 3 have largely remained unanswered in the traditional process, but could be answered if the acquisition of design knowledge could be accelerated as proposed. In an attempt to answer the research questions, the following three hypotheses were proposed:

Hypothesis 1: It is possible to use first-principles noise analysis at the conceptual design stage to predict the noise levels of an aircraft concept while still retaining the ability to evaluate a large design space.

Hypothesis 2: It is possible to quantify the effect of uncertainty in analysis, manufacture, and operation of an aircraft on the variation of the certification noise levels.

Hypothesis 3: It is possible—through reduction in absolute noise levels, variance due to uncertainty, or both—to develop a strategy for multidisciplinary optimization of a conceptual aircraft to reduce the risk of exceeding a set of targeted noise levels.

Hypothesis 1 makes no qualifications about the complexity or execution time the first-principles methods which can be used in conceptual design, so it was important that the methodology be applicable for any analysis process regardless of whether it requires a few seconds to run or a few days, and regardless of whether the analysis requires a simple description of the geometry or a full three-dimensional representation of the engine or airframe. For this reason it was important to demonstrate the methodology using an analysis process with sufficient complexity, complex problem setup, and detailed geometric definition to make it impossible to use directly in any sort of meaningful design studies.

Hypothesis 2 has been proven in previous work for simple physical models which can be executed rapidly. Accurate quantification of the variation of the noise levels tends to require many analysis runs which may be in addition to the many analyses required for design studies involving parametric variation and optimization. It is when the desire to use first-principles analysis is combined with the need to quantify the effects of uncertain that probabilistic analysis becomes a true challenge.

It is clear from Hypothesis 3 that simple estimates of the uncertainty are not sufficient for robust design studies which examine techniques for reducing both absolute noise levels and variance due to uncertainty. Robust design involves more than a quantification of the uncertainty at the deterministic optimum, since the robust design point often does not coincide with the deterministic optimum. A strategy for reducing the risk of exceeding the noise targets requires knowledge of the influence of the design variables on both the mean

noise levels and their variance.

To test these hypotheses, a research program was formulated whose goal was to devise a methodology for combining modern concurrent design and risk analysis methods with a physics-based noise analysis process and demonstrate its use as a conceptual design tool. First, a prototype analysis process was assembled to analyze the low-speed performance and noise characteristics of a conceptual aircraft concept based on its engine and airframe design characteristics. This analysis method uses FPA methods to compute the levels for two representative noise sources—fan rotor-stator interaction tones, and jet mixing broadband noise—but for reasons to be explained, not all of the sources were represented by FPA methods. Second, a methodology was devised for using the results of the new analysis process in rapid trade studies and risk analysis. Finally, the methodology was used to conduct a series of proof-of-concept conceptual trade studies which demonstrate how the physics-based analysis process can be used for the same types of studies as empirical methods, but can provide more knowledge about the design than a purely empirical analysis process.

The remainder of this thesis will describe the methods, results and conclusions of the research program. Chapter 2 provides background information on the aircraft noise assessment process, and briefly describes the various sources of aircraft noise and their physical mechanisms. Chapter 3 describes the two first-principles analysis methods used to analyze the fan interaction tones and jet mixing noise. Chapter 4 then describes how the noise analysis methods were integrated with methods for engine cycle analysis, fan rotor preliminary blade design, aircraft flight performance, and noise propagation analysis to create the prototype analysis process; results of validation studies for the two physics-based noise analysis methods are also discussed. Chapter 5 lays out the approximation and probabilistic analysis techniques used in conjunction with the analysis process to facilitate its use in conceptual design trade studies and risk analysis. Chapter 6 gives a detailed examination of the results of the analysis process as applied to the baseline aircraft, describes the process used to create the rapid metamodels used in subsequent analysis studies, and presents results of

a probabilistic analysis for the baseline. Chapter 7 discusses the results of the proof-of-concept trade studies. Finally, Chapter 8 discusses how the results of the research program relate to the hypotheses which were discussed in this section, lists the lessons learned in the process, and makes recommendations for further research in this area.

CHAPTER II

BACKGROUND

2.1 Aircraft noise assessment

Since the vast majority of problems caused by aircraft noise arise in the vicinity of airports and those restrictions which define the actual allowable noise levels have been made with the airport community in mind, this study focused only on the noise produced by the aircraft during the takeoff and landing portions of flight, also known as community noise. Noise produced during other portions of the flight envelope, such as high-altitude flight (en route noise) and sonic boom, was considered outside the scope of the research.

Community noise measurement and prediction involve a large array of different metrics, which are described in detail in Appendix A. Assessment of community noise impact can be divided into two categories:

1. Certification noise levels, which are measured and regulated under the requirements of the International Civil Aviation Organization (ICAO) Annex 16, Chapter 4 noise regulations, and in the United States under the Federal Aviation Regulations (FAR) Part 36, Stage 4[100]. An aircraft is flown through standardized takeoff and approach procedures, and the 1/3-octave band frequency spectrum time histories are measured at three locations: sideline and takeoff locations during the takeoff maneuver, and an approach location during the approach maneuver (Figure 4). The unit of measurement for certification noise is the effective perceived noise level (EPNL), described in Appendix A, and the maximum noise levels for the three measurement locations are specified as a function of maximum takeoff weight and the number of engines. The maximum EPNLs for the three locations are shown in Figure 5 for Stage 3 certification. As of January 1, 2006, all new commercial aircraft are required to meet ICAO Chapter 4 noise limits[16], which require that (a) Stage 3 limits are not exceeded at any measurement location, (b) the sum of the differences between the Stage 3 limit

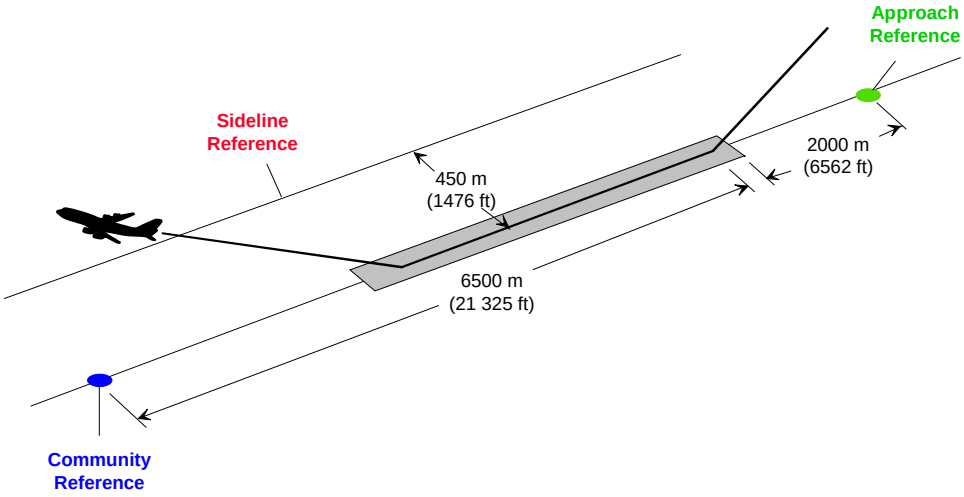

Figure 4: Observer locations for FAR 36 certification. The sideline observer is located along the sideline at the point where the noise level is greatest.

and the measured noise level at the three locations is at least 10 EPNdB, and (c) the sum of the differences is at least 2 EPNdB for any pair of locations.

2. Airport noise contours, which are a direct measure of the community noise exposure resulting from arrival and departure procedures of an aircraft at specific airports. The unit of measurement is the day-night noise level (DNL), which begins with the measured time history of the A-weighted noise level, which weights frequencies based on their perceived loudness to the average human ear, imposes an additional 10 dBA penalty to noise levels measured between 10 pm and 7 am to account for the potential for sleep disturbance, and integrates it over a 24-hour period. The community impact is then expressed as contours of the one-year average of the DNL. Under the requirements of FAR Part 150[1], each public airport in the U.S. is required to develop a noise exposure map which shows predicted DNL contours for the area surrounding the airport; such a noise exposure map is used for land use planning and for government-funded residential sound insulation programs.

Airport noise contours involve every aircraft flying into or out of an airport, and so they are not very useful as a noise metric for new conceptual aircraft designs. In this research, therefor, noise levels were only calculated at the three FAR 36 measurement locations. In general, reductions in the certification noise levels will correspond to reductions in the noise

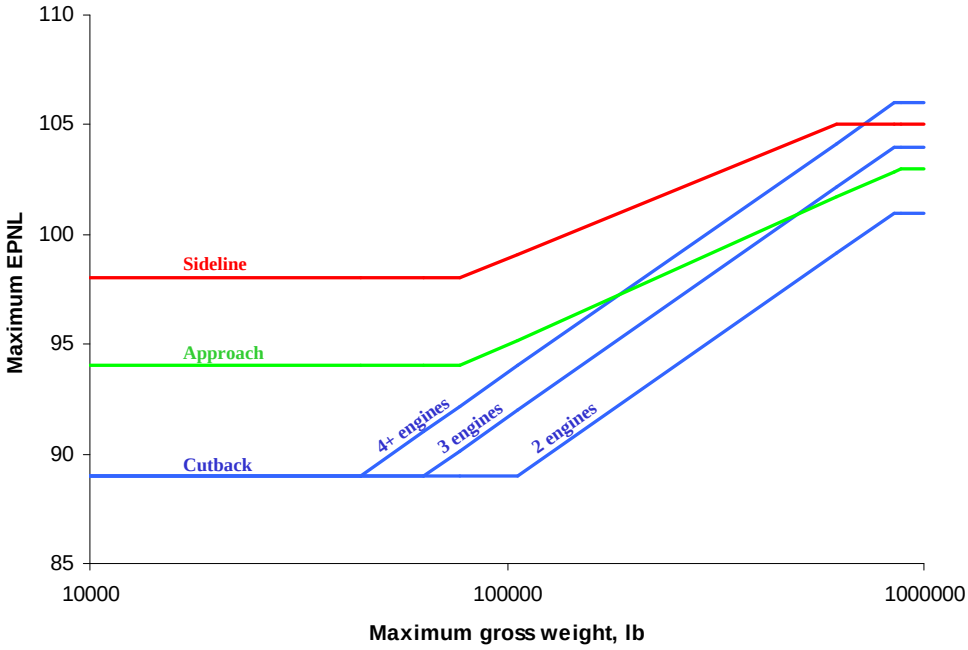

Figure 5: FAR 36, Stage 3 noise limits.

levels surrounding an airport during actual operations. Because of the differences in the frequency weighting curves of the two noise metrics, however, the reductions may not be of the same magnitude.

2.2 Sources of aircraft noise

Noise is generated whenever the passage of air over the aircraft or through its engines causes fluctuating pressure disturbances that propagate to an observer[123]. The majority of propulsion-system noise can be categorized as either *tonal* noise, which occurs at discrete frequencies, and *broadband* noise, which is composed of random and uncorrelated pressure fluctuations over a broad range of frequencies. Figure 6 shows the importance of the individual engine and airframe components to the total noise at the approach and takeoff measurement locations for a high-bypass turbofan engine. The noise generation mechanisms of each of these components are described individually in the following sections. Due to the logarithmic nature of the sound pressure level, the total noise level is almost entirely driven by the components with the highest levels, while any components which are significantly quieter have very little effect on the total. The levels of the individual components vary

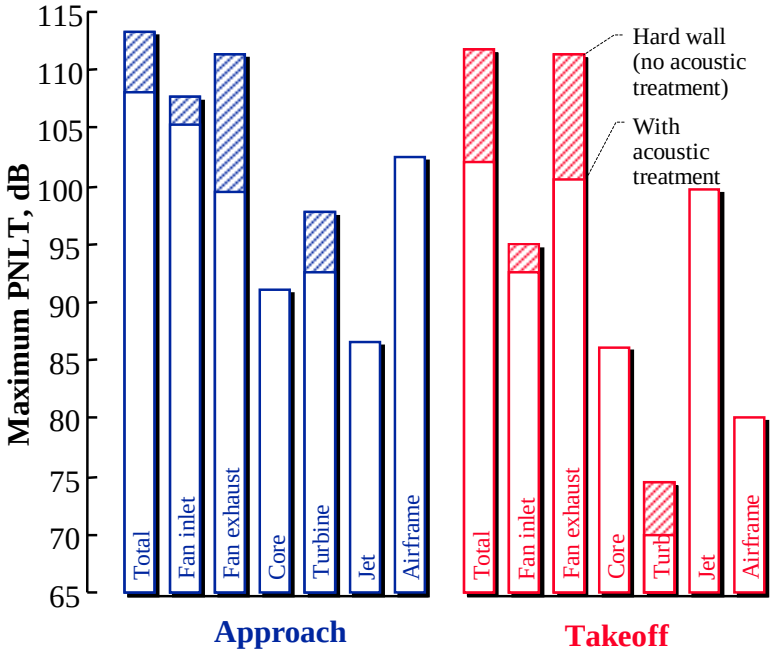

Figure 6: Relative contributions of individual components to approach and takeoff noise for a high-bypass turbofan engine[102].

individually as functions of the engine power setting and the flight conditions, so the noise sources which are dominant change from one flight condition to another. At takeoff power, the most important noise sources are the fan inlet and exhaust noise and the jet noise. At approach power, however, the jet noise is much lower, but the airframe noise becomes much more important due to the heavy use of high-lift devices during approach.

2.2.1 Fan and compressor noise

The primary fan noise source mechanisms are illustrated in Figure 7. Like all rotating machines, fan and compressor noise exhibits both tonal and broadband characteristics. The broadband noise results from pressure fluctuations associated with turbulent flow in the wall boundary layers and blade wakes, which interact with solid surfaces such as rotating blades and stationary vanes. Broadband noise is generated as the tip of the fan blade moves through the turbulent boundary layer close to the duct wall and as the turbulent blade wakes pass over the stator vanes[55].

Discrete tones are generated when there is a periodic interaction between pressure fields or turbulent-wake disturbances and a rotating or stationary blade row. These interactions

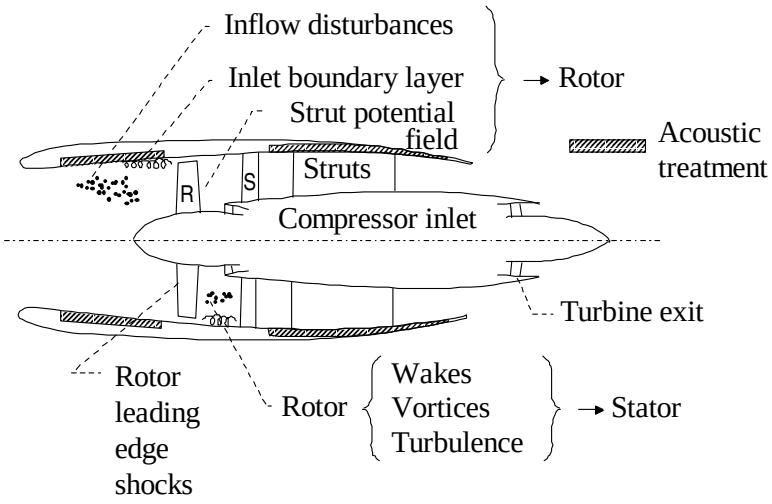

Figure 7: Fan noise source mechanisms.

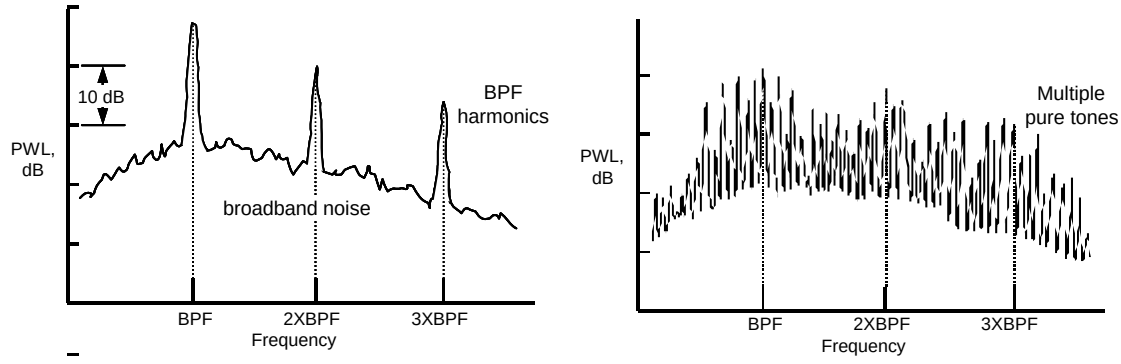

(a) subsonic (b) supersonic

Figure 8: Typical fan noise spectra for subsonic and supersonic tip relative Mach numbers.

can be the result of inflow distortion interacting with the rotor, interactions between the pressure field of the rotor with the stator or pylons, impingement of inlet guides vane wakes on the rotor blades, or impingement of the rotor wake on the stator. The rotating and stationary rows are normally spaced sufficiently to keep the pressure-field interaction below the level of wake interaction, but strong interaction tones can still result from the impingement of rotor wakes on the core and fan stators and downstream struts, and if the inflow air is significantly distorted—such as at high angle of attack—significant tones can be generated. These tones occur at harmonics of the blade-passing frequency (BPF), which is the shaft speed multiplied by the number of rotor blades.

Another source of discrete tones occurs at supersonic relative tip Mach numbers, when shocks develop at the blade tips; if the shocks do not impinge on neighboring blades but instead are free to propagate upstream, they result in multiple pure tones (MPT), also called combination or "buzz-saw" tones. Due to manufacturing differences and operational wear and tear, minor differences always exist in the shapes and aeroelastic response of the individual rotor blades in a fan, so each blade produces a unique shock pattern. As each shock rotates with the blade, the resulting pressure fluctuation is perceived in the far field as tones. Since the pressure fluctuations are unique for each blade, the multiple pure tones occur at harmonics of the shaft speed, rather than the BPF.

Figure 8 shows typical sound power level (PWL) spectra for a fan operating at subsonic and supersonic relative tip speeds. The subsonic spectrum consists of the broadband spectrum overlaid with discrete tones at harmonics of the BPF. The supersonic spectrum also consists of a broadband spectrum and interaction tones, with the addition of many multiple pure tones, at harmonics of the shaft speed, which can dominate the power spectrum over a wide range of frequencies.

2.2.2 Combustion noise

The combustion process in a gas turbine combustor is designed to be turbulent for several reasons. First, the turbulence facilitates efficient mixing of the fuel and air, and between the hot products of combustion and dilution air, which leads to a smaller flame, a shorter

mixing zone, produces a more-uniform exit temperature field and ensures more complete combustion for improved efficiency and lower harmful emissions. Second, the turbulent flow helps anchor the flame in a well-defined location. Unfortunately, the turbulent mixing and combustion process is a significant source of broadband noise[86][123].

Combustion noise can be categorized as either direct or indirect: *direct* combustion noise is produced when a volume of fuel-air mixture expands at constant pressure as it is rapidly heated by combustion, pushing back the cooler surrounding gas and therefore performing work on it; while *indirect* combustion noise results when relatively large-scale temperature non-uniformities are convected through pressure gradients in the turbine, producing density fluctuations which propagate through the surrounding gas. It is not clear which mechanism dominates in a gas-turbine combustor, although preliminary evidence indicates that the indirect mechanism is more important[86].

2.2.3 Turbine noise

Turbine noise is similar to fan and compressor noise in that it is produced by a combination of rotating and stationary components which contribute both tonal and broadband noise components to the overall spectrum. Since the spacing in a turbine is much smaller than in a fan, there are a great many sum and difference tones which dominate the spectrum. In addition, non-uniformities in the flow field leaving the combustion chamber can have a powerful influence on the generation of tones. At full power, the nozzle guide vanes between the combustion chamber and the first turbine run choked, so no noise propagates upstream and all the energy passes through the core nozzle. As the wave fronts propagate through the turbulent shear layer of the jet, the waves are diffracted so that the directivity pattern is shifted toward the inlet axis and the sharp tones become broadened, or "haystacked"[123].

2.2.4 Jet noise

Jet noise refers to the sources associated with the mixing between the exhaust flow of an engine and the atmosphere, and with the shock system that forms in an imperfectly-expanded exhaust with supersonic velocity. The origins of the jet mixing noise spectrum are shown in Figure 9(a), while Figure 9(b) shows a typical jet sound pressure level (SPL) spectrum for

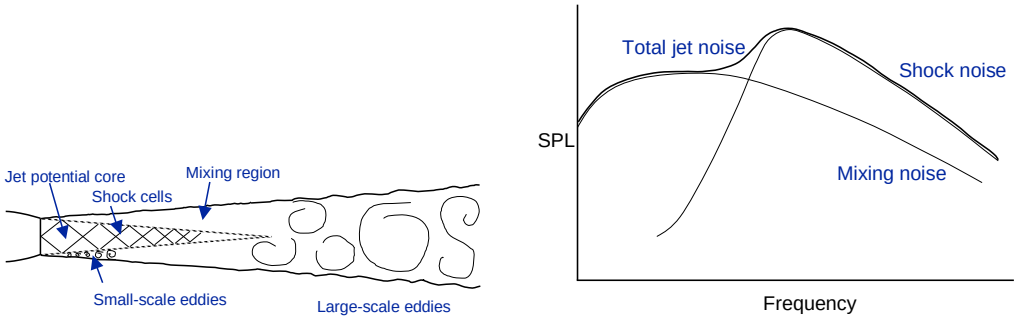

(a) jet structure (b) typical high-speed jet noise spectrum

Figure 9: Sources of jet mixing and shock noise[123].

a given directivity angle. The jet contains a combination of small-scale, quasi-homogeneous turbulence and large-scale eddies or instability waves, which control the growth of the mixing region and entrainment of ambient air into the jet. Both the small-scale turbulence and the eddies increase in size progressively downstream of the nozzle and decay in intensity as the mixing is completed, resulting in a broadband mixing noise spectrum over a wide range of frequencies[123].

For subsonic jets, large turbulence structures and instability waves play an important role in the dynamics of the fluid, but they do not appear to be efficient noise generators. Many experts believe that the small-scale turbulence is the dominant source of noise in subsonic jets, though this belief has not been universally accepted. In supersonic jets, large turbulence structures and instability waves are believed by some experts to be directly responsible for the dominant part of the noise generation mechanism; and additional shock-associated noise results from the turbulent eddies in the mixing layer interacting with the periodic shock structure in the potential core. Shock noise is usually more prevalent in the forward quadrant where the mixing noise is lower[126].

2.2.5 Airframe noise

With the landing gear, flaps and slats retracted, the noise from the airframe is produced by turbulence generated in the boundary layers surrounding the aircraft. Since the air travels over the airframe at a wide range of distances from several centimeters to many meters, the scale of turbulence generated varies considerably and the resulting broadband noise appears

over a large frequency range. Most of the noise from the clean configuration is believed to emanate from the wing. Fairly strong tones may also be observed due to vortex shedding at the wing trailing edge.

At most flight conditions important to community noise measurement, one or more of the flaps, slats and landing gear are usually deployed. In this case, the broadband noise from the high-lift devices and landing gear dominates the airframe noise levels. Airframe noise levels are most important at approach when the landing gear are extended, the high-lift devices are fully extended, and the engines are operating at very low power. The high-lift devices and landing gear can increase the overall airframe noise level by 10 dB relative to the clean airframe[123]. The noise due to high-lift devices is predominantly generated by strong vortices at the side edges of trailing-edge flaps interacting with the solid surface of the flap[84]. The noise due to landing gear is generated by unsteady separated flow over the blunt components of the undercarriage[28], including pipes, cables, ducts and linkage exposed to the air stream during gear deployment.

CHAPTER III

APPROACH

3.1 Assumptions

Even though the goal of this study was to use higher-fidelity noise analysis methods, there was still an upper limit to the execution time which could be tolerated while being able to analyze a sufficient number of design points. Computation of source noise generation and propagation through the atmosphere using computational aeroacoustics (CAA) methods was not feasible. The noise analysis methods which were used had to fit certain criteria to be appropriate for use in this study: (1) the method must be applicable to the aircraft and engine configurations and the technologies to be studied; (2) the acoustic method must be based primarily on the laws of physics, with empiricism limited to secondary aerodynamic phenomena such as computational fluid dynamics (CFD) turbulence models; and (3) the entire analysis for one configuration at one flight condition must run in a reasonable time—less than a day on a reasonably fast computer. Due to these requirements it was necessary to reject some of the most complex methods and limit the approach to more rapid methods which involve some simplification of the physical problem, either through a simpler representation of the geometry to allow closed-form solutions to the governing equations, or through linearity assumptions in the physical equations which allow decoupling of the mean-flow and acoustic portions of the flow field.

Table 1 gives a list of the existing physics-based or hybrid physics-based/analytical approaches for calculating the noise levels of the individual components of aircraft noise. This list only includes fully-implemented engineering analysis methods which can calculate the far field noise levels of an actual full-scale engine, rather than research codes that might be used to model the sound generation of the source without relating it to far field levels. For sources where more than one modelling approach exists, the methods are listed in decreasing order of complexity and analysis time. While research methods might currently

Table 1: Summary of existing physics-based noise analysis methods.

Noise source	Existing approaches
Fan rotor-stator tone	Unsteady Navier-Stokes[10][132]
	Linearized unsteady Euler[138]
	3D linear theory[133]
	Strip theory[106]
Fan broadband	Strip theory[32][43][67]
Fan MPT	Nonlinear propagation models[92][135]
Fan distortion	Ffowcs Williams-Hawkings[48]
	Strip theory[87]
Core	GE indirect method[51]
Turbine	None
Jet mixing	Large-eddy simulation
	CFD + linearized Euler
	CFD + Kirchhoff surface
	CFD + acoustic analogy methods
	Instability wave models
Jet shock	None
Airframe	Ffowcs Williams-Hawkings[121][122]

exist for turbine noise and jet shock noise, engineering methods do not currently exist for these sources.

Implementing an analysis process using FPA methods for every available noise source would be an enormous undertaking and could only be carried out by a large organization. For this study, it was necessary to limit the number of FPA methods used in the analysis process to a small subset of those in Table 1. As seen in Chapter 2, fan and jet noise are the two most important sources for a typical high-bypass engine at takeoff power, so high-fidelity analysis for these two sources was emphasized in this research. Independent methods exist for both the tonal and broadband components of fan noise, but to limit the scope of the research, attention was given to just the tonal component since without advanced noise reduction technology it is the dominant component of the generated fan noise. Computation of jet noise was limited to the turbulent mixing noise which is believed to be the dominant mechanism at subsonic speeds, and the analysis was restricted to engines with unmixed bypass flows so that the analysis could be limited to thin shear layers and axisymmetric computations rather than large-scale turbulent mixing on a three-dimensional grid. In the

following sections, the analysis methods used for these two sources will be described in detail.

3.2 Fan interaction tone noise

Several approaches exist for analysis of the fan rotor-stator interaction tones. These fall into two general categories: time-domain methods and modal decomposition methods. Time-domain methods involve direct computation of the rotor and stator viscous flow fields in the time domain of sufficient grid density and time accuracy to capture the fluctuating portion of the pressure field in the immediate vicinity of the rotor and stator[74][114]. Computation times are typically on the order of many hours even when a massively parallel architecture is used.

Modal-decomposition methods involve independent solution of the viscous rotor-stator aerodynamic flow field and the noise generation and thus are much less computationally intensive, so they were suitable for use in this research. The tone noise generated at the stator can be computed using a spectral decomposition of the computed rotor wake velocity deficit, combined with a linear stator response model. To model the generation of noise and its subsequent propagation to the far field, it is necessary to account for four physical processes: unsteady response of the rotating or stationary blades to an inhomogeneous flow field, acoustic coupling of generated pressure fields to the inlet and exhaust ducts, near-field propagation of the pressure field within the duct, and acoustic coupling—i.e., radiation—to the far field[55]. Modelling of each of these processes is described in the following sections.

3.2.1 Unsteady blade/vane response

Analysis of fan noise begins with knowledge of the steady aerodynamic flow field through the rotor and stator rows. The velocity deficit in the wakes must be established from experimental measurements or through empirical relationships, boundary layer analysis or CFD; at the stator vanes, the velocity deficit may then be modelled in the stationary frame of reference as a periodic gust. If the incident periodic gust is assumed to be invariant with position as it is transported with the mean flow velocity U across the stator row, the

mathematical description of the gust velocity, $\vec{u}_\infty$ takes the form

$$\vec{u}_\infty = \vec{a} \exp\left[i\left(\vec{k}\cdot\vec{y} - k_1 U t\right)\right] \tag{1}$$

where $\vec{a}$ is the vector magnitude, the coordinate system, $\vec{y}$, is fixed to the blade with the y_1 direction along the blade chord and y_2 normal to the chord, and the wave number vector is $\vec{k} = (k_1, k_2, k_3)$[55]. The velocity component along the y_2 direction is the upwash and is responsible for the blade pressure fluctuations in a linearized approximation. The time-varying normal force per unit span, F_2, is given by

$$F_2 = \pi \rho_\infty U a_2 c \exp\left[i\left(k_3 y_3 - k_1 U t\right)\right] G(k_1, k_3, M_r) \tag{2}$$

c is the blade chord, ρ_∞ is the ambient density, c is the local speed of sound and G is the response function for a gust of wave number vector $\vec{k}$ convecting at Mach number M_r relative to the blade. If the incident rotor wake is decomposed into a continuous frequency spectrum of vortical velocity disturbances, the solution for the fluctuating blade pressure can be found using a superposition of solutions in the form of Equation 2. Several analytical solutions for G exist for special simplified cases involving two-dimensional geometry, single airfoil, incompressible flow, infinite span or a high-frequency limit.

3.2.2 Coupling to the duct

A turbomachinery component is surrounded by a duct which acts as a wave guide to the acoustic pressure field; therefore, the coupling of the generated pressure field to the duct must be accounted for and the resulting modal pressure field predicted. Consider an infinite, hard-walled annular duct with inner radius r_h and outer radius r_t through which air is flowing with a uniform mean velocity U (Figure 10). In this case, the wave equation reduces to

$$\frac{1}{c^2}\left(\frac{\partial}{\partial t} + U\frac{\partial}{\partial z}\right)^2 p' = \nabla^2 p' \tag{3}$$

where p' is the acoustic pressure[42]. For a hard-walled duct, the boundary conditions at the inner and outer duct walls are given by

$$\begin{aligned} \frac{\partial p'}{\partial r} &= 0 \quad \text{at} \quad r = r_t \\ \frac{\partial p'}{\partial r} &= 0 \quad \text{at} \quad r = r_h \end{aligned} \tag{4}$$

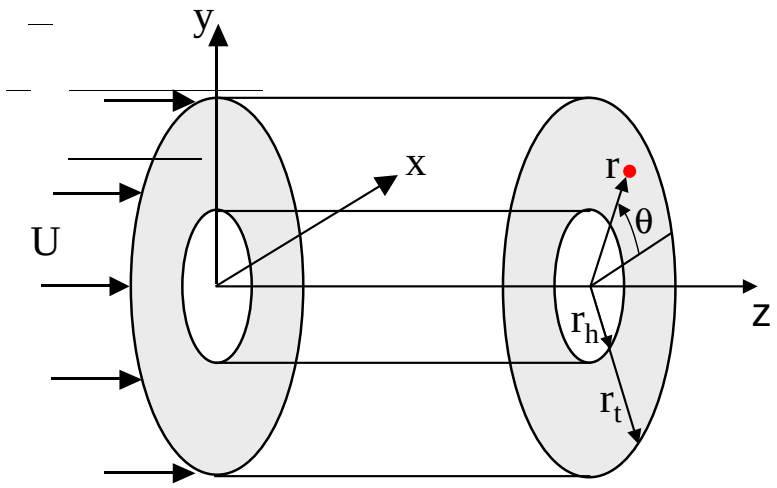

Figure 10: Infinite annular cylinder with uniform mean flow.

A separable solution to Equation 3 exists of the form

$$p'(r,\theta,z,t) = P(r)\exp i\left(\omega t - k_z z \pm m\theta\right) \tag{5}$$

where $\omega = kc$ is the radial frequency, m is the circumferential mode number, and k_z is the axial wave number. The general solution for the radial component of the solution, P(r), is

$$P(r) = AJ_m\left(\kappa r\right) + BY_m\left(\kappa r\right) \tag{6}$$

where

$$\kappa^2 = k^2 - 2kk_z M - k_z^2\left(1 - M^2\right) \tag{7}$$

J_m and Y_m are the Bessel functions of the first and second kind, respectively, of order m, A and B are constants, and $M = U/c$ is the mean-flow Mach number. To satisfy the wall boundary condition (Equations 4), the radial derivatives of $P(r)$ must be zero at the inner and outer walls, so if both A_m and B_m are to be non-zero it is necessary that

$$\begin{vmatrix} J'_m\left(\kappa r_t\right) & Y'_m\left(\kappa r_t\right) \\ J'_m\left(\kappa r_h\right) & Y'_m\left(\kappa r_h\right) \end{vmatrix} = 0 \tag{8}$$

This is a transcendental equation with countably infinite number of roots for each value of m. If $\kappa_{mn} r_t$ is defined as the n^{th} root of the equation, $n = 1, 2, 3, \ldots$, then p'_{mn} is the corresponding acoustic pressure and n represents the radial mode order. Since the analysis

is linear, it is possible to build up the acoustic pressure from a superposition of an infinite number of modes, (m, n). Therefore, the general solution for the acoustic pressure is

$$p'(r,\theta,z,t) = \sum_{m=-\infty}^{\infty} \sum_{n=0}^{\infty} \left[A_{mn} J_m(\kappa_{mn} r) + B_{mn} Y_m(\kappa_{mn} r)\right] \exp i\left(\omega t - k_z z \pm m\theta\right) \tag{9}$$

where

$$\frac{k_z}{k} = \frac{-M \pm \sqrt{1 - (1 - M^2)\left(\kappa_{mn}/k\right)^2}}{1 - M^2} \tag{10}$$

As seen in Equation 10, for each mode the relationship between k_z and k is solely a function of κ_{mn}. When $\kappa_{mn} < k/\sqrt{1 - M^2}$, k_z is a real number and propagation of the mode can occur in either direction in the duct. When $\kappa_{mn} > k/\sqrt{1 - M^2}$, however, k_z is imaginary and the solution decays exponentially; in this case, the mode is said to be *cut off*. For modes which are cut off, decay occurs quite rapidly and the duct is typically long enough for the mode to be essentially eliminated.

For a rotor with B blades turning at an angular velocity Ω, and V stationary stator vanes, only the following circumferential modes can exist:

$$m = qB + sV, \qquad q = 1, 2, 3, \ldots, \qquad s = 0, \pm 1, \pm 2, \ldots \tag{11}$$

Note that m can be either positive or negative. In Equation 11, q represents multiples of BPF, so the circumferential modes corresponding to the different harmonics of BPF are

$$\begin{aligned} m &= \ldots, B - 2V, B - V, B, B + V, B + 2V, \ldots && \text{for BPF} \\ m &= \ldots, 2B - 2V, 2B - V, 2B, 2B + V, 2B + 2V, \ldots && \text{for 2BPF} \\ m &= \ldots, qB - 2V, qB - V, qB, qB + V, qB + 2V, \ldots && \text{for qBPF} \end{aligned} \tag{12}$$

For each circumferential mode, there are once again an infinite number of radial modes, and the corresponding eigenfunctions are of the form

$$p'_{mn}(r,\theta,z,t) = \left[A_{mn} J_m\left(\kappa_{mn} r\right) + B_{mn} Y_m\left(\kappa_{mn} r\right)\right] \exp i\left(qB\Omega t - k_z z - m\theta\right) \tag{13}$$

To find the magnitudes A_{mn} and B_{mn} of the duct modes, the stator surface pressures computed from Equation 2 can be expressed as an infinite series in the form of Equation 13; the solution is then matched at $z = 0$ to the general solution (Equation 9) for those modes which are not cut off.

The analysis in this section assumes that the fan duct is hard-walled; if the duct is acoustically lined, then the boundary conditions of Equation 4 are different and the solution for the duct modes is affected. The assumption here is that the duct walls are acoustically hard at the stator leading edge where the modes originate, and that the presence of acoustic lining upstream or downstream of the stator leading edge does not affect which modes propagate and which are cut off. The effect of the lining in the inlet and aft fan ducts on the propagating modes can be properly accounted for in the boundary conditions of the propagation analysis of the following section.

3.2.3 Duct propagation and radiation

Consider a model of the fan inlet duct and its immediate surroundings, bounded by as source plane, the nacelle and centerline surfaces, a far field boundary and an acoustic baffle (Figure 11). If it is assumed that no reflection of the propagating waves occurs at the inlet or exhaust of the fan duct, the generation of the duct modes can be calculated as if it occurred in an infinite duct like in the previous section; the modal amplitudes can then be used as a boundary condition at the source plane for separate upstream and downstream propagation calculations.

To solve a radiation problem of this form, it is usually more efficient to combine separate methods for handling the propagation in the near field—the duct interior and the region immediately surrounding the inlet—and the radiation to the far field. In the near field, propagation of the acoustic waves has been modelled using a parabolic approximation to the Helmholtz equation[79]; linear or nonlinear potential flow[105][125], Euler or Navier-Stokes analysis[36][103][118]; or through a CAA approach[75] which calculates the sound generation and near-field propagation together. Radiation to the far field has been analyzed using wave envelope elements[41] or surface integral methods such as the Kirchhoff[103][124] or Ffowcs Williams-Hawkings[34][96][75] methods.

In this study, the near-field propagation is analyzed using axisymmetric linearized potential flow, which reduces the computational time sufficiently for use in this study. By

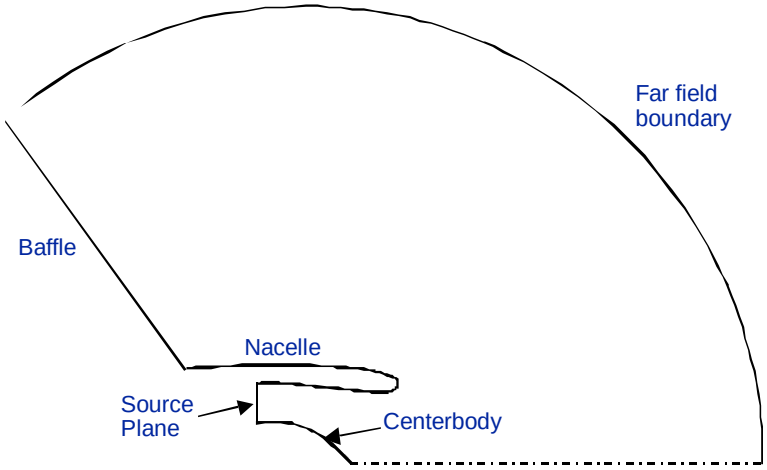

Figure 11: Domain for fan inlet noise propagation calculations.

assuming that all flow and acoustic processes are isentropic and that the acoustic disturbances are small, the governing equations can be separated into mean flow and acoustic contributions of the form

$$\begin{aligned} \nabla \cdot (\rho \nabla \phi) &= 0 \\ \rho &= \left(1 - \tfrac{\gamma-1}{2} \nabla\phi \cdot \nabla\phi\right)^{\frac{1}{\gamma-1}} \end{aligned} \tag{14}$$

$$\begin{aligned} \tfrac{\partial \rho'}{\partial t} + \nabla \cdot (\rho \nabla \phi' + \rho' \nabla \phi) &= 0 \\ \rho' &= -\tfrac{\rho}{c^2}\left(\tfrac{\partial \phi'}{\partial t} + \nabla\phi \cdot \nabla\phi'\right) \\ p' &= -\rho\left(\tfrac{\partial \phi'}{\partial t} + \nabla\phi \cdot \nabla\phi'\right) \end{aligned} \tag{15}$$

where ϕ is the velocity potential and the pressure, density, velocity, velocity potential, and time are non-dimensionalized by the far-field quantities $\rho_\infty c_\infty^2$, ρ_∞, c_∞, $c_\infty R$ and R/c_∞, respectively[115], where R is the gas constant for air. The boundary conditions for the mean flow equations (Equations 14) are

$$\begin{aligned} \nabla\phi \cdot \hat{n} &= U_f && \text{on the fan face} \\ \nabla\phi \cdot \hat{n} &= U\hat{i} \cdot \hat{n} && \text{at the far field boundary and baffle} \\ \nabla\phi \cdot \hat{n} &= 0 && \text{on the nacelle surface} \end{aligned} \tag{16}$$

where $\hat{n}$ is a local normal vector for the surface of interest.

A weak formulation of the steady-state acoustics problem provides a method for computing the acoustic field at the far-field boundary:

$$\iiint \left[\psi \frac{\partial \rho'}{\partial t} - \nabla\psi \cdot (\rho\nabla\phi' + \rho'\nabla\phi)\right] dV = -\iint \psi \left(\rho\nabla\phi' + \rho'\nabla\phi\right) \cdot \hat{n} dS \tag{17}$$

where ψ is a suitable test function and the integrals are performed over the three-dimensional or axisymmetric space in and around the inlet. The nacelle and center body are impervious to both mean flow and acoustic perturbations so they have no contribution to the surface integral on the right-hand side. Assuming that there is no reflection in the far field, a Sommerfield radiation condition can be applied at the far-field boundary so that only an outgoing wave exists. The duct radiation problem can be computed numerically by first solving Equations 14 on a computational grid, subject to the boundary conditions (Equations 16), to arrive at the mean flow properties; after which the radiation problem (Equation 15) can be solved by integrating the acoustic field over the computational domain. Since the boundary conditions at the source plane are defined as modal amplitudes, the integration of the acoustic field also is carried out on a mode-by-mode basis.

3.3 Jet mixing noise

Methods which make a direct prediction of the generation and propagation of jet mixing noise, such as large-eddy simulation or direct numerical simulation methods[56][94], were deemed much too computationally intensive to apply in this study. Methods based on Lighthill's acoustic analogy[80][81] use a mean aerodynamic flow field which is computed independently of the acoustic waves; the mean flow field is then used to predict the noise generated by fine-scale turbulence, making the methods less computationally intensive. To correctly predict the noise generated by a subsonic jet, it is necessary to start with accurate modelling of the jet flow field and the turbulence intensities in the mixing layer. Next, the near-field noise levels generated by the fine-scale turbulence must be predicted. Finally, an accurate model of the propagation of the generated noise levels through the inhomogeneous medium—known as flow-acoustic interaction—must be applied.

3.3.1 Source noise generation

If the mean and turbulent flow fields of the jet plume are known, noise generation by turbulent fluctuations can be analyzed using Lighthill's acoustic analogy. Lighthill's equation is derived from the exact continuity and momentum equations for a perfect gas, neglecting

gravity and externally applied forces, yielding the inhomogeneous wave equation[82]

$$\frac{\partial^2 \rho'}{\partial t} - c_\infty^2 \nabla^2 \rho' = A(\vec{x}, t) \tag{18}$$

where $A(\vec{x}, t)$ is a quadrupole noise source given by

$$A(\vec{x}, t) = \frac{\partial^2 T_{ij}}{\partial x_i \partial x_j}, \quad i = 1, 2, 3 \tag{19}$$

The term T_{ij} is the Lighthill acoustic analogy instantaneous applied stress tensor, for which the exact expression in a viscous, compressible flow is

$$\begin{gathered} T_{ij} = \rho' v_i' v_j' + \left(p' - \rho' c_\infty^2\right) \delta_{ij} - \tau_{ij} \\ \text{where} \quad \delta_{ij} = \begin{cases} 1 & i = j \\ 0 & i \neq j \end{cases} \end{gathered} \tag{20}$$

and τ_{ij} is the shear stress. Lighthill's equation is exact and has the following solution for an unbounded flow:

$$\rho'(\vec{x}, t) = \frac{1}{4\pi c_\infty^2} \iiint \frac{A(y, \tau)}{|\vec{x} - \vec{y}|} dy \tag{21}$$

Equation 21 gives the density fluctuation at time t for an observer located at point $\vec{x}$, due to a disturbance at point $\vec{y}$ and at retarded time $\tau = t - \frac{|\vec{x}-\vec{y}|}{c_\infty}$. In Lighthill's acoustic analogy, the actual fluid flow is replaced by a distribution of moving quadrupoles in a quiescent medium with density and speed of sound equal to the values external to the flow.

If the jet flow field is divided into elemental eddy volumes, the jet noise generation can be represented by a collection of convecting, uncorrelated quadrupole sources of various orientations, each radiating noise with an intensity spectrum which is a direct function of the local flow properties. Ribner used a model of homogeneous, isotropic turbulence in the moving-eddy reference frame; and taking the azimuthal average of the sound field, found that a weighted combination of quadrupoles of various orientations contributes to the net far-field radiation[52]. The net acoustic intensity from each elemental volume in the flow, in the absence of convection and acoustic-mean flow interaction, is

$$dI(\omega) = \frac{\rho_\infty l^3}{c_\infty^5 R^2} (u')^4 \omega^4 H\left(\frac{\omega}{\omega_0}\right) dV \tag{22}$$

where ω is the emitted frequency, l is the characteristic turbulent eddy size, R is the source-to-observer distance, u' is the local turbulence intensity, $H(\omega/\omega_0)$ is the Fourier transform of

the moving-frame space-time cross correlation of u', and ω_0 is the characteristic frequency. The characteristic quantities can be estimated from empirically-derived similarity relations:

$$\begin{aligned} \omega_0 &\approx \tfrac{\partial U}{\partial r} \\ l &\approx \tfrac{u'}{\omega_0} \end{aligned} \tag{23}$$

and the turbulence intensity can be estimated using the shear stress:

$$u' \approx \sqrt{\frac{\tau}{\rho}} \tag{24}$$

If it is assumed that the individual eddy volumes are uncorrelated with each other, then the local flow properties throughout the flow field can be used to compute the radiated noise levels by summing over all volume elements[35]. The Lighthill-Ribner mixing-noise spectrum (Equation 22) does not account for the additional effects of source convection and flow-acoustic interaction, so these need to be computed separately and their effects added to the intrinsic sound spectrum.

3.3.2 Convection and propagation through inhomogeneous medium

The previous section described how to calculate the noise generated by turbulence in the jet. To determine how the noise radiates to the far field, however, requires additional analysis because the source is surrounded by a rapidly-moving, high-temperature jet[6]. Lilley's equation[83] describes propagation of jet noise through an inhomogeneous medium:

$$\frac{1}{c^2} D_\bullet^3 p - D_\bullet \left(\Delta p\right) \frac{d}{dr} \left(\log c^2\right) D_\bullet \left(\frac{\partial p}{\partial r}\right) + 2 \frac{\partial u}{\partial r} \frac{\partial^2 p}{\partial x \partial r} = S \tag{25}$$

where

$$D_\bullet = \frac{\partial}{\partial t} + U \frac{\partial}{\partial x} \quad \text{and} \quad S = \rho D_\bullet \left[\nabla \cdot \nabla \cdot \left(u' \cdot u'\right)\right] \tag{26}$$

The symbol Δ is the Laplacian operator, and S is roughly equivalent to the noise source strength of the quadrupoles of various orientations which drives the acoustic pressure fluctuations, as described in the previous section. Equation 25 can be thought of as a multiplier to the intrinsic sound source spectrum which explicitly accounts for the influence of the mean velocity and temperature profiles on the noise propagation. In addition, the effects of convection, refraction and shielding are captured, as well as Mach wave radiation in the case of a supersonic jet.

CHAPTER IV

ANALYSIS PROCESS

Two physics-based noise analysis methods were used in this study: a method for the analysis of fan rotor-stator interaction tones and one for analysis of jet mixing noise. The theory behind the analysis of these two sources was discussed in Chapter 3, showing how the far field noise levels are affected by the engine geometry and flow fields. During conceptual design, however, decisions are made on a system level regarding the best overall layout of the engine and aircraft configuration and the optimum values for such system-level variables as design bypass ratio, number of engines, aircraft wing planform area, etc. To conduct trade studies and risk analysis at this level, it is important for the analysis process to provide the relationships between the system-level design variables and the performance, geometry and noise metrics and constraints. The noise analysis methods themselves do not use system-level information as inputs, so it was necessary to include additional components in the analysis process which could create an interface between the system-level variables and the detailed engine geometry and internal and external flow fields required by the noise analysis methods.

The first step in the development of the full analysis process was to identify the data requirements for the noise analysis methods. An Ishikawa diagram, also known as a cause-and-effect or "fishbone" diagram, is useful for identification of all the potential inputs that are needed to produce a single output in a complex process. Inputs are arranged according to their level of detail to result in a hierarchy of relationships. Figure 12 shows an Ishikawa diagram for the fan rotor-stator interaction tone noise analysis process, giving a list of the data required for the analysis, and grouping the data into their respective categories; within each category, a non-comprehensive list of parameters is listed. To analyze the rotor-stator tones according the methods of Section 3.2, it is necessary to start with a definition of the fan rotor and stator geometry, the axisymmetric geometry of the inlet and bypass duct

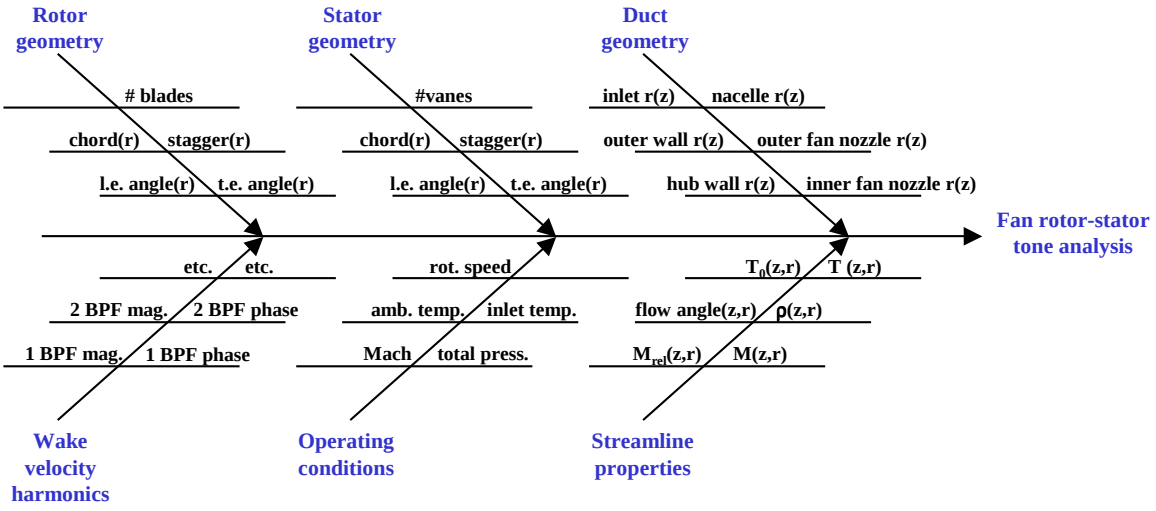

Figure 12: Ishikawa diagram for fan rotor-stator interaction tone noise input requirements.

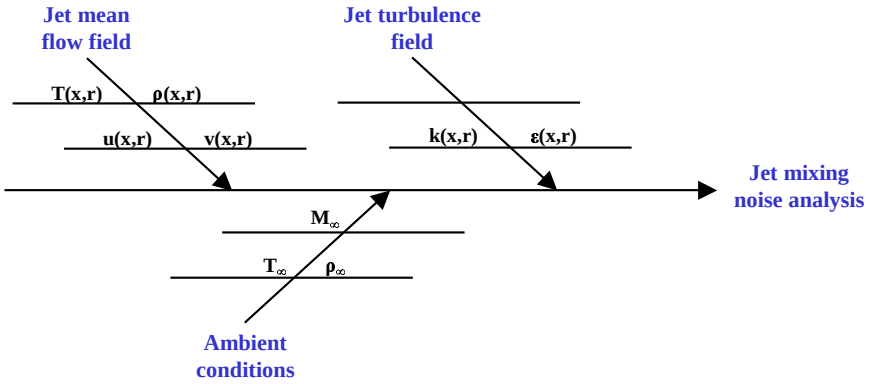

Figure 13: Ishikawa diagram for jet mixing noise input requirements.

walls, operating conditions of the engine, flow properties along the fan streamlines, and the radial distribution of wake velocity deficit magnitudes and phases at the harmonics of the BPF. Figure 13 shows an Ishikawa diagram for the jet mixing noise analysis process. The data requirements are somewhat simpler than the fan analysis, requiring a definition of the mean and turbulent jet flow fields downstream of the core and fan nozzles, plus the ambient conditions.

By examining the data inputs for the noise analysis methods as diagrammed in Figures 12 and 13, it was apparent that significant prior analysis was required to define the engine operating conditions, fan rotor and stator geometry, engine duct geometry, fan streamlines properties and wake velocity deficit, and jet external flow field. To define these data as functions of the system-level engine and airframe variables, the analysis process must

contain all of the following elements:

1. Design of the engine cycle, and off-design steady-state analysis to determine the engine component operating conditions at the takeoff and approach flight conditions at which noise is to be analyzed. Input requirements include the definition of the engine cycle architecture, engine cycle design variables, and performance maps for the engine components.

2. Physical layout of the engine components, determination of their physical dimension and definition of the internal duct contours and nacelle shape. Input requirements include the design engine component flow properties and parametric geometric definition of engine components.

3. Determination of the stator parametric shape for noise analysis, and the three-dimensional rotor shape at a level of detail appropriate for CFD analysis. Input requirements include the design fan flow properties, fan duct geometry and rotor and stator design constraints.

4. Aircraft flight performance analysis to determine the takeoff and approach flight paths and the flight conditions at which noise is to be analyzed. Input requirements include the airframe weight and size, low-speed aerodynamic performance, and off-design engine cycle performance.

5. CFD analysis of the rotor to determine the fan flow properties along streamlines and the wake velocity harmonic amplitudes. Inputs requirements include the off-design fan flow properties, fan duct geometry, and three-dimensional rotor geometry, and flight conditions.

6. CFD analysis of the jet exhaust to determine the mean and turbulent flow properties. Input requirements include the off-design nozzle entrance flow properties, nozzle geometry and flight conditions.

7. Calculation of the far field fan rotor-stator interaction tone noise and jet mixing noise.

8. Calculation of the additional engine and airframe noise sources. Input requirements include the off-design engine component flow properties, parametric geometry and flight conditions.

9. Analysis of the propagation of the noise sources to observers on the ground. Input requirements include the component source noise levels, takeoff and approach flight paths and observer locations.

10. Calculation of the appropriate noise metrics. Input requirements include the noise levels at the observers as a function of time.

An collection of analysis methods was assembled which addresses each of the required analysis list above; in some cases analysis methods were used which were able to fulfill multiple requirements in a single step. Next, the component analysis methods were integrated into an analysis process which defines the data interfaces between the methods and lays out the execution order to assure that necessary input data are available to each of the components. See Figure 14 for a flow chart of the analysis process, including the analysis steps and the data requirements at each step. The Detailed Noise Analysis block in the flow chart is shown in greater detail in Figure 15. The individual components of the process will be discussed in later sections, but it is important to first describe the techniques with which the components were "wrapped" to facilitate their use in an integrated system.

4.1 Wrapper architecture

Each of the methods in the analysis process (Figures 14 and 15) was integrated into the methodology using a *wrapper* (Figure 16), which is a program that provides a modular interface for a particular analysis method and comprises three necessary components—a pre-processor, an execution routine, and a post-processor—as well as optional components such as a grid generator or an optimizer. The wrapper concept allows for a modular format which makes it possible for different methods to draw on the same common database and makes it simple to switch methods in and out of a design process easily. With this format, each method can exist in its original, unmodified form rather than needing to be converted

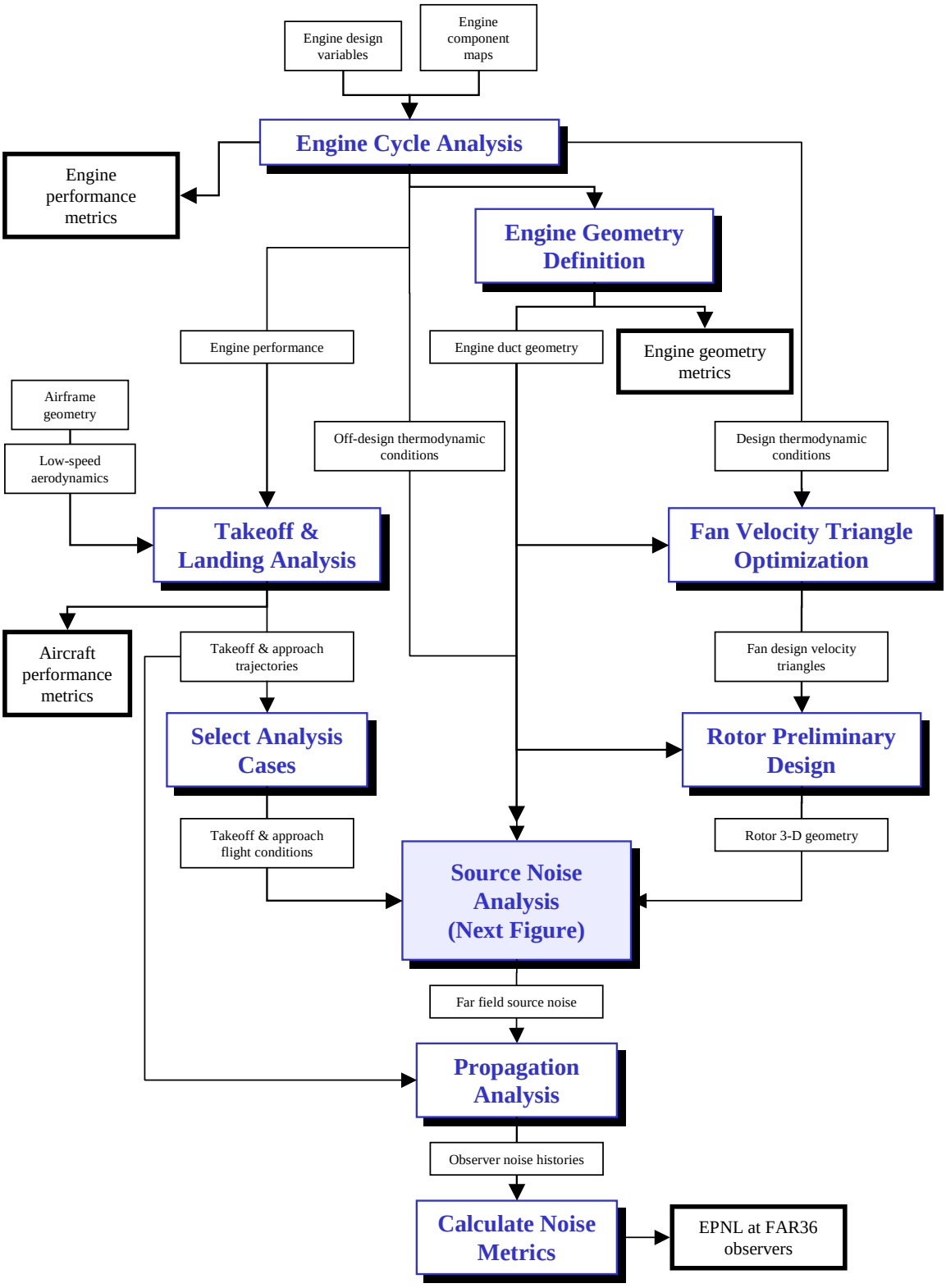

Figure 14: Performance and noise analysis flow chart.

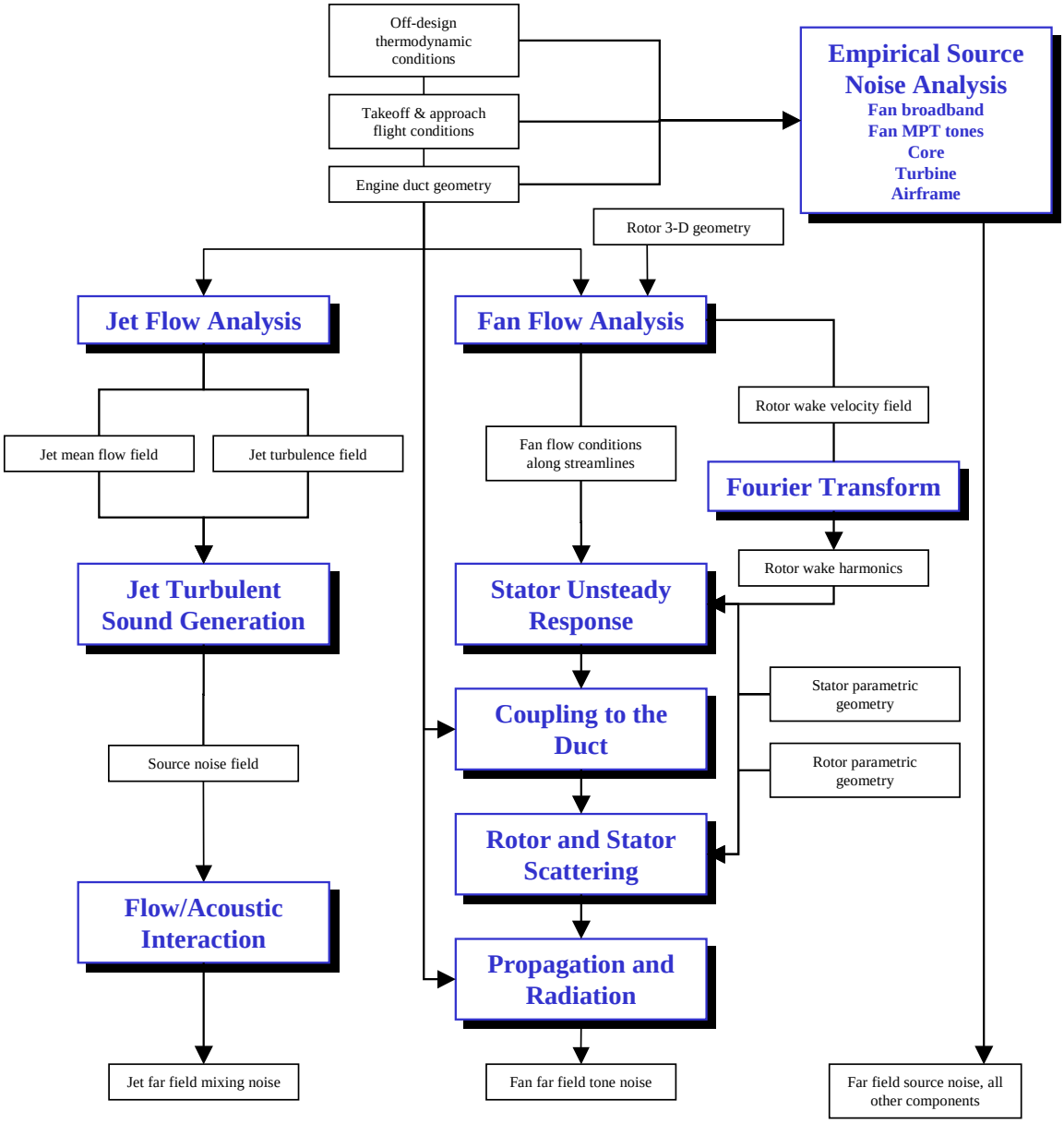

Figure 15: Detailed noise analysis flow chart.

to a subroutine form, which can be a difficult and time-consuming process which would need be repeated each time a new version of the stand-alone method becomes available. The main wrapper routine controls which analysis cases are to be run and designates appropriate file names for the input, output and data files. The wrapper routine then passes this information to the pre-processing, execution and post-processing routines. The pre-processing routine reads data from a central design database, separates out the data necessary for use in the current analysis, and computes the additional input values needed for the analysis; it then writes out the necessary input files in the correct format. The execution routine controls execution of the analysis; in some cases the output and data file names are fixed by the analysis routine, so the execution routine renames them to give them more descriptive names and to keep them from being overwritten by other methods. Finally, the post-processing routine reads the output files and converts the data into the format used in the central design database. The post-processing routine also writes data files suitable for plotting which the user can use to check the results of the analysis. In addition to the above elements, the wrapper may also contain an optimizer which controls the pre-processor, execution routine and post-processor to optimize external design variables or internal variables used only by the method.

4.1.1 Design database

All the input design variables and analysis options, intermediate information such as engine geometry, flow field, and aircraft flight path, and output variables were organized into a central design database which could be accessed by the individual wrappers. The design database was organized in FORTRAN namelist format and a full description of the variables is given in Appendix C.

4.2 Engine performance

In this analysis process, the engine cycle analysis program ENGGEN[45][46] was used to compute the design and off-design steady-state performance and thermodynamic properties of the engine. ENGGEN is based on the QNEP program[47], which in turn is a modified version of the Navy Engine Performance Computer Program (NEPCOMP)[15]. The engine

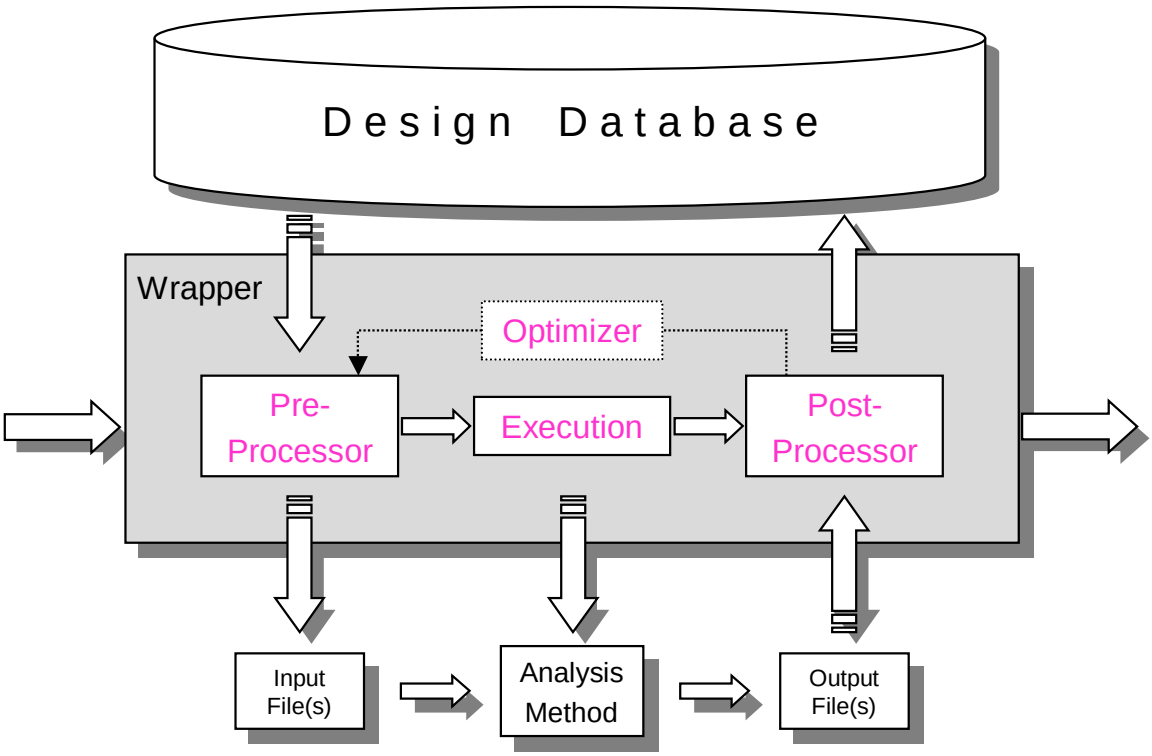

Figure 16: Illustration of the wrapper concept for modularization of routines.

is represented as a one-dimensional flow path and thermodynamic conditions are computed at the entrance and exit of each component. Input variables include the system-level design variables such as bypass ratio, fan pressure ratio, turbine inlet temperature, overall pressure ratio, throttle ratio, high-pressure compressor pressure ratio; and the fan hub-tip ratio, gear ratio and design tip speed. Off-design performance is computed using input performance maps for the individual engine components.

ENGGEN also computes the weights and dimensions of each of the components of the engine using empirical relationships and a database of material properties[46]. For rotating components, the required number of stages and disk dimensions are based on aerodynamic and mechanical design considerations assuming repeating-stage, repeating-row mean-line analysis [88]. Once all the component dimensions have been calculated, they are assembled according to the engine architecture to form a layout of the complete engine geometry. The engine flow path geometry is output as a postscript file which serves as the starting point for further refinement of the geometry, as described in the next section.

4.3 Geometry post-processing

A new geometry post-processing routine was written to process the simplified engine duct geometry from ENGGEN, enforce slope, curvature and wall intersection constraints, and modify the geometry based on additional design variables which could not be specified within ENGGEN. For example, ENGGEN only allows for a constant-area fan and the geometry output does not have the ability to extend the fan bypass duct beyond the minimum required length. To correct these and other shortcomings, the desired values for fan blade aspect ratio and contraction ratio are used to modify the duct in the vicinity of the fan, an inlet cone is added, the engine immediately behind the fan exit is extended to create a rotor-core stator spacing, a stator row is created with the desired aspect ratio, rotor-stator chord ratio and rotor-stator spacing, and the aft nacelle, fan nozzle, core cowl, core nozzle and plug are redrawn to enforce slope and curvature constraints on the outer nacelle. All these changes are made while keeping the compressor, burner and turbine geometry fixed and a constant fan inlet area. The number of stator vanes, V, is specified so that the first harmonic of the BPF will be cut off at the design operating condition with a sufficient safety margin:

$$V = \Big(1 + \frac{\Omega r_t}{c\sqrt{1 - M^2}}\Big)B + 10 \tag{27}$$

To be consistent with the method used to lay out the initial engine geometry in ENGGEN, the post-processing routine defines each segment of a duct wall as a clamped cubic spline segment between the point (z_l, r_l) with slope m_l and ending at point (z_r, r_r) with slope m_r. Beginning with the engine geometry output by ENGGEN, the post-processing routine takes the following steps to produce a complete engine cross-section:

1. Redefine the basic rotor geometry based on desired values of rotor aspect ratio and rotor area contraction ratio, AVDR, which is the ratio of the rotor cross-sectional area at the exit to the cross-sectional area at the inlet.

2. Create an inlet cone with an elliptical cross-section which is tangent to the inner wall at the rotor leading edge.

3. Calculate a new splitter radius based on the design bypass ratio and the new rotor

exit cross-sectional area.

4. Add a constant-area annular duct to accommodate the rotor-stator spacing and stator vane row, and define the basic stator geometry based on desired values of stator aspect ratio and stator sweep.

5. Find the minimum value for the fan nozzle outer radius such that the desired nacelle curvature and slope limits are not violated.

6. Find the minimum value for the core nozzle outer radius such that the desired core cowl curvature and slope limits are not violated.

7. Increase the size of the plug, if necessary, to ensure a smooth transition in the core nozzle inner wall between the low-pressure turbine exit and the plug.

8. Redraw the core nozzle between the low-pressure turbine and the plug.

9. Redraw the bypass duct between the stator and the fan nozzle exit.

10. If the core nozzle outer wall and the bypass duct inner wall intersect, increase the fan nozzle exit radius to give more room for the core nozzle; if that fails, reduce the slope of the bypass duct inner wall instead.

Once these steps have been taken, the inlet, bypass duct, fan nozzle, core nozzle and plug have been redrawn and slope and curvature continuity have been ensured between the line segments defining the duct walls. The definition of the aft nacelle and nozzle contours is of sufficient detail for axisymmetric jet flow solutions, but additional definition of the fan rotor and stator three-dimensional geometries is needed before the fan flow solutions and rotor-stator interaction tone analysis can be carried out.

4.4 Fan preliminary design and analysis

At the conceptual design level, the engine is usually only specified using one-dimensional flow paths and mean thermodynamic data at the entrance and exit of each engine component, which is the case with ENGGEN. This level of detail is sufficient for most empirically-based

noise prediction methods, but for the more detailed fan noise analysis method used in this study it was necessary to obtain a realistic three-dimensional definition of the fan rotor and stator blades. To assure that the fan geometry was always matched to the engine cycle design, it was necessary incorporate a preliminary design methodology for the fan rotor and stator blades into the overall design and analysis process. Furthermore, it was essential that the preliminary design method be automated to allow for timely design and analysis of many design points without constant involvement by the user. This fan blade design process uses a two-step process which first determines the desired fan velocity triangles, then designs a rotor camber surface to produce the desired rotor outlet conditions with an appropriate chordwise and spanwise distribution of swirl. Aeromechanical design constraints for preventing flutter and instability of the rotor blades at cruise and other critical off-design conditions are not included in the design process. The two elements are described in the following sections.

4.4.1 Fan design velocity triangles

The first step in the fan design process is to determine an appropriate spanwise distribution of rotor exit flow properties to ensure that the required fan pressure ratio is met while keeping the work required by each section of the blade span within a reasonable range. The streamline curvature code MERIDLN is used to analyze the flow through the fan rotor and stator rows. MERIDLN is an unpublished revision of MERIDL[69] which obtains a detailed subsonic or shock-free transonic flow solution on the midchannel stream surface (meridional plane) of a turbomachine or annular duct. Required input includes the fan mass flow, rotational speed, and the radial distributions of total temperature and total pressure at rotor inlet. The distribution of tangential velocity is specified along a radial line downstream of each blade row, and the total pressure loss for each blade is input as a function of radius. Output includes the velocities, streamlines and flow angles on the stream surface and approximate blade surface velocities. Subsonic solutions are obtained by a finite-difference stream function solution, while transonic solutions use a velocity-gradient method that uses information from a reduced-mass-flow subsonic solution. The

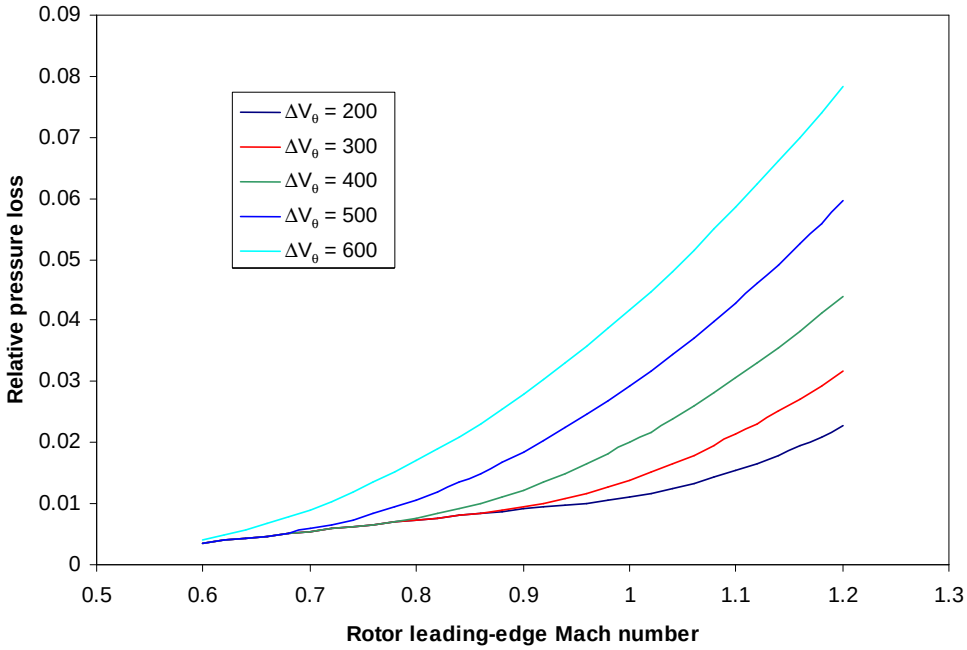

Figure 17: Rotor relative pressure loss as a function of rotor leading-edge Mach number and rotor turning.

radial variations of tangential velocity and blade pressure loss are given as input. The flow turning and pressure loss are applied to the flow linearly through the blade row.

The pre-processing routine creates a MERIDLN input file with the inlet and bypass duct geometry, detailed blade cross-sectional geometry, fan operating conditions, options for generation of the computational mesh, and the tangential velocity distributions along three radial lines: before the rotor, between the rotor and stator, and after the stator. The rotor total pressure loss at each radius is calculated by the pre-processor using an empirical function which relates the rotor relative pressure loss, $\overline{p}$, to the rotor inlet relative Mach number, M_{le}, and the rotor flow turning, V_θ:

$$\Delta\overline{p} = C_1 + C_2 M_{le} + C_3 \Delta V_\theta + C_4 M_{le}^2 + C_5 M_{le} \Delta V_\theta + C_6 V_\theta^2 + C_7 M_{le}^3 + C_8 M_{le}^2 V_\theta \qquad (28)$$

The coefficients C_1 through C_8 for the empirical loss function were derived using statistical regression on a set of three-dimensional viscous calculations which were used in the verification of the rotor flow field analysis method described in Section 4.6.1. Figure 17 gives a plot of Equation 28 for a range of values for leading-edge Mach number and rotor turning.

MERIDLN is only capable of analyzing flows in a single duct, so the duct arrangement

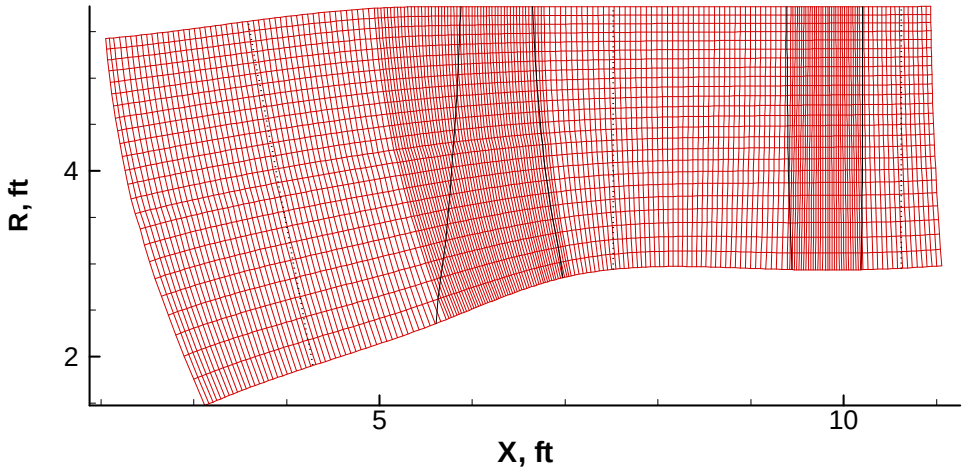

Figure 18: Example representation of rotor and stator flow path in MERIDLN.

is abstracted as a single-stream duct through which the entire air flow passes, and the stator is extended across the core airflow (Figure 18). The contraction of the airflow in the inlet also is smoothed because MERIDLN uses spline curves to represent the hub and tip duct walls and thus is not able to properly fit a true geometric representation of the inlet cone. Since the only portions of the flow field which are of interest in this analysis are in the vicinity of the fan and stator, the simplification of the duct geometry is acceptable.

The program outputs the velocity components and flow angles along each streamline, and also outputs this information at each of the mesh points, as well as the static and total pressure and temperature. Since it also is desirable to have the pressure and temperature information along the streamlines, the post-processing routine interpolates for this information at each of the points along the streamline. The post-processor then calculates the diffusion factor D for both the rotor and stator, the rotor flow turning angle, the stage reaction R, and the stator inlet Mach number. The diffusion factor and stage reaction are defined as

$$D = 1 - \frac{W_e}{W_i} + \frac{\Delta V_\theta}{2\sigma W_i} \tag{29}$$

$$R = \frac{\Delta p_{rotor,i}}{\Delta p_{stage,i}} \tag{30}$$

where W_i and W_e are the inlet and exit relative velocities, respectively; σ is the blade solidity; and $\Delta p_{rotor,i}$ and $\Delta p_{stage,i}$ are the static pressure rise across the rotor and across

the entire stage, respectively. The rotor and stator diffusion factors provide a measure of how highly loaded a single blade row is considered to be[101] and can be constrained to prevent the work distribution from being unobtainable. The stage reaction should be kept positive to avoid a static pressure drop in the rotor, and should be kept less than one, or not very much larger than one, to avoid a large static pressure drop in the stator[141].

To find an optimum radial work distribution, the meridional analysis is used in combination with the CONMIN optimization routine[137]. CONMIN is a free optimizer which uses the Method of Feasible Directions to perform constrained optimization of a user-supplied objective function. The design variables are the values of tangential velocity at a number of discrete radial locations, typically 6 to 10 values, from hub to tip at a location just aft of the rotor. The radial work profile is optimized by minimizing the objective function

$$F = \sum_{i=1}^{n} (p_{r,i} - p_{r,des})^2 \tag{31}$$

where n is the number of streamlines, $p_{r,i}$ is the computed total pressure ratio along the i^{th} streamline and $p_{r,des}$ is the design fan pressure ratio. This formulation for the objective function seeks to minimize the radial variation in pressure coefficient, so a minimum value of zero would be achieved by a constant-work rotor design. The constraints are

$$\begin{aligned}
D_{R,i} - D_{R,max} &\leq 0, \quad i = 1, n \\
D_{S,i} - D_{S,max} &\leq 0, \quad i = 1, n \\
\frac{\Delta V_{\theta,i} - \Delta V_{\theta,max}}{\Delta V_{\theta,max}} &\leq 0, \quad i = 1, n \\
M_{R,i} - M_{R,max} &\leq 0, \quad i = 1, n \\
M_{S,i} - M_{S,max} &\leq 0, \quad i = 1, n \\
R - 1 &\leq 0, \quad i = 1, n \\
-R &\leq 0, \quad i = 1, n \\
\frac{p_r - p_{r,des}}{0.01} - 1 &\leq 0 \\
\frac{p_{r,des} - p_r}{0.01} - 1 &\leq 0
\end{aligned} \tag{32}$$

Equations 32 are, in order, constraints on maximum rotor and stator diffusion factors, rotor flow turning, rotor exit relative Mach number, stator inlet Mach number, and maximum and minimum rotor degree of reaction for each streamline, with the final two inequality

constraints forming an acceptable bounding region on the fan pressure ratio. The stator diffusion constraints are ignored along streamlines which pass through the core, since the core stator would not be required to completely remove the swirl from the flow entering the intermediate pressure compressor. There are thus a maximum of $7n + 2$ constraints in the optimization problem.

The initial rotor exit tangential velocity distribution is automatically defined to give a constant work distribution, i.e. $F = 0$, which is the unconstrained optimum. Often all the constraints are satisfied for the initial distribution and the optimizer is not needed, but if one or more constraints are violated, the optimizer is run until the constrained optimum can be found. The optimized design rotor exit tangential velocity distribution can then be used in the detailed design of the rotor blade geometry, as described in the following sections.

4.4.2 Fan blade geometry definition

The initial geometry of the rotor and stator blades is defined using a new blade stacking routine. The three-dimensional shape of a rotor blade or stator vane is defined with several discrete blade sections between the hub and the tip. The overall shape of the blade section is created by defining separate curves for the mean camber line and thickness distribution, and the overall shape of the blade surface is created by adding half of the thickness normal to each side of the camber line.

The shape of the mean camber line for each of the blade sections is defined by the chord, c, the setting angle and a set of points through which the camber line passes, as illustrated in Figure 19(a). The leading- and trailing-edge points are fixed at (0,0) and (1,0), respectively, and the spline angles at the leading and trailing edges are set by input values of incidence and deviation angles, β_1 and β_2, respectively. Between the defining points, the camber line is generated by clamped cubic spline interpolation.

The thickness distribution of each of the blade sections is defined similarly, as shown in Figure 19(b), although the values for the thickness are non-zero at the leading and trailing edges to allow room for the edges to be rounded. In the immediate vicinity of the leading and trailing edges, the thickness is defined by third-degree polynomial functions of the

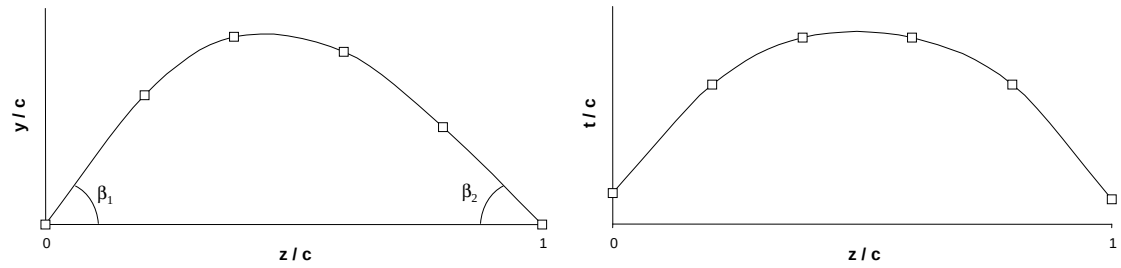

Figure 19: Definition of blade section camber line and thickness using spline fits.

normalized centerline distance, s:

$$t_{le}(s) = A_{le}\sqrt{s} + B_{le}s + C_{le}s^2 + D_{le}s^3 \quad (33)$$

$$t_{te}(s) = A_{le}\sqrt{1-s} + B_{le}(1-s) + C_{le}(1-s)^2 + D_{le}(1-s)^3 \quad (34)$$

The coefficients A_{le}, B_{le}, C_{le}, D_{le}, A_{te}, B_{te}, C_{te} and D_{te} are found by enforcing slope, curvature and slope of curvature continuity conditions at the points of intersection between the leading- or trailing-edge thickness curve and the main thickness distribution curve.

Using, as an example, four radial locations for blade section definition and four interior points each for the camber line and the thickness distribution, each blade surface is completely defined by 94 variables. If the blade chord, the normalized shape of the thickness distribution, and the chordwise locations of the defining points are kept the same at all radial locations, the blade section is defined by 46 variables.

Once the shapes of the blade sections are set, a stacking line is defined which can be a radial line in the case of the rotor or a conventional stator, or can be swept and leaned for an advanced stator. Each blade section is shifted so that its center of area is located at the stacking point (Figure 20). To define the blade geometry at intermediate radial locations, each of the points along the surface of the section is located using natural cubic spline interpolation between the corresponding points on the two nearest defining sections.

4.4.3 Rotor geometric design

Once the design radial work distribution has been chosen and the initial blade surface as been laid out using the procedures in the previous section, the fan rotor blade surface geometry is optimized through a three-dimensional inverse design procedure in combination with

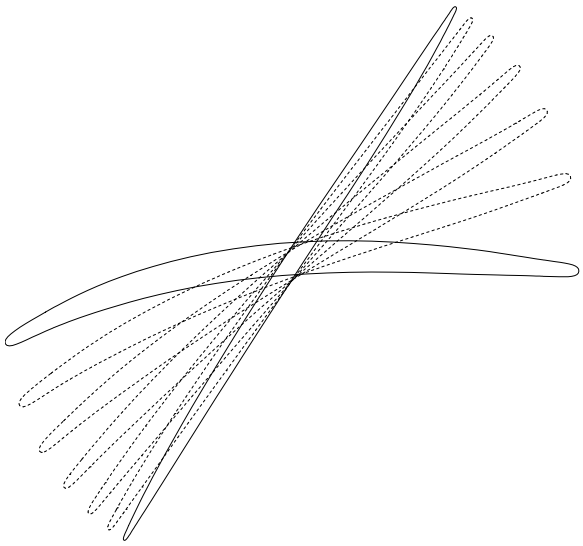

Figure 20: Example fan rotor blade cross sections.

Swift[23][24][25][26]. Swift is a multi-block computer version of the Rotor Viscous 3-D code (RVC3D)[19][21][22][134] and is used for computational fluid dynamics analysis of three-dimensional viscous or inviscid flows in turbomachinery. The program solves the thin-layer Navier-Stokes equations using an explicit finite-difference technique. The rotor computational grid used in Swift is generated using the companion TCGRID computer program[20]. TCGRID is an elliptic grid generator originally intended for isolated airfoils, but has been modified to allow generation of periodic C-type grids for turbomachinery applications. The fan flow path is abstracted as a single-stream duct in the same manner as was used in the velocity triangle optimization (Figure 18). Inner and outer boundary grid points are arbitrarily specified, and interior points are generation by solution of Poisson's Equation with forcing terms such that the grid spacing and intersection angles are maintained at the inner and outer boundaries. To limit the amount of user involvement required in the grid generation process, most of the grid generation input control parameters for TCGRID are automatically computed by the wrapper based on the geometry of the blade to be analyzed.

In the inverse design procedure, the goal is to arrive at a three-dimensional blade shape which will achieve a proper axial distribution of swirl, $rV_\theta(z)$, through the rotor at each radial station along the blade. An appropriate swirl distribution can be prescribed for the purpose of achieving the design pressure ratio while avoiding large rotor surface pressure

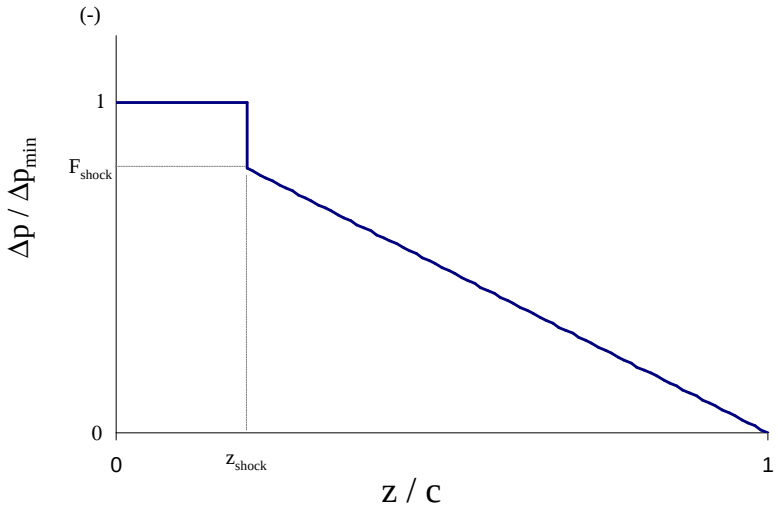

Figure 21: Prescribed blade pressure loading.

gradients which could lead to separated flow.

Rather than prescribing the swirl distribution directly, though, it is more natural instead to start with a prescribed axial distribution for the static pressure differential between the upper and lower surfaces of the blade. An appropriate pressure differential $\Delta p(z)$ begins with a minimum (negative) value Δp_{min} at the leading edge of the blade and remains nearly constant up to a shock location z_{shock}, followed by a discontinuous jump in pressure differential through the shock and then a gradual increase to zero at the trailing edge[60] (Figure 21). In formal terms, the prescribed pressure differential can be written as

$$\Delta p(z) = \begin{cases} \Delta p_{min} & \frac{z}{c} \leq z_{shock} \\ \frac{F_{shock}\Delta p_{min}}{1-z_{shock}}(1-\frac{z}{c}) & \frac{z}{c} > z_{shock} \end{cases} \tag{35}$$

where F_{shock} is the factor defining the ratio of the pressure differential before and after the shock.

The y-momentum equation can be used to show that the axial variation of $\overline{V}_\theta$ is directly related to the blade pressure loading:

$$\Delta p(z) = \dot{m}\frac{d\overline{V}_\theta}{dz} \tag{36}$$

where $\dot{m}$ is the mass flow rate[98]. Given the overall change in swirl across the blade row $\Delta\overline{V}_\theta$ as defined by the design velocity triangle, equation 36 can then be integrated to obtain

the swirl schedule:

$$\overline{V}^*_{\theta,des} = \begin{cases} \dfrac{\Delta\overline{V}_\theta(\frac{z}{c})}{z_{shock}+\frac{F_{shock}}{2}(1-z_{shock})} & \frac{z}{c} \le z_{shock} \\ \Delta\overline{V}_\theta \left\{ 1 - \dfrac{(1-\frac{z}{c})^2}{\frac{2z_{shock}}{F_{shock}}(1-z_{shock})+(1-z_{shock})^2} \right\} & \frac{z}{c} \ge z_{shock} \end{cases} \tag{37}$$

The swirl schedule is starred to indicate that it is the prescribed distribution. Thus, the swirl distribution can be defined entirely by the overall change in swirl and the location and strength of the shock. For this study, the shock location was specified to force the blade to be unstarted at the design condition—that is, the suction-surface shock does not intersect the pressure surface of the next blade. Forcing the blade to be unstarted made the inverse design procedure much more well-behaved, but an unstarted rotor design would be very inefficient so this normally would not be done in the design of an actual fan rotor. The shock strength was an empirical function of the leading-edge Mach number: for leading-edge Mach numbers less than 1.3, values of $z_{shock} = 0.3$ and $F_{shock} = 1$ were used to defined a controlled-diffusion or supercritical blade section, and for leading-edge Mach numbers greater than 1.3, the empirical equation

$$F_{shock} = 1 - 3.3(M_{le} - 1.3) \tag{38}$$

was used, based on observations of shock strength made during verification of the design methodology.

Once the swirl distribution has been prescribed, it can be used to define the required axial and radial distributions of the blade camber. The blade camber surface is defined by a blade shape function $f(r, z)$ which is the tangential coordinate of the blade camber line in radians. For a thin blade the circumferentially-averaged tangential velocity is approximately tangent to the blade camber surface, so an initial camber surface can be defined by enforcing the flow-tangency condition along the blade surface:

$$V_r \frac{\partial f}{\partial r} + V_z \frac{\partial f}{\partial z} = \frac{V^*_\theta}{r} - \Omega \tag{39}$$

where V_z and V_r are the axial and radial components of velocity and Ω is the blade rotational speed[31]. The flow field through the blade is not initially known, however, so initial estimates of the velocity components must be used, and the camber surface must

be refined through iteration to find the surface which produces a swirl distribution exactly equal to the prescribed one. Of course, the circumferentially-averaged tangential velocity is only approximately tangent to the blade camber surface, so it also is necessary to correct the prescribed swirl distribution during each iteration to account for the actual difference between the circumferentially-averaged and camber line tangential velocities.

The flow field computed in the fan velocity triangle optimization procedure is used to initialize the solution procedure. For each iteration $(n+1)$ of the blade design procedure, the following steps are taken:

1. A new camber definition is found by integrating Equation 39 using an iterative procedure. For each iteration $(j+1)$, the integration is performed along each axial line while holding the $\frac{\partial f}{\partial r}$ term constant:

$$f(z,r)^{(j+1)} = \int_{le}^{te} \frac{1}{V_z}\left(\frac{V_\theta^*}{r} - \Omega - V_r\left[\frac{\partial f}{\partial r}\right]^{(j)}\right)dz \tag{40}$$

   after which the blade sections are reset to their stacking locations. The $\frac{\partial f}{\partial r}$ term is updated after each pass, and the solution continues until the camber line residual is sufficiently small.

2. The rotor blade is laid out using the new camber surface, a revised computational grid is generated using TCGRID, and the circumferentially-averaged axial, radial and tangential components of the flow field, $V_z(z,r)$, $V_r(z,r)$ and $V_\theta(z,r)$, are computed in Swift. For the first iteration the Swift analysis must be started from scratch, but in the second and subsequent iterations the Swift analysis can be restarted from the previous solution. The downstream hub static pressure ratio boundary condition also is updated during each iteration, if necessary, to keep the mass flow ratio within 1% of the design value.

3. The flow field information is updated using the new Swift results, but to keep the iterations stable a relaxation factor, Ω_V, is used:

$$V_r^{(n+1)} = V_r^{(n)} + \Omega_V\left[V_r - V_r^{(n)}\right] \tag{41}$$

$$V_z^{(n+1)} = V_z^{(n)} + \Omega_V\left[V_z - V_z^{(n)}\right] \tag{42}$$

4. The prescribed tangential velocity is corrected to account for the difference between the circumferentially-averaged and camber line tangential velocities:

$$(V_\theta^*)^{(n+1)} = (V_\theta^*)^{(n)} + \Omega_E \left[(V_\theta^*)^{(n)} - V_\theta^{(n)} \right] \tag{43}$$

where Ω_E is the error correction relaxation factor.

The solution procedure continues until two convergence criteria—the maximum tangential velocity error, $\left[V_\theta^* - V_\theta \right]_{max}$, and the maximum meridional velocity residual, $\left[V_m^{(n+1)} - V_m^{(n)} \right]_{max}$, where $V_m = \sqrt{V_r^2 + V_z^2}$—are sufficiently small.

4.5 Flight performance

Once the engine cycle has been designed and its design and off-design performance computed, the operating conditions of the different components of the engine can be used to compute the noise produced. However, it is first necessary to determine the conditions under which the engine will be operating—i.e. the velocity, altitude and throttle setting—during takeoff and landing when the noise is produced. To obtain this information, the low-speed flight performance of the engine and aircraft combination must be analyzed. The takeoff and approach trajectories of the aircraft are also needed when analyzing the propagation of the noise to observer locations on the ground.

Using the computed engine performance and input aircraft low-speed aerodynamics and weight information, the takeoff and landing field lengths and flight trajectories are computed by the takeoff and landing module of the Flight Optimization System (FLOPS) computer program[93]. FLOPS is a multidisciplinary suite of computer routines for mission analysis and optimization of aircraft, which are integrated in a monolithic structure. The takeoff and landing module computes detailed performance of the aircraft using time-integrated solution of the equations of motion. The analysis is carried out while obeying all relevant FAR 25 rules[2] regarding engine-out takeoff and aborted takeoff, all-engine aborted takeoff, engine-out aborted landing, and minimum first-segment, second-segment, and missed-approach available engine-out climb gradients.

When a fast empirical noise prediction method is being used, the noise is typically

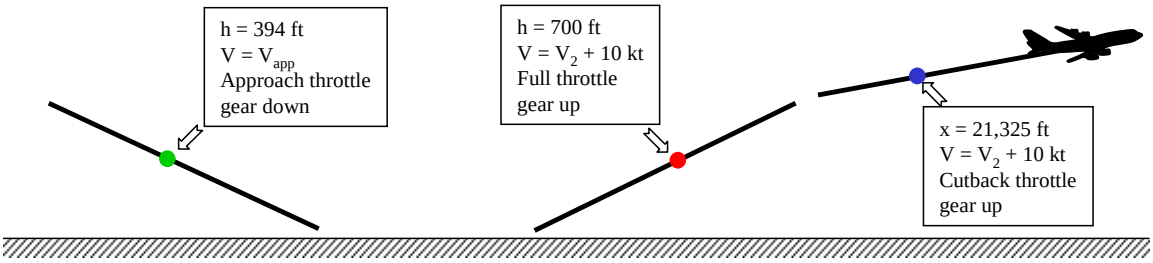

Figure 22: Selection of takeoff and landing flight conditions.

computed along the entire flight path at half-second intervals. When the more complex analysis methods are used, however, it is not feasible to compute the noise at hundreds of points. Instead, it is necessary to select a smaller subset of points at which the noise can be computed. As seen in Figure 22, the airborne portion of the takeoff flight path can be divided into two sections at which the flight conditions—excluding the altitude—are nearly constant: the portion between lift-off and before engine cutback, which will be referred to as the sideline flight condition because the received noise level at the sideline reference point is affected by the noise emitted during this portion of the flight path; and the flight segment after engine cutback, which will be referred to as the cutback flight condition because the received noise level at the cutback reference point is affected. Although the aircraft altitude is varying rapidly during these two segments, it has a minor effect on the actual engine operating conditions and so has little effect on the noise being emitted by the engine and airframe. The effect of the altitude on the propagation of the noise from the aircraft to the observer on the ground can still be accounted for in the propagation routine. Similarly, the operating conditions are nearly constant during the entire approach flight path, so the noise needs to be computed at only one flight condition for approach.

A new utility was created to carry out the interpolation of the engine operating conditions and flight conditions at the sideline, cutback and approach flight conditions. The routine examines the takeoff and approach flight paths that are output from FLOPS and locates the points in the takeoff flight path at which the aircraft passes through the defined sideline altitude and the defined cutback distance, and the point in the approach flight path at which the aircraft descends through the defined approach altitude. For each of these

points, the flight velocity, altitude and engine throttle setting are linearly interpolated from the two nearest flight path points, then used to look up the operating conditions of the engine components from the data tables which were output by ENGGEN. The engine component operating conditions can then be used by the physics-based noise analysis routines to calculate the source noise at the three flight conditions.

4.6 Noise analysis

As explained in Chapter 3, two physics-based noise analysis methods were used in this study: a method for computation of fan rotor-stator interaction tones, and a method for jet turbulent mixing noise. These methods are discussed in detail in the following sections. All additional sources, including fan broadband and multiple pure tone noise, core noise, turbine noise, jet shock cell noise, and airframe noise, as well as the effects of fan inlet and exhaust duct acoustic treatment, were computed using empirical methods.

4.6.1 Fan flow field

As discussed in Section 2.2.1, fan tone noise is produced by a periodic upwash at the stator which is due to the velocity deficit in the rotor wakes. The wake velocity deficit can be obtained through empirical methods, or through an analysis of the viscous flow field in the vicinity of the rotor blades and downstream to the stator leading edge. To make the analysis of the fan tone noise truly physics-based, the rotor flow field and downstream wake profiles are computed in this methodology using Swift, which was described previously in Section 4.4.3.

The wrapper for the Swift flow field analysis implements coarse-grained parallelism using the Message Passing Interface (MPI) libraries[57], allowing the analysis of the separate flight cases to be performed simultaneously to greatly speed up the analysis. The rotor grid is generated using TCGRID with the outlet plane of the grid located at the leading edge of the stator to capture the rotor wake properties. The wrapper automatically runs the Swift analysis and checks progress against three convergence criteria: the RMS residual, the variation in rotor pressure ratio from iteration to iteration, and the mass flow error. The Swift analysis first is carried out for a fixed number of iterations, then the convergence criteria

are checked against their allowable values; if the solution is unconverged, the Swift analysis is restarted and the convergence criteria are periodically rechecked until convergence is achieved. The downstream hub static pressure ratio boundary condition also is periodically updated, if necessary, to match the computed rotor pressure ratio to the required value for that flight condition from the engine cycle off-design analysis.

Once convergence has been achieved, the post-processor reads the computed three-dimensional flow field, extracts the wake velocities at the stator leading edge, and performs circumferential averaging of the flow field properties to arrive at the coordinates of the streamlines and the velocity components and thermodynamic properties along the streamlines.

4.6.2 Fan rotor-stator tone noise

Once the fan flow field and blade wake shapes have been determined, the fan rotor/stator interaction tone noise and coupling to the duct can be computed as outlined Section 3.2. An existing computer program, the Tone Fan Noise Design/Prediction System (TFaNS)[8][77][129][130][131], has already implemented this type of analysis and so was chosen for integration into the methodology. TFaNS is a loosely-coupled set of computer programs for computing the tone noise at the far field for a number of BPF harmonics.

TFaNS computes the tones generated from the interactions of the rotor blade wakes with the stator vanes using simplified fan geometry with a constant-area annular duct and flat plate stators. The program divides the annulus into streamlines and unwraps each strip to form a two-dimensional flow in the circumferential and axial directions. An incompressible mean flow is calculated analytically along each streamline and a series of rotor wakes is superimposed on the mean. TFaNS has the ability to calculate the rotor wake characteristics using a semi-empirical wake prediction methodology, but in this methodology the calculation is bypassed and the wake velocities extracted from the Swift analysis are used. Given the unsteady wake flow, the program calculates the unsteady chordwise pressure distributions on the stator vanes using the assumptions of two-dimensional compressible flow over a cascade of unloaded flat plates at zero incidence to the flow direction.

The program determines the coupling of the generated tones with the duct modes in the immediate vicinity of the stator row, assuming mean axial flow. The pressures are integrated for each mode to give inlet and aft power levels and complex radial mode amplitude for each of the propagating modes. The power levels are summed to give the circumferential mode power levels and total power levels for each harmonic of the BPF. Flat-plate models are also used to calculate the scattering of upstream and downstream propagating modes by both the rotor and stator.

Within TFaNS, the propagation of the modes through the duct and their eventual radiation to the far field is calculated using inlet and exhaust finite element radiation codes[115][116][117]. The suite of codes consists of a mesh generator for creation of separate computational meshes for the inlet and exhaust fan ducts, a potential flow solver for solution of the mean flow equations, and a hybrid finite-element and wave-envelope radiation model for solution of the duct radiation equations. The radiation calculations are performed on a mode-by-mode basis assuming a unit mode strength.

Finally, the results for the rotor/stator interaction source noise, rotor and stator scattering coefficients, and radiation calculations are combined into a coupled system to account for the reflection and transmission of acoustic and vorticity waves in both the inlet and aft directions. The program outputs the far field SPL directivities for each of the calculated BPF harmonics.

The wrapper for TFaNS also was written using the MPI libraries, allowing the analyses for multiple flight conditions to be carried out in parallel. The post-processor reads the far field tone noise levels for all of the flight conditions and writes them to a data file suitable for use in noise propagation calculations (Section 4.6.6).

4.6.3 Jet flow field

The two-stage methodology described in Section 3.3 is used to compute the jet mixing noise. First, aerodynamic calculations of the time-averaged turbulent flow field are carried out using CFD analysis, and the computed time-averaged mean flow and turbulence properties are used for the noise calculations. To correctly predict the noise generated by a subsonic

jet using an acoustic analogy method, it is necessary to start with accurate modelling of the jet plume flow field and turbulence intensities in the mixing layer. Next, the near-field noise levels generated by the fine-scale turbulence must be predicted. Finally, an accurate model of the propagation of the generated noise levels through the inhomogeneous medium (flow-acoustic interaction) must be applied.

Computation of the flow field is carried out using the WIND flow solver[14], which solves the Reynolds-Averaged Navier-Stokes or Euler equations in conservation law form. The program can solve for flows using two-dimensional, quasi-two-dimensional, axisymmetric or three-dimensional grids, which can be structured or unstructured. In this methodology the second-order upwind-biased Roe differencing is used, and the gas is treated as a thermally perfect gas. A two-equation shear stress transport (SST) turbulence model is used to initialize the flow field, after which the Chien k-ϵ model is used to complete the convergence. Inlet conditions for the core nozzle, fan nozzle and freestream are automatically looked up by the pre-processor from the engine cycle data for the flight conditions of interest. Execution of the code is parallelized using the parallel virtual machine (PVM) software package to distribute the analysis of individual grid blocks to multiple processors, and three levels of grid sequencing are used to accelerate convergence of the solution. Finally, the post-processor saves the reference conditions and writes the grid and flow field in a format suitable for use in computation of the jet mixing noise.

A suitable axisymmetric computational grid for the aft engine geometry and downstream flow field is generated using a new algebraic grid generation method within the WIND wrapper. Since WIND requires that boundary conditions be applied only on external boundaries of a grid block, the computational domain must first be subdivided into six blocks. The interfaces between the six blocks and the boundary conditions for each block depend on the arrangement of the core and fan nozzle exits and the plug tip (Figure 23). Finally, the main blocks are in turn subdivided into smaller computational units to facilitate parallel execution by the flow solver.

Within each block, the grid spacing is stretched uniformly in the axial direction to allow clustering of grid points at each nozzle exit and at the plug tip. The number of points

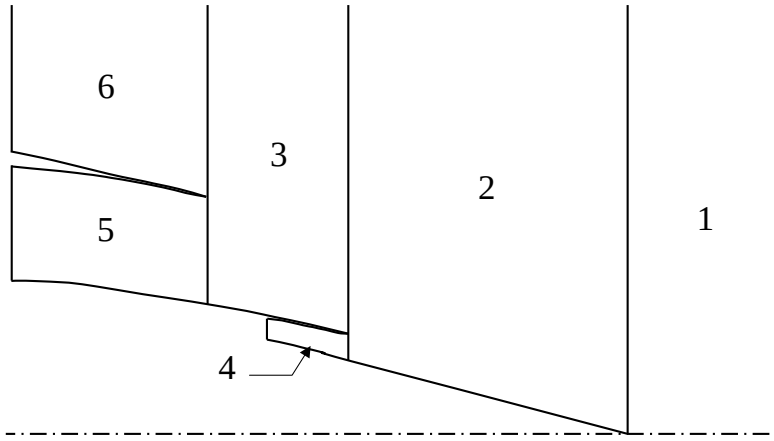

(a) core nozzle downstream of fan nozzle

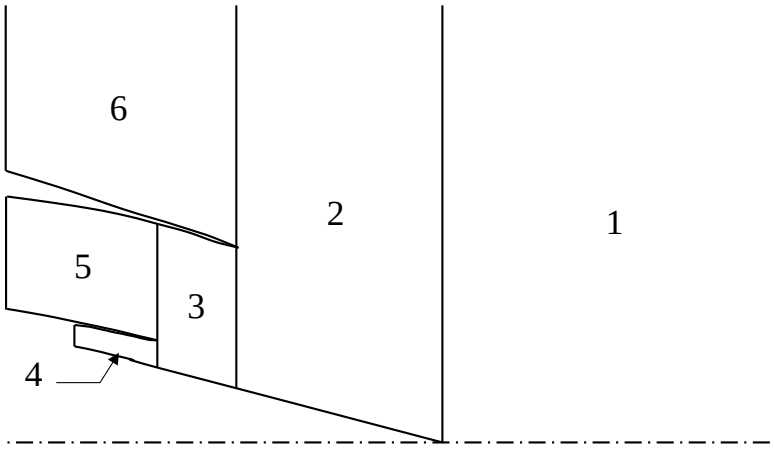

(b) fan nozzle downstream of core nozzle

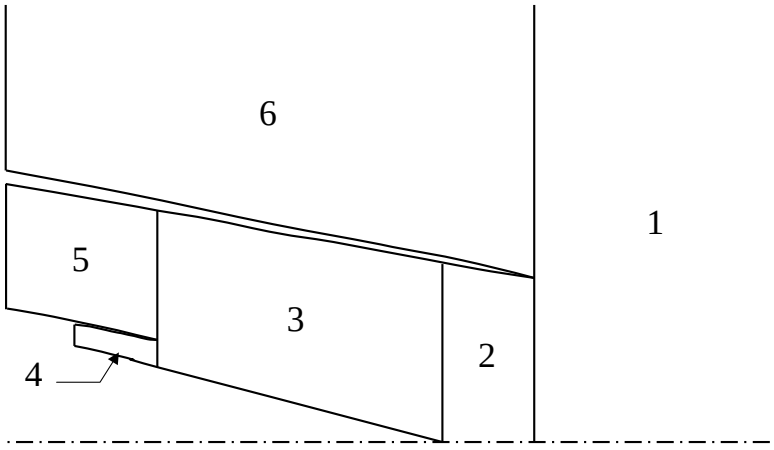

(c) fan nozzle downstream of both core nozzle and plug

Figure 23: Grid topologies based on positions of nozzle exits and plug tip.

in the axial direction in the primary grid block (Block #1) is set by user input, but the number of axial points in the five secondary grids is calculated automatically based on the requirement that the axial stretching across the block interfaces—the three radial lines in Figure 23—be kept as constant as possible.

The grid also is stretched in the radial direction to allow clustering at each duct wall and in the two shear layers downstream of the nozzle exit planes. The radial stretching is constant within each duct, then is relaxed exponentially downstream of each nozzle exit to allow the clustering to be expanded as the shear layers expand:

$$S(z) = \begin{cases} S_0 & z \leq z_{noz} \\ S_0 + (1 - S_0)\left(1 - e^{-\Phi_s \frac{z - z_{noz}}{D_{noz}}}\right) & z > z_{noz} \end{cases} \tag{44}$$

where S_0 is the stretching factor inside the nozzle, z_{noz} is the axial location of the nozzle exit, D_{noz} is the fan nozzle outer diameter, and Φ_s is a user-input parameter used to control the rate at which the stretching becomes uniform. Large values of Φ_s result in faster reduction in the stretching parameter.

The radial locations of the fan nozzle/freestream shear interface can be varied linearly downstream according to user input to make sure the clustering stays within the shear layer. The location of the core nozzle/fan nozzle shear interface is adjusted automatically at each axial location to keep the radial grid spacing constant across that shear layer. Finally, the radial stretching factor outside the fan nozzle/freestream shear interface is adjusted to keep the radial grid spacing constant across that shear layer.

4.6.4 Jet mixing noise

Jet mixing noise is computed using the analysis described in Section 2.2.4. This analysis is implemented in the MGBK computer program[72], which is a modified version of the original MGB program[53]. From the mean flow properties and the k and ϵ fields calculated in the CFD analysis, MGBK uses the Lighthill-Ribner method to predict the source noise generated by turbulent fluctuations in the mixing regions, and Lilley's equation for sound/flow interaction and propagation to the far field. The program uses two empirical factors; the first, α_c, is a convection constant used to computed a modified convection factor

$\overline{C}$:

$$\overline{C} = \sqrt{(1 - M_c \cos\theta)^2 + (\alpha_c k^{1/2}/c_\infty)^2} \tag{45}$$

where θ is the directivity angle, k is the wave number, c_∞ is the ambient speed of sound, and M_c is the convection Mach number, defined with the aid of the second convection constant, β_c:

$$M_c = .5M + \beta_c M_j \tag{46}$$

where M is the local Mach number and M_j is the Mach number at the nozzle exit plane. The convection factor modifies the far field directivity of the jet to account for the effect of the aircraft's forward speed. The post-processor reads the output far field noise levels for all of the flight conditions being analyzed and writes them to a data file suitable for use in noise propagation calculations (Section 4.6.6).

4.6.5 Additional noise sources

The additional sources, including fan broadband and multiple pure tone noise, core noise, turbine noise, jet shock cell noise, airframe noise, and fan inlet and exhaust duct treatment suppression, are computed using the empirical methods in ANOPP, which is described in the next section. The modularity of the methodology, though, assures that additional physics-base methods for these other noise sources could be integrated into the methodology in the future without having to restructure the entire process.

4.6.6 Far-field propagation

Output from the detailed noise analysis block (Figure 15) consists of the total fan rotor-stator interaction tone and jet mixing far field noise spectra, as a function of directivity angle, for each of the three flight conditions. The far field source noise levels are passed to the Aircraft Noise Prediction Program (ANOPP)[49][145] for propagation to the sideline, cutback and approach observer locations. ANOPP is a computer program for the prediction of aircraft noise levels using empirical methods for the various engine and airframe noise sources. The analysis assumes a straight-line propagation from the aircraft to the ground, neglecting refraction of sound waves due to density gradients. Atmospheric absorption along

the propagation path is calculated using separate semi-empirical relationships for attenuation of the sound pressure due to thermal and viscous effects and rotational and vibrational relaxation of oxygen and nitrogen molecules, as functions of temperature, pressure and humidity. A locally-reacting model is used to analyze the reflection and attenuation of the ground, using an empirical equation for the average specific admittance of a grass-covered surface. Finally, the EPNL metric at each observer location is computed from the time history of the noise spectra at the observer.

ANOPP allows the user to bypass some or all of its empirical prediction methods and use input tables for the far-field source noise levels of certain sources. This flexibility allows the previously-computed fan interaction tone and jet mixing noise levels to be read in and combined with the empirical methods for the remaining sources; in addition, the effects of fan duct treatment can be applied to the fan tone noise.

4.7 Model integration

To make a complete and accurate assessment of the noise of an aircraft/engine combination, it was essential that the methodology be able to account for the effects of engine design variables and geometry, aircraft design variables and performance characteristics, and noise-reduction technologies, thus requiring a large number of different programs to be assembled into a coherent system. The wide variety of independent programs possessed different data handling procedures and different output formats, so it was imperative that the programs be integrated to minimize the amount of repetitive work required by the designer. A well-integrated system could be made to run overnight or over weekends to make efficient use of the time available to the designer.

Once the individual components of the methodology were assembled and their wrappers created, the programs and wrappers were compiled on a Silicon Graphics Origin 2000 computer and the entire analysis process was integrated into a complete system using ModelCenter®. ModelCenter is a Windows-based commercial software package that provides a graphical system for integration of engineering processes for use in optimization, design exploration and risk analysis studies. Figure 24 shows the ModelCenter graphic interface

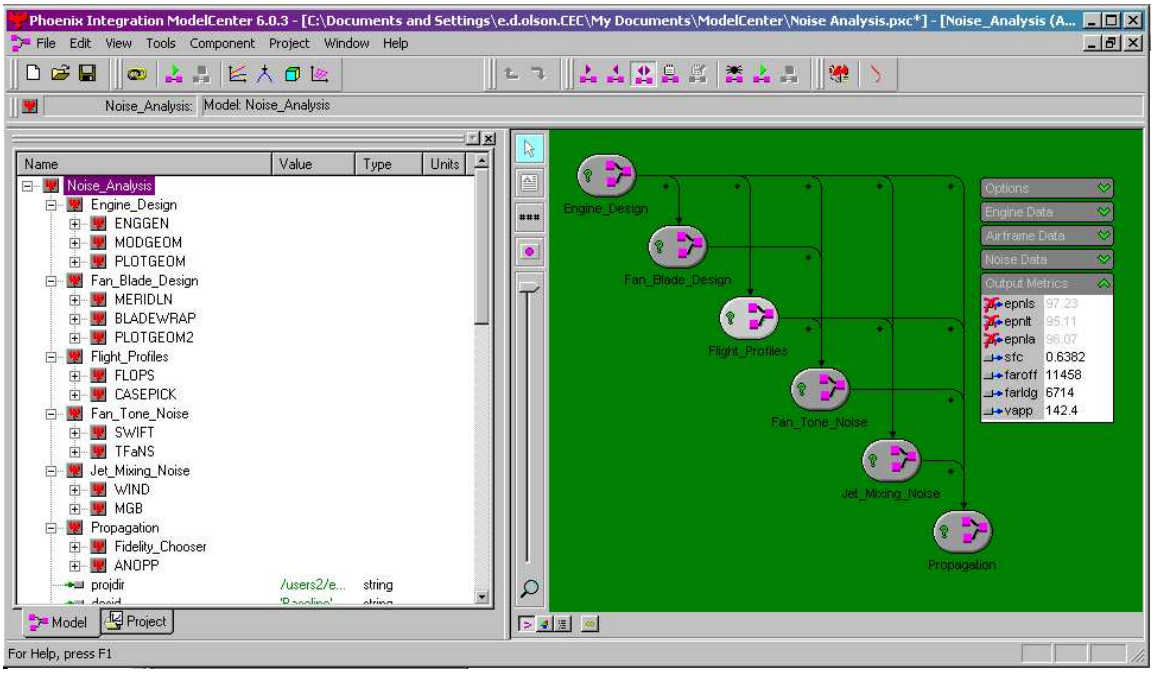

Figure 24: Integration of methodology in ModelCenter®.

with the integrated wrappers. The wrappers are organized into Assemblies based on their functionality—engine design, fan blade design, flight profiles, fan tone noise, jet mixing noise, or noise propagation. The wrappers that exist within each of the assemblies are listed in the left-most window. The arrows indicate the passing of design variables, geometry and flow field information between the different assemblies. Pull-down menus on the right side of the main window give direct access the to most important design and uncertainty variables and output metrics. Various optimization and trade study tools can be accessed from the pull-down menus and the top of the screen.

4.8 Validation of noise predictions

Several validation studies were conducted to verify the proper implementation of the noise analysis methods and to assess the accuracy of the fan and jet noise analysis methods described in Section 4.6. The goal was to carry out the analysis on configurations which were similar to the types of configurations to be analyzed in the subsequent design studies.

Table 2: SDT fan performance at acoustic rating points[64].

Fan operating condition	Corrected wt. flow, lb_m/sec	Total pressure ratio	Total temp. ratio	Adiabatic efficiency
Takeoff (100%)	96.65	1.511	1.138	0.9092
Cutback (87.5%)	83.92	1.359	1.102	0.9010
Approach (61.7%)	59.04	1.158	1.048	0.8909

4.8.1 Fan noise validation

To validate the fan rotor-stator interaction noise analysis method, flow field analysis and tone noise predictions were made for the Source Diagnostic Test (SDT) fan, which is a 22-inch diameter turbofan model that has been tested at the NASA Glenn 9 X 15 Foot Wind Tunnel. Test data for this model include rotor-alone aerodynamic performance measurements[64], acoustic mode measurements using sensors on the inner surface of the duct[112], inlet and exhaust duct spinning mode measurements using a rotating rake[58], unsteady stator surface pressure measurements[40], detailed flow field diagnostic measurements with laser Doppler and hot-wire anemometry[110], and far field noise measurements[143]. The three operating conditions at which the fan was tested are shown in Table 2.

The SDT fan is equipped with two different rotors and three different stator configurations. Only the rotor designated R4 was used during measurement of interaction modes, so it was the only rotor analyzed in this study. The first stator configuration has 54 radial vanes so that the BPF is cut off at takeoff power, the second has 26 radial vanes and is cut on, and the third has 26 vanes swept at 30°. For consistency, the three stators were designed to have equivalent aerodynamic performance with essentially the same solidity.

The geometric definition for the rotor blades, stator vanes, and duct wall were obtained from a computational grid which was originally generated for validation of fan broadband noise computational methods. Figure 25 gives a meridional view of the original computational geometry. The dotted line in the figure indicates the location of the LDV1 measurement plane at which rotor wake flow field measurements were made using laser Doppler anemometry. Experimental data available at the LDV1 station include the axial and tangential components of the velocity and the turbulence kinetic energy.

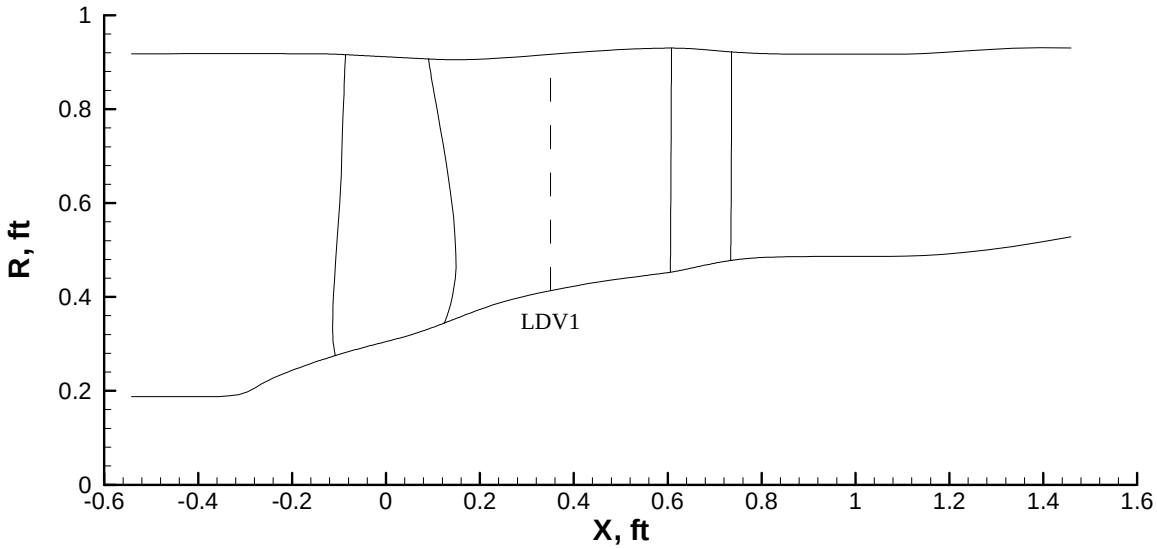

Figure 25: Meridional view of SDT geometry with 54 radial vanes.

The geometry and operating conditions were extracted from the original computational grid and converted to the appropriate database format for the noise analysis method. The new computational grid for the rotor, as generated by TCGRID, is shown in Figure 26. To improve the convergence of the flow analysis, the rotor was modelled without tip clearance. The fan viscous flow field was computed in Swift for the three experimental operating conditions, and the wake velocity information was extracted at both the LDV1 station and the stator leading edge. The rotor-stator interaction tones were then computed with TFaNS using the results of the Swift analysis.

The computed radial distributions of the circumferentially-averaged total pressure and total temperature are compared with experimental results in Figures 27 and 28 at the LDV1 measurement plane, for each of the three acoustic rating points. The Swift computations compare well with the experimental results[110], showing that the mean flow field is computed correctly and that the viscous and shock losses are quantified correctly.

Figures 29 through 31 show contour plots of the axial and tangential velocities at the LDV1 measurement plane, juxtaposed with experimental results. The Swift analysis was carried out without modelling of the rotor tip clearance, so the most obvious difference between the contours is in the lack of a tip vortex in the computed results. Swift does a good job of modelling both the mean velocity and rotor wake velocity deficit, as well as

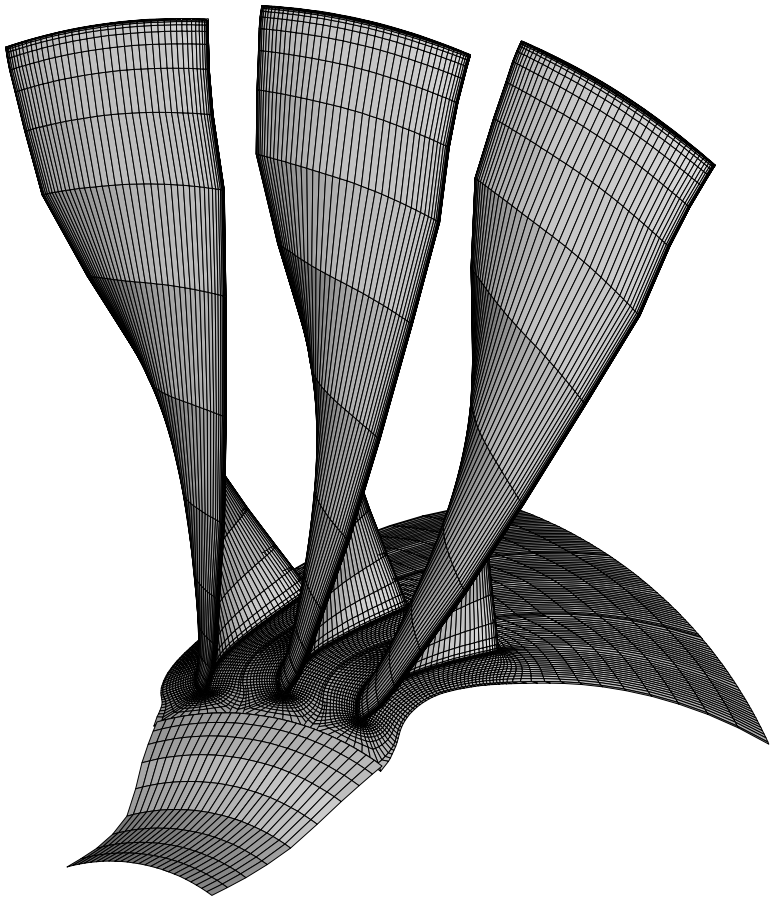

Figure 26: SDT rotor blade computational grid, with every other point removed for clarity.

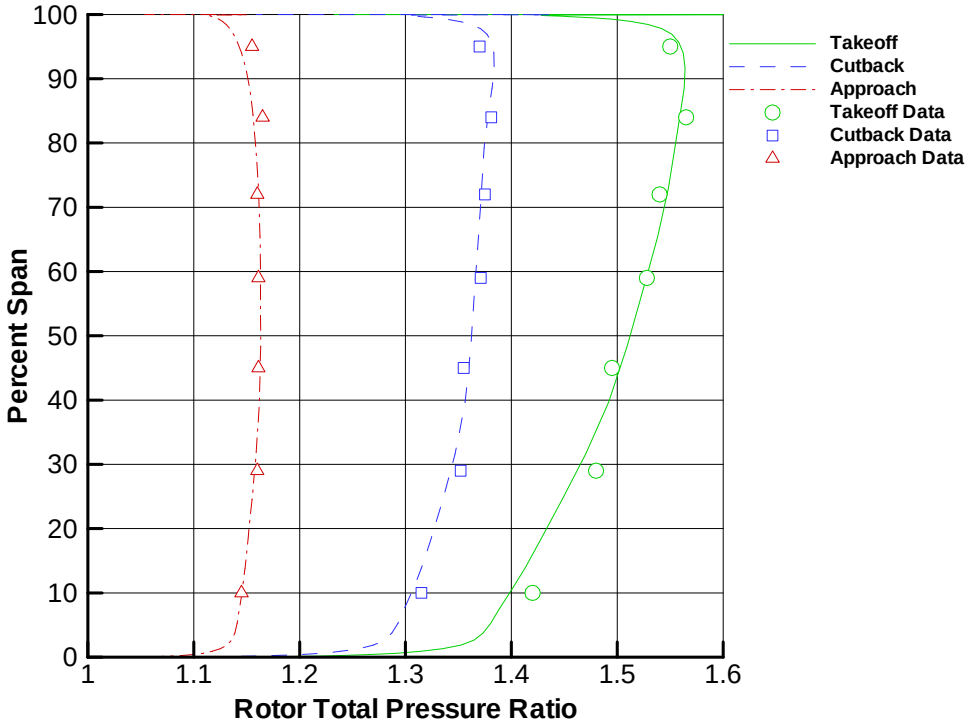

Figure 27: Comparison of computed SDT rotor total pressure ratio to experiment.

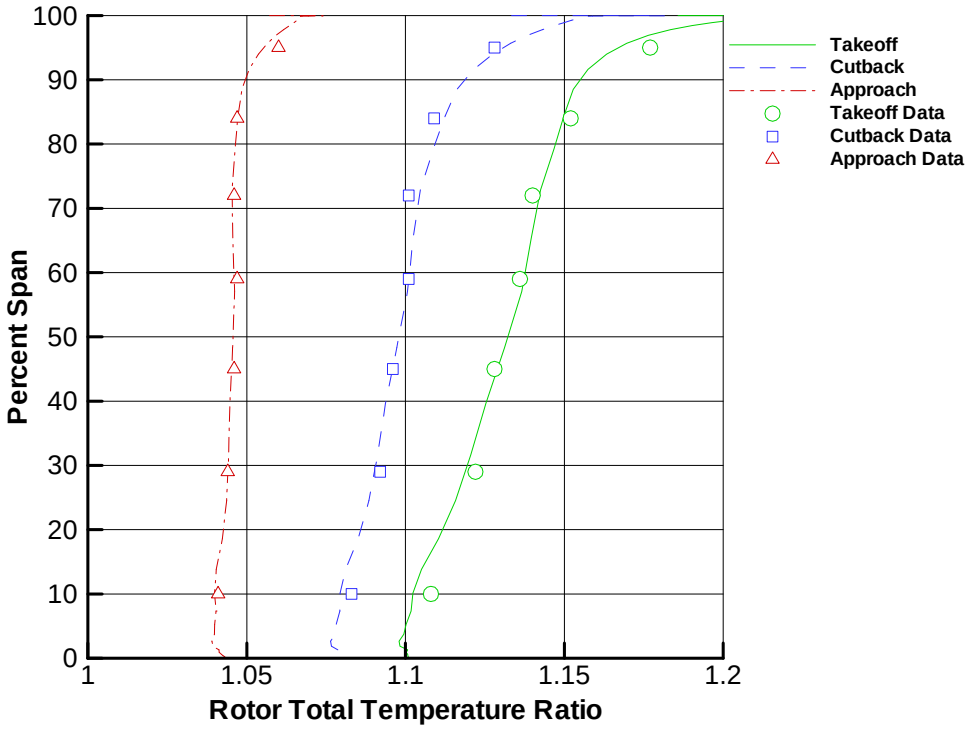

Figure 28: Comparison of computed SDT rotor total temperature ratio to experiment.

the shape of the wakes as they are convected downstream. The lobed structures which can be seen in the rotor wakes near the hub in the experimental data are merely artifacts of interpolation of the contour levels in the plotting software, rather than physical phenomena. In the computational results, there is some shearing of the wakes near the hub, particularly at the approach operating condition, due to shearing the of rotor C-grid. This does not seem to affect the computed maximum wake velocity deficit, but does affect the tangential convection of the wake near the hub, as will be seen below.

Figures 32 through 37 give a comparison of the computed and measured values of the circumferential variation of axial velocity at the LDV1 station, at different percentages of the duct height. The actual value of the circumferential angle is arbitrary, so the reference angle for the computational results was adjusted so that the locations of maximum wake velocity deficit line up with each other at 50% span. The plots show that Swift does a fairly good job of predicting the wake velocity deficit, the width of the wake, and the circumferential location of the wake at different radial locations for all three operating conditions. Closer to the hub and tip, the comparisons are not as good due to differences in the boundary layer widths on the duct walls, the lack of analysis of the tip clearance flow, and the errors resulting from the shearing of the computational grid near the hub.

The fan rotor-stator interaction tones were computed in TFaNS using the meridional flow field and fan wake velocity deficit information extracted from the Swift analyses. Inlet and exhaust tone power levels were computed for the first two harmonics of the blade passing frequency for the three operating conditions. Nacelle geometry information was not available for the SDT fan, so the coupling routine was run using non-reflecting boundaries upstream and downstream of the fan, and the far field noise levels were not computed.

The computed tone power levels are shown in Figures 38 through 40. Inlet power levels are not available at takeoff conditions in the experimental data, so those data are missing from Figure 38. For the first vane geometry—with 54 radial vanes—the first BPF harmonic is cut off so the measured tone levels are extraneous. With a few significant exceptions, the combination of Swift and TFaNS usually does an adequate job of predicting the total interaction tone power levels at different frequencies and operating conditions. By

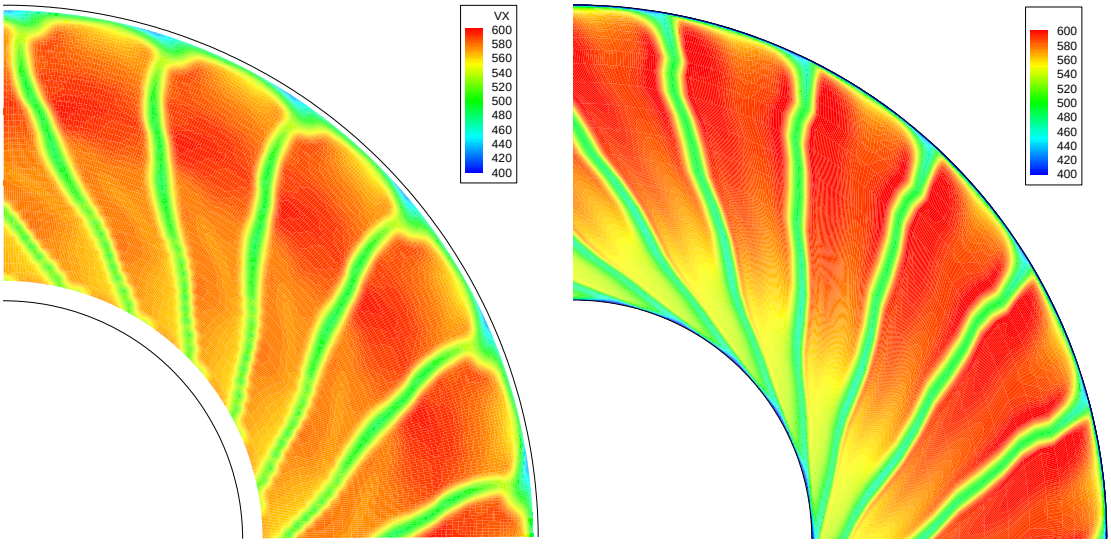

(a) axial velocity data

(b) axial velocity computed

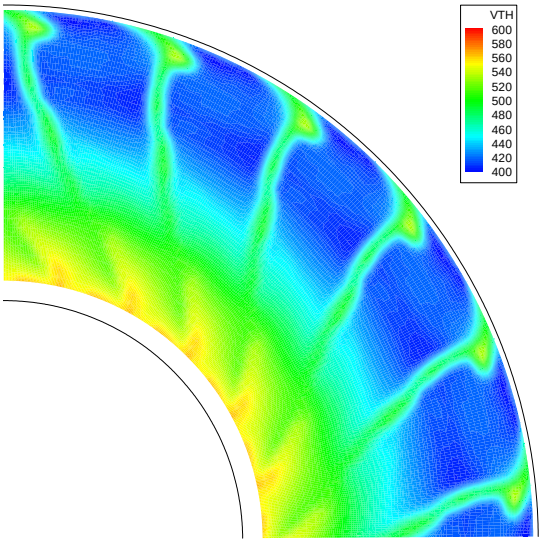

(c) tangential velocity data

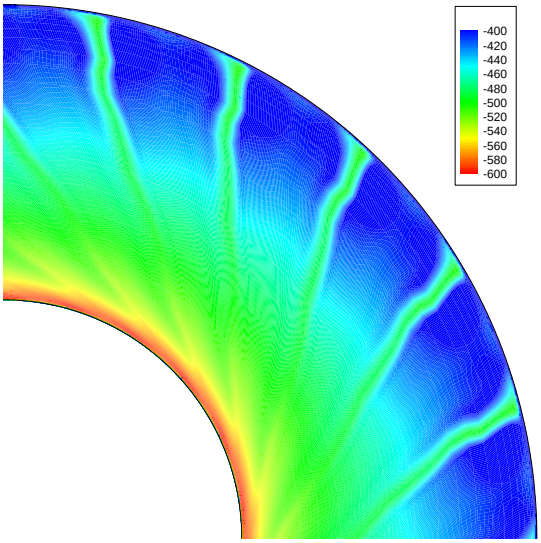

(d) tangential velocity computed

Figure 29: Average passage mean axial and tangential velocity at axial station LDV1 at takeoff.

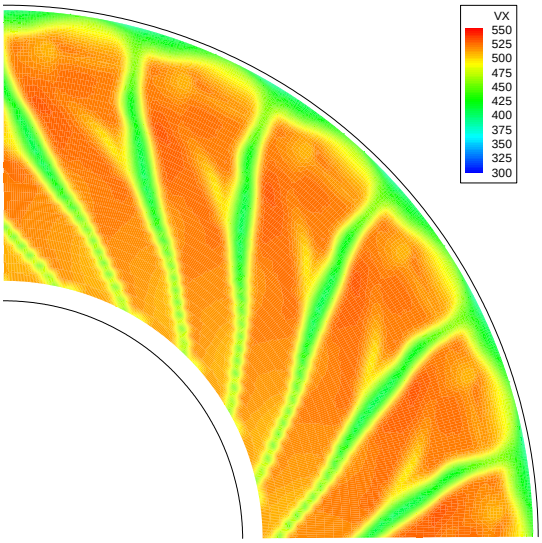

(a) axial velocity data

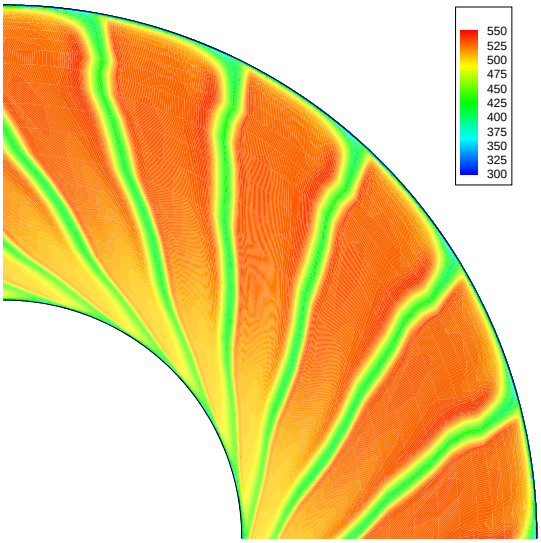

(b) axial velocity computed

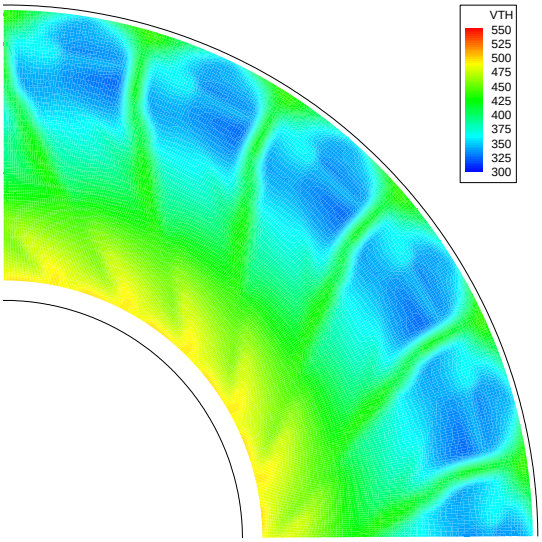

(c) tangential velocity data

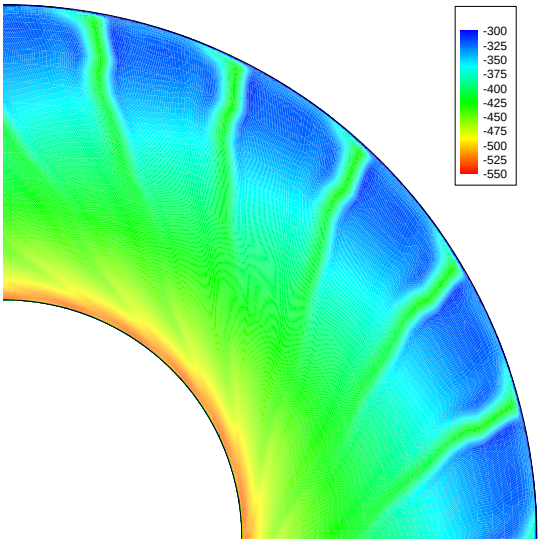

(d) tangential velocity computed

Figure 30: Average passage mean axial and tangential velocity at axial station LDV1 at cutback.

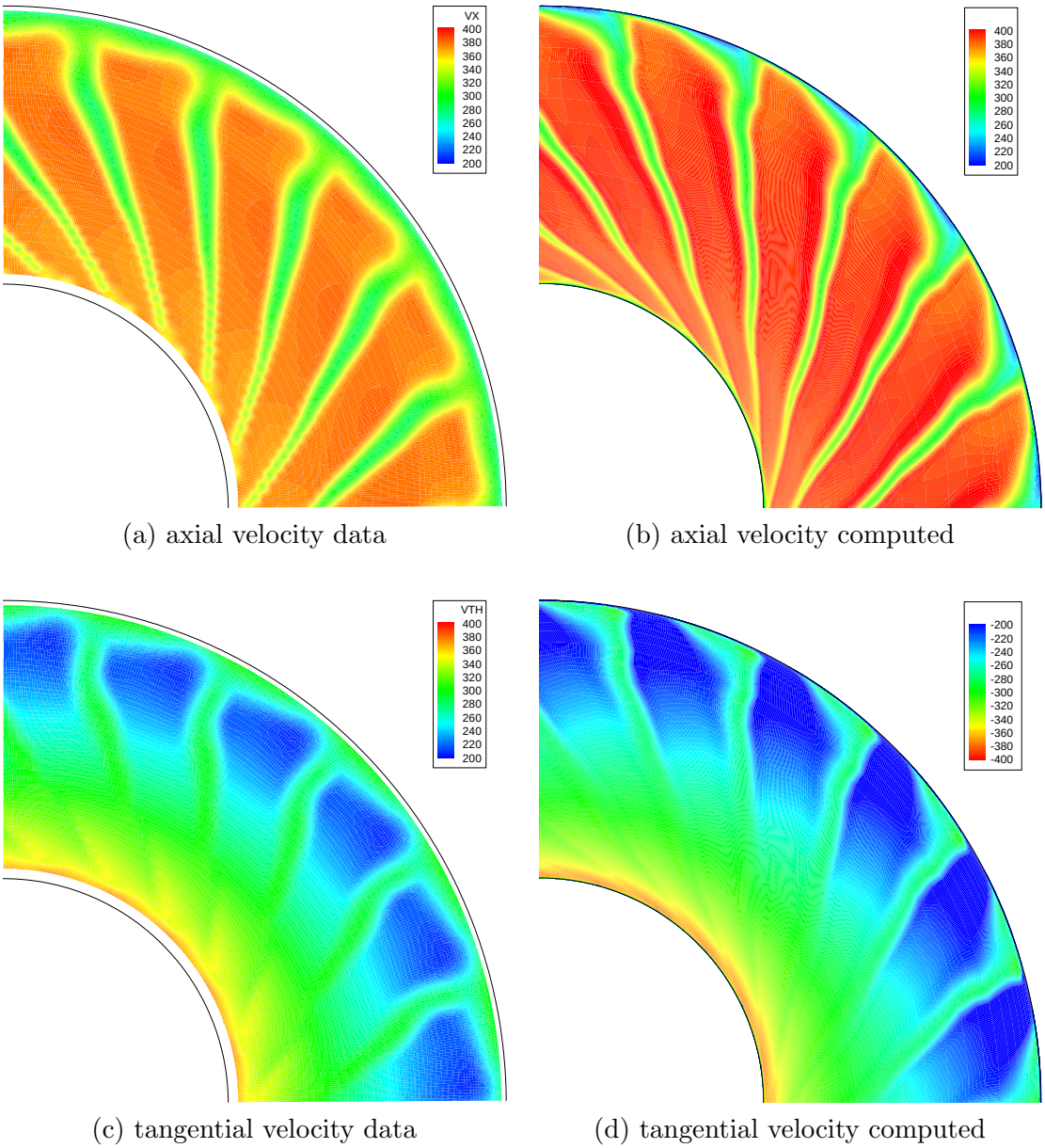

(a) axial velocity data

(b) axial velocity computed

(c) tangential velocity data

(d) tangential velocity computed

Figure 31: Average passage mean axial and tangential velocity at axial station LDV1 at approach.

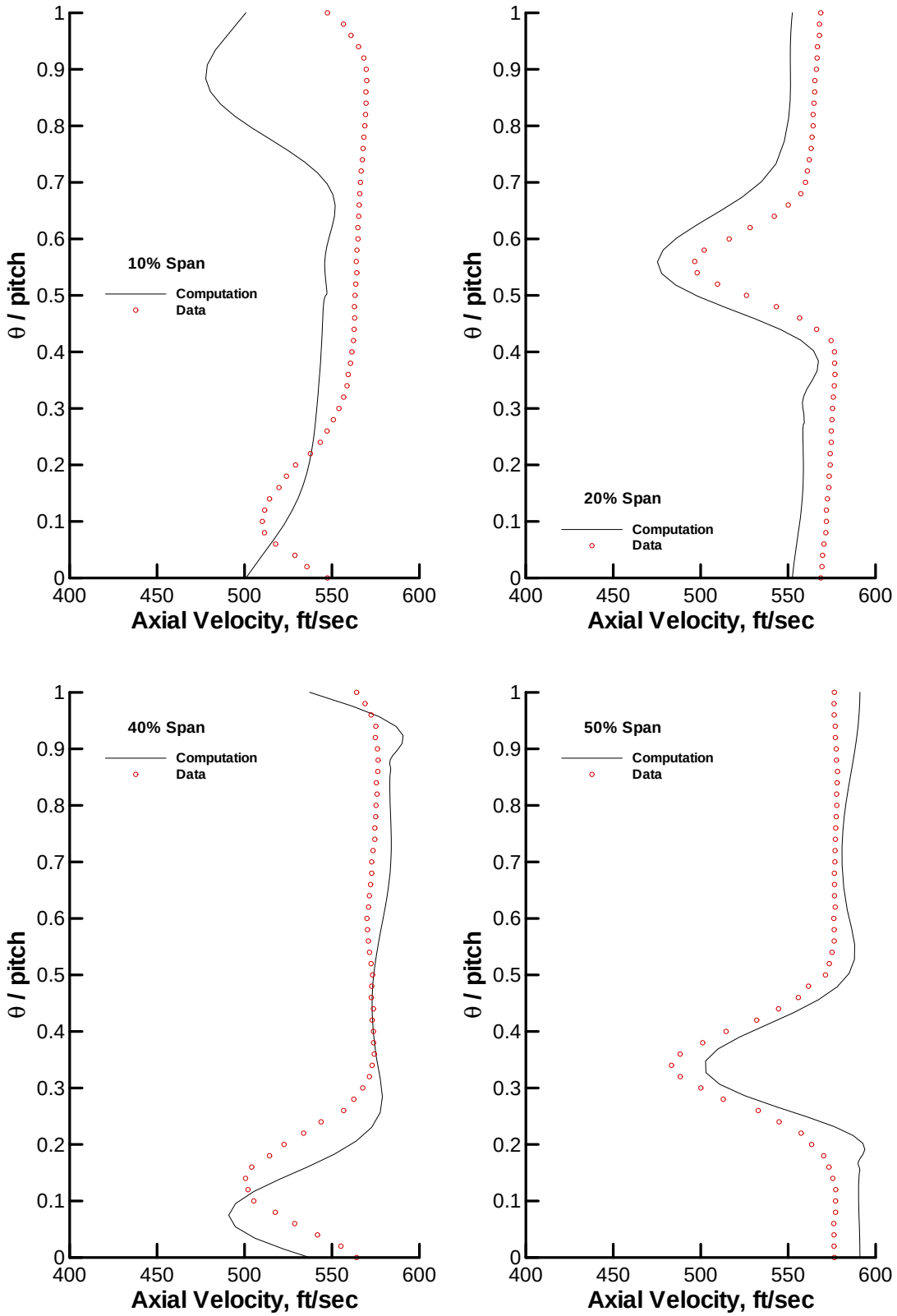

Figure 32: Axial velocity at LDV1 plan, takeoff.

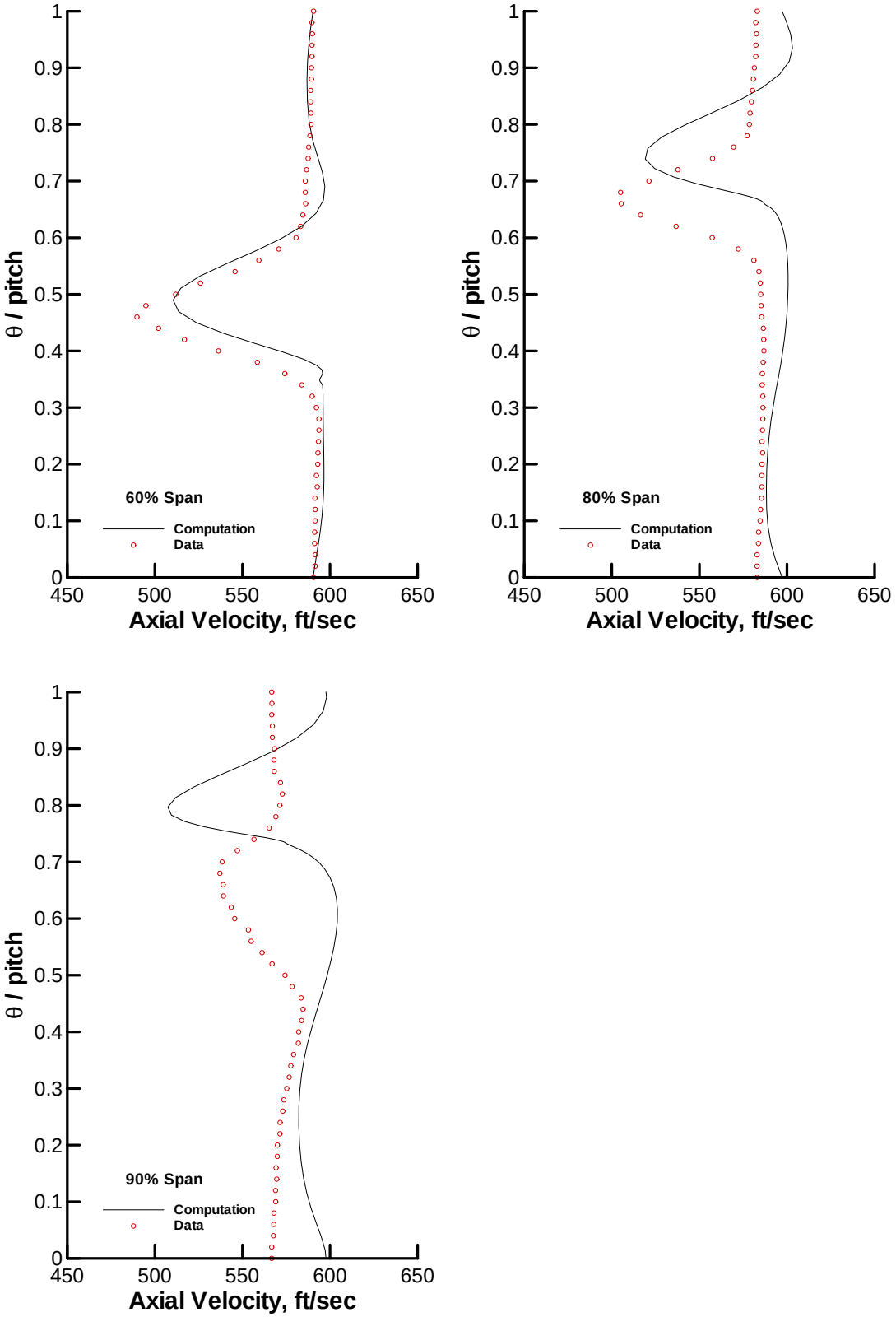

Figure 33: Axial velocity at LDV1 plan, takeoff cont.

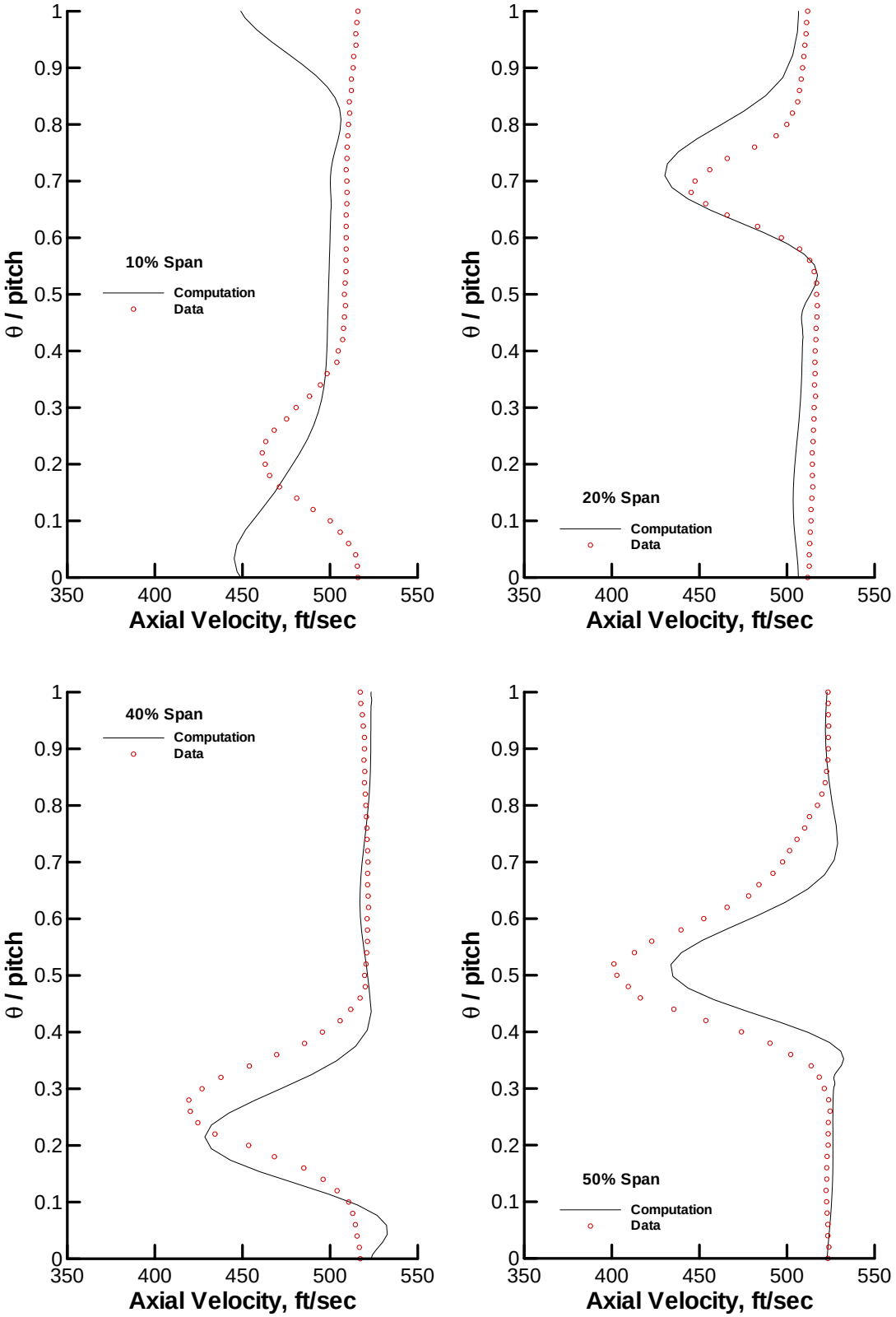

Figure 34: Axial velocity at LDV1 plan, cutback.

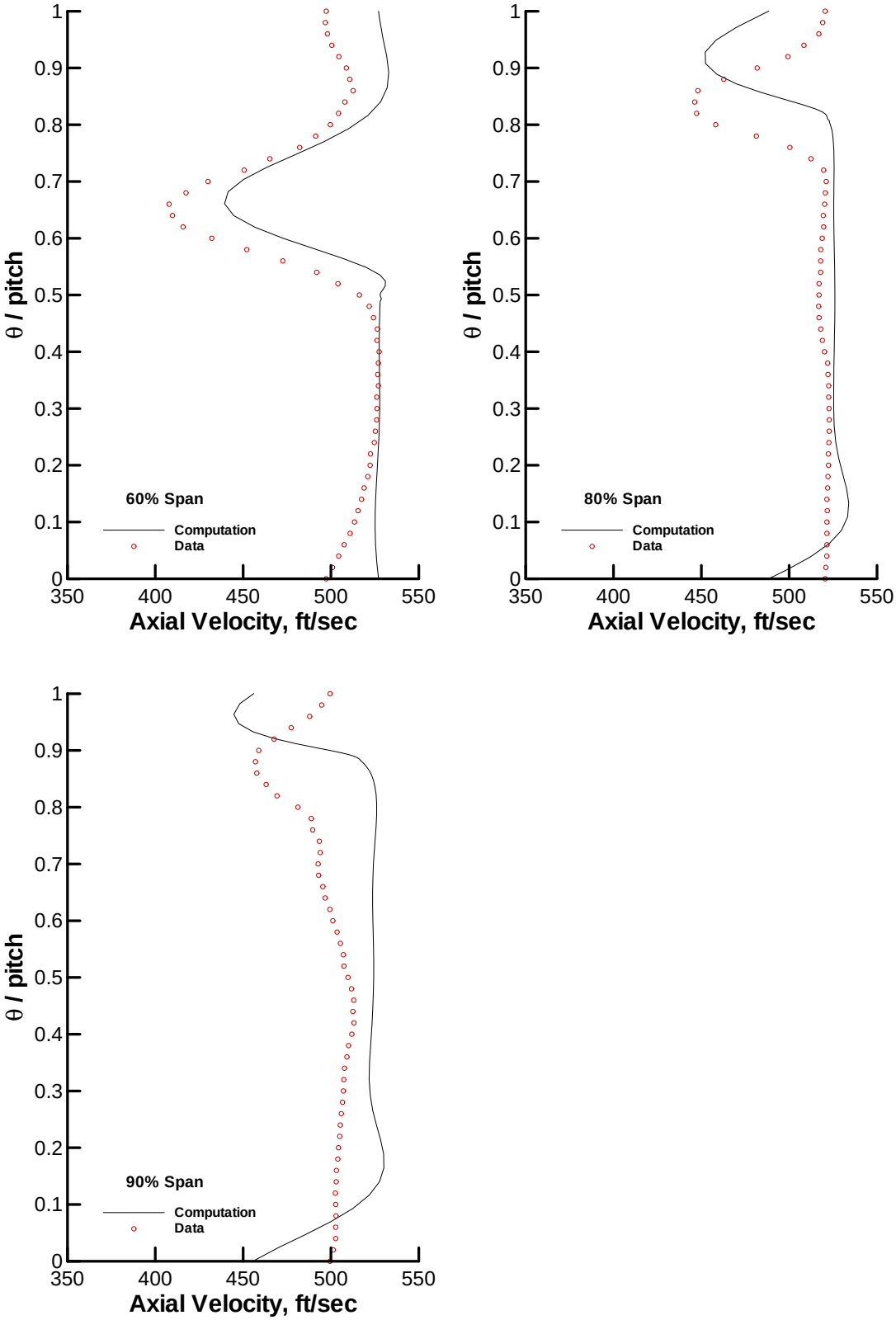

Figure 35: Axial velocity at LDV1 plan, cutback cont.

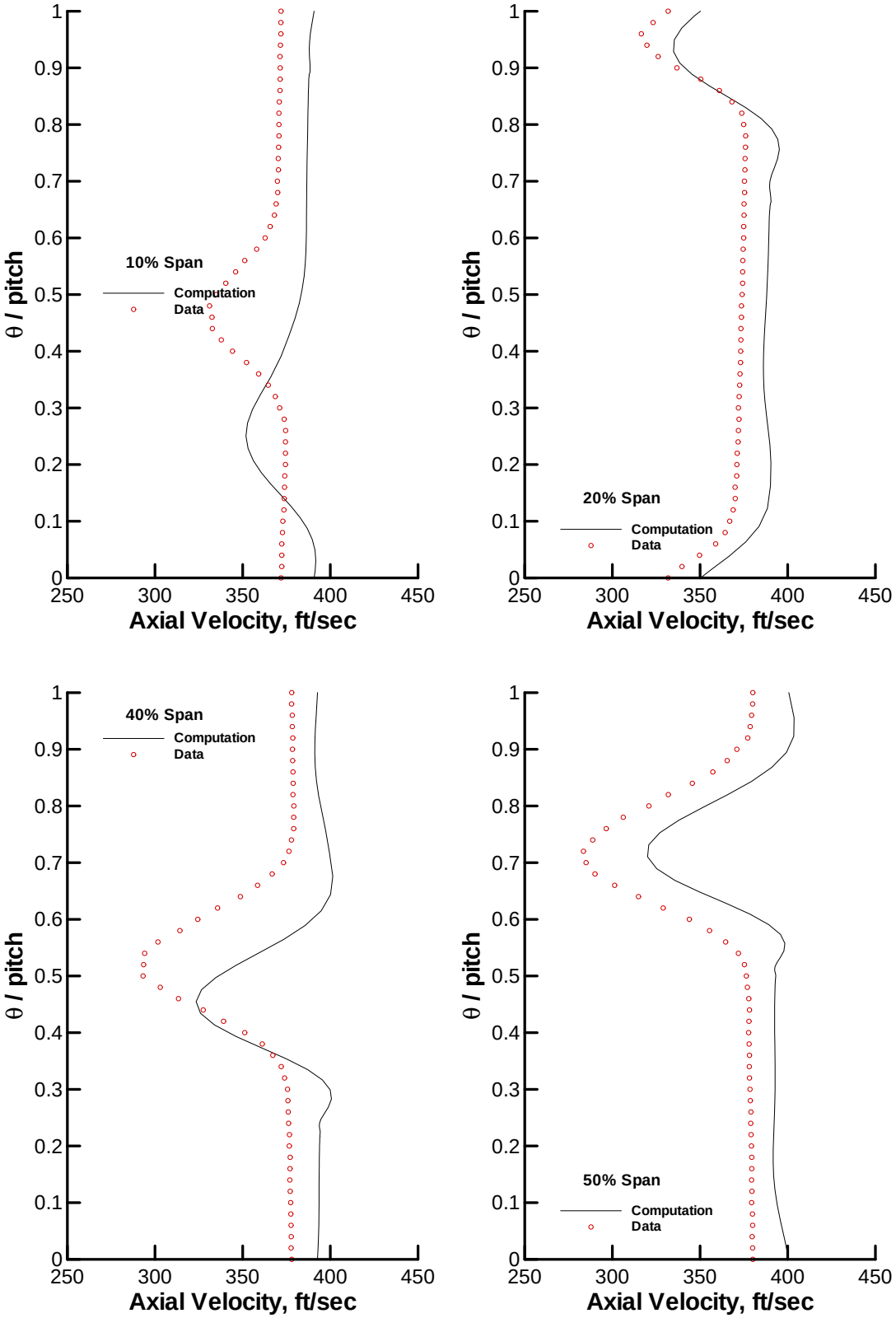

Figure 36: Axial velocity at LDV1 plan, approach.

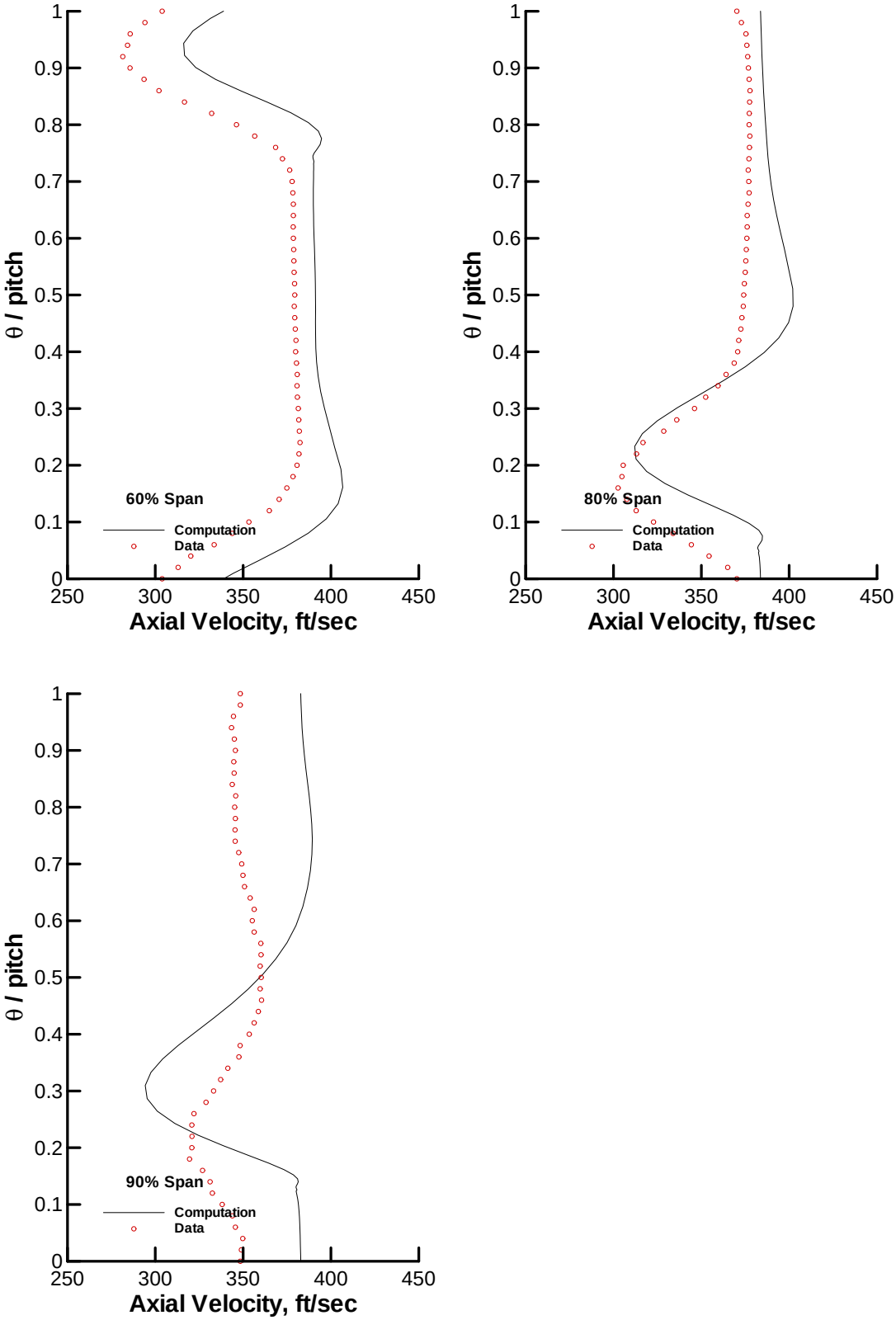

Figure 37: Axial velocity at LDV1 plan, approach cont.

Table 3: Flow conditions for jet noise validation case.

Pressure ratio	3.121
Total temperature	1716 R
Design exit velocity	2409 ft/sec
Ambient pressure	14.30 psi
Ambient temperature	532.4 R
Ambient velocity	400 ft/sec

comparing results for swept versus radial vanes, one important result that can be seen is that TFaNS succeeds in capturing the reduction in tone power levels due to vane sweep, making it an appropriate method for analysis of the benefits of that technology.

4.8.2 Jet noise validation

The jet mixing noise analysis method was validated by carrying out computations for a round convergent-divergent nozzle. Experimental results for a dual-flow nozzle actually would be more appropriate as a validation case, but this case was chosen based on the availability of both flow field and acoustic data and the existence of previous analysis results. This configuration was tested previously in the General Electric anechoic free-jet facility, so laser velocimetry, shadowgraph and acoustic data were available with which to assess the quality of both the CFD analysis and the noise computations[144]. In addition, previous computational studies have been performed for this configuration with MGBK using a mean turbulent flow field computed by different CFD methods[65][72], making it easier to check calculations from the current analysis against those from the previous studies.

The computational grid for the previous CFD analyses, shown in Figure 41, were reused for this study. The nozzle contours were designed to obtain an isentropic, uniform and parallel flow at the nozzle exit to eliminate as much as possible any shock-induced noise at the design Mach number of 1.4[9]. Analysis was performed at the flow conditions from the experimental test point which most closely matches the design conditions of the nozzle so that the mixing noise predictions could be assessed without the influence of any shock noise which might have been measured in the experiment. The data for this test point are listed in Table 3.

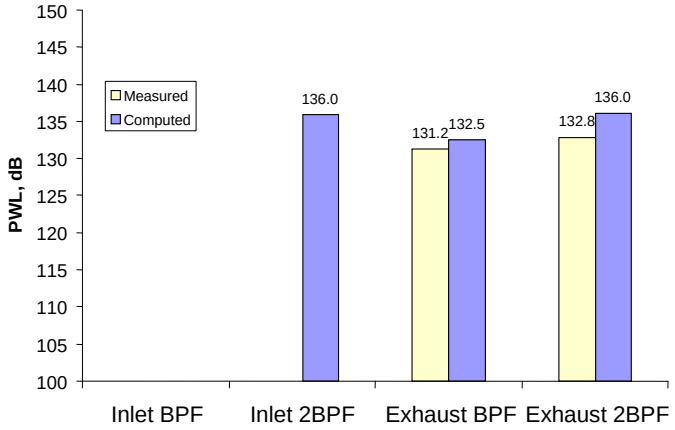

(a) 54 radial vanes

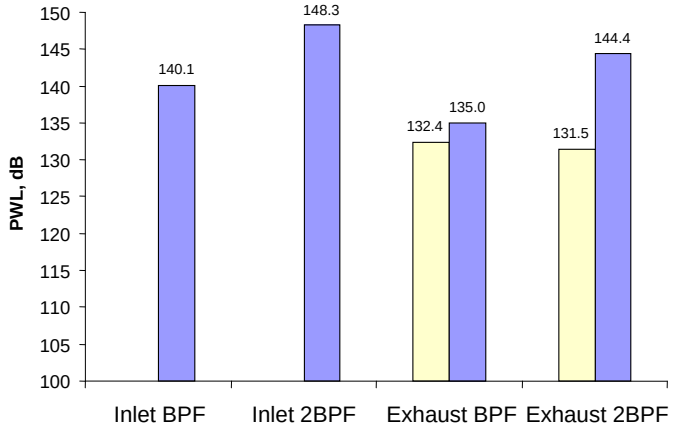

(b) 26 radial vanes

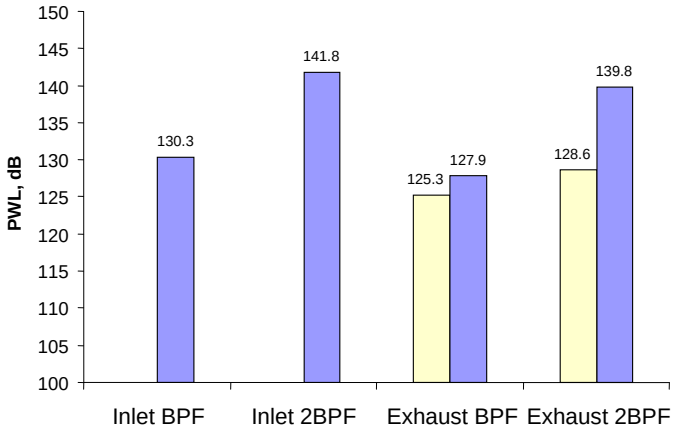

(c) 26 swept vanes

Figure 38: Comparison of computed and measured total rotor-stator interaction tone power levels, takeoff.

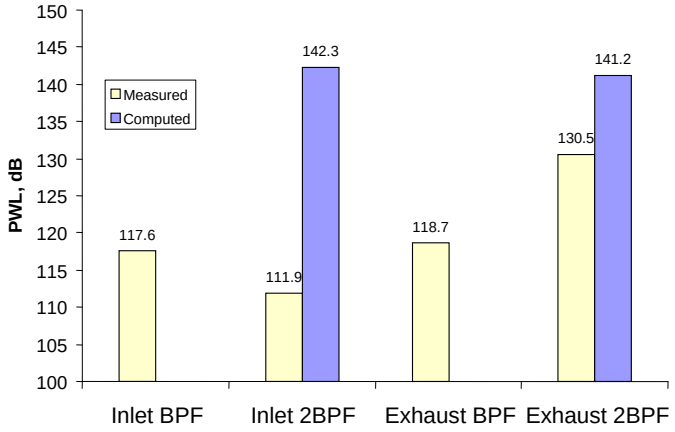

(a) 54 radial vanes

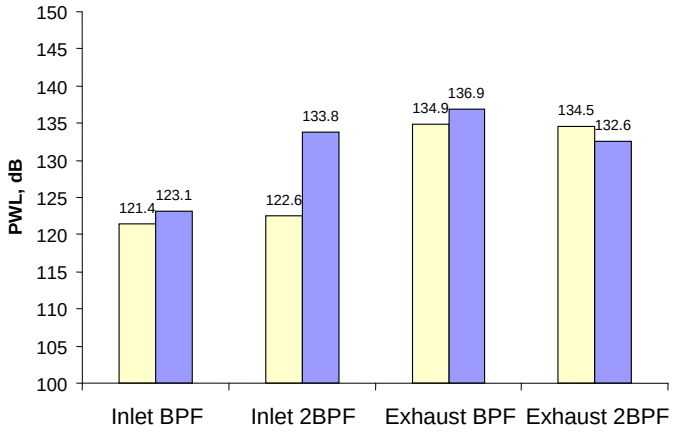

(b) 26 radial vanes

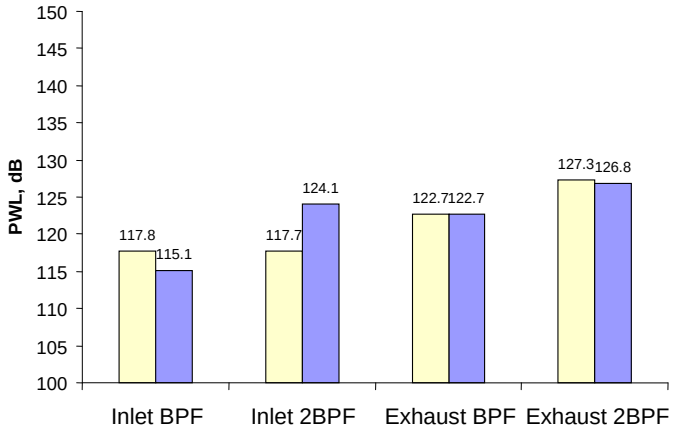

(c) 26 swept vanes

Figure 39: Comparison of computed and measured total rotor-stator interaction tone power levels, cutback.

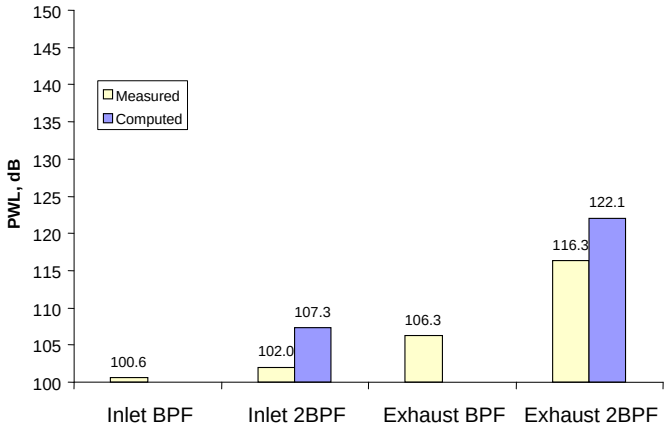

(a) 54 radial vanes

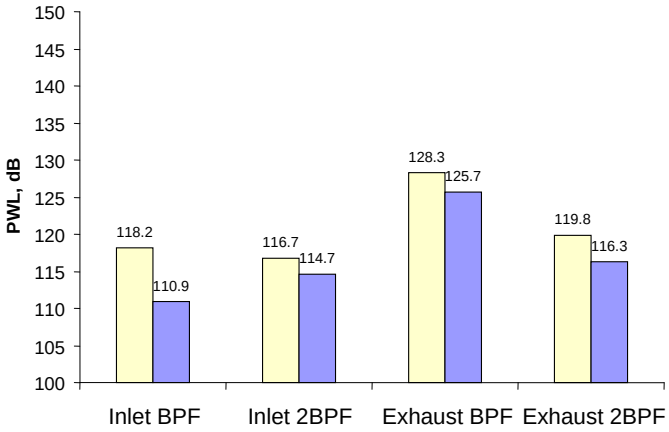

(b) 26 radial vanes

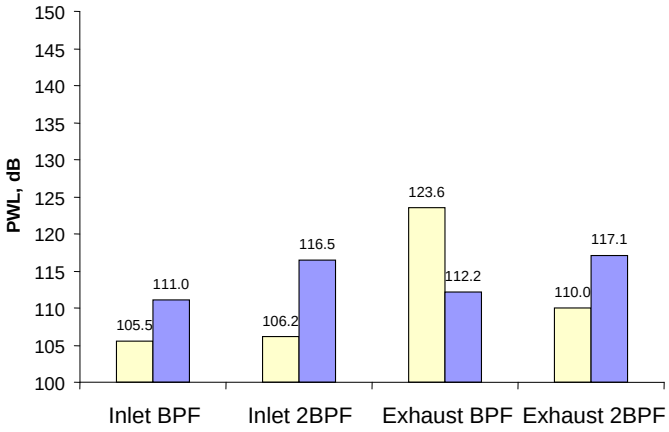

(c) 26 swept vanes

Figure 40: Comparison of computed and measured total rotor-stator interaction tone power levels, approach.

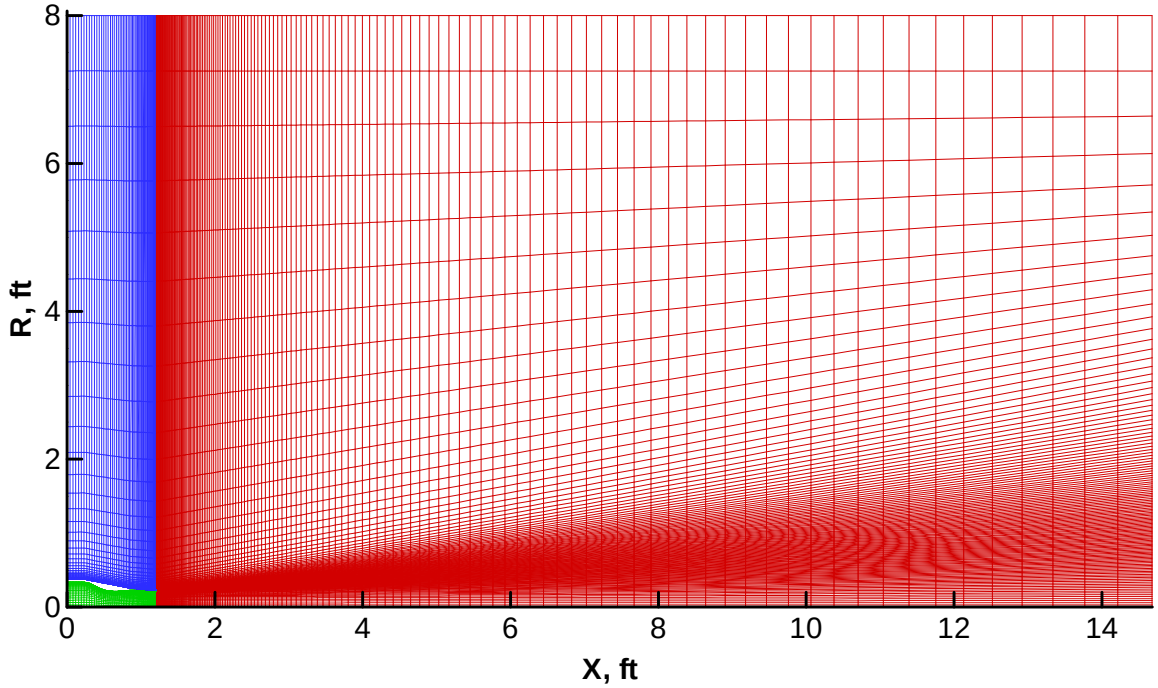

(a) full grid

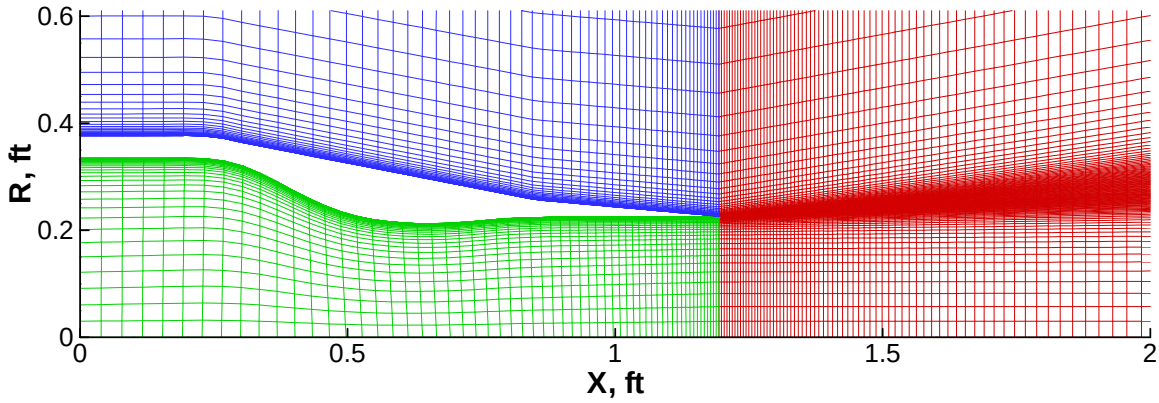

(b) close-up of nozzle

Figure 41: Nozzle geometry and computational grid for validation case.

Mach contours computed by WIND are shown in Figure 42, and the computed turbulent kinetic energy field is shown in Figure 43. Even though the test point is at the nozzle's design pressure ratio, a Mach disc can be seen inside the nozzle, and multiple shock cells exist in the potential region outside the nozzle, as shown in greater detail in Figure 42(b). External shocks were observed in the experimental results for this test point, but were much weaker than those in the CFD computations. It will be seen below that even though the flow field in the potential core is significantly different, the turbulence level in the shear layer is computed correctly and thus the mixing noise prediction is not impacted too severely. If the CFD results were to be used in a physics-based prediction of the shock-generated noise, the correct estimation of the strength of the shocks in the external flow field would be much more important.

The computed flow field was compared to measured data to assess the quality of the CFD analysis. The velocity at the nozzle lip line is plotted in Figure 44 as a function of distance downstream of the nozzle exit. The WIND predictions agree reasonably well with the data except for the additional oscillations due to the shock structure. The computed and measured turbulence intensities at the lip line are plotted in Figure 45. The oscillations in the computed turbulence intensity in the vicinity of the shocks are due primarily to spacial fluctuations in the location of the shear layer centerline, rather than variation in the magnitude of the turbulence intensity. The turbulence intensity is somewhat under-predicted in the vicinity of the end of the potential core ($x/D_{eq} = 5$) but the axial decay is otherwise predicted well. Radial profiles of axial velocity and turbulence intensity are plotted in Figures 46 and 47 at an axial distance $x/D_{eq} = 8.7$, which is in the fully turbulent mixing region. The predicted velocity decay and turbulence levels in the shear layer agree well with the experimental data. The comparisons with experimental data show that even though the shock structure in the potential core is not modelled correctly, WIND is able to accurately model the mixing rate and turbulence levels in the jet flow field, which is essential for an accurate prediction of the mixing noise levels.

The mean flow field from WIND was used to predict the mixing noise of the jet in MGBK. The default value for α_c (Equation 45) was used, but a modified value for β_c was

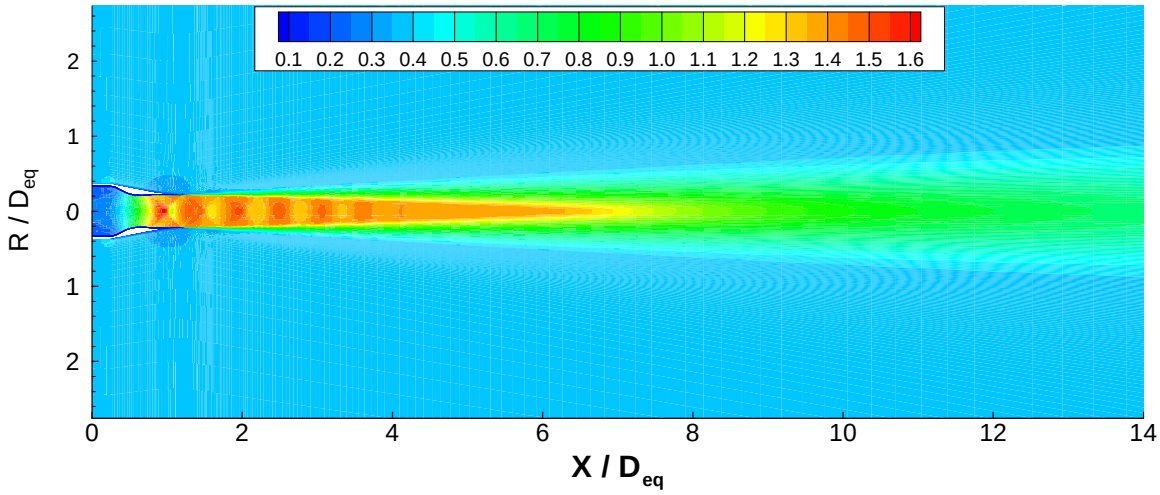

(a) full grid

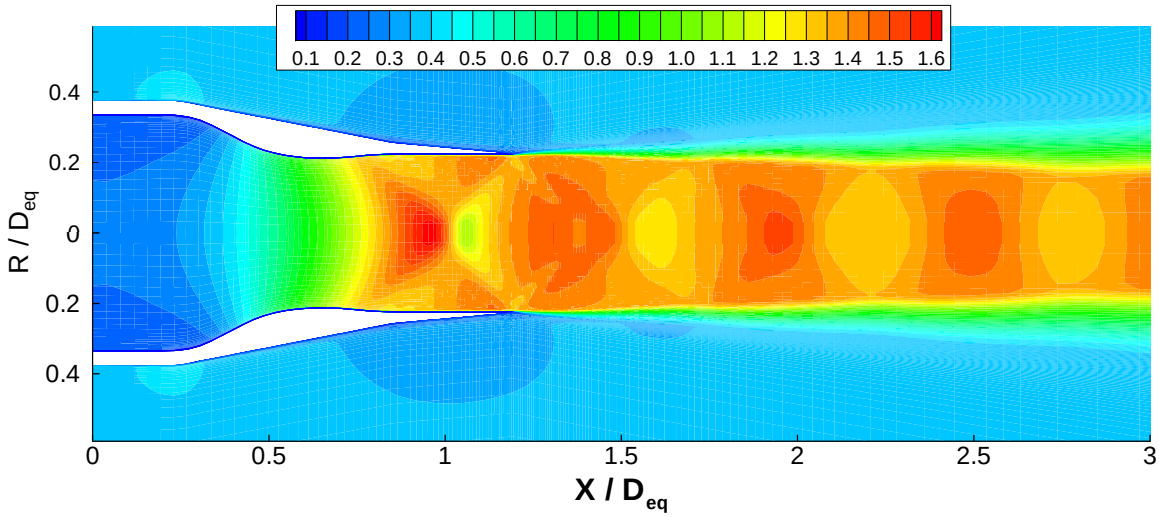

(b) detail of shock structure

Figure 42: Mach number contours computed by WIND.

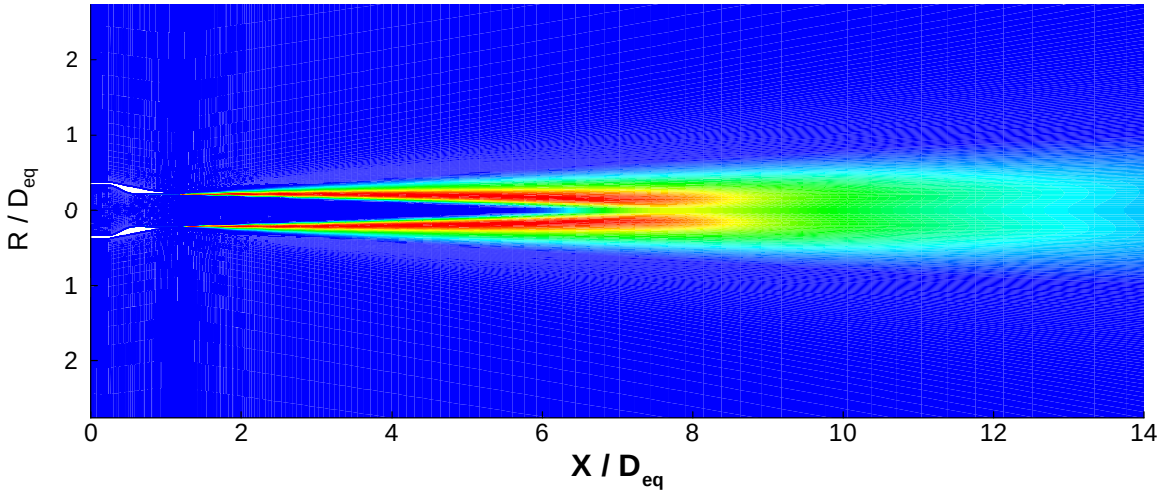

Figure 43: Turbulence kinetic energy contours computed by WIND.

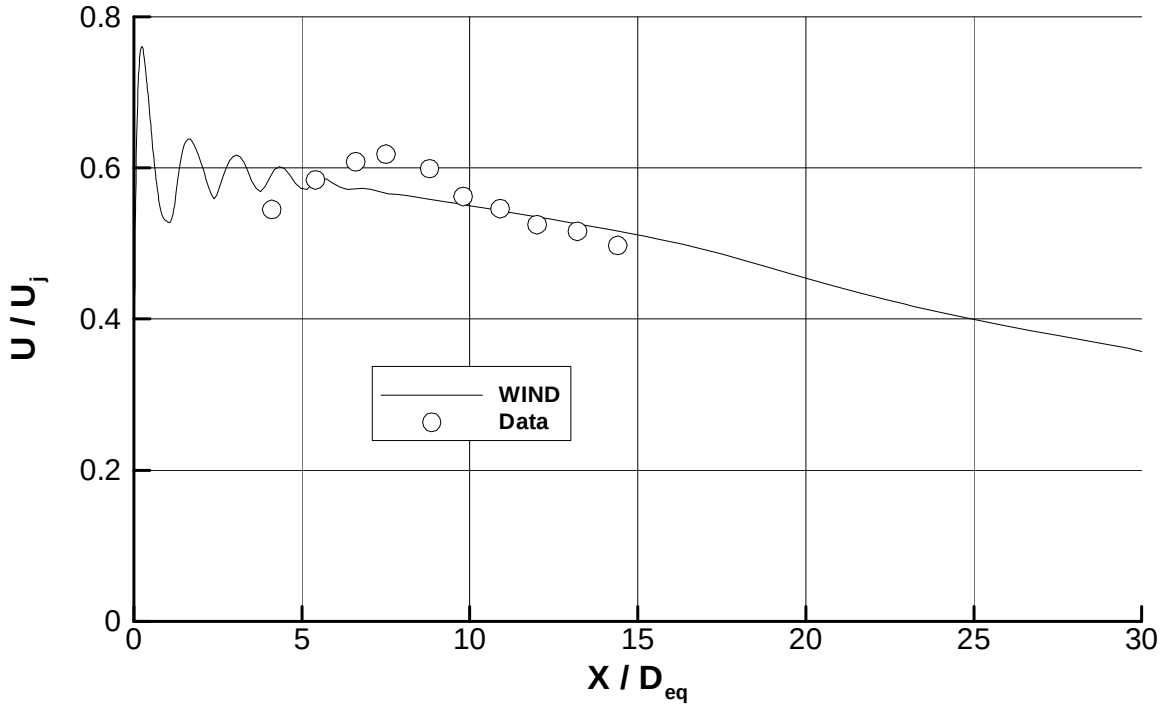

Figure 44: Comparison of lip line velocity with data.

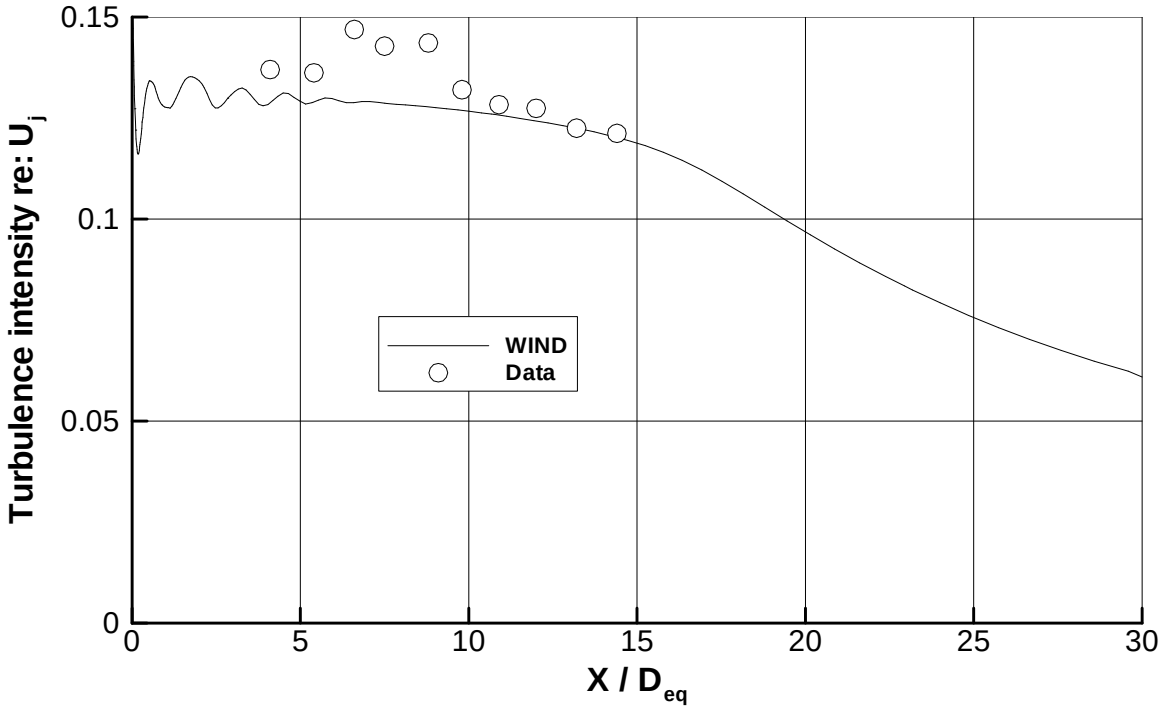

Figure 45: Comparison of lip line turbulence intensity with data.

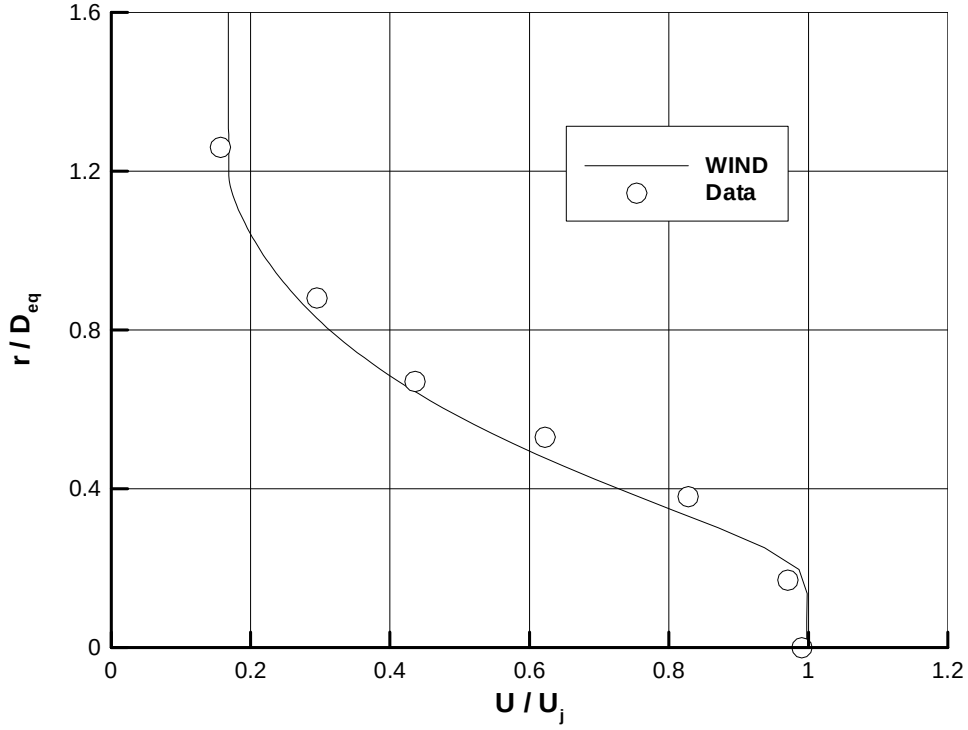

Figure 46: Comparison of radial velocity profile with data at $x/D_{eq} = 8.7$.

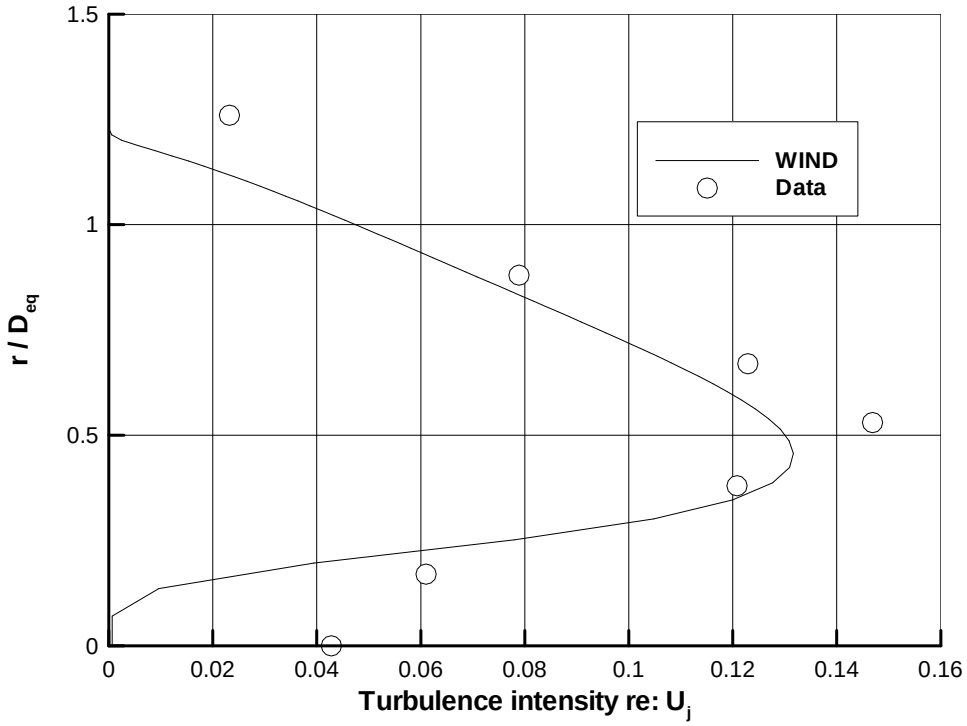

Figure 47: Comparison of radial turbulence profile with data at $x/D_{eq} = 8.7$.

used. In calculating the effects of convection on the directivity (Equation 46), MGBK uses the peak Mach number at the exit plane, rather than the average, so due to the presence of shocks within the nozzle a value of $M_j = 1.47$ was used; to avoid an over-prediction of the convection effects, β_c was reduced by the factor 1.4/1.47.

Figure 48 shows a comparison of the predicted overall sound pressure level (OASPL) directivity with the experimental data. Also shown are predicted levels from ANOPP's single-stream jet noise method. MGBK does a better job of predicting the mixing noise directivity, especially at angles near the peak OASPL. ANOPP seems to incorrectly predict the convection effects for this case. Predicted and measured noise spectra are shown at a number of different directivity angles in Figure 49. MGBK does a good job of predicting both the spectral shape and peak frequency of the mixing noise spectrum, particularly at the directivity angles near the OASPL peak where the overall level is correctly predicted.

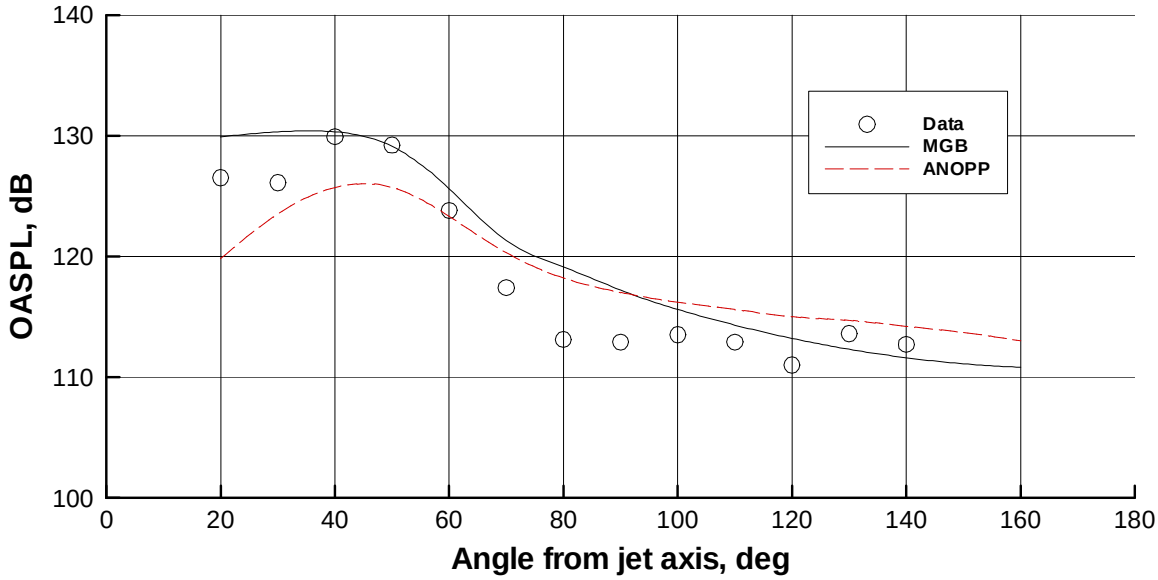

Figure 48: Comparison of far field OASPL directivity with data at a distance of 40 feet.

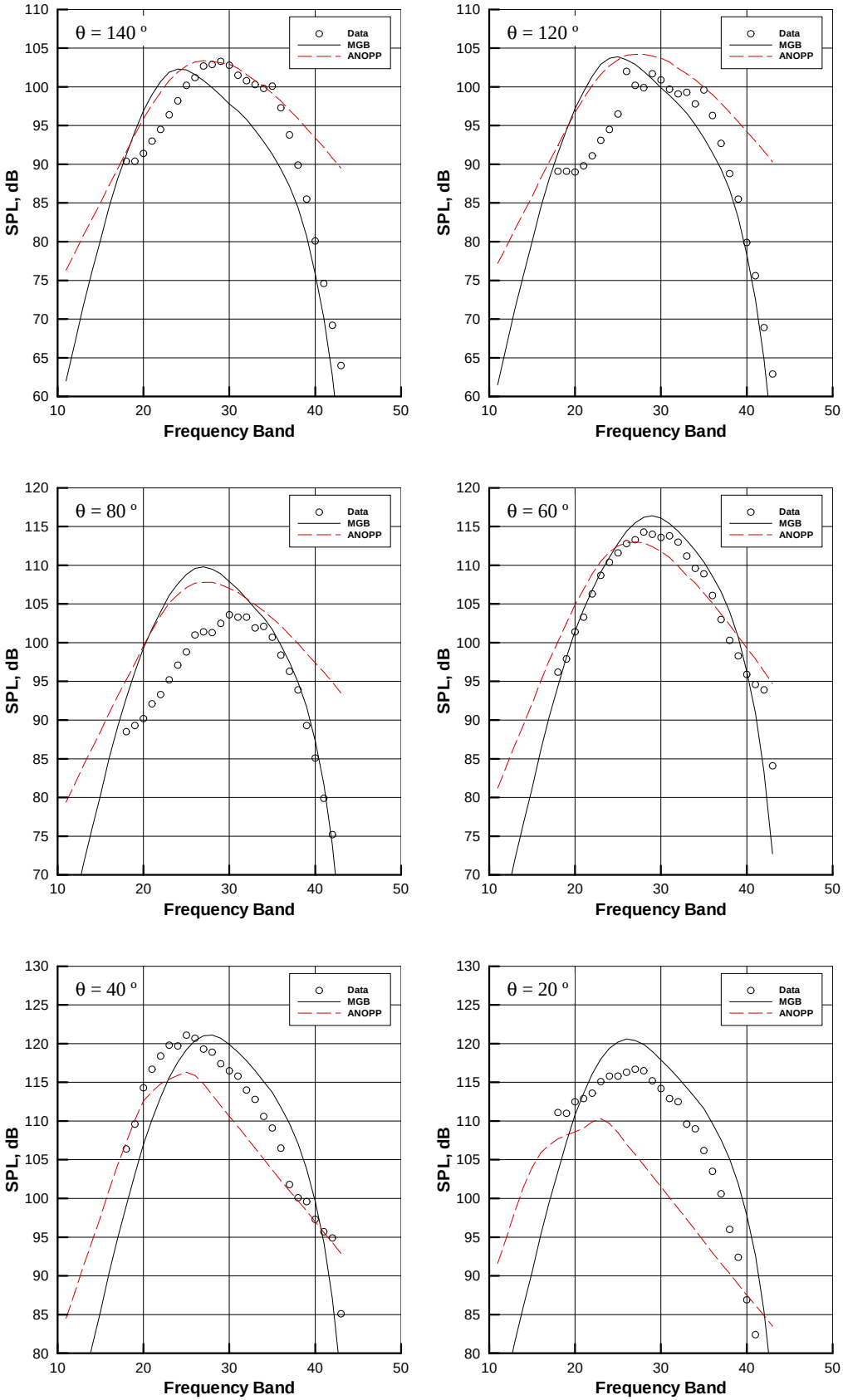

Figure 49: Comparison of 1/3 octave-band spectra with data at a distance of 40 feet.

CHAPTER V

IMPLEMENTATION

The advantages of physics-based noise analysis were discussed in Chapter 1; unfortunately, the use of higher-fidelity analysis methods greatly increases the time required to obtain noise predictions for each aircraft concept. The increased computation times make it impossible to use the higher-fidelity methods directly in applications where rapid evaluations are required. The methodology that was assembled in this study, described in Chapter 4, accelerates the evolution of an aircraft and engine concept from conceptual-level definition of engine geometry and operating conditions to a preliminary-level analysis of the noise levels. Execution of the methodology still requires approximately one day per design point, however, so it was necessary to take additional steps in the implementation of the methodology before it became practical for use as a conceptual design tool.

5.1 Global approximation methods

One way to increase the utility of high-fidelity analysis methods is through the use of surrogate-based optimization, which uses fast-executing *surrogate* models in place of the high-fidelity analysis when conducting optimization problems that require large numbers of function evaluations. Two categories of surrogate models are *variable fidelity* type models and *data fit* models. Variable fidelity models are still physics-based but are faster to execute because of either simpler physics, coarser discretization or higher convergence tolerances; Data fit models use a set of results generated with the high-fidelity analysis methods and apply interpolation or regression to extend the applicability of the results over a range of variable values. Two categories of data fit surrogates are *local approximation methods*, which use a small number of data points to make an approximation to the function in the vicinity of a given design point, and *global approximation methods*, which use larger numbers of data points to form an approximation of the function applicable to the entire domain of

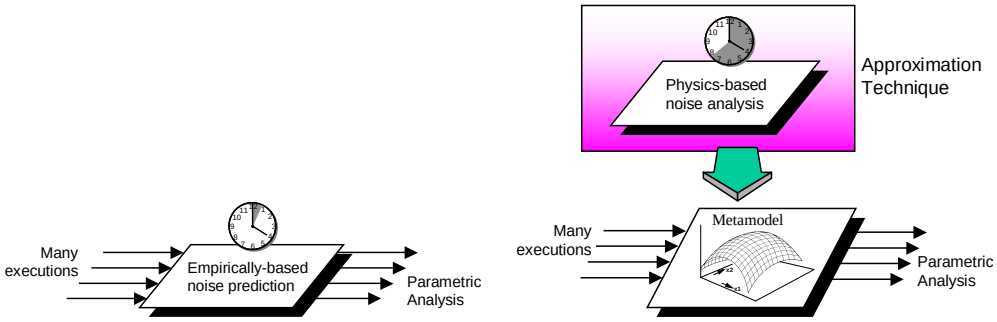

(a) traditional process (b) use of a metamodel

Figure 50: Use of global approximation methods to create a metamodel.

interest[37].

Among all categories of surrogate models, global approximation methods are of particular interest in conceptual design, because once created they can be used in any number of studies to explore the full domain of possible designs without the need to return repeatedly to the high-fidelity methods for additional analysis. Global approximation methods seek to create a *metamodel* which retains the overall properties of the complex analysis, but can be executed much more quickly[89]. Figure 50 illustrates how a metamodel can be used in place of empirically-based methods. The first step is to make multiple runs with the physics-based analysis and apply the approximation method to create a metamodel, which can then be used in all subsequent design studies so that rapid evaluations can be made. Multiple metamodels can be created for the various disciplines—such as aerodynamics, structures, propulsion, and stability and control—and be integrated at the system level. The metamodels provide the various responses necessary to compute the overall system-level performance and economics of the aircraft, as well as constraints on handling qualities and environmental impact (Figure 51). The results of this study are intended to represent the development of metamodels for the acoustics discipline, as part of a larger hypothetical conceptual design study.

In general, metamodels are created by executing the analysis method for a limited number of points distributed throughout the design space, and the results are used to infer relationships between the design variables and the analysis outputs which can be used to obtain the approximated value at any point in the design space. The primary types

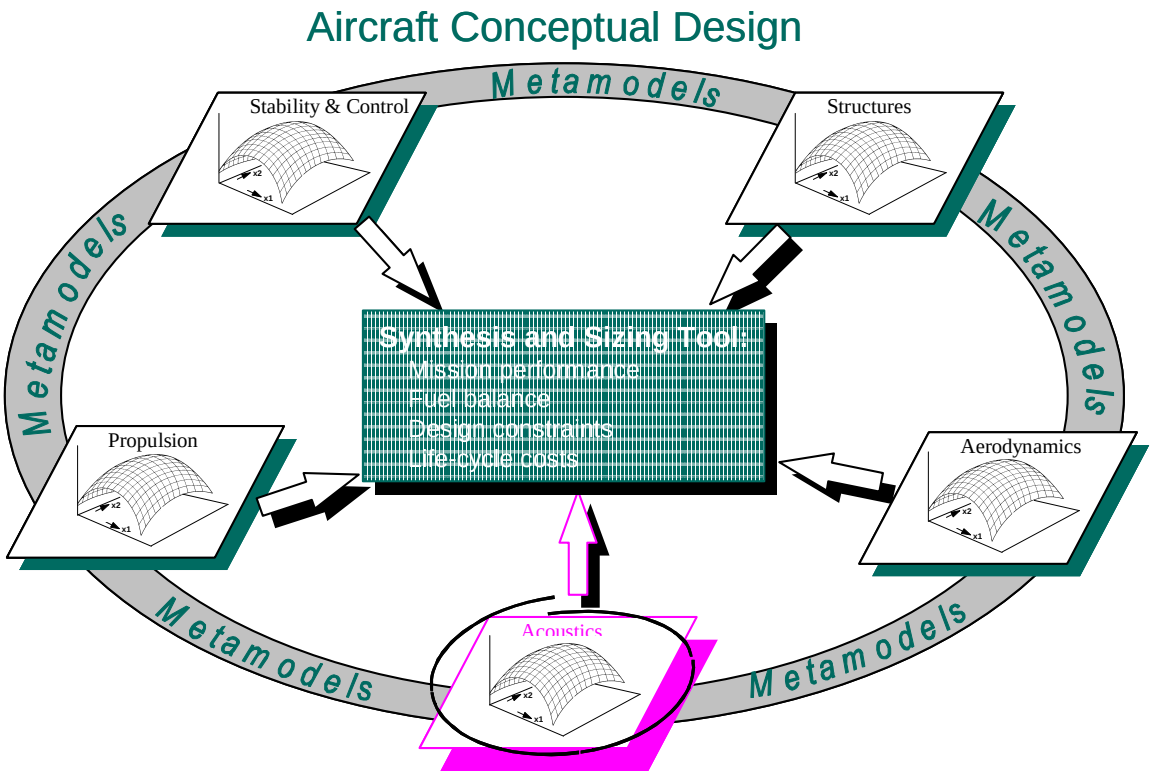

Figure 51: Use of disciplinary metamodels in system-level design studies.

of approximation methods are Kriging, radial basis functions, artificial neural networks, response surface methodology[37].

A neural network (NN) is a computational system which is an idealized simplified version of a brain cell. An NN generally consists of a large number of simple processing units, called artificial neurons, which are interconnected in a specific way. The strengths of the connections are known as weights, which are adjusted during a "learning" process. Multiple artificial neurons can be grouped together in layers, and a complete network is composed of input, hidden, and output layers, with appropriate transfer functions. An NN can approximate any continuous function perfectly as long as there are enough neurons in the hidden layer[30]. NNs are flexible in form and are well-suited to complex functions which are not easily approximated by polynomials, such as those with discontinuous changes. This advantage is most useful when there is little computational noise[104].

Response surface methodology (RSM) is composed of a number of statistical techniques for empirically relating an output variable, or response, to the values of several selected

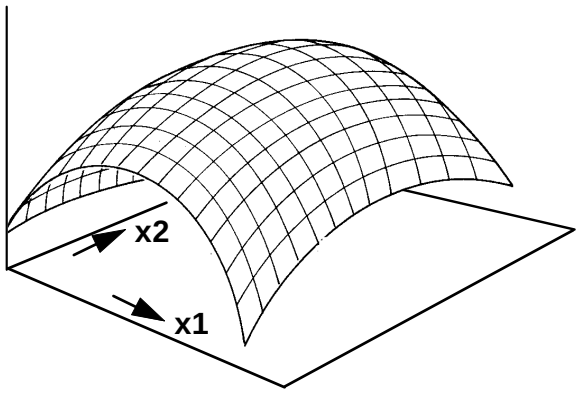

Figure 52: Illustration of a two-variable RSE.

input variables[73]. The relationship is specified as a response surface equation (RSE), which is an algebraic function, usually polynomial, for the response as a function of the input variables. A second-degree polynomial RSE has the following form:

$$R = b_0 + \sum_{i=1}^{n} b_i x_i + \sum_{i=1}^{n} b_{ii} x_i^2 + \sum_{i=1}^{n-1} \sum_{j=i+1}^{n} b_{ij} x_i x_j \tag{47}$$

where b_0 is the intercept, b_i are regression coefficients for the linear terms, b_{ii} are regression coefficients for the pure quadratic terms, and b_{ij} are regression coefficients for the cross-product terms. The x_i variables represent normalized values of each of the input variables, or *factors*, affecting the response. The second-degree model allows for both linear and non-linear behavior in individual factors, as well as simple interactions between factors. An illustration of a simple two-variable RSE is shown in Figure 52.

RSM was originally developed to filter noise from experimental data, so it is particularly well-suited to approximating functions with significant numerical noise. RSM can be of limited usefulness in cases with many input variables exist, and can suffer in accuracy with large variable ranges or when the analysis displays complex behaviors which cannot be modelled with a smooth polynomial[30].

RSM is an integral part of the ModelCenter integration software, and so was instantly available for use with the integrated analysis process described in Chapter 4. For this reason plus its applicability to the current study, its ease of use and the large amount of experience in its use in engineering design applications, it was chosen as the approximation method to be used in this study.

Table 4: Example two-level full-factorial DOE table for three variables.

	Factors			Response
Run	$\overline{x_1}$	$\overline{x_2}$	$\overline{x_3}$	**y**
1	-1	-1	-1	y_1
2	+1	-1	-1	y_2
3	-1	+1	-1	y_3
4	+1	+1	-1	y_4
5	-1	-1	+1	y_5
6	+1	-1	+1	y_6
7	-1	+1	+1	y_7
8	+1	+1	+1	y_8

5.1.1 Design of experiments

The most common method of obtaining the regression coefficients in the RSE is through Design of Experiments (DOE), which provides an efficient and methodical system for determining the necessary combinations of factor levels for obtaining the maximum regression information with a minimum number of runs[11]. The specified combinations of factors are organized into a *DOE table*, whose rows represent a number of analysis runs and whose columns represent the specified factor combinations for each of those runs. For example, Table 4 represents a simple two-level, full-factorial DOE table for three design variables: x_1, x_2, and x_3. Each of the rows in the table represents one of eight analysis runs, while the first three columns represent the values of the three factors and the final column is used to record the output values from each of the analysis runs. The variable ranges are normalized so the minimum value corresponds to -1, while the maximum value corresponds to $+1$, as follows:

$$\overline{x_j} = \frac{2x_j - x_{j,max} - x_{j,min}}{x_{j,max} - x_{j,min}} \tag{48}$$

where $\overline{x_j}$ is the normalized value of the design variable x_j having a minimum x_{min} and maximum x_{max}. Normalization of the factors in this manner serves to reduce the potential numerical error during calculation of the RSE coefficients and simplifies the mathematics.

Table 5: Example two-level half-factorial DOE table for three variables.

	Factors			Response
Run	$\overline{x_1}$	$\overline{x_2}$	$\overline{x_3}$	**y**
1	+1	-1	-1	y_1
2	-1	+1	-1	y_2
3	-1	-1	+1	y_3
4	+1	+1	+1	y_4

5.1.1.1 Two-level designs

The DOE table in Table 4 is a *two-level* design, in that each of the factors takes on only one of two values, ± 1, and it is a *full-factorial* design because it contains all of the 2^3 combinations of values for the three factors. Since the factors in the two-level design only take on one of two levels, only the coefficients for the linear terms and first-order interactions in the RSE can be estimated. As the number of factors increases, the number of runs in a full-factorial design grows exponentially, and can quickly become impractical. Alternatively, a *fractional-factorial* table can be used, which contains only a fraction of the factor level combinations but will still provide important information about the linear terms and a select set of first-order interactions in the RSE[99]. Fractional-factorial designs can be half-factorial, quarter-factorial, eighth-factorial, etc. A two-level half-factorial DOE table is shown in Table 5.

5.1.1.2 Higher-level designs

To use the full quadratic RSE model (Equation 47), it is necessary to use a three- or higher-level experimental design. Table 6 illustrates a three-level, full-factorial DOE table for three design variables, in which the factors take on the value -1, 0 or +1. The number of runs in a three-level design can be much greater than in a two-level design, so full-factorial designs are usually not practical to use for more than a handful of variables. If more factors are desired, there are multiple options for types of DOE tables which can be used for a quadratic model but are much more efficient than a full-factorial design. These designs retain the ability to estimate all of the linear, quadratic and interaction terms in the RSE

Table 6: Example three-level full-factorial DOE table for three variables.

	Factors			Response
Run	$\overline{x_1}$	$\overline{x_2}$	$\overline{x_3}$	**y**
1	-1	-1	-1	y_1
2	0	-1	-1	y_2
3	+1	-1	-1	y_3
4	-1	0	-1	y_4
5	0	0	-1	y_5
6	+1	0	-1	y_6
7	-1	+1	-1	y_7
8	0	+1	-1	y_8
9	+1	+1	-1	y_9
10	-1	-1	0	y_{10}
11	0	-1	0	y_{11}
12	+1	-1	0	y_{12}
13	-1	0	0	y_{13}
14	0	0	0	y_{14}
15	+1	0	0	y_{15}
16	-1	+1	0	y_{16}
17	0	+1	0	y_{17}
18	+1	+1	0	y_{18}
19	-1	-1	+1	y_{19}
20	0	-1	+1	y_{20}
21	+1	-1	+1	y_{21}
22	-1	0	+1	y_{22}
23	0	0	+1	y_{23}
24	+1	0	+1	y_{24}
25	-1	+1	+1	y_{25}
26	0	+1	+1	y_{26}
27	+1	+1	+1	y_{27}

while greatly reducing the number of runs required for a given number of variables relative to a full-factorial design.

Table 8 lists several design types which are appropriate for use with a quadratic RSE. A central-composite design (CCD) uses a two-level full- or fraction-factorial design, augmented by a center point and a series of "star points" along each variable axis. Table 7 gives the factor combinations for a sample three-variable CCD, and Figure 53 shows a plot of the factor combinations on three axes. Two star points are created by setting all the factors but one to their midpoints, and toggling the remaining variable between the values $\pm\alpha$;

Table 7: Example central-composite design for three variables.

	Factors			Response
Run	$\overline{x_1}$	$\overline{x_2}$	$\overline{x_3}$	**y**
1	-1	-1	-1	y_1
2	+1	-1	-1	y_2
3	-1	+1	-1	y_3
4	+1	+1	-1	y_4
5	-1	-1	+1	y_5
6	+1	-1	+1	y_6
7	-1	+1	+1	y_7
8	+1	+1	+1	y_8
9	0	0	0	y_9
10	-1	0	0	y_{10}
11	+1	0	0	y_{11}
12	0	-1	0	y_{12}
13	0	+1	0	y_{13}
14	0	0	-1	y_{14}
15	0	0	+1	y_{15}

the remaining star points are then created by repeating the process for the other variables. When a value of $\alpha = 1$ is used, the start points are located on the center of the faces of the "cube", and a special class of CCD is created, called a *face-centered* design. Face-centered CCDs are especially useful when the outputs are the result of computational simulation rather than actual experimental measurements.

Another category of designs which is useful for generation of RSEs are D-optimal designs, which can be used in cases where the design space is irregular, where a nonstandard model is desired, or when the number of sample sizes needs to be kept as small as possible. To construct a D-optimal design, three elements are specified: the maximum number of analysis runs, n_T; the response function, R; and a candidate list of feasible designs. The goal is to find an appropriate design matrix for the specified response function and with n_T runs, which gives the best precision in the estimation of the RSE coefficients. The design matrix, $\mathbf{X}$, is defined in Section 5.1.2. The D-optimal design is the value of $\mathbf{X}$ which minimizes the D criterion:

$$D = |(\mathbf{X}'\mathbf{X})^{-1}| \tag{49}$$

Table 8: Number of required runs for various DOE types.

DOE	3 variables	7 variables	12 variables	n variables
3-level, full factorial	27	2187	531,441	3^n
Central composite	15	143	4,121	$2^n + 2n + 1$
Box-Behnken	13	62	2,187	-
D-optimal	10	36	91	$\frac{(n+1)(n+2)}{2}$

If the number of candidate feasible designs is large, finding the optimum design is not feasible, but a numerical optimizer can be used to find a design table with a sufficiently low value of D[4][99].

5.1.1.3 Variable screening

Analysis outputs for a complex system such as an aircraft can be affected by a very large number of different variables. As seen in Table 8, as the number of factors is increased, the number of runs can quickly become impractical for the quadratic model, even when using an efficient design. To reduce the number of variables required to a manageable level, it is often necessary to conduct a screening study: first, a two-level DOE is used to estimate the linear terms in the RSE, and the results analyzed to determine which variables have the largest effect on the variation of the response. Only the most important variables are retained for development of the final quadratic equation using a DOE table with three or more levels. In this way, the variables which do not contribute significantly to the variation of the response are eliminated, greatly reducing the number of runs without significantly degrading the accuracy of the metamodel.

5.1.2 Estimation of RSE coefficients

The coefficients $b_i, i = 1 \ldots n$ and $b_{ij}, i = 1 \ldots n, j = 1 \ldots n$ of the RSE equation (Equation 47) can be determined through standard least-squares regression. First a design matrix, $\mathbf{X}$, is created by writing the factors and their products in the order in which they appear in the RSE equation. For example, a linear three-variable RSE can be written as

$$R = b_0 + b_1 x_1 + b_2 x_2 + b_3 x_3 + b_{12} x_1 x_2 + b_{13} x_1 x_3 + b_{23} x_2 x_3 \tag{50}$$

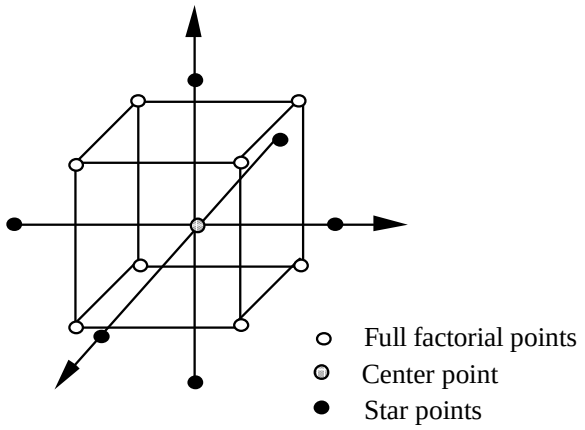

Figure 53: Three-variable central composite design.

There are six coefficients in the equation, so at least 6 output values are needed to estimate the values of the coefficients. If the two-level full-factorial DOE table from Table 4 is used, the design matrix which corresponds to Equation 50 is

$$\mathbf{X} = \begin{bmatrix} x_1^{(1)} & x_2^{(1)} & x_3^{(1)} & x_1^{(1)}x_2^{(1)} & x_1^{(1)}x_3^{(1)} & x_2^{(1)}x_3^{(1)} \\ x_1^{(2)} & x_2^{(2)} & x_3^{(2)} & x_1^{(2)}x_2^{(2)} & x_1^{(2)}x_3^{(2)} & x_2^{(2)}x_3^{(2)} \\ \vdots & \vdots & \vdots & \vdots & \vdots & \vdots \\ x_1^{(8)} & x_2^{(8)} & x_3^{(8)} & x_1^{(8)}x_2^{(8)} & x_1^{(8)}x_3^{(8)} & x_2^{(8)}x_3^{(8)} \end{bmatrix} \tag{51}$$

where $x_i^{(j)}$ is the value of factor x_i for the j^{th} run, etc. Thus the numerical entries in the design matrix are

$$\mathbf{X} = \begin{bmatrix} -1 & -1 & -1 & 1 & 1 & 1 \\ 1 & -1 & -1 & -1 & -1 & 1 \\ -1 & 1 & -1 & -1 & 1 & -1 \\ 1 & 1 & -1 & 1 & -1 & -1 \\ -1 & -1 & 1 & 1 & -1 & -1 \\ 1 & -1 & 1 & -1 & 1 & -1 \\ -1 & 1 & 1 & -1 & -1 & 1 \\ 1 & 1 & 1 & 1 & 1 & 1 \end{bmatrix} \tag{52}$$

The coefficients vector, **b**, is vector of the RSE coefficients in the same order they appear in the RSE,

$$\mathbf{b} = \begin{bmatrix} b_0 \\ b_1 \\ b_2 \\ b_3 \\ b_{12} \\ b_{13} \\ b_{23} \end{bmatrix} \tag{53}$$

and the response vector, **Y**, contains the output values for the eight analyses:

$$\mathbf{Y} = \begin{bmatrix} y_1 \\ y_2 \\ y_3 \\ y_4 \\ y_5 \\ y_6 \\ y_7 \\ y_8 \end{bmatrix} \tag{54}$$

The least-squares normal equations for a linear regression model can be written in matrix form as

$$\mathbf{X'Xb} = \mathbf{X'Y} \tag{55}$$

so the RSE coefficients can be found by solving for **b**:

$$\mathbf{b} = (\mathbf{X'X})^{-1}\mathbf{X'Y} \tag{56}$$

5.1.3 Process for screening and RSE creation

The automation of the analysis process in ModelCenter served to simplify the use of Design of Experiments for conducting screening studies and creating the RSEs in this study. Figure 54 shows a generic diagram of the process used to run the analysis process in a DOE framework. The software used in this study to create the DOE tables, integrate and

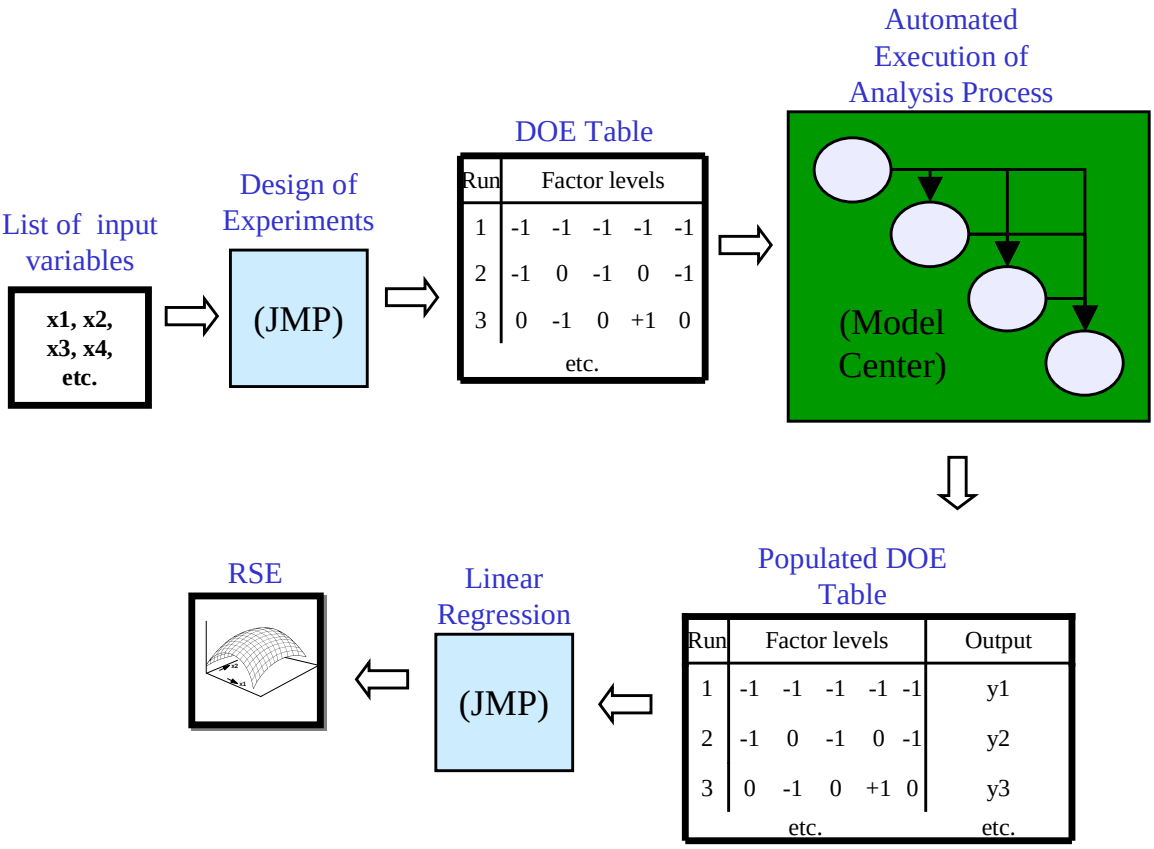

Figure 54: Process diagram for screening studies and creation of RSEs.

execute the analysis process, and perform regression on the analysis results are indicated on Figure 54 in parentheses; the actual software used might vary but the general process remains the same regardless of the application. First, an appropriate DOE table is created for the desired variables. For a screening study, a two-level fractional-factorial DOE table is created; for creation of RSEs, a CCD, D-optimal, or other type of design is created. Next, using the DOE table, the analysis process is executed; the DOE table defines the values to use for the design variables for each run. Execution of the analysis process produces output values which populate the design table. Finally, linear regression is performed for each of the output metrics to produce an RSE which serves as a metamodel for that metric. An RSE is created for each of the desired metrics to be tracked during trade studies,

5.2 Probabilistic analysis

As discussed previously in Section 1.3, uncertainties in mission requirements and operating conditions, new technologies and limited model fidelity contribute to significant uncertainty in the actual performance metrics and noise levels of an aircraft in the conceptual design stage. To properly assess the risk of failing to meet the design constraints or performance and noise targets, it is necessary to accurately predict the probability distributions for each of the design metrics using *probabilistic methods*. Probabilistic methods were originally developed to predict the reliability of a system, i.e. the probability of failure, so many are focused on increasing the accuracy or efficiency of the calculations in or near the failure domain. Others instead are used to calculate the probability density function (PDF) of the response and use them in reliability calculations; these methods are more accurate near the mean of the distribution, so if the failure probability is very low, the risk calculation is less accurate. Probabilistic methods are built from three essential pieces: models for the probability distributions of the input variables, response models that describe the relationship between the output metrics and input variables, and *limit-state functions*. A limit-state function $g(\bar{x})$ describes the response such that $g(\bar{x}) = 0$ represents the boundary between the acceptable and failure domains. The primary types of probabilistic analysis are, in decreasing order of accuracy, simulation methods, importance sampling methods, first- or second-order reliability methods (FORM or SORM), and mean-based methods[71].

Simulation methods generate a set of design points in accordance with defined probability distributions for the individual variables, calculate the deterministic response of the system for the selected variable values, and then calculate the probability, mean and variance of the output metrics using the collected analysis results. The most common simulation method is Monte Carlo analysis, in which the sample points are generated by selecting random samples from the probability distributions of the input variables. Simulation methods in general are the most accurate types of probabilistic methods, since they involve direct calculation of both the output values and the PDF of the output. Also, the implementation of simulation methods is simple since the analysis methods can be used directly and no gradient calculations or iteration are needed. For Monte Carlo analysis, the level of accuracy

can be controlled through the use of greater numbers of simulations, and any number of input variables can be used. However, simulation methods are not practical if the analysis cannot be performed quickly because they can require thousands of analysis runs to accurately calculate the PDF, and they are not efficient for calculating failure probabilities for highly-reliable systems.

Importance sampling methods are an extension of simulation methods in which the choice of design points is biased to increase the number of points which are in near the failure boundary of the system. This increases the efficiency of the method in calculating the probability of failure, especially for very small probabilities. The disadvantage to this approach is that it is less simple to implement than standard simulation methods, because it introduces gradient calculations and iterations to the problem.

FORM and SORM approximate a limit-state surface with a first- or second-order polynomial approximation about a point on the failure boundary, which is usually the most-probable point, i.e. the point on the failure boundary with the highest probability. The efficiency of these methods depends on the ability to quickly identify one or more MPPs in the design space. They are significantly more efficient than simulation methods for calculating failure probabilities but they also require gradient calculations and iterations.

Finally, mean-based methods use a first- or second-order Taylor series expansion of the response model or the limit-state function around the mean values of the random input variables, and are used to calculate the mean and variance of the outputs. These methods are easy to implement, particulary when they do not require any iterations of the algorithm. The approximations to the distribution of the response model are more accurate in the vicinity of the mean, so mean-based methods are not accurate for estimating failure probabilities of high-reliability problems. Also, mean-based methods assume that the input variables are normally-distributed, so they are not as accurate for problems where one or more of the variables have a distribution which is significantly different than the normal distribution.

In this study, the failure domain is the portion of the design space in which the aircraft fails to meet design requirements for takeoff field length, landing field length, or approach velocity, or fails to meet a guaranteed performance or noise goal. Rather than specify

performance and noise goals *a priori*, it was instead desired to calculate the probability distributions for the metrics and to determine through optimization what the guarantee levels should be to meet a certain risk level. Importance sampling, FORM and SORM methods are focused on predicting failure probabilities when the failure conditions has been specified beforehand, so they were deemed to not be as useful for this study as mean-based and simulation methods. As will be seen in Chapter 7, robust design studies were planned which use uniform distributions for some of the design variables, so mean-based methods were not a good choice for these types of problems. Based on these criteria, simulation methods were chosen as the best type of methods for use in the risk analysis calculations in this study.

Like RSM, Monte Carlo analysis is an integral part of the ModelCenter software. However, because of the large number of simulations required to calculate the PDF of the output metrics, Monte Carlo analysis was not practical for use with the full analysis process directly. When used in combination with metamodels, however, Monte Carlo analysis became practical to use, but with the disadvantage that the problem became subject to the limitations on numbers of variables and accuracy that were inherent to the metamodels.

5.2.1 Process for probabilistic analysis

Figure 55 shows a generic diagram of the process used to perform probabilistic analysis. Since Monte Carlo analysis requires thousands of output values for an accurate estimation of the PDF for each metric, the actual high-fidelity analysis process could not be used directly; instead, the RSEs created using the process in Section 5.1.3 were used as surrogates. To perform probabilistic analysis for a given output metric, the uncertain variables and their probability distributions are defined, and random sampling is used to select values for each of the analysis runs. The values of the outputs, as calculated by the RSEs, are collected, and statistical analysis is used to plot the empirical probability distribution and to calculate the mean, standard deviation and values at various confidence levels. Different software could be used for each of the different steps; in this research, the built-in Monte Carlo analysis method in ModelCenter was used to perform the entire process.

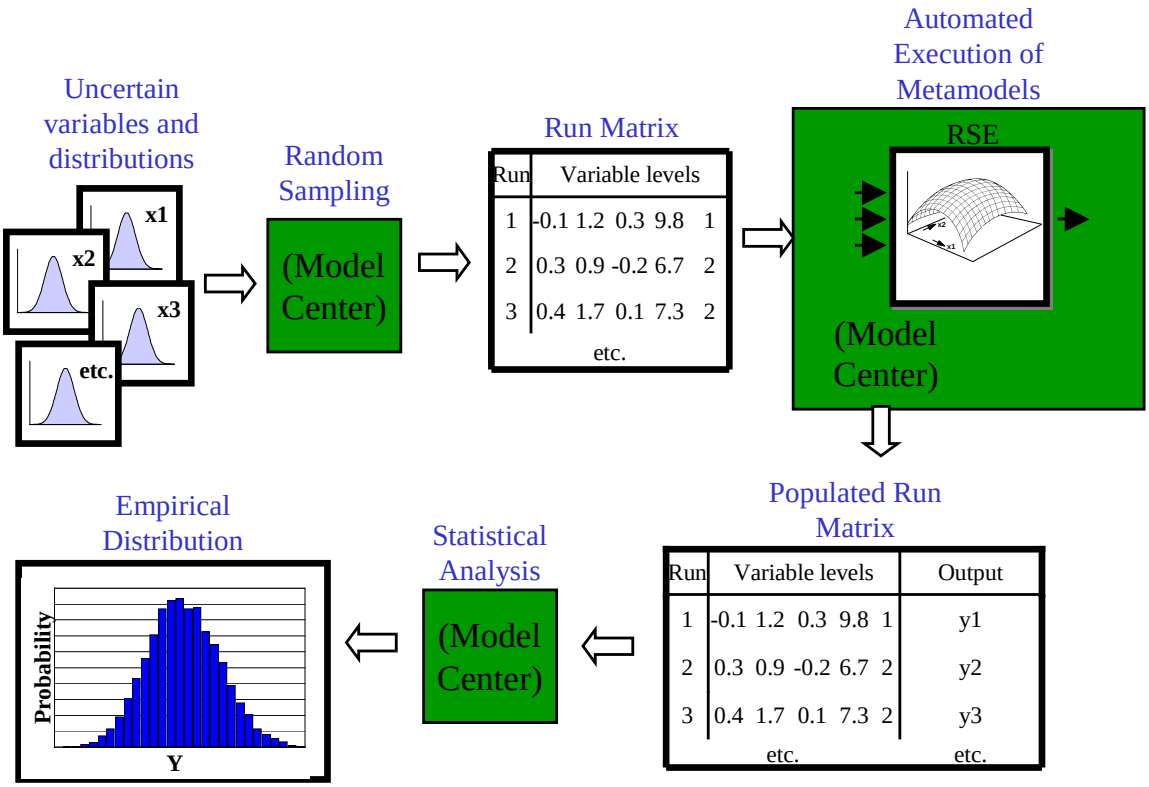

Figure 55: Process diagram for Monte Carlo analysis.

CHAPTER VI

RESULTS

Once the analysis process had been assembled and a strategy had been developed for implementing it in the design process, a series of design studies were carried out to serve as a proof of concept for a conceptual design study which uses physics-based analysis for part or all of the disciplinary analyses. As explained in Section 5.1, the studies presented here should be considered to represent the contributions of just the acoustics discipline to a larger multidisciplinary design process, and not the entire aircraft and engine design process itself. This chapter details the full results of the analysis process as applied to the baseline aircraft and engine, and then describes the development of response surface equations for engine and aircraft performance metrics and constraints for the entire design space.

6.1 Baseline definition

To make the problem tractable, the study was limited to a single class of aircraft and engine, though in the design and risk analysis studies the major design variables—such as gross weight, bypass ratio, etc.—were varied significantly relative to the baseline values. Figure 56 shows the baseline aircraft used in the study, and Table 9 gives the major design variables. The aircraft is based on the NASA Inter-center Systems Analysis Team 300-passenger twin-engine baseline, with a maximum gross weight of 600,000 pounds and a nominal design range of 6500 nautical miles, and is similar in size and mission to a Boeing 777. Aircraft in this class are expected to see some of the largest increases in demand by the year 2015[7], and due to their size are noisier than comparably-powered smaller aircraft. The baseline is powered by a separate-flow, two-spool high-bypass turbofan engine with a sea-level static thrust of 90,000 pounds and a design bypass ratio of 8.5, which is similar to a General Electric GE90 engine.

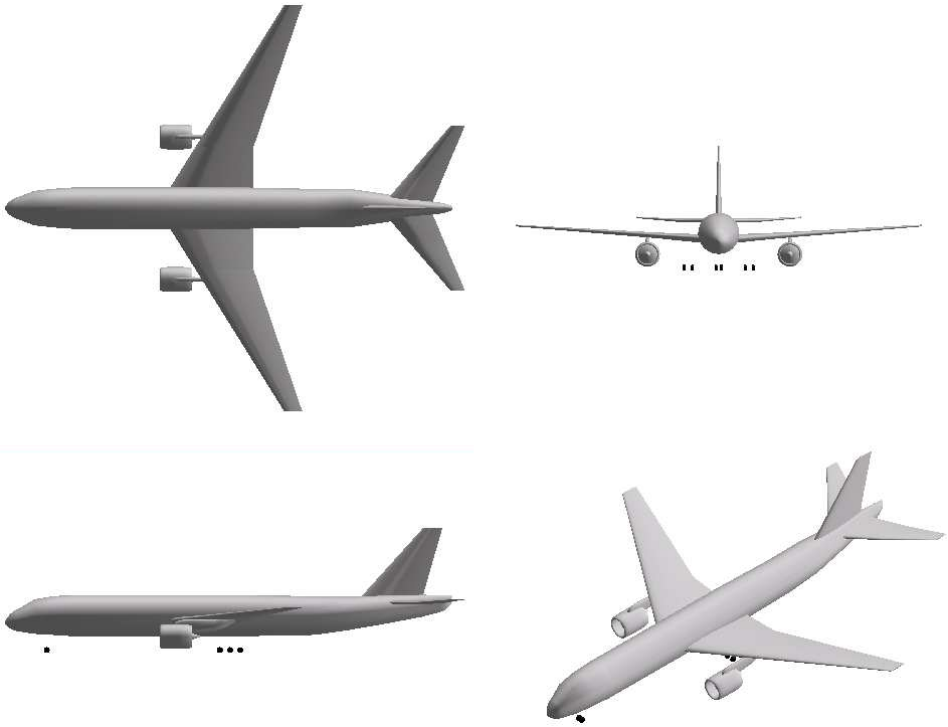

Figure 56: Baseline aircraft.

Table 9: Baseline aircraft and engine design variables.

Baseline aircraft	**Baseline engine**
Passengers: 300	Low-speed fan
Range: 6500 nmi	Thrust: 90,000 lb
Gross weight: 600,000 lb	Bypass ratio: 8.5
Wing area: 4600 ft^2	Fan pressure ratio: 1.5
Wing aspect ratio: 8.7	Overall pressure ratio: 38
Fuselage length: 220 ft	Turbine inlet temperature: 3285 R
	22 Fan rotor blades, 58 vanes

6.2 Baseline analysis

As a first step in the design studies, the analysis process was applied to the baseline engine and aircraft. In addition to verifying the integration of the analysis methods, this served as an opportunity to fine-tune the convergence of the fan blade design methods and to conduct grid refinement studies to determine the appropriate grid densities for the fan and jet flow field analyses. In this section a detailed documentation of the analysis process and results is given for the baseline configuration; the same analysis process is carried out for each engine and aircraft configuration to be examined.

6.2.1 Engine cycle analysis and geometry

The engine cycle design and analysis for the baseline was carried out with sea-level static conditions for the design point. Since the flight performance was only to be computed for takeoff and landing, the engine cycle data were only needed for Mach numbers up to 0.4 and altitudes up to 5000 ft, although for reference purposes the cycle analysis also was run for full power at the nominal cruise condition of Mach 0.85 and 35000 ft. Figure 57 shows the specific fuel consumption (SFC), which is the fuel flow rate per pound of thrust, versus the net thrust per engine for a few of the Mach number and altitude combinations at which the analysis was performed.

The initial engine geometry as output by ENGGEN is shown in Figure 58(a). The engine geometric definition is insufficient for use in this form because it lacks an inlet cone and fan stator, there is no user control over the fan streamline contraction and rotor geometry, and the slope and curvature of the aft nacelle are too severe and likely would cause large drag penalties. To correct these deficiencies, the initial duct geometry was automatically modified using the geometry utility; the final modified engine geometry is shown in Figure 58(b).

6.2.2 Fan blade design

The design radial distribution of rotor exit tangential velocity was specified using the combination of through flow solutions with a gradient-based optimizer. The radial velocity distribution was constrained to a maximum rotor diffusion factor of 0.55, maximum stator

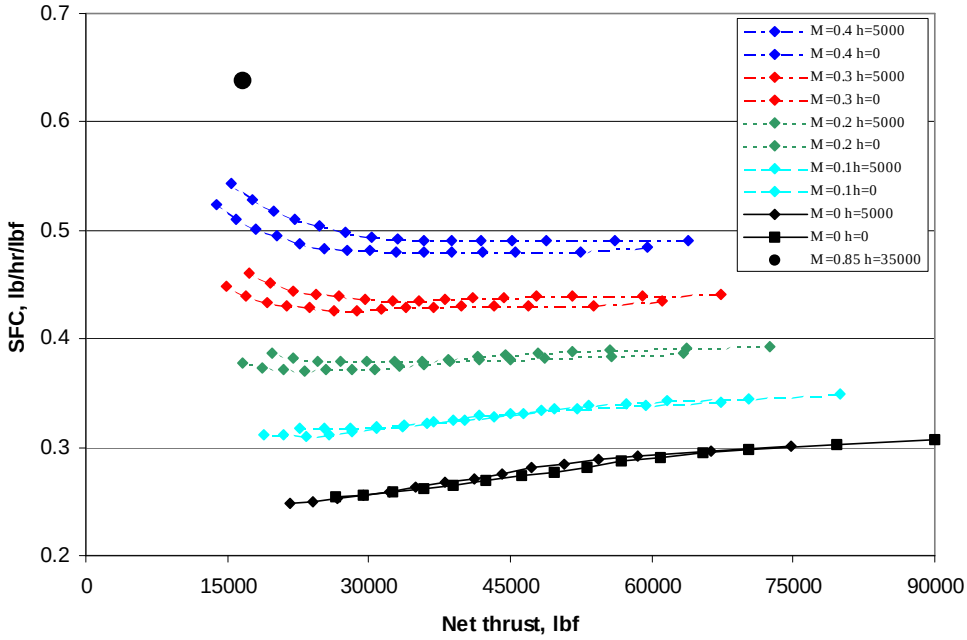

Figure 57: Baseline engine SFC vs. net thrust.

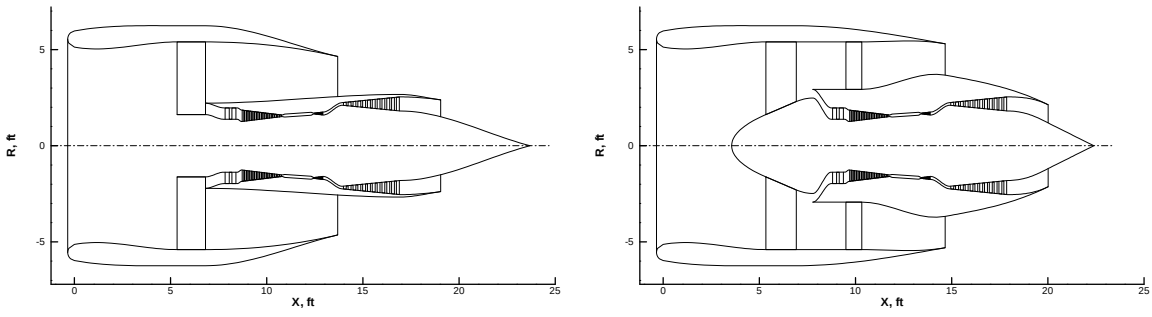

(a) extracted from ENGGEN plot file (b) as modified

Figure 58: Baseline engine geometry before and after modification.

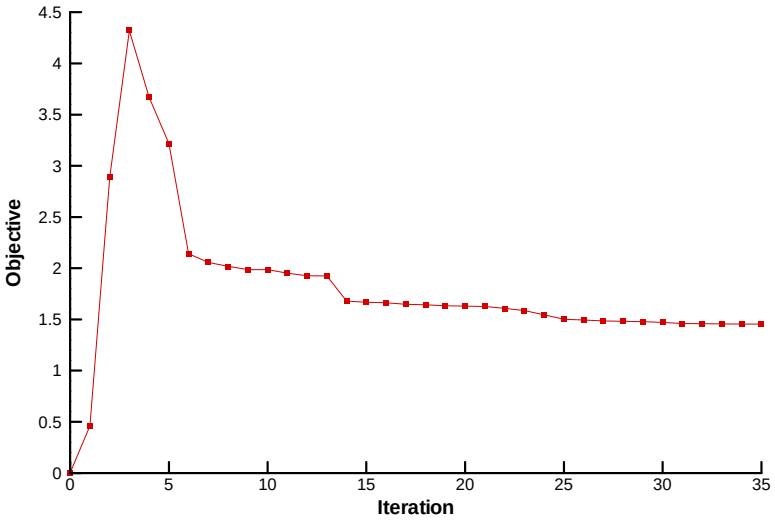

Figure 59: Convergence history for rotor exit tangential velocity optimization.

diffusion factor of 0.60, maximum stator inlet Mach number of 0.85, maximum rotor turning of 45 degrees, maximum rotor tip degree of reaction of 1.0 and positive degree of reaction at the hub. The initial constant-work tangential velocity distribution was not able to satisfy all the constraints, so the velocity distribution was automatically adjusted through the optimization process until the solution was arrived at with the minimum objective function while satisfying all the constraints. The convergence history is shown in Figure 59. Initially the objective function increased while the optimizer searched for the feasible region, and then the objective function gradually decreased until the optimum was found.

The optimized rotor design exit tangential velocity and pressure ratio distributions are shown in Figure 60 along with the radial distributions of all the constraints. As is typical for fans with low hub-to-tip ratios, it was necessary to reduce the rotor pressure ratio near the hub where the wheel speed is much lower to avoid imposing too much turning on the flow and overloading the stator hub. The work distribution at the optimum was constrained near the hub by the maximum stator diffusion ratio, requiring an increase in the pressure ratio nearer the tip to match the design value of the fan pressure ratio. Note that the stator diffusion ratio constraint appears to be violated at the hub; this is because the streamlines nearest the hub are actually swallowed by the engine core and do not pass through the stator, so they are ignored in the optimization process. All the other rotor and stator

constraints were satisfied by a comfortable margin.

Next, the rotor camber surface was designed using Swift with the inverse blade design method. A design two-dimensional tangential velocity distribution for the rotor was automatically chosen by the wrapper to impose a smooth turning on the flow through the rotor blade row, ultimately arriving at the design radial velocity distribution at the rotor exit. At the rotor hub, where only subsonic flow was expected, a linear chordwise increase in tangential velocity was prescribed to produce a controlled-diffusion blade section, which features a smooth increase in surface pressure toward the aft end of the blade to control the increase in the boundary-layer thickness and avoid separation on the suction surface. Near the mid-section of the blade, the prescribed distribution was two-segmented with a slope continuity at 30% of the blade chord to produce a supercritical flow field, which allows a supersonic bubble to form on the suction surface without a shock and the accompanying pressure loss. Finally, at the tip the chordwise distribution was two-segmented with a slope and pressure discontinuity to fix the shock location. Between these radial locations the chordwise distributions transitioned smoothly to avoid any serious discontinuities in the blade shape.

Before running the blade design procedure, an informal grid refinement study was conducted to assure that the computational grid used for Swift analysis was of sufficient detail to resolve the mean flow properties to a small enough length scale for the blade design and noise analysis. The grid spacing is controlled by two input variables: Δx_v, which is the grid spacing away from the rotor surface relative to the chord; and Δx_w, which is the grid spacing away from the hub and tip walls relative to the rotor span. For an initial non-optimized rotor blade geometry, Swift analysis was performed using a range of values for Δx_v and Δx_w, and the resulting spanwise flow properties were compared. Figure 61 shows the effects of grid refinement in the two coordinate directions. For the coarsest levels, the grid was not fine enough to resolve the spanwise flow properties sufficiently. Figure 61 shows that values of $\Delta x_v = 3 \times 10^{-5}$ and $\Delta x_w = 6 \times 10^{-5}$ are sufficient to resolve the rotor outlet properties; larger grid spacings result in noticeable errors in the computed radial velocity and pressure ratio profiles, while smaller spacings increase the computation time

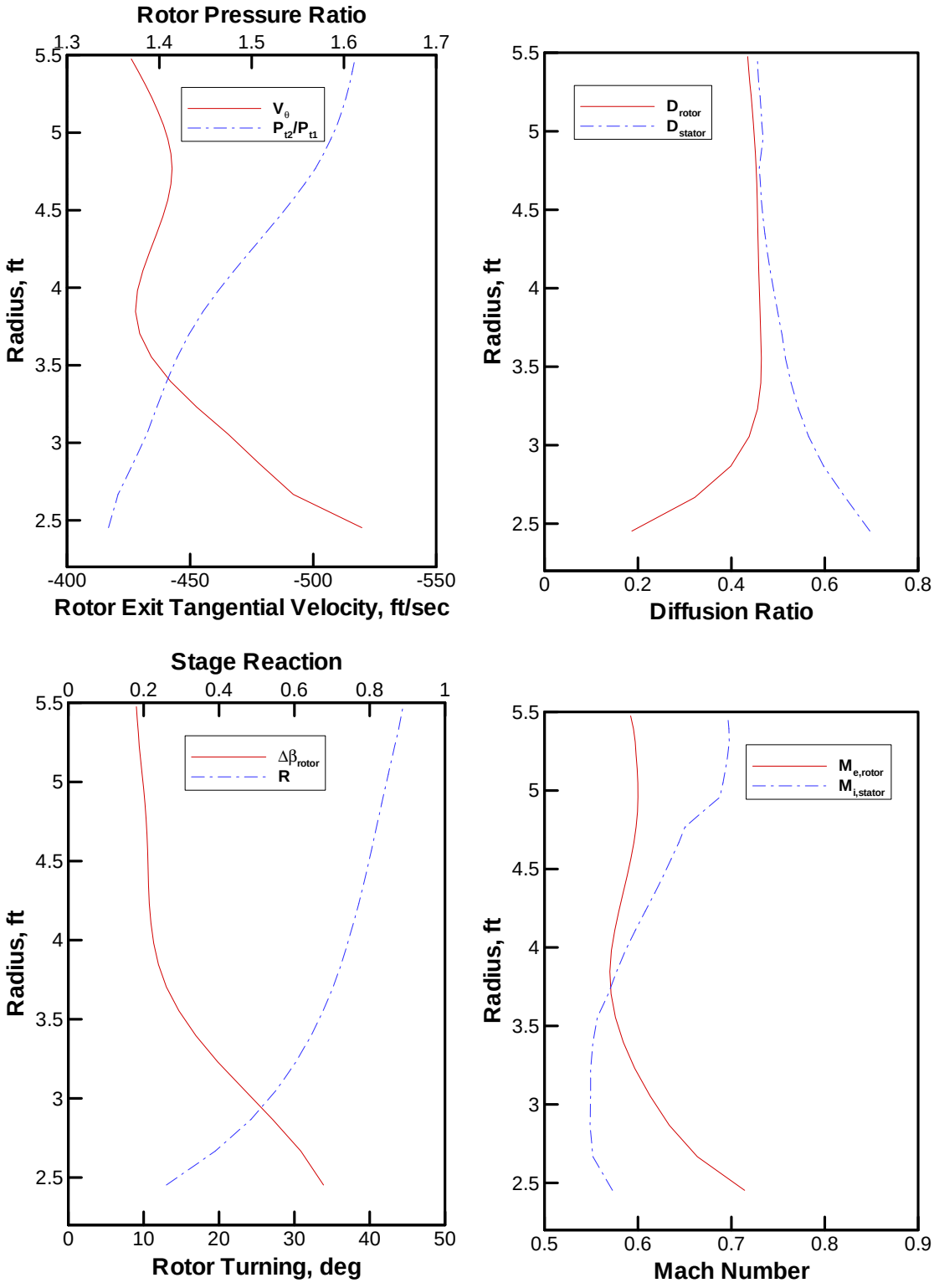

Figure 60: Rotor radial design parameters.

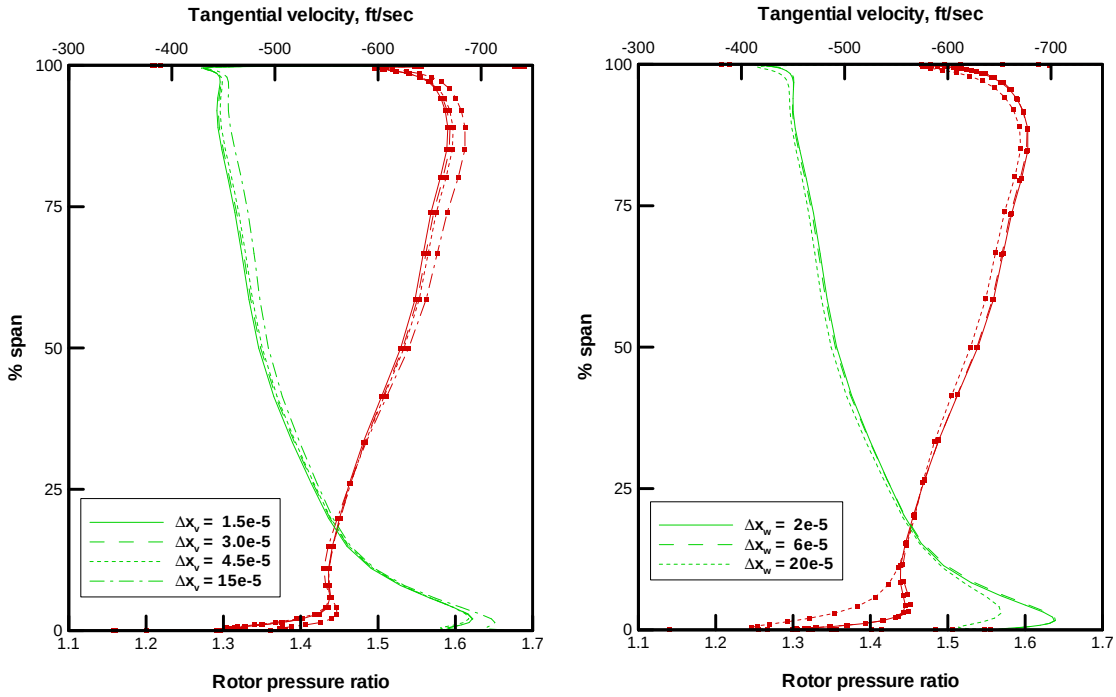

(a) chordwise spacing, $\Delta x_w = 6 \times 10^{-5}$ (b) spanwise spacing, $\Delta x_v = 3 \times 10^{-5}$

Figure 61: Effect of chordwise and radial grid spacing on computed rotor exit properties.

while failing to increase the precision of the computations. These values were used for all rotor flow field computations for the baseline engine, as well as subsequent analyses of all other engines.

The inverse design procedure was run using a flow solution relaxation factor Ω_V of 0.1 (Equation 41) and an error correction relaxation factor Ω_E of 0.3 (Equation 43). These relaxation factors were chosen based on trial and error to give the most reliable convergence of the design method. The convergence history of the inverse design is shown in Figure 62, which shows the residual of the camber surface, the maximum error in tangential velocity in the blade, and the maximum error in total velocity in the blade after each iteration. The corresponding convergence history for Swift in shown in Figure 63, which shows the flow solution residual, the rotor pressure ratio, and the mass flow error, which is the difference between the exit and inlet mass flows relative to the inlet mass flow. The large jumps in the residual correspond to the iterations of the blade design procedure, when changes to the blade shape are made and the flow solution is restarted, while the discontinuous jumps

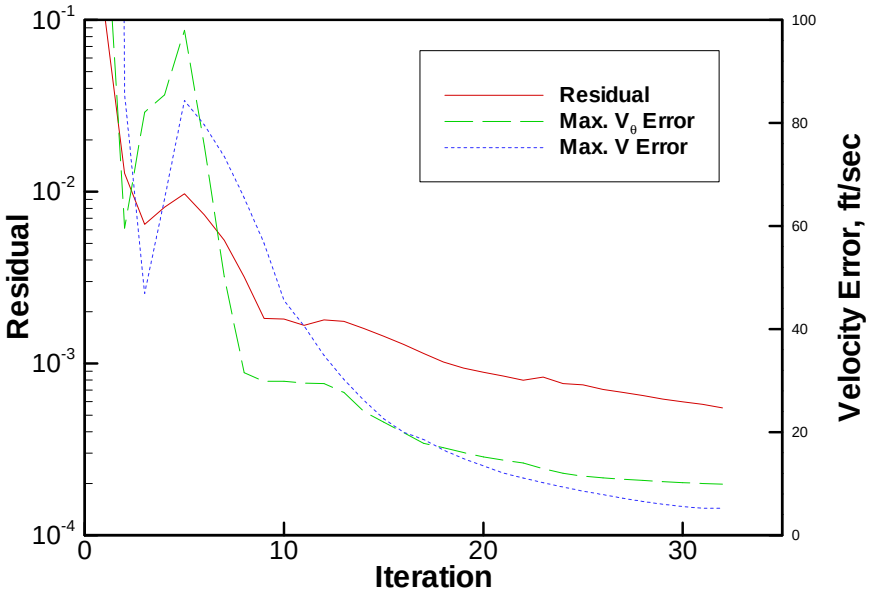

Figure 62: Convergence history for fan rotor blade design.

in the pressure ratio correspond to changes in the downstream hub static pressure ratio boundary condition required to keep the mass flow ratio within 1% of the design value. The initial flow solution and the first few iterations of the inverse method required the greatest number of iterations of the flow solver due to the large initial changes in the blade shape; the final iterations of the inverse method required few iterations of the flow solver since only minor changes were made in the blade shape near the optimum. Figure 64 shows the final error residual contours for tangential velocity and axial velocity. The contour patterns are typical for a converged blade design and show that the largest value for the velocity error usually exists just behind the shock location near the tip. This part of the blade generally requires the largest number of iterations until convergence because very small changes in the blade camber angle can shift the shock location appreciably.

Figure 65 shows the initial and final shapes of the defining rotor blade sections. The initial blade shape was defined using the input lower-fidelity flow solution from MERIDLN, while the second and subsequent iterations refined the shape using the flow solutions from Swift. The initial blade shape resulted in a mass flow rate approximately 3% too high, so in subsequent iterations the section setting angles were automatically reduced at almost all radial stations to simultaneously reduce the mass flow to its design value and to meet the

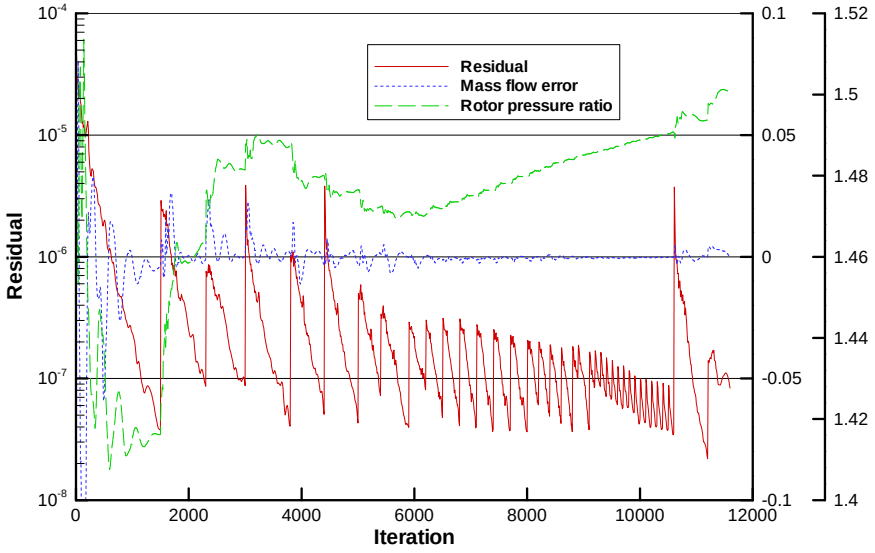

Figure 63: Convergence history for Swift flow field calculations during blade design.

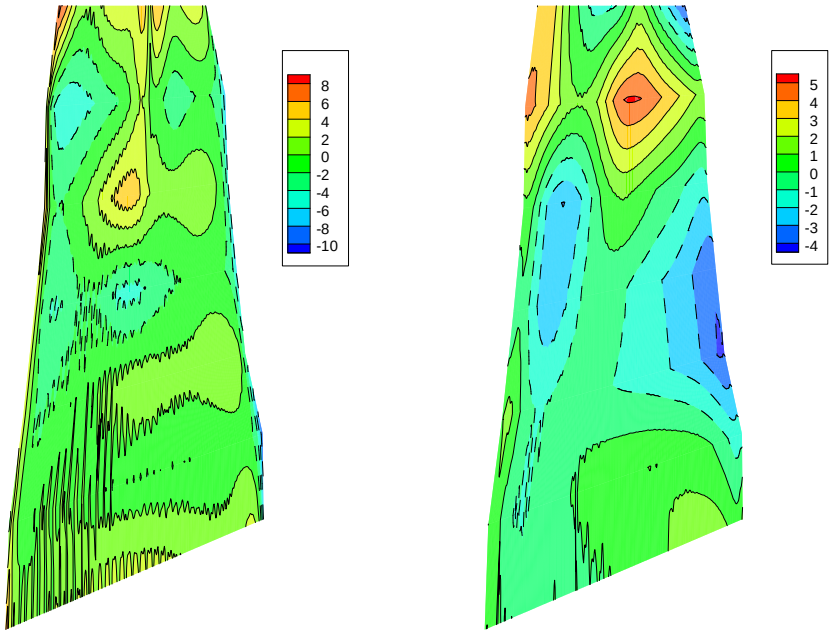

(a) tangential velocity residual, ft/sec (b) axial velocity residual, ft/sec

Figure 64: Contours of the final error residual in the meridional plane for the converged blade.

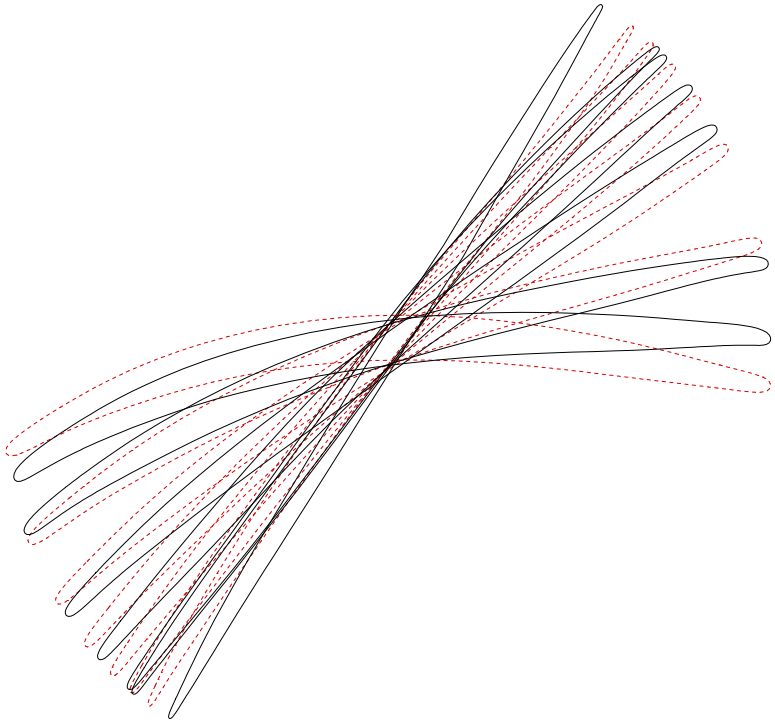

Figure 65: Initial (dotted line) and final (solid line) blade section shapes.

prescribed radial pressure ratio variation. The final blade shape also required less camber than was estimated for the initial blade shape.

The converged tangential velocity distribution is compared to the design distribution in Figure 66, showing that the inverse procedure successfully matched the actual velocities to the target. The final tangential velocity distribution and pressure ratio downstream of the rotor are compared with the design distributions in Figure 67. Since the inverse design method seeks to match the prescribed velocities in the blade row rather than directly matching the design velocity profile downstream of the blade, some difference remains between the design and final velocity distributions. Nevertheless, the rotor exit velocity distribution reasonably approximates the design distribution, and the corresponding pressure ratio distribution also is reasonably close.

6.2.3 Flight performance

The flight performance analysis for the baseline was carried out in FLOPS using the engine performance tables from ENGGEN and the design values for aircraft gross weight,

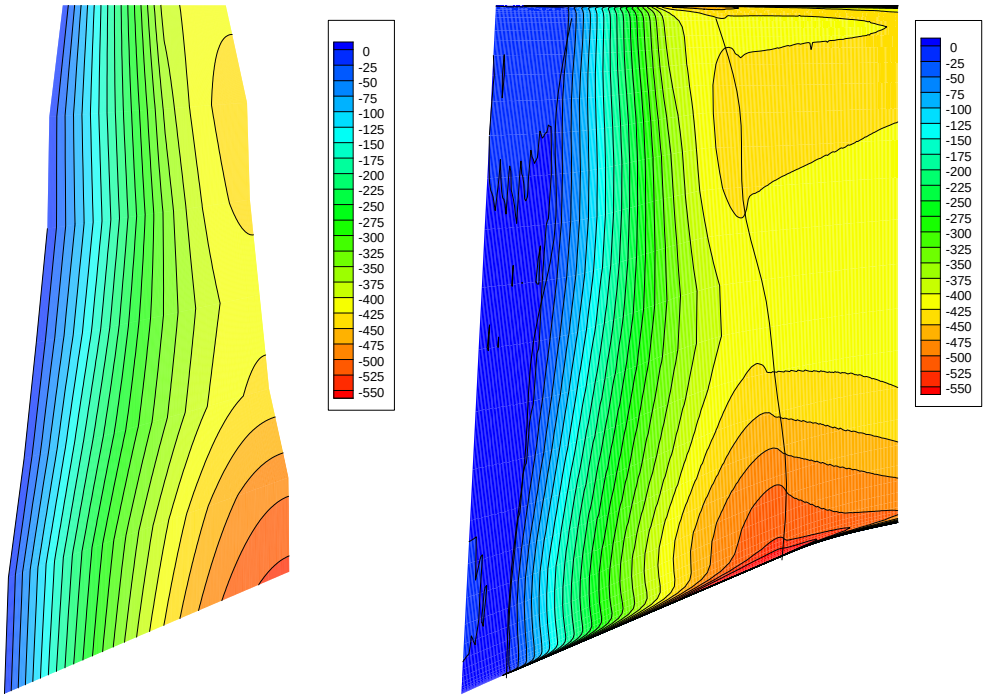

(a) design tangential velocity, ft/sec (b) final tangential velocity, ft/sec

Figure 66: Comparison of design and final tangential velocity contours.

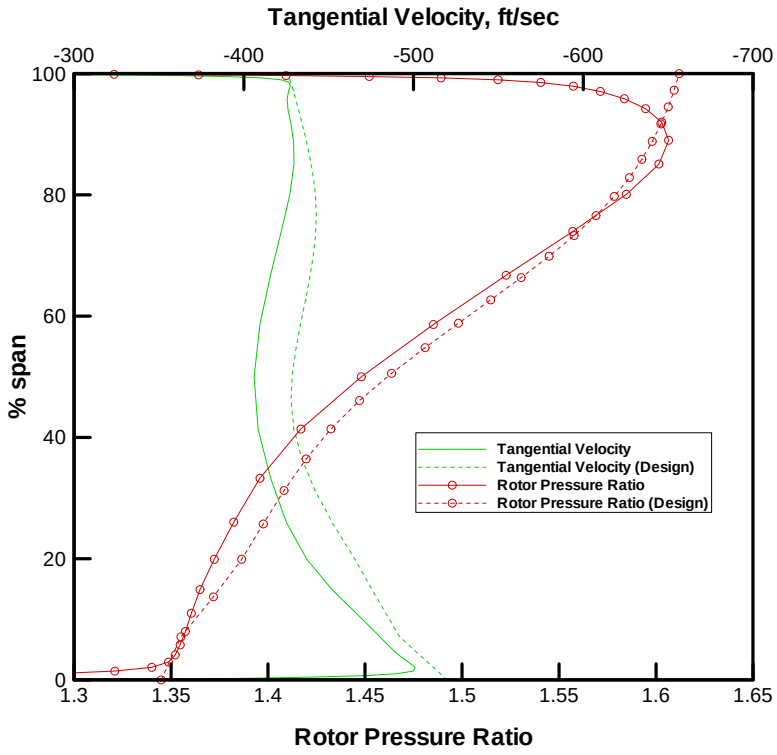

Figure 67: Final radial velocity and pressure ratio distributions.

Table 10: Baseline aircraft flight performance metrics.

Takeoff field length	9978 ft
Cutback altitude	1667 ft
Landing field length	6486 ft
Approach velocity	142.4 kt

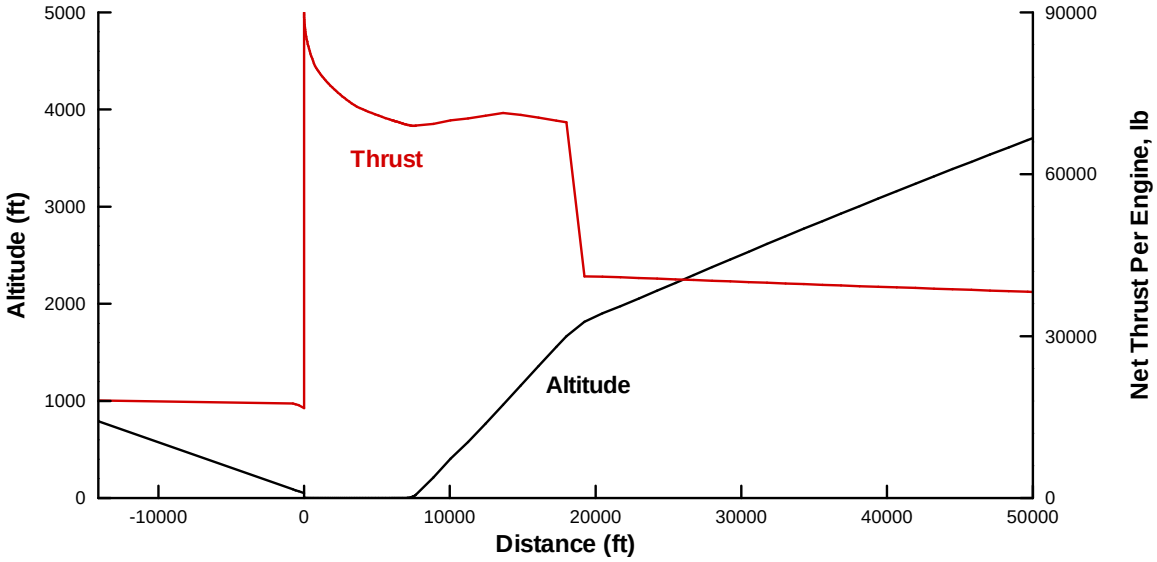

Figure 68: Baseline approach and takeoff flight paths.

thrust/weight ratio, takeoff and landing aerodynamics, etc. Table 10 gives the pertinent takeoff and landing flight performance metrics as calculated in FLOPS, and Figure 68 shows the computed takeoff and approach flight paths to be used for FAR 36 noise certification.

The sideline, cutback and approach flight conditions extracted from these flight paths are listed in Table 11. For the sideline case, the aircraft was at full power and the velocity was interpolated from the takeoff flight path at the point where the aircraft reached an altitude of 700 ft. For the cutback case, the altitude, velocity and throttle setting were interpolated at the point on the takeoff flight path where the aircraft reached a distance of 21325 ft from brake release. For the approach case, the velocity and throttle setting were interpolated from the approach flight path at the point where the aircraft descended through an altitude of 394 ft. Once the throttle setting, altitude and velocity for each flight condition were defined, the engine operating conditions and ambient conditions for

Table 11: Flight conditions for analysis cases.

Case	Defining pt.	Velocity (kt)	Altitude (ft)	Throttle
Sideline	$h = 700$ ft	181	700	100%
Cutback	$x = 21325$ ft	185	1953	59.5%
Approach	$h = 394$ ft	142	394	24.6%

the detailed flow field and noise analysis could be looked up using the engine cycle analysis results and a standard atmospheric table.

6.2.4 Fan rotor flow field

The fan rotor-stator interaction tone noise was computed using the two-step procedure outlined in Chapter 4. First, the fan viscous flow field was computed in Swift, and the resulting streamlines and wake velocity deficit field were used by TFaNS to compute the interaction tones.

Using the appropriate grid densities determined through the prior refinement study, the grid generation and Swift analysis were carried out for each of the noise analysis cases. The computational mesh created by TCGRID is shown in Figure 69, with two additional neighboring blades shown for illustration purposes. For clarity, only the rotor surface and hub surface points are shown, and every other point is removed. The inlet H-grid (not shown) had 27 x 19 x 43 points, and the blade C-grid had 173 x 40 x 43 points, for a total of approximately 320,000 grid points.

The flight conditions for the analysis cases (Table 11) were used to look up the fan inlet and entrance thermodynamic conditions and the rotational speed of the fan for each case. Table 12 gives a few of the important parameters—the fan pressure ratio and the corrected speed, tip rotational speed, and approximate relative tip Mach number of the rotor—for the three cases. The fan operating conditions were used to set the inlet and exit boundary conditions, the rotational speed of the rotor grid, and to estimate additional parameters such as the boundary layer thickness for each of the Swift analyses.

The Swift convergence histories for the three noise cases are shown in Figure 70. The

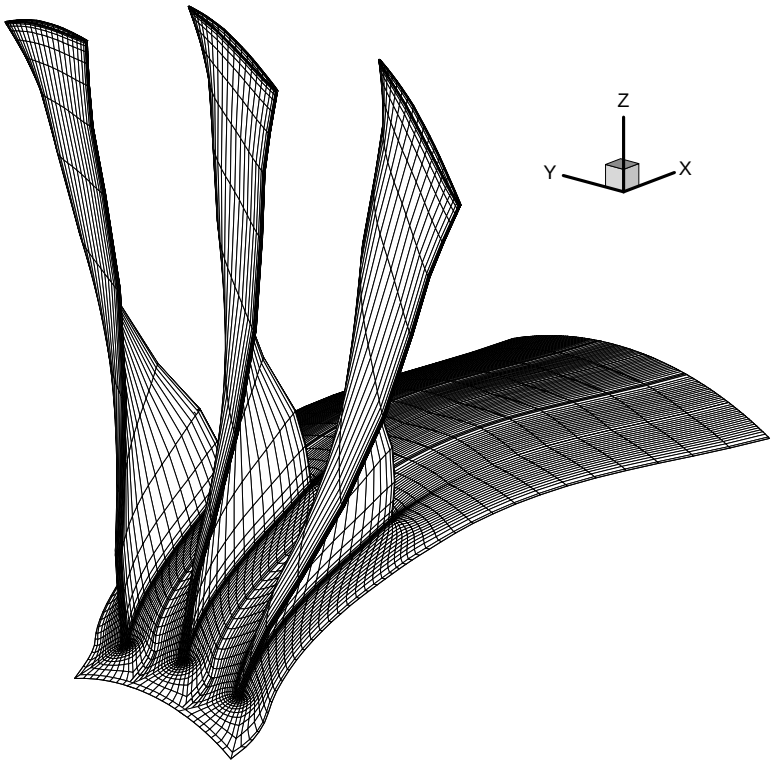

Figure 69: Rotor blade computational grid, with every other point removed for clarity.

Table 12: Fan operating conditions for noise analysis cases.

Case	Pressure ratio	Corrected speed (RPM)	Tip speed (ft/sec)	Approx. rel. tip Mach
Sideline	1.528	2149	1239	1.43
Cutback	1.375	1889	1086	1.20
Approach	1.144	1261	725	0.74

simultaneous discontinuous jumps in the residual, mass flow error and rotor pressure ratio correspond to the occasional adjustments to the downstream hub static pressure ratio boundary condition required to match the design rotor pressure ratio. The solutions were deemed to be converged when the residual was less than 10^{-7}, the pressure ratio was within 0.01 of the design pressure ratio, the pressure ratio changed by less than 5×10^{-4} over the last 100 iterations, and the absolute value of the mass flow error was less than 0.005.

The computed radial variation of rotor pressure ratio for each case is shown in Figure 71 and compared to the design case. Like the design case, the sideline case requires the engine to operate at full power, but due to the forward speed the rotor operates at a pressure ratio higher than its design condition. At the cutback condition (60% throttle) and approach condition (25% throttle), the fan operates at lower pressure ratios and has more uniform work distributions. Circumferential averaging of the flow solution was carried out in the Swift post-processor, and the streamline coordinates were located by radially integrating the mass flow at axial stations through the grid. Figure 72 shows the circumferentially-averaged tangential velocity field through the rotor and downstream to the leading edge of the stator, which is indicated on the figure, with overlaid streamlines. The amount of flow turning is lower for the cutback and approach cases since the fan is operating at a slower rotational speed to reduce the pressure ratio. Finally, Figure 73 shows the axial velocity field at the stator leading edge, looking downstream through the fan duct, clearing showing the rotor wake velocity deficit. The rotor wake flow field information was extracted for each case to be used by TFaNS to compute the wake velocity deficit harmonic amplitudes in the course of analyzing the fan rotor-stator interaction tones.

6.2.5 Fan tone noise

Using the streamlines, flow properties along the streamlines, and wake velocity deficits calculated from Swift, the duct mode power levels for the rotor-stator interaction tones were computed using TFaNS. Figure 74 shows the computational grids used for calculation of the propagation and radiation of the duct modes for the inlet and aft engine ducts. The inlet mesh comprises three sections: an interior finite element mesh beginning at the fan

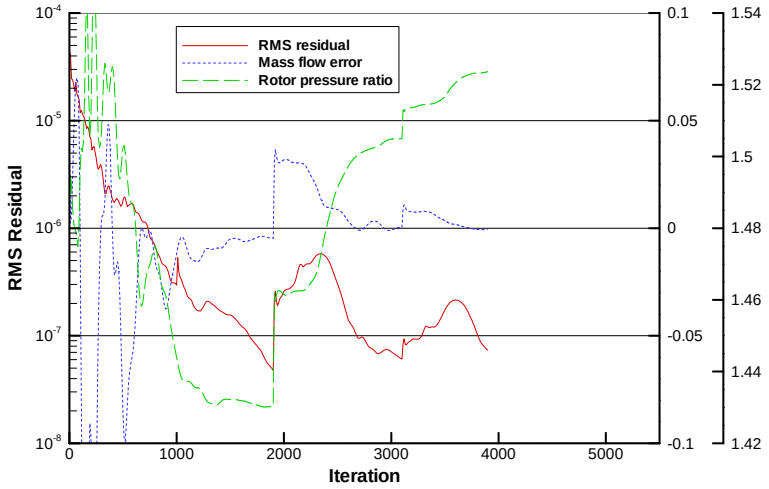

(a) sideline

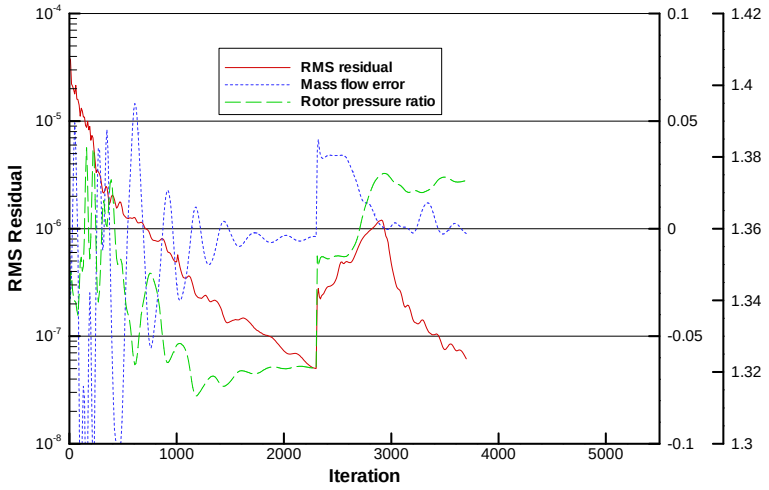

(b) cutback

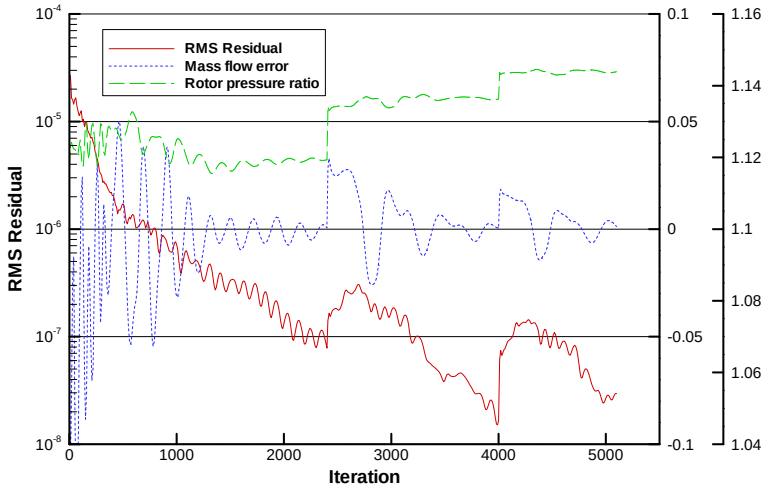

(c) approach

Figure 70: Convergence histories for Swift rotor flow field computations.

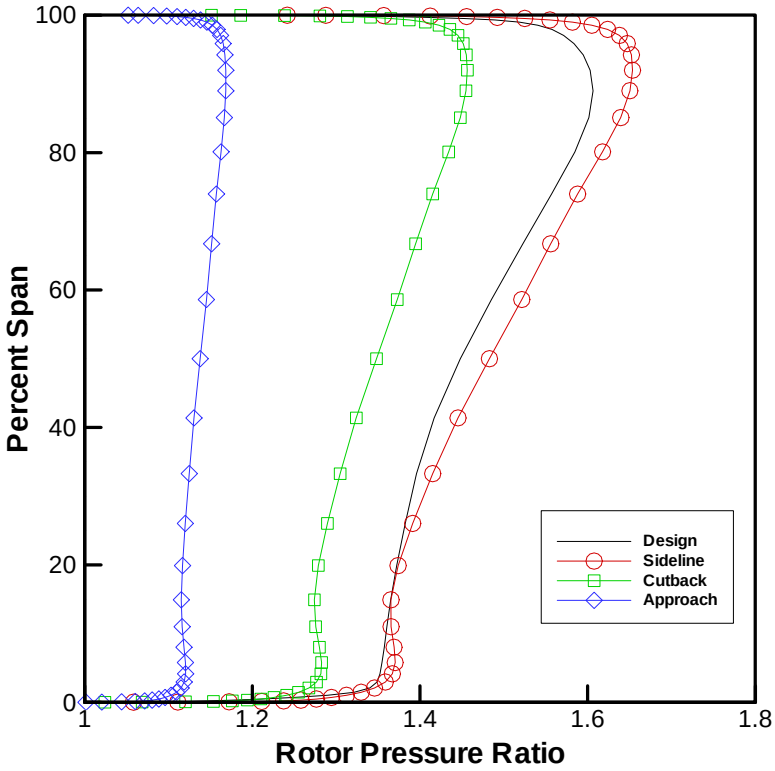

Figure 71: Computed rotor pressure ratio for noise analysis cases.

hub leading edge and extending to a highlight circle, an exterior finite element mesh which extends several diameters outside the nacelle, and a mesh of wave envelope elements that define the transition from the near field to the far field. The aft mesh comprises an interior fan nozzle mesh beginning at the stator leading edge, an exterior finite element mesh with a discontinuity extending downstream several diameters from the fan nozzle lip to simulate the jet shear layer, a region of triangular finite elements for transition of the sound waves through the shear layer, and a mesh of wave envelope elements. The core cowl surface is extended several nozzle diameters downstream of the nozzle exit to simulate the impedance discontinuity at the boundary of the high-temperature core flow.

Computation of the inlet and aft duct propagation and radiation was carried out on a mode-by-mode basis using TFaNS's finite element analysis. Figure 75 shows combined inlet and aft sample results for the (-14,4) mode of the 2BPF tone. The figure illustrates how the far field directivity pattern is formed as the mode transitions from the near field in the duct to form lobes in the far field. The diffraction of the aft-travelling wave through the shear

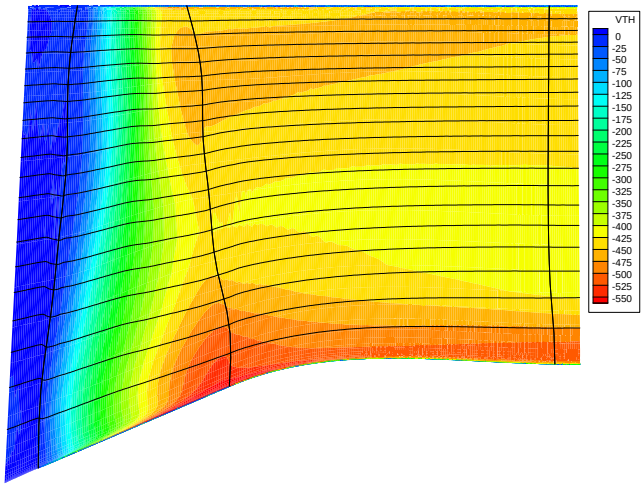

(a) sideline

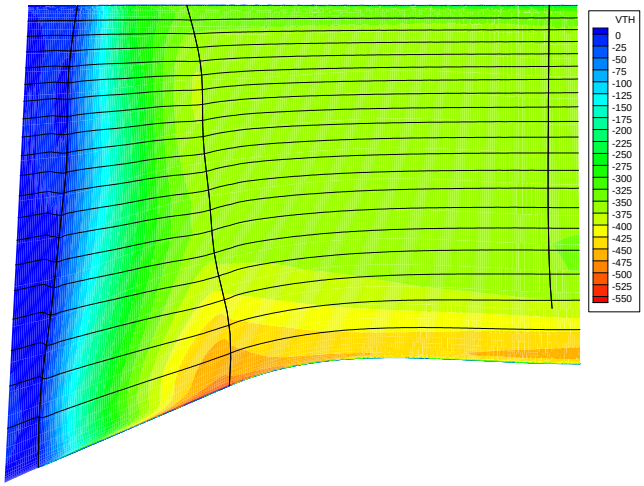

(b) cutback

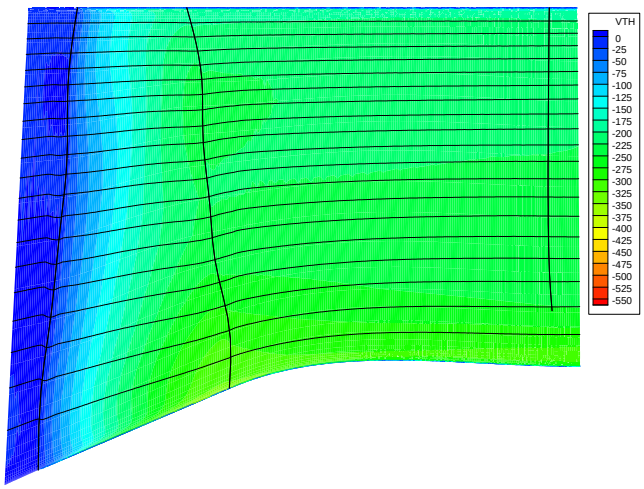

(c) approach

Figure 72: Computed circumferentially-averaged tangential velocity contours.

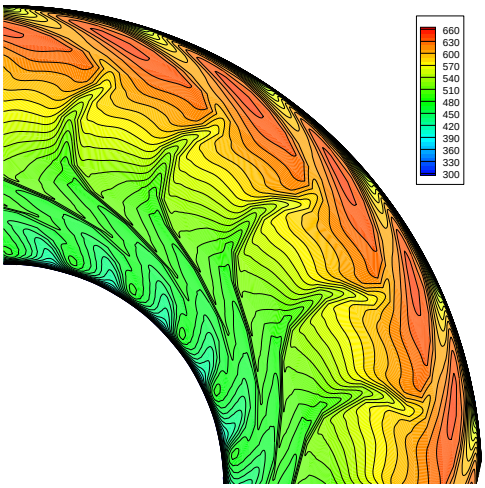

(a) sideline

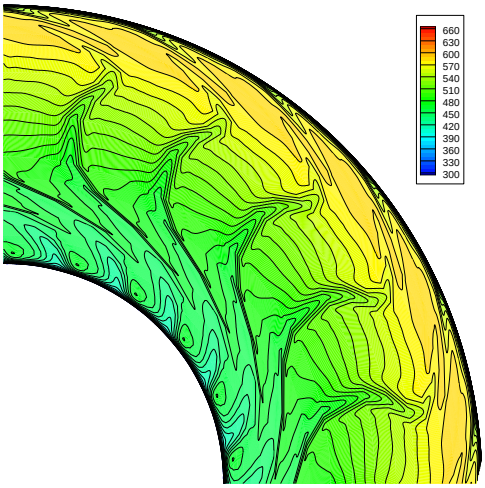

(b) cutback

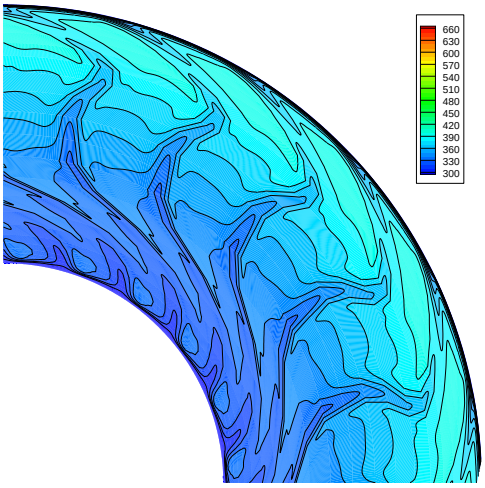

(c) approach

Figure 73: Computed axial velocity contours at the stator leading edge.

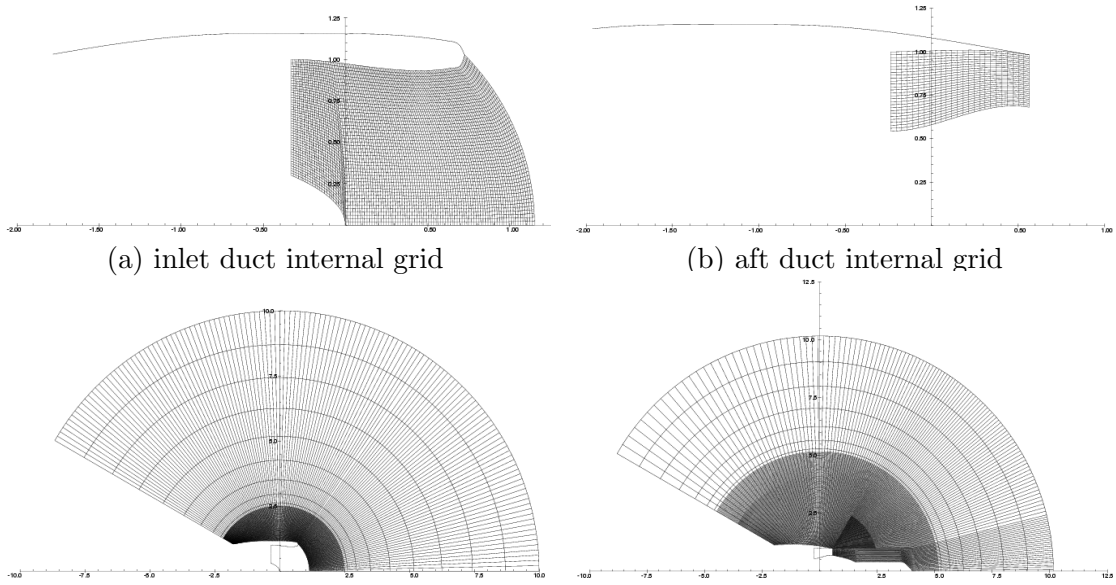

(a) inlet duct internal grid (b) aft duct internal grid

(c) inlet external grid (d) aft external grid

Figure 74: Computational meshes for fan radiation calculations.

layer also is evident. The far-field SPL as a function of directivity angle was extracted by the post-processor for each of the three noise cases and combined to create an output table of fan interaction tone noise levels as a function of frequency, directivity angle and throttle setting.

Figure 76 shows the computed far-field SPL as a function of directivity for the first three BPF harmonics for each of the noise analysis cases. The 1BPF tone is cut-on at the sideline flight condition due to the supersonic tip speed of the fan at full power, but at lower speeds the tone is cut off due to the appropriate choice of fan vane-to-blade ratio. The computational time and memory required to perform the finite element calculations increases exponentially with grid density, so only the first three BPF harmonics could be reasonably be calculated. The noise levels for the fourth and higher harmonics were extrapolated from the 3BPF tone with a 3 dB per harmonic drop-off, which is consistent with the methodology used in ANOPP to compute rotor-stator interaction tones[59].

6.2.6 Jet flow field

Another informal grid refinement study was conducted to assure that the computational grid used for WIND analysis was of sufficient detail to resolve the mean flow and turbulent

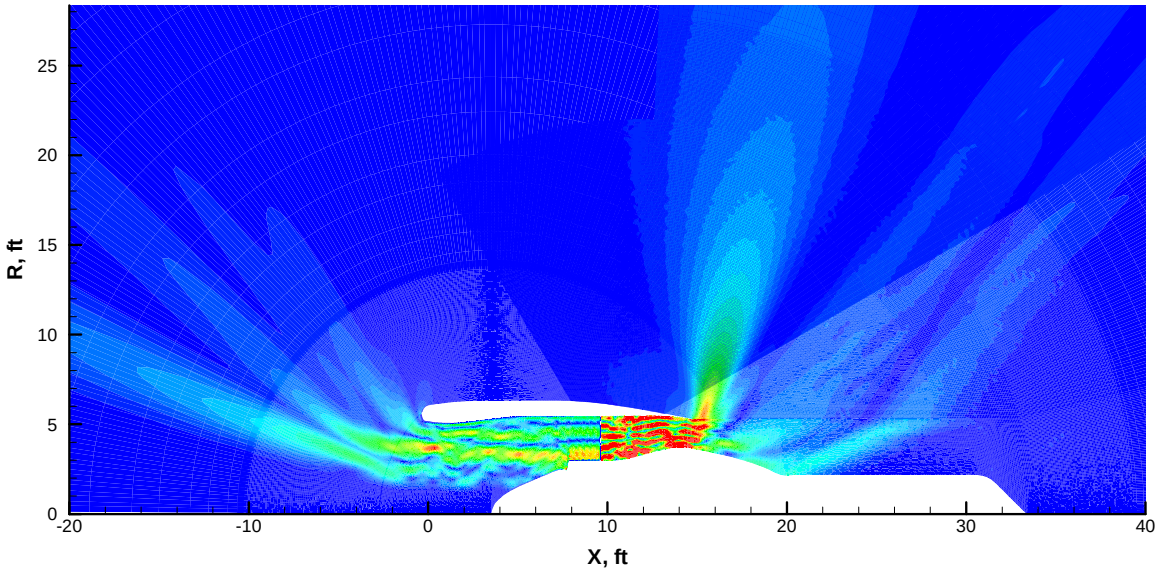

Figure 75: Fan tone inlet and aft sound fields, 2BPF tone, (-14,4) mode.

properties to a small enough length scale for the noise analysis. The axial grid spacing is controlled by the input variable Δx_g, which is the axial spacing at the left side of the primary grid block relative to the fan nozzle diameter, and ultimately controls the spacing at the nozzle exits and the plug tip. The radial grid spacing is controlled by input variable $y+$, which is the spacing away from the wall at each nozzle exit, relative to the estimated non-dimensional boundary layer coefficient at that point. For a sample nozzle, WIND analysis was performed using a range of values for Δx_g and $y+$, and the resulting flow field was used to compute the jet noise levels with MGBK. Figure 77 shows the effects of grid refinement in the two coordinate directions. For the coarsest levels, the grid is not fine enough to resolve the turbulence levels for small length scales which correspond to the highest frequencies of mixing noise. As a result, the noise levels at high frequencies are underestimated, and the PNLT calculation is impacted, particularly at forward propagation angles where the high frequency noise contributes more to the total. Figure 77 shows that values of $\Delta x_g = 1.5 \times 10^{-3}$ and $y^+ = 10$ are sufficient to resolve the high-frequency noise levels.

Using the appropriate grid spacing parameters, a grid for jet flow field was generated for the baseline engine geometry using the new grid generation procedure. A closeup of

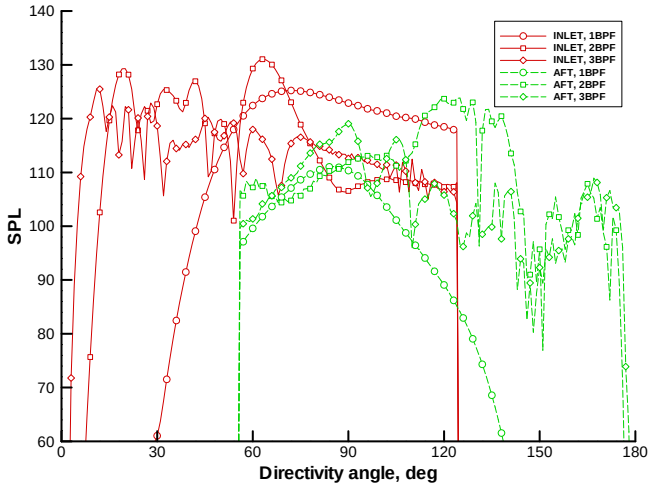

(a) sideline

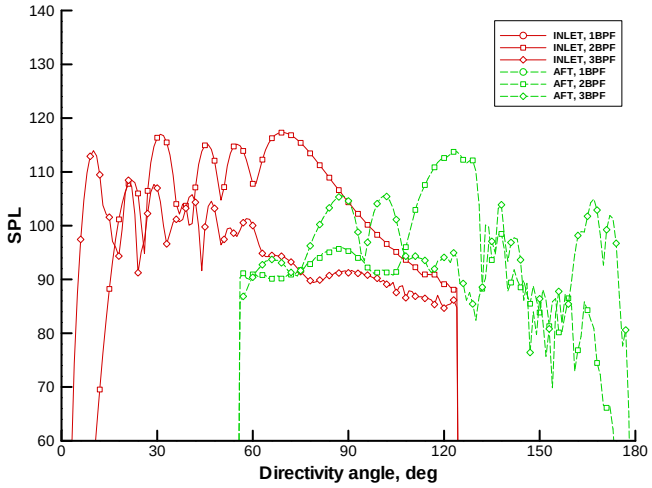

(b) cutback

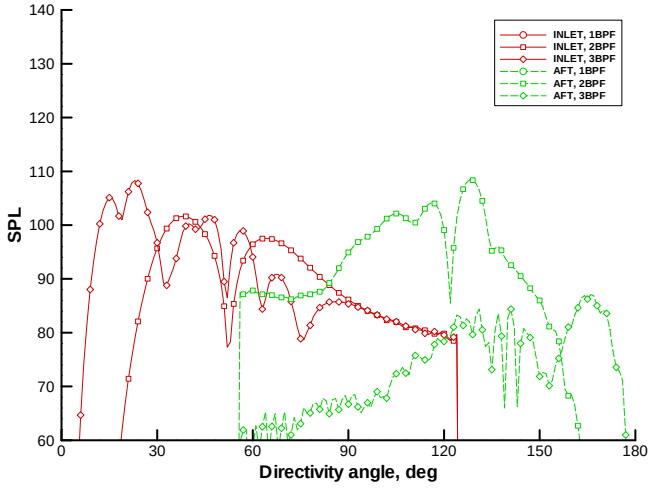

(c) approach

Figure 76: Fan rotor-stator interaction tone directivities.

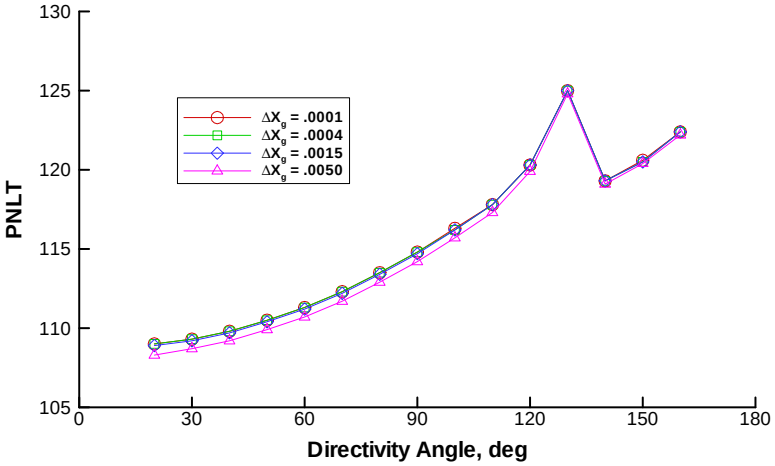

(a) axial grid spacing, $y^+ = 10$

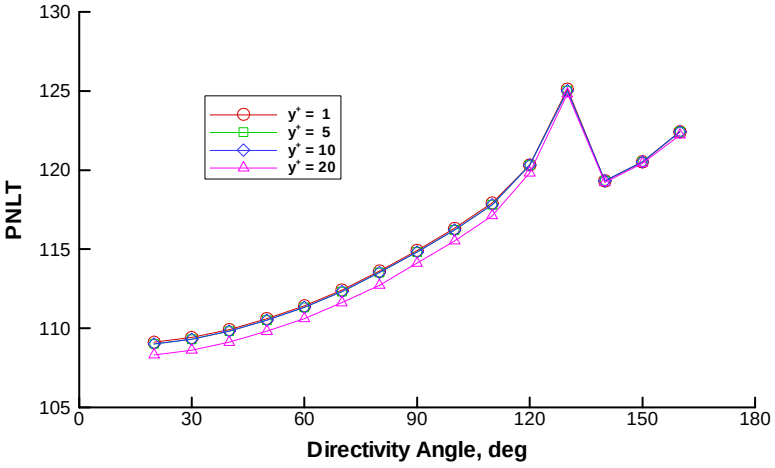

(b) radial grid spacing, $\Delta x_g = 1.5 \times 10^{-3}$

Figure 77: Effect of axial and radial grid spacing on computed PNLT directivity.

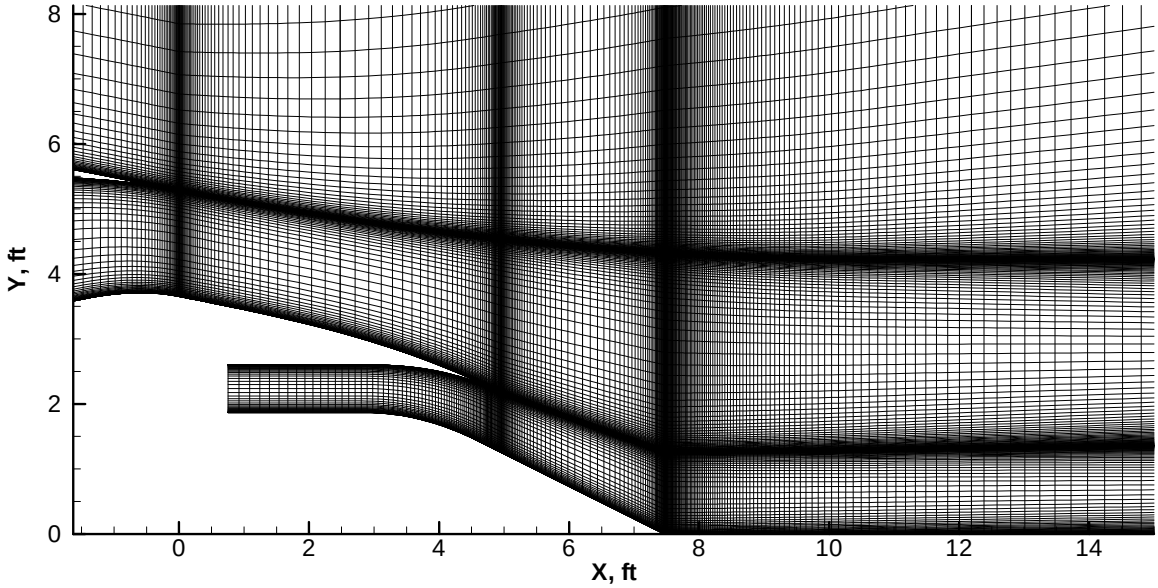

Figure 78: Jet plume computational grid in the vicinity of the nozzle exits.

the grid in the vicinity of the aft of the engine is shown in Figure 78. The grid comprises 12 blocks with a total of approximately 85,500 points. The input grid parameters were adjusted to cause an external contraction of the high-density fan nozzle lip shear layer and keep it parallel to the actual computed shear layer. The correct amount of contraction was manually selected based on feedback from an initial coarse-grid flow analysis.

The flight conditions for the analysis cases (Table 11) were used to look up the core nozzle and fan nozzle inlet conditions, which are shown in Table 11. The nozzle inlet conditions and free stream conditions were used to set the inlet and exit boundary conditions for WIND. Unlike lower bypass ratio engines, the pressure ratio for the core nozzle is actually less than that of the fan nozzle at each of the flight conditions, although the total temperature is much higher. In fact, at the approach condition the total pressure leaving the turbine is only slight higher than the ambient static pressure, so the core jet velocity would be expected to be very low. A pressure ratio of unity would be physically impossible since it would cause the nozzle flow to be reversed, violating the law of mass conservation.

The jet flow field for each of the three noise cases was computed in WIND, using four levels of grid refinement. The analysis was run for 400 iterations on the coarsest grid, then 800 iterations on the second-coarsest grid, then 1200 iterations on the second-finest

Table 13: Nozzle operating conditions for noise analysis cases.

	Core nozzle		Fan nozzle	
Case	**Press. ratio**	**Total temp. (R)**	**Press. ratio**	**Total temp. (R)**
Sideline	1.15	1573	1.50	578
Cutback	1.11	1456	1.37	559
Approach	1.05	1223	1.15	534

grid, and finally for 1800 iterations on the original grid. Each case was run using coarse parallel processing, with each of the 12 different grid blocks distributed between individual processors on the executing machine. The convergence histories for the three cases are shown in Figure 79, clearly showing the jump in residual at each transition to a finer grids. Convergence of the solution was verified by visual inspection of the convergence history.

Figure 80 shows the computed axial velocity field, normalized by the ambient speed of sound, downstream of the nozzle exits for each noise case. As the core airflow and fan airflow leave their respective nozzles, they begin as distinctive flow regions but are gradually mixed with each other and with the ambient air as the flow moves downstream. For the sideline case, there is not a large difference between the core and bypass jet velocities, and in the approach case the bypass jet velocity is actually higher than the core jet velocity.

Figure 81 shows the turbulent kinetic energy in the jet plume. There are two distinct shear layers where turbulent mixing occurs: one between the core airflow and the fan airflow, and the other between the fan airflow and the ambient air. The shear layers start out very thin but gradually increase in width and intensity downstream as the mixing of the streams progresses. Eventually the two shear layers merge into one, and gradually dissipate far downstream of the engine, beyond the exit of the computational grid. The turbulence intensity and mixing rate are proportional to the velocity gradient across the shear layer. Unlike engines with lower bypass ratios, the highest turbulence is actually in the shear layer between the bypass stream and the ambient air, since the velocity gradient in the outer shear layer is larger than in the inner shear layer.

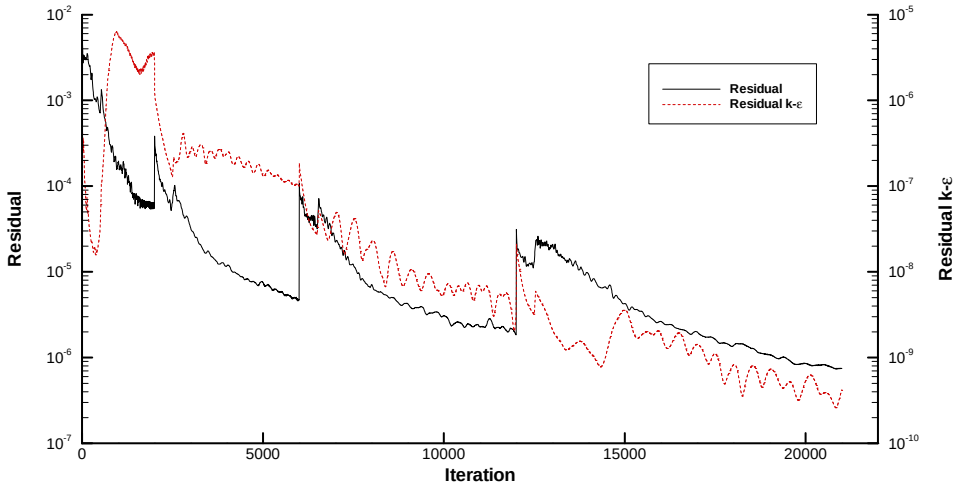

(a) sideline

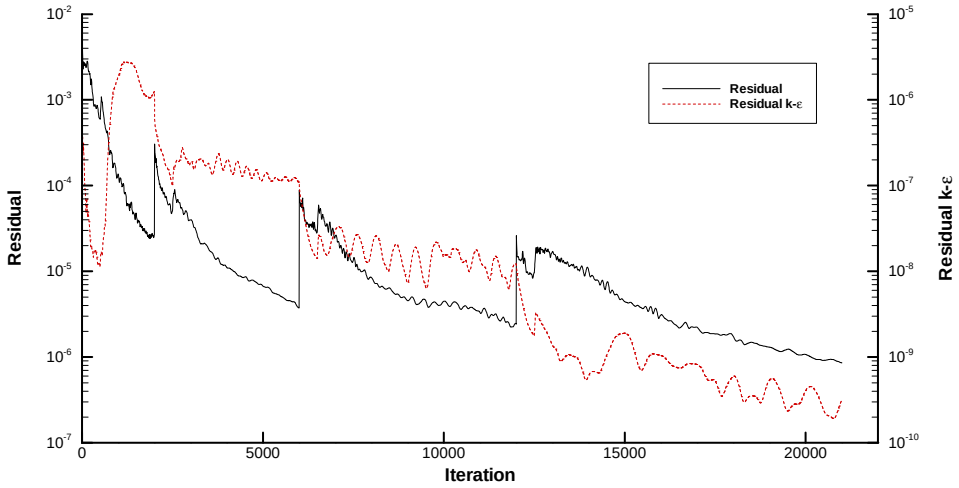

(b) cutback

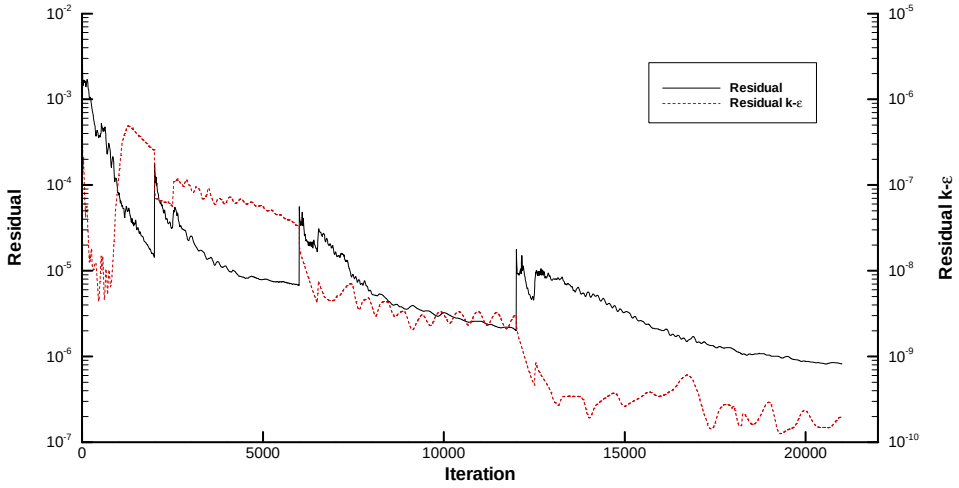

(c) approach

Figure 79: WIND residual histories.

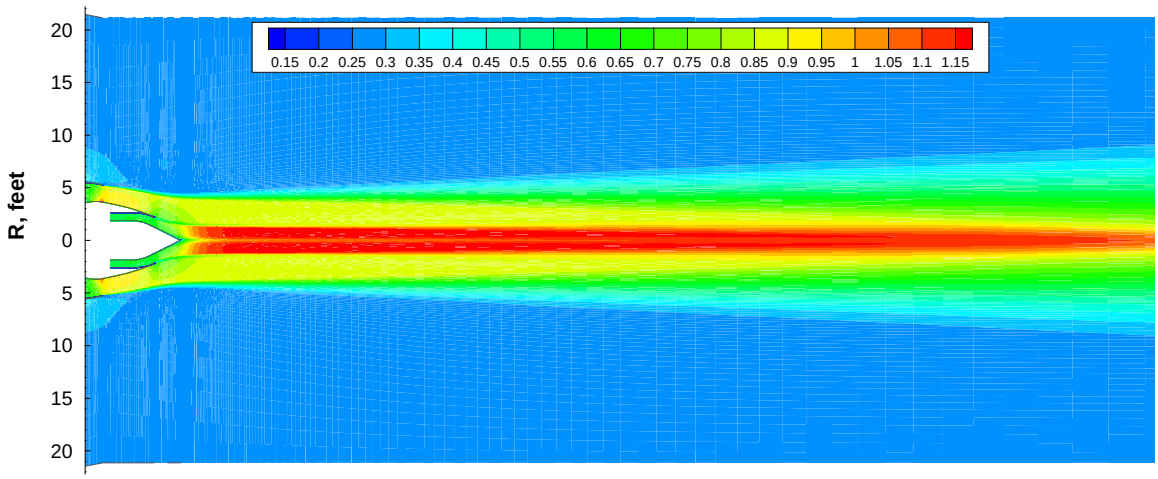

(a) sideline

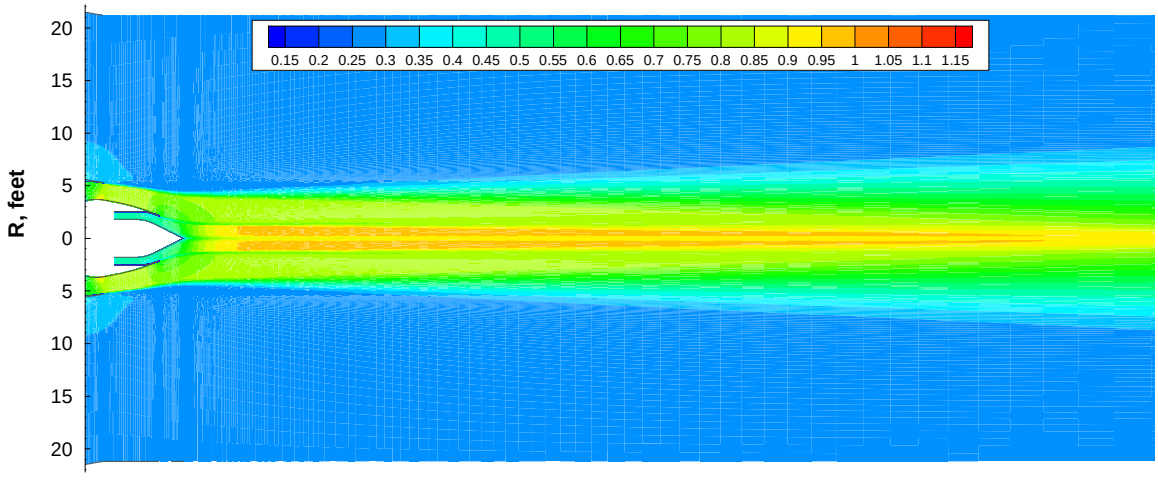

(b) cutback

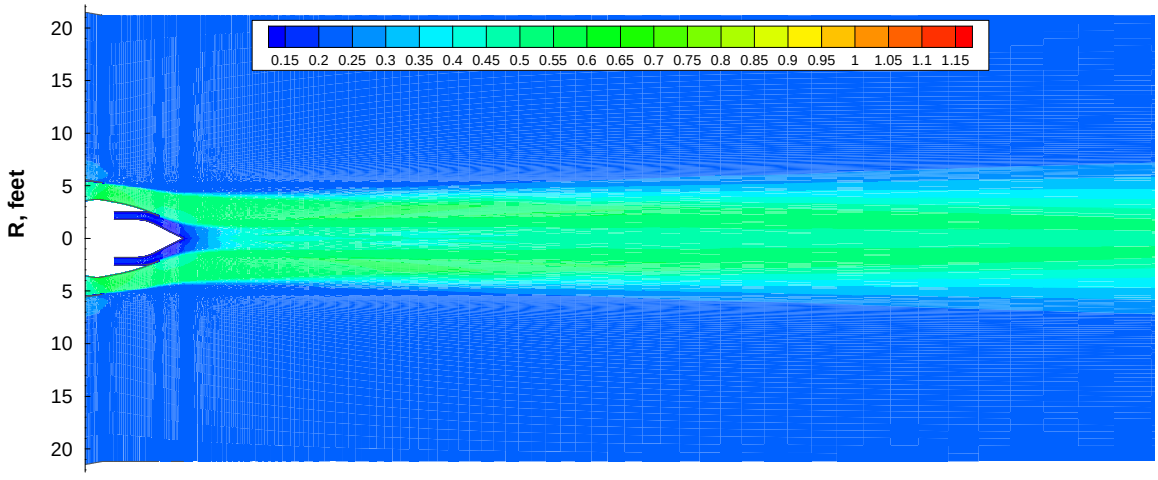

(c) approach

Figure 80: Jet normalized axial velocity fields.

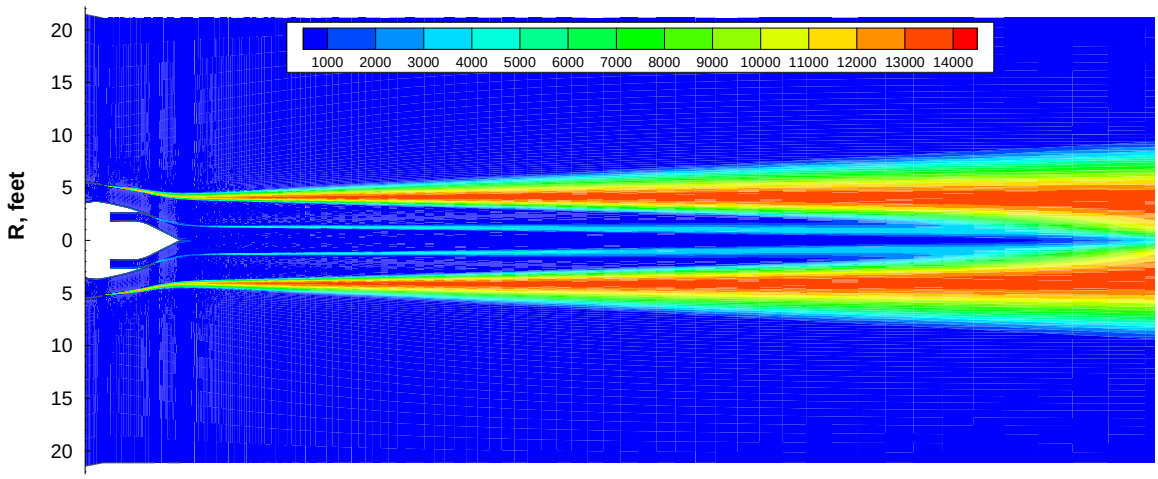

(a) sideline

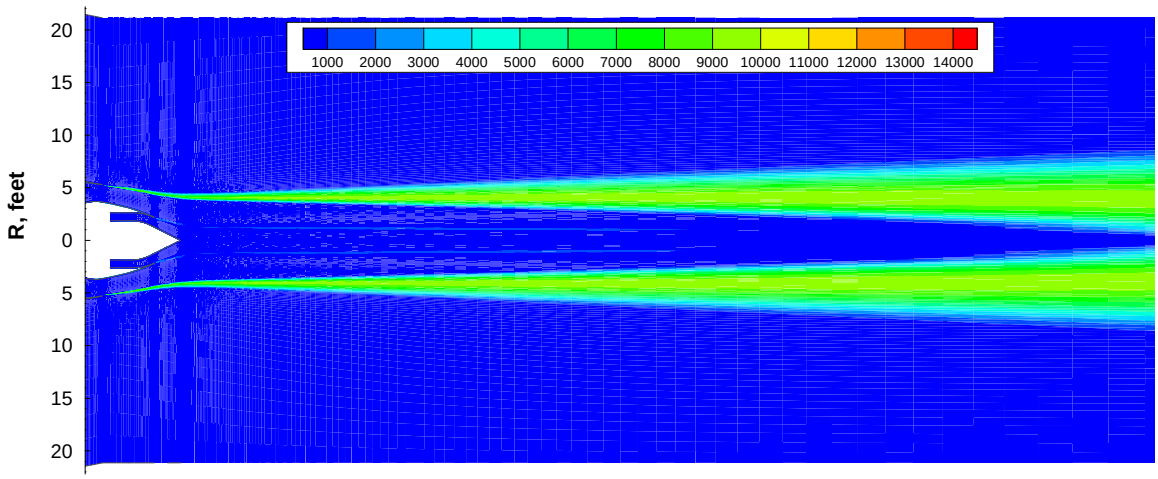

(b) cutback

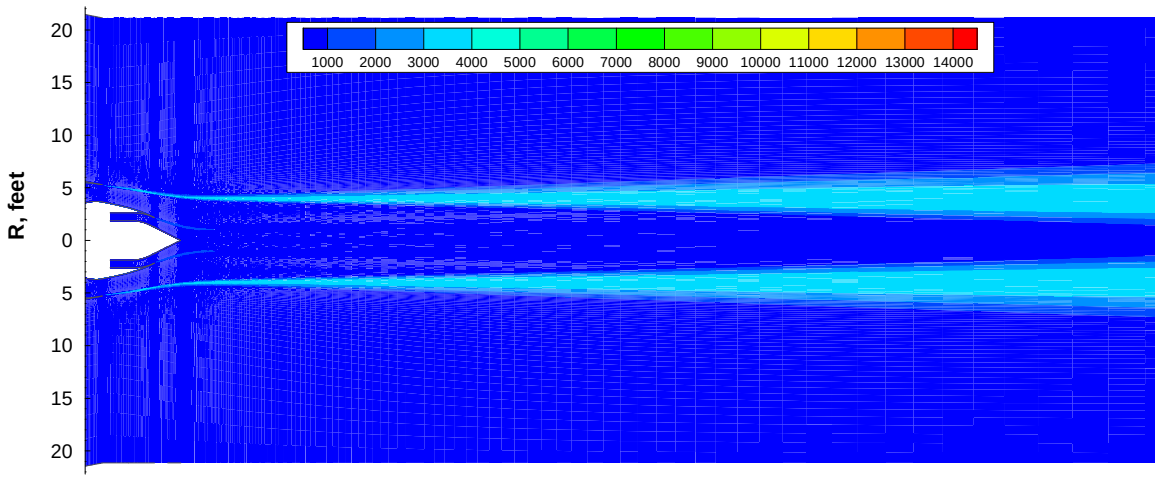

(c) approach

Figure 81: Jet turbulent kinetic energy fields.

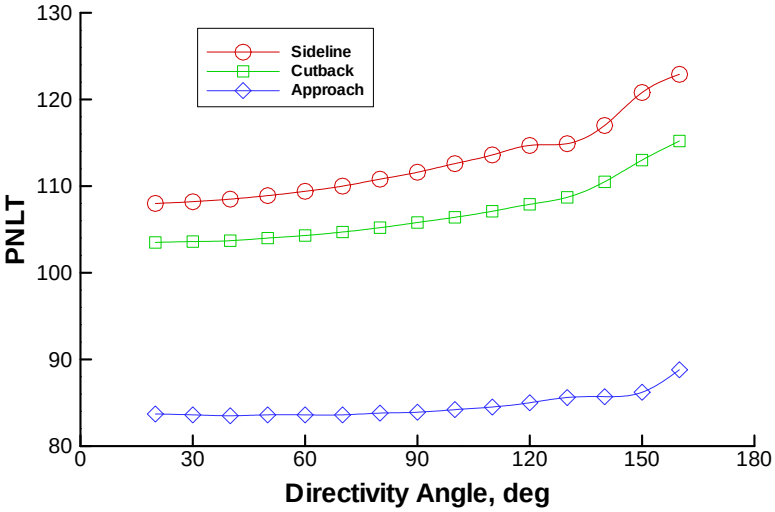

Figure 82: Jet mixing far field PNLT directivity, R = 40 ft.

6.2.7 Jet mixing noise

The computed jet flow fields were used in MGBK to compute the turbulent jet mixing noise for the three flight conditions. The empirical convection factors α_c and β_c were left at the values which were deemed to be adequate in the jet noise validation studies in Section 4.8.2. The far-field PNLT directivities for the three cases are shown in Figure 82. Unlike the typical directivity function for a dual-stream nozzle, the PNLT does not drop off at angles in the "zone of silence" near 180 degrees. This is presumably because the noise is primarily generated in the outer shear layer and experiences little change in impedance between the fan flow and the ambient area, whereas noise generated by the inner shear layer would be diffracted forward due to the large impedance change between the core and fan flows. The far-field SPL values were extracted by the post-processor for each of the three noise cases and combined to create an output table of the jet mixing noise level as a function of frequency, directivity angle and throttle setting.

6.2.8 Total noise levels

As the final step in the analysis of the baseline configuration, the sideline, cutback and approach noise levels were computed in ANOPP using the engine component thermodynamic properties and geometric parameters, the takeoff and landing flight paths, the far-field fan

rotor-stator interaction tone noise levels, and the far-field jet mixing noise levels. The computed high-fidelity noise levels were input as tables of SPL as a function of frequency, directivity angle and throttle setting, and the pre-processor was used to look up the noise levels at each flight path point based on the throttle setting. The noise levels for the fan broadband noise, combustor, turbine and airframe were predicted using ANOPP's empirical methods, noise reduction due to fan inlet and aft treatment was applied to both the fan tone and broadband noise components, and all the components were combined to arrive at the total EPNL at the sideline, cutback and approach observers.

Due to the logarithmic nature of the EPNL it is always imperative for the relative balance of the individual noise components and their contribution to the total noise to be correctly predicted. Since the design variables affect the noise of the different components unequally, or may only affect a single component, the relative levels of the individual components must be accurately assessed if the influence of certain design variables on the total noise level can be correctly estimated. For these reasons, it was necessary to compare the levels of the components to expected values and make adjustments to the predictions where needed.

The baseline engine is based on a General Electric GE90 engine, so the predicted component and total noise levels were compared to the actual levels for the GE90 engine[54]. To bring the predictions in line with the expected values for the engine, it was necessary to apply calibrations to some of the individual sources, as shown in Table 14. The broadband fan noise levels were reduced uniformly by 5 EPNdB for all throttle settings; the difference between the calculated and expected values could be due to differences between the actual GE90 and the fan as modelled in ENGGEN, failure to account for newer technologies in the empirical database, or just might be within the error band for the prediction method. The empirically-predicted core noise levels were significantly higher than would be expected for the baseline engine, which could be due to causes similar to the fan broadband noise error, or even an incorrect implementation model when running ANOPP. Also, the TFaNS predictions proved to be significantly higher than expected when compared to the GE90 at higher power settings, though for the approach condition the calibration was similar to the calibration for the fan broadband source. As mentioned previously, TFaNS is not

Table 14: Individual noise source EPNL calibrations.

Variable	Sideline (EPNdB)	Cutback (EPNdB)	Approach (EPNdB)
Fan inlet broadband	-5	-5	-5
Fan exhaust broadband	-5	-5	-5
Fan inlet R/S tones	-22	-10	+6
Fan exhaust R/S tones	-12	-2	+7
Core	-16	-16	-16
Turbine	0	0	0
Jet mixing	0	0	0
Shock	0	0	0
Airframe	0	0	0

strictly applicable to fans with supersonic tip Mach numbers, so this could account for the over-prediction of the interaction tones; the fact that the over-prediction is largest at higher power settings with greater tip Mach numbers suggests this could be the cause. Nevertheless, it is most important for later design studies that the methodology be able to assess the relative change in fan noise due to the design variables, and the results to be presented later tend to confirm that it does.

Figure 83 shows the adjusted noise levels at each observer, broken down by component. The fan inlet and exhaust EPNLs include both the rotor-stator interaction tones computed by TFaNS and the broadband noise computed empirically by ANOPP, while the jet EPNL includes both the jet mixing and shock sources. The sideline EPNL is dominated by the fan and jet sources and the approach EPNL is dominated by the fan and airframe sources, while the cutback EPNL is controlled by all noise sources relatively equally. The relative contributions of the individual sources play a role in which variables have the largest impact on changes in the total EPNLs, as will be seen in Section 6.4.

6.3 Design and uncertain variables

As a first step in conducting design studies of interest, a complete catalog of the major design variables was assembled. The list is compiled from traditional engine and airframe design variables, geometry parameters, and all the inputs to the different analyses which could affect the final noise levels of the aircraft. These variables fall into two categories: design

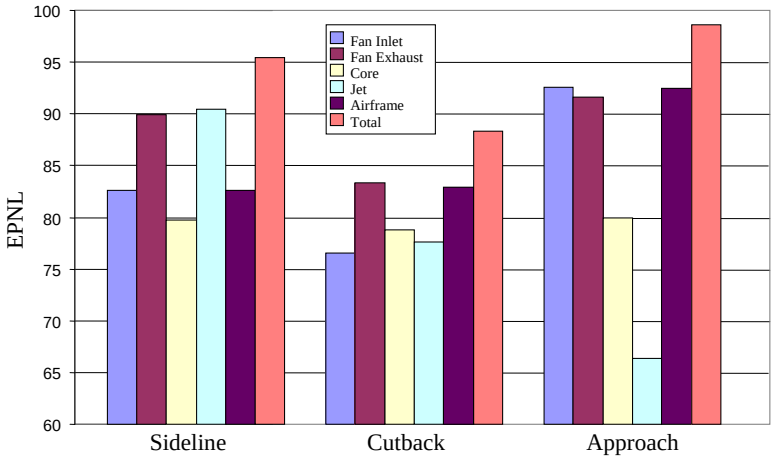

Figure 83: Baseline noise levels at FAR 36 certification points.

variables, whose values can be chosen by the engine or airframe designer or at least can be known with reasonable accuracy in the early stages of the design process, and uncertain variables, whose values are not accurately known or can vary appreciably based on the operating environment. The complete list of variables is broken down below into engine design variables, airframe design variables, and uncertain variables; these three groups will be discussed in detail in the following sections.

6.3.1 Engine design variables

A list of system-level engine design variables is given in Table 15. Most of these variables are inputs to ENGGEN, while some are used to refine the engine geometry. Minimum and maximum values are given for each variable, indicating the desired range within which each variable was allowed to vary in this study to affect the design. The maximum thrust of the engine was kept fixed at 90,000 lb and the maximum turbine inlet temperature was kept at its baseline value since one would always want to use the highest feasible value. The ranges for the bypass ratio and overall pressure ratio were chosen to represent modest, non-revolutionary changes to the baseline engine, while the ranges for the other engine cycle design variables were chosen to ensure that the optimum cycle would be expected to fall within the design space for any value of bypass ratio or overall pressure ratio. The ranges for the most of geometric variables were based on a typical variation for this class of engine, while the range for stator sweep was limited to a 20^o range to ensure reliable convergence

Table 15: Engine design variables and ranges.

Variable	Variable Name	Min	Max
Bypass ratio	BPRDES	8	11
Fan pressure ratio	FPRDES	1.3	1.5
Overall pressure ratio	OPRDES	30	50
HPC press. ratio	HPCPR	20	25
Fan tip rotational speed, ft/sec	UTIP1	1000	1200
Fan/turbine gear ratio	GRATIO	1	3
Fan hub/tip ratio	RH2T1	0.3	0.4
Number of fan blades	NB	20	24
Fan rotor-stator spacing	RSSF	1.5	2.0
Fan stator sweep, deg	SSWP	0	20

during MERIDLN analysis. Figure 84 shows a sample of the types of engines which can be studied by varying a few of the proposed design variables within their allowed ranges. It is clear that the defined design space contains a wide array of different engines of varying geometry.

6.3.2 Airframe design variables

A list of airframe variables is given in Table 16. The aerodynamic design variables are derived by representing the takeoff and landing aerodynamics with lift-curve and drag polar equations of the following form:

$$C_L = C_{L,0} + C_{L,\alpha}\alpha \tag{57}$$

$$C_D = C_{D,0} + K_1 C_L + K_2 C_L^2 \tag{58}$$

where C_L and C_D are the lift and drag coefficients, respectively, at angle of attack α. The coefficients $C_{L,0}$, $C_{L,\alpha}$, $C_{D,0}$, K_1 and K_2 can be varied to represent virtually any set of low-speed aerodynamics using just five variables for takeoff and five for landing. To further narrow the required list of aerodynamic variables, the coefficients were expressed as increments relative to the baseline values, with the increments applying to both the takeoff and landing polars.

The ranges for the airframe variables in Table 16 were chosen to represent the amount by which airframes in this class might be expected to vary and still be powered by the same

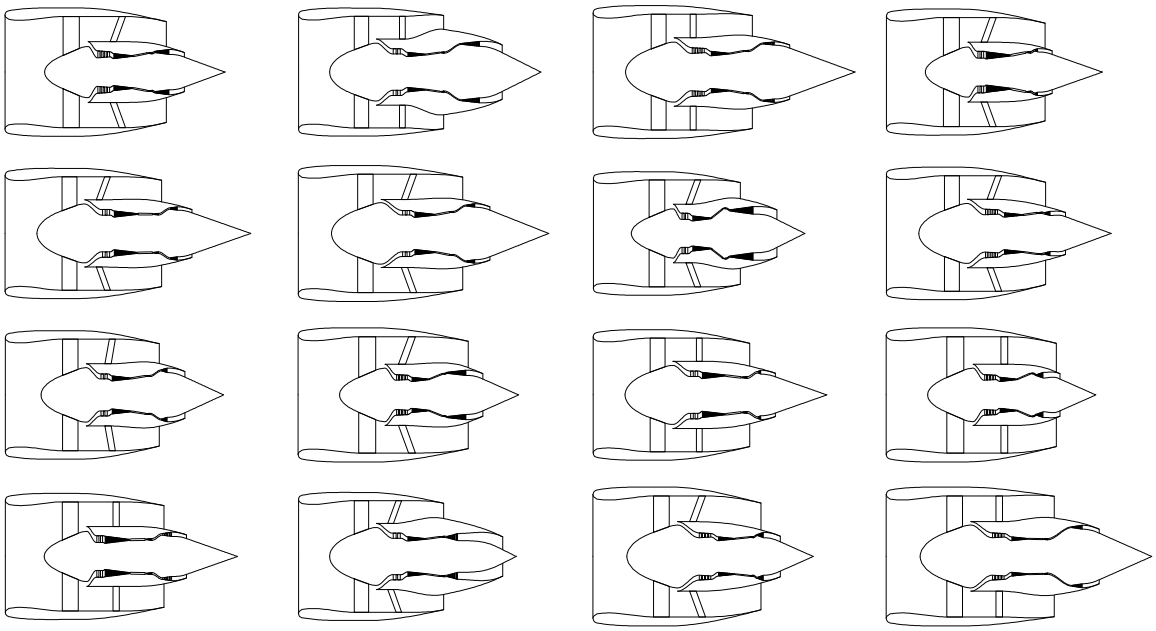

Figure 84: Sampling of engines which can be studied by varying design variables.

class of engine. Figure 85 shows the range of low-speed polars which can be represented by varying the aerodynamic design variables within their allowed ranges. The variation in low-speed aerodynamics, along with the variations in thrust-to-weight ratio, wing loading, and other airframe variables, makes it possible to indirectly account for many different variations in the design of the aircraft.

6.3.3 Uncertain variables

A list of uncertain variables was compiled by examining the input variables for all the computer programs used in the methodology, determining which variables could be expected to be different from their defaults due to lack of knowledge about the engine and aircraft at the conceptual design stage, and using engineering judgement to decide how much the variables might be expected to vary for the engines and airframes in the design space. The complete list of uncertain variables is shown in Table 17. The list includes engine component efficiencies and mass flow and power bleed requirements, aircraft takeoff and landing operating conditions and performance, and allowances for modelling errors for the individual noise components.

Table 16: Airframe variables and ranges.

Variable	Variable Name	Min	Max
Aircraft thrust/weight ratio	TWRAT	0.24	0.30
Wing loading, lb/sq. ft.	SW	120	140
Wing aspect ratio	AR	8	9
Flap area ratio	FLAPR	0.25	0.35
Horizontal tail area, sq. ft.	SHT	1000	1500
Vertical tail area, sq. ft.	SVT	600	900
$\Delta C_{L,0}$	DCL0	-0.05	0.05
$\Delta C_{L,\alpha}$, **deg**$^{-1}$	DCLALF	-0.01	0.01
$\Delta C_{D,0}$	DCD0	-0.011	0.011
ΔK_1	DZK1	-0.004	0.004
ΔK_2	DZK2	-0.005	0.005
$\Delta C_{L,\max}$	DCLMAX	-0.25	0.25
Number of main gear trucks	NMG	2	4
Number of nose gear trucks	NNG	1	2
Number of wheels per main truck	NWMG	2	4
Number of wheels per nose truck	NWNG	2	4
Main gear wheel diameter, ft	DMG	2.5	4
Nose gear wheel diameter, ft	DNG	2.5	4
Number of flap slots	NSA	1	3
Thrust inclination on the ground, deg	TINC	0	2
Angle of attack on the ground, deg	ALPRUN	-1	2

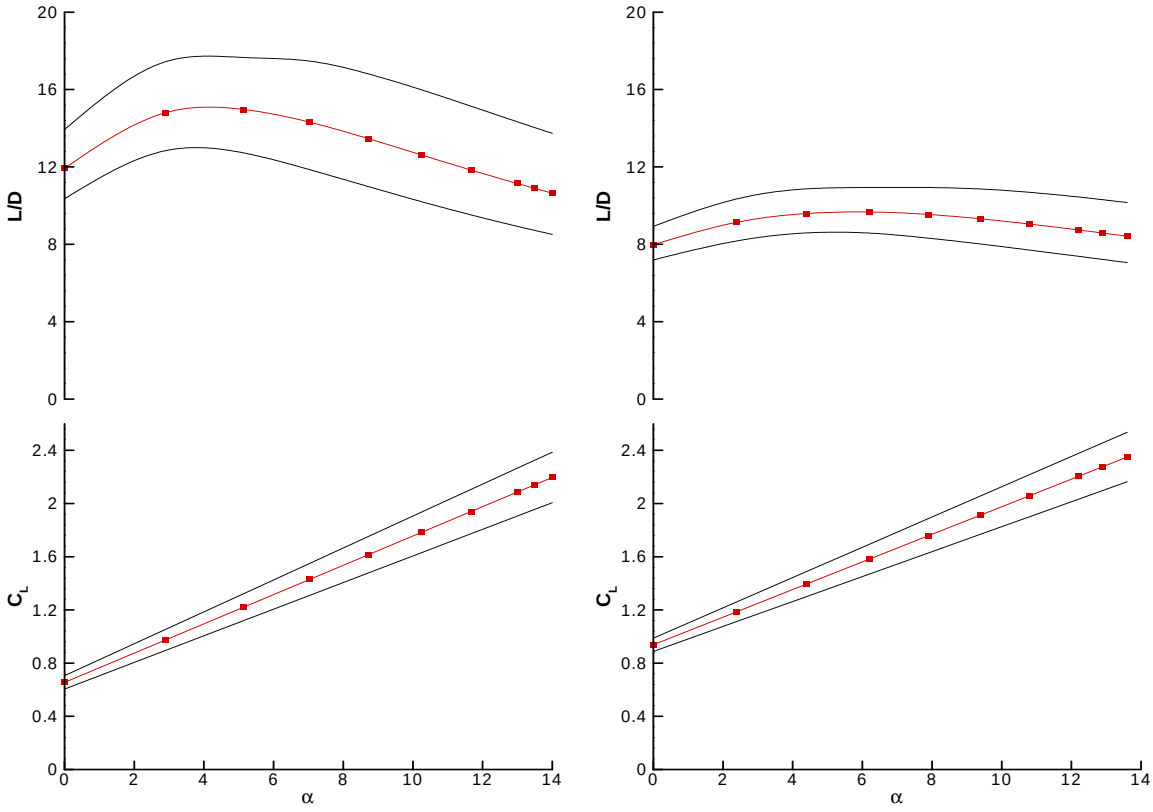

(a) takeoff polars (b) landing polars

Figure 85: Range of takeoff and landing aerodynamics in the design space. The symbols represent the baseline polars.

Table 17: Uncertain variables and ranges.

Variable	Variable Name	Min	Max
ΔFan efficiency	DEFFFAN	-0.005	0.005
ΔHPC efficiency	DEFFHPC	-0.005	0.005
ΔBurner efficiency	DEFFBURN	-0.005	0.005
ΔTurbine efficiency	DEFFTUR	-0.005	0.005
ΔPrimary nozzle thrust coefficient	DEFFNOZ1	-0.005	0.005
ΔFan nozzle thrust coefficient	DEFFNOZ2	-0.005	0.005
Turbine cooling mass flow / HPC mass flow	WCOOL	0.25	0.30
Customer power extraction, Hp	HPEXT	0	100
Customer bleed, lb/sec	COSTBL	3	5
Rolling friction coefficient	ROLLMU	0.023	0.027
Braking friction coefficient	BRAKMU	0.25	0.35
Aspect ratio for ground effect / AR	ARGEF	0.8	1.2
Engine cutback rate	SPRATE	0.05	0.15
Aircraft rotation rate, deg/sec	VANGL	1.5	2.5
Braking delay after touchdown, sec	TIBRAK	2	5
Pilot reaction time after engine failure, sec	PILOTT	1	3
Gear drag coefficient	CDGEAR	0.015	0.025
Engine out drag coefficient	CDEOUT	0.001	0.002
Ground specific flow resistance	SIGMA	450	500
Fan inlet noise modelling error, dB	-SUPPLI	-3	3
Fan aft noise modelling error, dB	-SUPPLE	-3	3
Core noise modelling error, dB	-SUPPLC	-4	4
Turbine noise modelling error, dB	-SUPPLT	-4	4
Jet noise modelling error, dB	-SUPPLJ	-2	2
Airframe noise modelling error, dB	-SUPPLR	-5	5

6.3.4 Design space limitations

Ideally, the design space for a DOE would be a hypercube in which all of the design variables were allowed to vary between their minimum and maximum values regardless of the values of all other variables. In reality, however, there are combinations of design variables which result in designs which are infeasible either because they violate physical laws or because it is impossible for the design to meet all its constraints or to perform at all required operating conditions. Aircraft engines in particular can encounter these types of limitations on the design space. If the bypass ratio (BPR), overall pressure ratio (OPR) and fan pressure ratio (FPR) are all set to the maximum values from Table 15, the power required by the fan at the design point becomes greater than the power which can be supplied by the low-speed turbine, resulting in a core nozzle pressure ratio (NPR) less than unity and causing abnormal termination of the ENGGEN design cycle without producing the required output values. Similarly, if the OPR is less than the product of the FPR and the high-pressure compressor pressure ratio (HPCPR), this results in an intermediate compressor pressure ratio (IPCPR) of less than one and also abnormally terminates the design cycle. Also, for certain combinations of high BPR, OPR and FPR and turbine cooling, along with a low fan tip speed, the engine design cycle will successfully run, but the fan velocity triangle design cycle will be unable to meet all of the constraints, and there will be no way to design a rotor blade for which the fan noise can be computed.

When a DOE table hypercube is restricted, the corners of the hypercube are no longer orthogonal; this non-orthogonality can cause a significant increase in undesirable *correlation* between the estimates for the coefficients in the RSE equation. The presence of correlation means that the effects of one variable can "bleed" into the effects of another, so that part of the effect of the first variable on the response is falsely attributed to the other variable, and vice versa.

An extensive study was conducted to find the combinations of design variable values under which the engine cycle design or the fan velocity triangle design methods fail. The findings were then used to define a set of constraints defining the combinations of values which exist within the feasible region of the design space. The three constraints are

Table 18: Constraints on the feasible region of the engine design space.

Constraint equation	Reason for constraint
FPR - OPR $\leq$ 1.5	IPCPR $>$ 1
WCOOL + 2FPR + 2BPR + OPR $\leq$ 0.5	Core NPR $>$ 1
5FPR + OPR + 0.75BPR + 0.074WCOOL - 1.86UTIP1 $\leq$ 2.331	Fan design triangles

shown in Table 18. The values of the design variables are constrained relative to their non-dimensional values, which are normalized as in Equation48. Unfortunately, the combination of constraints resulted in elimination of approximately half of the original design space. The restriction of the design space had important implications regarding the choice of DOE tables used to create the RSEs and ultimately proved to have a significant impact on the accuracy of the analysis results, as will be seen in later sections.

6.3.5 Choice of metrics

Table 19 lists the outputs from the analysis process that were chosen as responses to be approximated using RSEs. The three primary metrics of interest are the total aircraft EPNL values at the three FAR 36 observer locations: sideline, cutback and approach. Several additional secondary outputs also were selected as alternate performance metrics against which the noise levels could be compared, and as constraints on the engine and airframe design. As a measure of fuel efficiency, the required mission fuel would have been the most preferable metric, but the analysis process does not include simulation of the full aircraft mission; instead, the engine's full-power SFC at the cruise condition—Mach number of 0.85 and altitude of 35000 ft—was used as a surrogate metric. The core nozzle design NPR was included to be used as a constraint to ensure the feasibility of the engine cycle. The fan diameter also was chosen since engine cycle designs are typically constrained in size to ensure that they can be integrated with the airframe without too much difficulty. Finally, three aircraft performance metrics—takeoff field length, landing field length, approach velocity—were chosen to be used to judge the feasibility of an airframe design and to avoid assessing the noise levels of aircraft with unreasonably poor flight performance.

Table 19 is by no means a complete list of the performance measures, environmental

Table 19: List of noise, performance and constraint metrics to be approximated.

Noise levels	Engine metrics	Airframe metrics
Sideline EPNL	Full-power cruise SFC	Takeoff field length
Cutback EPNL	Core nozzle design NPR	Landing field length
Approach EPNL	Fan diameter	Approach velocity

constraints, and design feasibility constraints that could be assembled. In a more comprehensive design study, these additional outputs would need to be tracked during design optimization. For example, the ability of the engine to provide the minimum required cruise insertion thrust is an important constraint on the design cycle, but is not included here due to the lack of a full aircraft mission analysis. Some additional constraints, such as aeromechanical design considerations, are accounted for by the empirical and simple analytical methods in ENGGEN.

6.4 Variable screening

A screening study was conducted to determine which of the engine design variables, airframe variables and uncertain variables in Tables 15 through 17 had the largest effect on the noise levels, and to arrive at a subset of variables which should be used in developing metamodels for design studies. The metrics that were calculated were the sideline, cutback and approach EPNLs, fan diameter, NPR, takeoff and landing field lengths and the approach velocity. Two-level fractional-factorial DOE tables were created and the analysis process was executed for each of the design variable combinations.

Due to the long execution time of the full high-fidelity noise analysis and the very long initial list of candidate variables, it was not possible to perform a full screening study for the noise metrics for every single variable. Instead, the sideline, cutback and approach EPNL screening studies were conducted in two phases: first, a screening was conducted on all of the variables using low-fidelity analysis for the fan tone and jet mixing noise levels to get an initial list of the most important variables, followed by a second screening study using the shortened list of variables and with the noise computed using the high-fidelity analysis methods.

Figure 86 shows Pareto screening plots for the sideline, cutback and approach EPNLs. The Pareto plots give the average change in EPNL when varying each of the variables from its minimum to its maximum value. For clarity, only the 15 most important variables have been included and the engine design variables have been indicated with dark bars, the airframe variables with light-colored bars and the uncertain variables with white bars.

As one would expect, the sideline noise is primarily a function of engine design variables and engine-related uncertain variables. The engine manufacturer has a good amount of control over the sideline noise levels through the choice of design bypass ratio, fan pressure ratio and overall pressure ratio, but uncertainty exists due to jet noise modelling errors and uncertainty in the amount of turbine cooling mass flow that will be required for the new design. Seeing this, the designer can conclude that close attention should paid to the cooling mass flow estimates during the initial stages of the design and to improving the prediction of the jet noise.

The cutback noise level is still a function of the BPR and FPR but not as strongly as it was for sideline noise, and many more variables contribute to the total variation in the noise level. Due to the influence of the airframe size and aerodynamics on the throttle setting at cutback, the airframe design variables have a larger effect on the cutback noise level than they did for the sideline level. At the cutback throttle setting, the jet noise is reduced and the other noise sources, particularly the fan and airframe, contribute to the total level.

Approach noise is a strong function of the engine design and uncertain variables which affect the fan and airframe noise the most. The strong effect of fan noise indicates that there is room for improvement through reduction in the fan source noise level through new technologies such as swept stators.

Finally, Pareto plots for the engine performance and geometry metrics are shown in Figure 87 and for the airframe performance metrics in 88. The engine manufacturer has a good amount of control over the engine SFC and it can probably be quantified fairly accurately given the small effect that the uncertainty variables have. The core nozzle design NPR and fan diameter have a moderate degree of uncertainty caused by the range of the required turbine cooling mass flow at the design point. The takeoff field length is almost

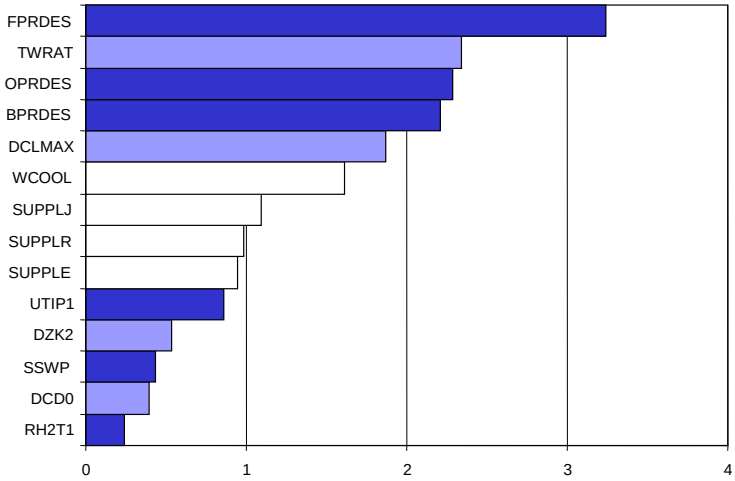

(a) sideline

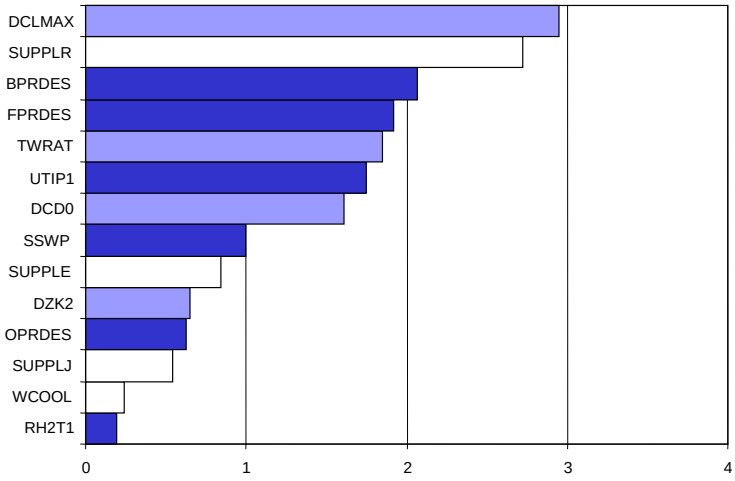

(b) cutback

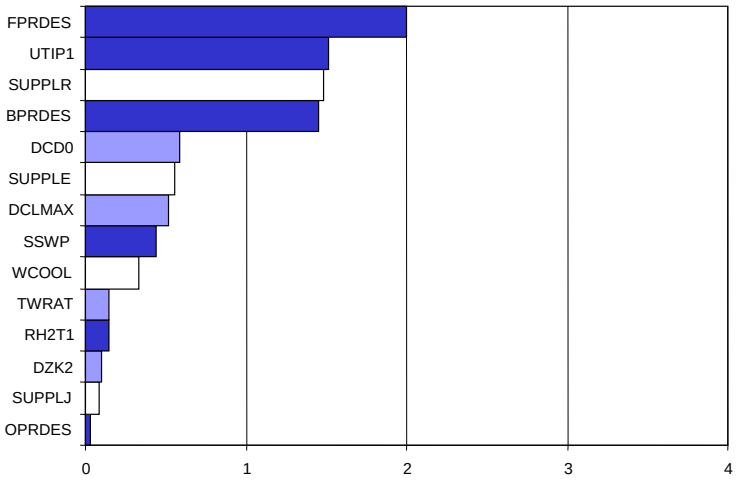

(c) approach

Figure 86: Pareto screening plot for EPNLs at FAR 36 certification points.

entirely determined by the airframe variables and the airframe-related uncertain variables, and for a fixed engine thrust the engine design variables have very little effect. The small effect of the engine design variables on the takeoff field length is presumably a result of differences in the thrust vs. velocity curve for different engine cycles. As one would expect, landing field length and approach velocity are entirely a function of the airframe and are not affected at all by the engine cycle.

6.5 Development of response surface equations

Using the results of the screening studies as guidance, a final list of variables was selected for use in development of RSEs for each of the metrics, as shown in Table 20. Table 21 gives a description of the type and size of the DOE tables for each of the metrics. The analyses for the noise levels required considerable time to execute, so to maximize the number of analyses that could be performed in a reasonable time the design variables were chosen strategically. First, the variables were grouped into three types:

1. Engine variables. Changing one of these values means that the entire analysis process must be executed from beginning to end, including engine cycle design, fan blade design, flight performance, fan noise analysis, jet noise analysis and propagation.

2. Flight path variables. Changing one of these values has no effect on the engine or fan blade designs, but the flight performance, fan noise analysis, jet noise analysis and propagation analysis must be executed.

3. Propagation variables. Changing one of these values only has an effect on the propagation analysis, which executes quickly.

Since the variables in the first two categories had the greatest impact on the execution times, only a limited number of them could be used in the DOE table. In order to limit the total analysis time required to create the RSEs to approximately two months, it was necessary to limit the number of high-fidelity analyses to approximately 40 cases, which in turn limited the number of variables from the first two categories to eight. Consequently, six variables

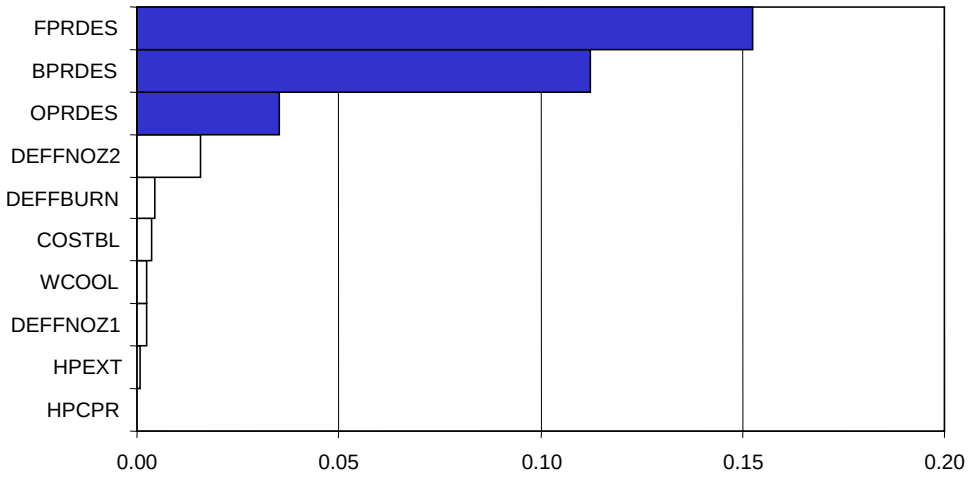

(a) full-power SFC at Mach 0.85 and 35000 ft.

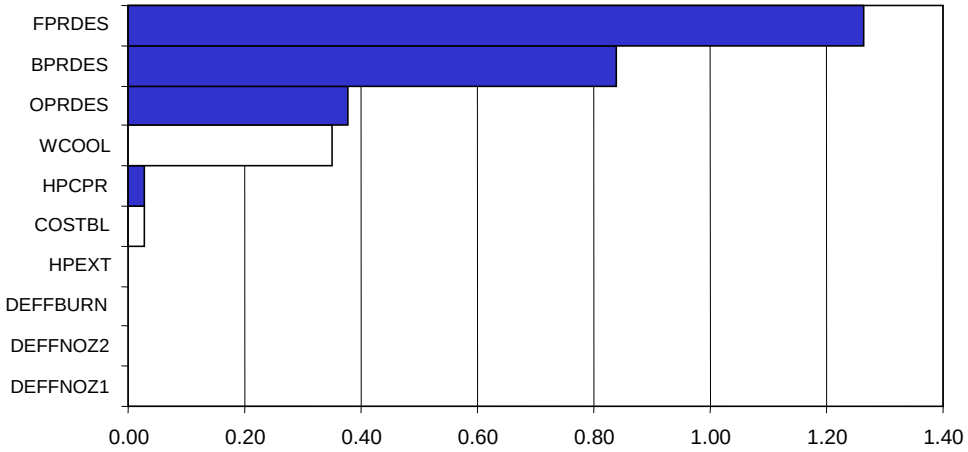

(b) core nozzle design NPR

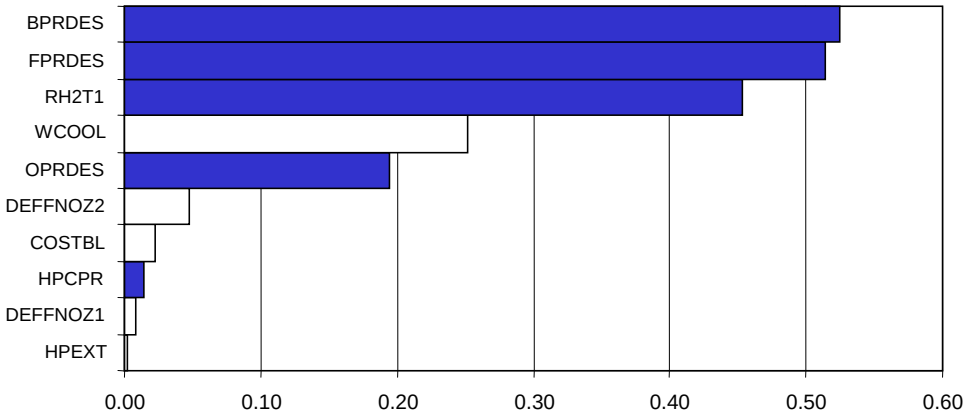

(c) fan diameter

Figure 87: Pareto screening plot for engine performance and geometry metrics.

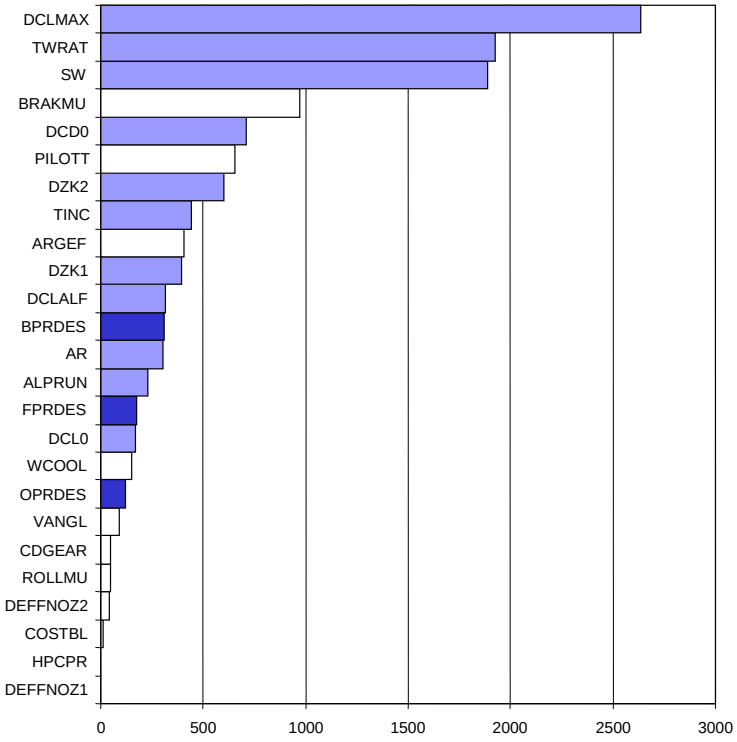

(a) take-off field length

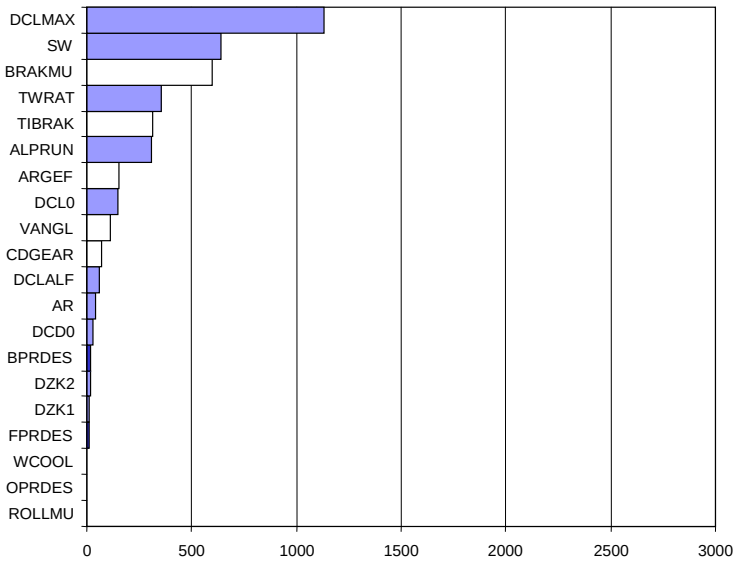

(b) landing field length

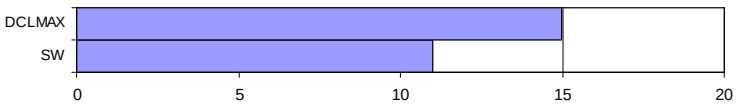

(c) approach velocity

Figure 88: Pareto screening plot for airframe performance metrics.

Table 20: Final list of design and uncertain variables for each RSE.

Metric	Variables
Sideline EPNL	BPR, FPR, OPR, fan tip speed, stator sweep, turbine cooling mass flow, aircraft thrust/weight, $\Delta C_{L,max}$, jet noise error, fan exhaust noise error, airframe noise error
Cutback EPNL	BPR, FPR, OPR, fan tip speed, stator sweep, turbine cooling mass flow, aircraft thrust/weight, $\Delta C_{L,max}$, jet noise error, fan exhaust noise error, airframe noise error
Approach EPNL	BPR, FPR, OPR, fan tip speed, stator sweep, turbine cooling mass flow, $\Delta C_{D,0}$, $\Delta C_{L,max}$, number of flap slots, fan exhaust noise error, airframe noise error
Cruise SFC	BPR, FPR, OPR, fan nozzle efficiency, turbine cooling mass flow
Nozzle NPR	BPR, FPR, OPR, turbine cooling mass flow
Fan diameter	BPR, FPR, OPR, fan nozzle efficiency, turbine cooling mass flow, customer bleed, fan hub/tip
Takeoff field length	BPR, FPR, aircraft thrust/weight, wing loading, $\Delta C_{D,0}$, $\Delta C_{L,max}$, ΔK_2, pilot reaction time
Landing field length	$\Delta C_{D,0}$, $\Delta C_{L,max}$, ground roll angle of attack, aspect ratio for ground effects, braking friction coefficient, braking delay after touchdown, aircraft rotation rate, wing loading, aircraft thrust/weight
Approach velocity	Wing loading, $\Delta C_{L,max}$

were chosen from the engine variables and two from the flight path variables, and a set of 40-run D-optimal designs was created for each of the noise metrics. The D-optimal designs were constrained to the feasible design space according to the equations in Table 18, and to limit the number of terms in the RSE to less than 40, the interaction terms between the engine variables and the flight path variables were neglected. Separately, a three-variable, 15-run face-centered CCD was created to handle three propagation variables, and the two DOE tables were crossed with each other to create a large 600-run hybrid DOE. This means that the engine design, fan rotor design, fan noise analysis and jet noise analysis were performed for each of 40 engines, with an additional 15 rapid propagation analyses for each engine.

Unlike the noise metrics, which require a very long execution time to analyze, the performance and geometric metrics are outputs from fast-executing methods, so it was feasible to assemble independent lists of design variables for each of the RSEs and conduct the analyses separately. The analyses for SFC, core NPR and fan diameter were dependent

Table 21: DOE types for RSE development.

Metric	DOE Type	Variables	Runs
Sideline EPNL	Hybrid	11	600
Cutback EPNL	Hybrid	11	600
Approach EPNL	Hybrid	11	600
SFC	D-optimal	5	243
Core NPR	D-optimal	4	81
Fan diameter	D-optimal	7	256
Takeoff field length	CCD	8	273
Landing field length	CCD	9	527
Approach velocity	Full-factorial	2	9

on the requirement that the engine cycle design be within the feasible region of the design space, so it was necessary to use constrained D-optimal DOE tables for these three metrics. The analyses were quick to execute, however, so it was possible to use a large number of runs in the table. The takeoff field length, landing field length and approach velocity DOEs did not have any variable combinations lying outside the feasible region, so simple designs could be used for those metrics.

The DOEs were executed using the built-in capabilities of ModelCenter, and the results were analyzed statistically in JMP®, which is a commercial software package for statistical analysis, visualization and data mining. Parametric sensitivity plots for the three noise levels are shown in Figure 89, with two additional rows showing the sensitivities for the two most dominant noise sources: fan and jet noise for sideline and cutback, and fan and airframe noise for approach. Parametric sensitivity plots for the performance and geometry metrics are shown in Figure 90. These plots show the relationship between each of the individual variables and the noise level when all other variables values are kept constant at their midpoints; they help to demonstrate the general trend as the individual variable is varied, but are not able to show the interactions between the variables. Error bars indicate the range of the mean regression error resulting from fitting the RSE to the points in the DOE, and are particularly evident in the sensitivity plot for takeoff field length in Figure 90(d).

The sideline EPNL is a mostly-linear function of the design variables, and is driven by jet noise, which is the loudest component for the baseline engine. Increasing the FPR extracts

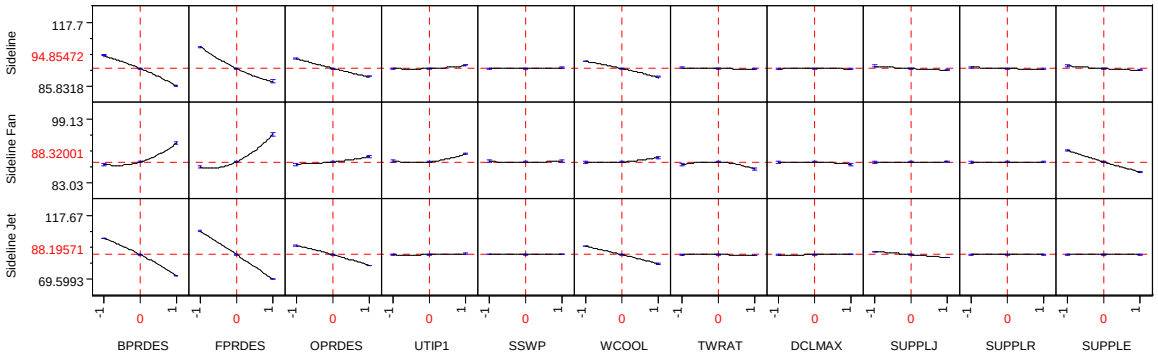

(a) sideline EPNL

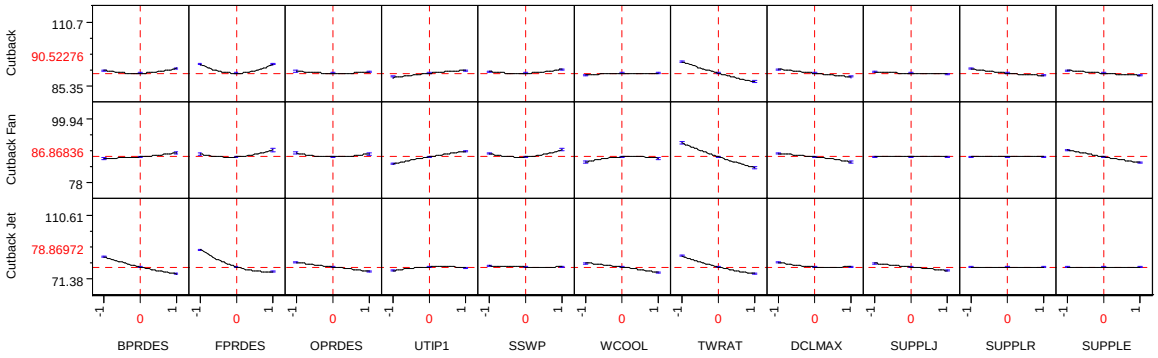

(b) cutback EPNL

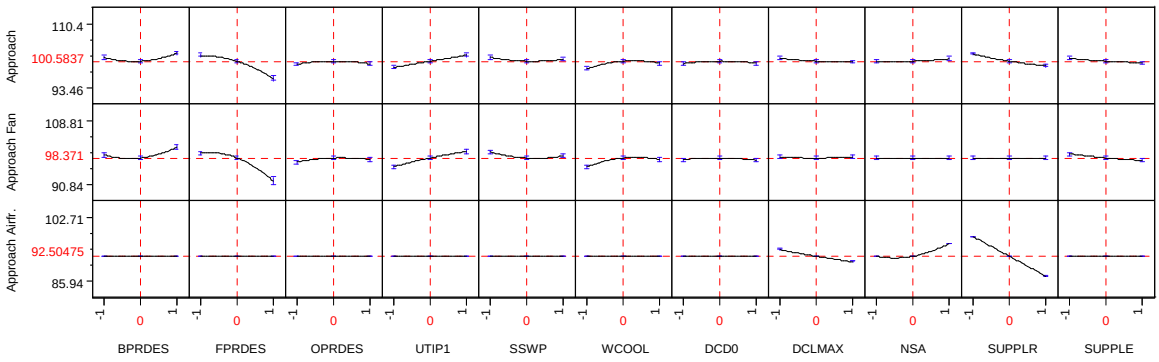

(c) approach EPNL

Figure 89: Parametric sensitivity plots for sideline, cutback and approach noise levels.

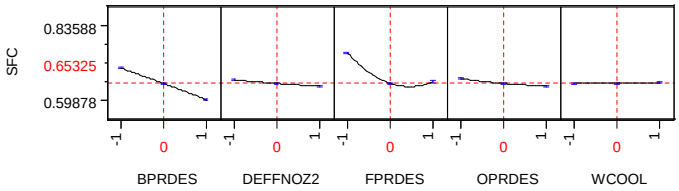

(a) cruise SFC

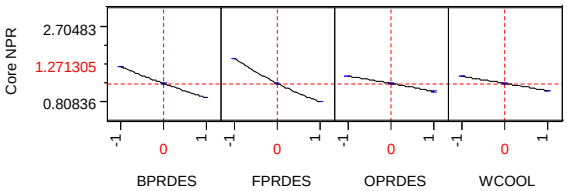

(b) core NPR

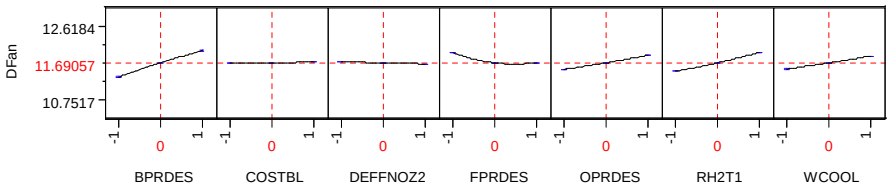

(c) fan diameter

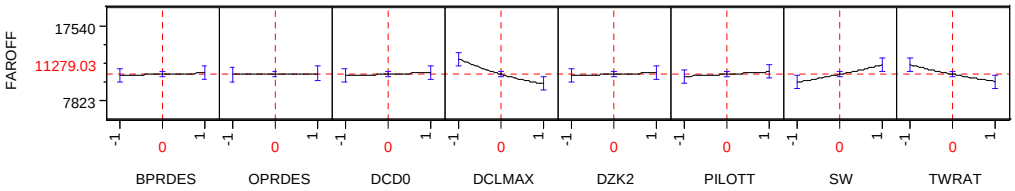

(d) takeoff field length

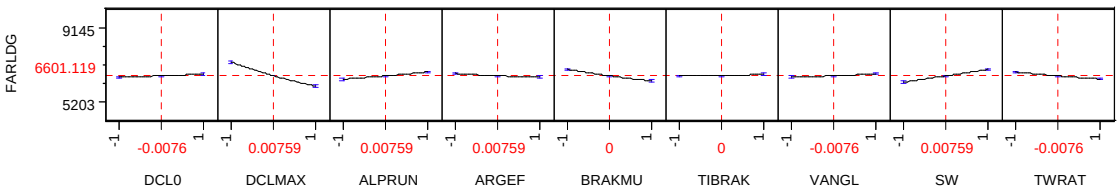

(e) landing field length

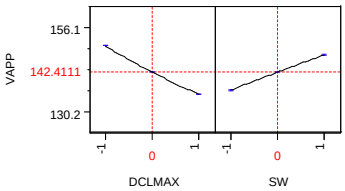

(f) approach velocity

Figure 90: Parametric sensitivity plots for geometric and performance constraints.

power from the core airflow, reducing the core nozzle exit velocity and thus the jet noise; but the fan noise is increased because of the additional power of the fan. Similarly, increasing the BPR while all other variables are held constant causes the fan power to increase and extract more power from the core and produce more noise. Increasing the turbine cooling mass flow extracts energy from the turbines and, while this has a deleterious effect on the engine efficiency, it ultimately reduces the core NPR and thus the jet noise. Most of the other variables have smaller contributions to the overall change in sideline EPNL compared to these effects.

The cutback noise, on the other hand, can be driven by either the fan or jet noise, and the lowest total noise level occurs when the two sources are balanced. At reduced power, the engine design variables have an effect on the fan and jet noise similar to that at the full-power sideline flight condition, but the magnitude of the changes in EPNL are somewhat smaller. Increasing the aircraft thrust-to-weight ratio results in a significant reduction in cutback noise because the resulting improvement in the aircraft's climb performance allows it to use a lower throttle setting after cutback.

The engine design variables affect the approach EPNL through changes in the fan noise component, while the flight path and airframe variables operate primarily on the airframe noise component. Changes in the total approach EPNL are primarily driven by the variation of the fan noise, while the airframe noise contributes has a smaller effect and consequently the impact of the airframe variables is reduced.

As seen in the Pareto screening plots (Figure 87), Cruise SFC is most strongly affected by changes in the BPR and OPR. Within the defined design space, increasing the BPR alone always improves the engine's cruise SFC, but there is an optimum value of FPR at which the engine operates most efficiently. As will be seen below, the optimum FPR is a function of the BPR but this fact cannot be gleaned from the parametric sensitivity plots alone.

The fan diameter is largely determined by the mass flow required by the fan at the design point, so it is minimized for values of the design variables at which the engine produces the design thrust of 90,000 lb with a smaller fan mass flow: this occurs for lower BPR because

the fan produces a smaller fraction of the total thrust, higher FPR because the thrust is produced by accelerating less air to a higher velocity, and at lower OPR because the core produces the same power with less airflow.

Finally, the three aircraft performance metrics—takeoff field length, landing field length, and approach velocity—show the trends with the engine and airframe variables that would be expected. The aircraft performance is best for aerodynamic variables and airframe design variables that produce the best climb performance: high maximum lift coefficient, low wing loading and high aircraft thrust-to-weight ratio. The landing field length also is improved by a lower angle of attack on the ground since this reduces the lift during roll-out and increases the deceleration of the brakes.

As mentioned previously, the parametric sensitivity plots do not show the interactions between the different design variables. To show how such interactions are captured by the RSEs, two sample interaction plots are shown in Figure 91. These show the relationship between the BPR and the cutback EPNL when the FPR is held at either its low, middle or upper value and all other variables are held at their middle value. Conversely, the second interaction plot shows the relationship between FPR and cutback EPNL when the BPR is varied. Similar interactions occur between BPR, FPR, OPR and UTIP1. These plots show that through the inclusion of interaction terms, the RSE is able to express how the influence of a variable on the noise levels can change throughout the design space, and indeed, the upward or downward trend can even be reversed.

Table 22 gives diagnostics metrics for each of the RSEs to give an indication of the quality of the fit. The RMS error is the root-mean-square value of the differences between the RSE output and the actual value for all of the rows in the DOE table, and quantifies the error inherent in approximating the function with a second-degree quadratic equation. The coefficient of multiple determination, or R^2, measures the mean-square error normalized by the total variation of the RSE, so that a value of unity indicates a perfect fit. R^2 values less than 0.99 generally indicate a less-than-optimal fit. The worst fit is exhibited by the approach EPNL, which has an R^2 of only 0.87 and an RMS error of greater than 1 EPNdB. The poor fit might be due to the omission of interaction terms between the engine and flight

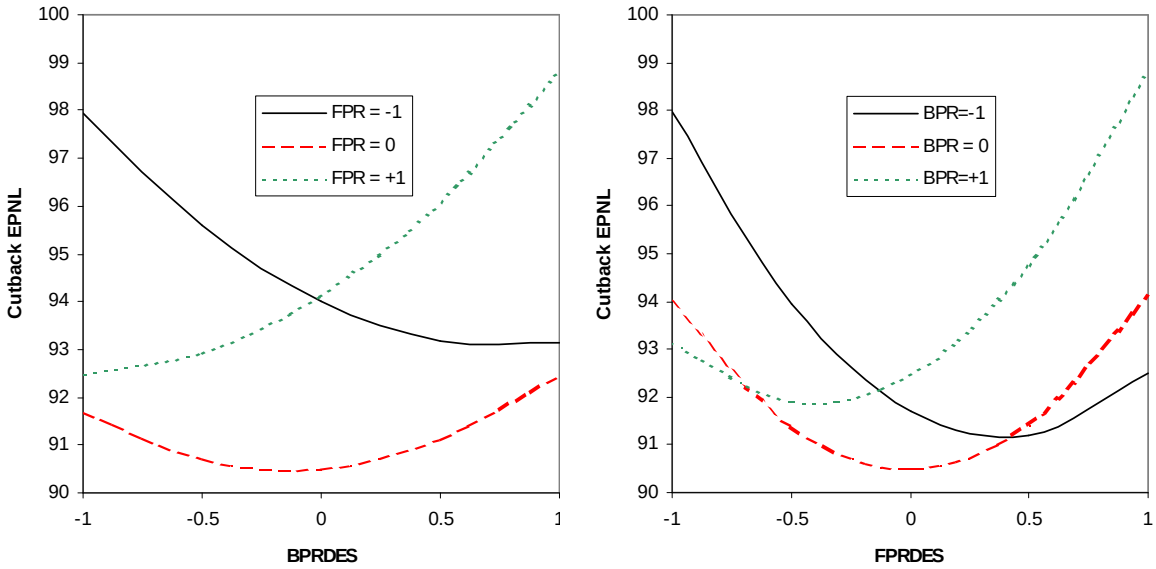

(a) bypass ratio vs. fan pressure ratio (b) fan pressure ratio vs. bypass ratio

Figure 91: Cutback EPNL interaction plots for bypass ratio and fan pressure ratio.

path variables, which do not seem to be important for sideline and cutback noise but might be more important at approach, or it might be a result of spurious correlations in the DOE table resulting from the severe restrictions on the design space. The takeoff field length RSE also shows a relatively poor fit, even though as a low-fidelity metric it was created from a rather large DOE table with many different variables. The fitting errors in the RSE are mostly like due to the fact that takeoff field length is affected by a large set of variables with three-variable and higher interactions. In contrast, the core NPR fit is nearly perfect because the core nozzle exit pressure is affected by only a handful of variables, and within the current design space the behavior is nearly linear.

The newly-created response surface equations were used to create a new analysis process in ModelCenter®, in which the various analysis codes were replaced by metamodels (Figure 92). Each component of the model is an RSE which, instead of representing individual analysis codes, represents a performance or noise metric that may be the result of multiple analyses in the original model. The new components are simply interfaces to spreadsheets that perform the rapid algebraic calculations of the RSE. Also included in the model are an optimizer and a Monte Carlo driver that can be linked to the inputs and outputs of the

Table 22: Quality of fit metrics for RSEs.

Metric	RMS Error	R^2
Sideline EPNL	0.7149 EPNdB	0.9913
Cutback EPNL	0.6528 EPNdB	0.9844
Approach EPNL	1.122 EPNdB	0.8720
Cruise SFC	0.008122	0.9898
Core NPR	0.004259	0.9999
Fan diameter	0.006539 ft	0.9997
Takeoff field length	628.3 ft	0.9380
Landing field length	39.79 ft	0.9980
Approach velocity	0.3768 kt	0.9986

RSEs.

Each metamodel accepts as input the design variables and uncertain variables which are used in the RSE. An additional input variable was added to each metamodel to account for the approximation errors in the RSE itself. Consistent with standard statistical methods, the approximation error was assumed to be normally distributed with a standard deviation equal to the RMS error of the RSE. During a Monte Carlo simulation, each metamodel accepts a random sample from a $N(0, 1)$ normal distribution, scales it by the RMS error of the RSE, and adds it to the output response.

6.6 Validation of RSEs

The previous section presented measures of the accuracy of the RSEs in fitting approximated values of the metrics to the actual values from the DOE table. In addition, it was important to also assess the accuracy of the RSEs in fitting design points which were not part of the DOE tables used in their creation. To make this assessment, a set of design points was generated for each of the RSEs by randomly selecting values for the input variables from within the allowable ranges given in Tables 15 through 17. Triangular distributions were used to bias the selection of engine design variable values toward the feasible region of the design space, uniform distributions were used for other design variables, and normal distributions were used to select values of the uncertain variables. For the performance and geometric metrics, a set of 250 design points was generated for each metric, while for the

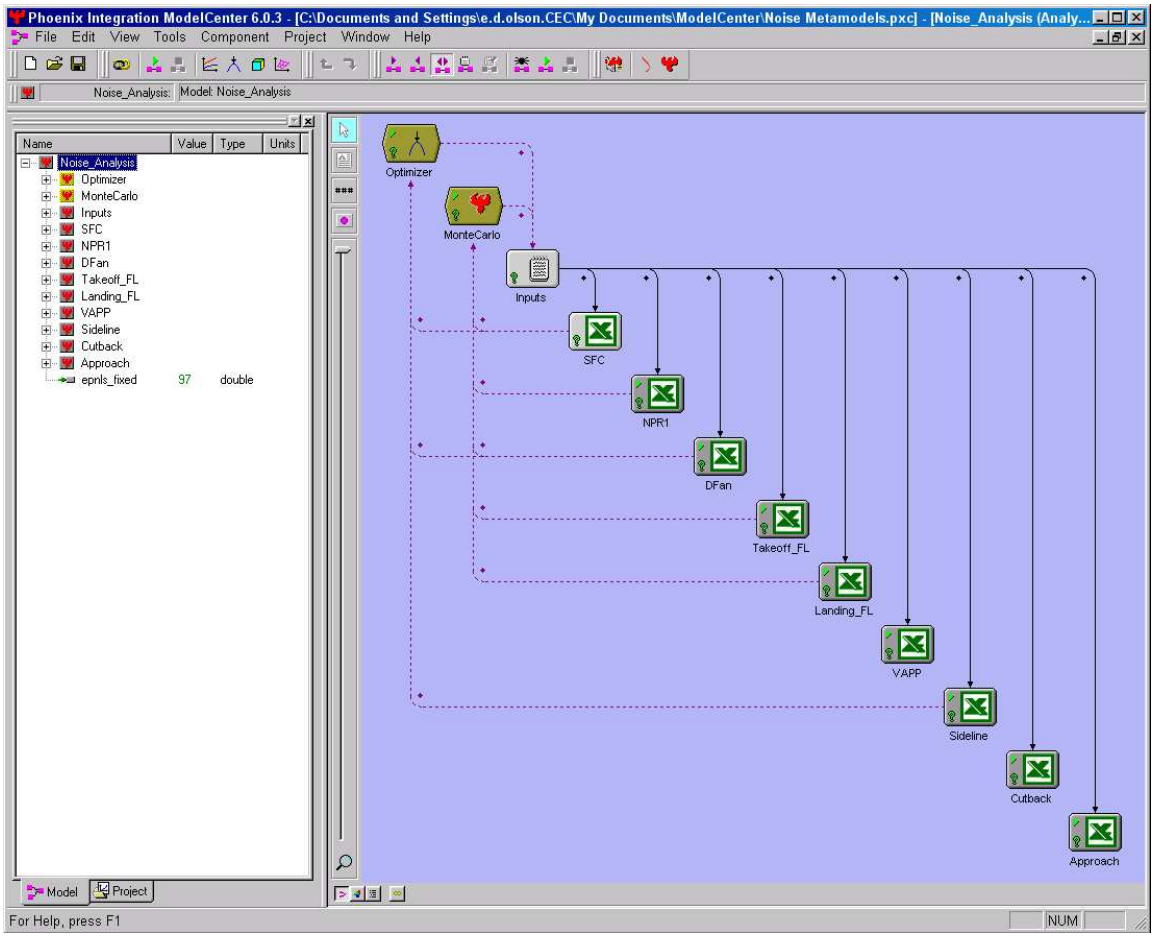

Figure 92: New ModelCenter® model using metamodels.

Table 23: Statistical analysis of RSE validation cases for engine metrics.

Metric	Mean error	RMS error	Max. error
SFC	-0.86%	3.96%	16.56%
Core NPR	0.11%	0.70%	2.06%
Fan diameter	-0.04%	0.43%	1.90%
Takeoff field length	-0.35%	4.48%	15.99%
Landing field length	0.34%	0.90%	3.86%
Approach velocity	-0.09%	0.18%	0.53%
Sideline EPNL	-0.35 EPNdB	1.57 EPNdB	4.09 EPNdB
Cutback EPNL	-0.10 EPNdB	1.16 EPNdB	2.05 EPNdB
Approach EPNL	-2.11 EPNdB	3.02 EPNdB	6.65 EPNdB

noise metrics a common set of 12 design points was generated. A portion of the points in each set were rejected because they fell outside the feasible region, so the actual error analysis was made with slightly less than the full set.

Values of the metrics were computed both directly with the analysis methods and indirectly with the RSEs, and the approximation errors were calculated for each of the validation points. Table 23 shows a statistical analysis of the calculated approximations errors. The first column is the arithmetic mean of the errors at all validation points, and shows whether the errors are biased toward under-prediction or over-prediction; the second column shows the mean approximation error which can be expected whenever the RSE is used to give an approximated value; and the third column gives the maximum absolute error encountered at any of the design points examined.

Even though the RSE for the cruise SFC does a good job of fitting the points in the original DOE table (Table 22), the errors are significant when the RSE is used to predict SFC for other design points. Much of the errors are probably due to the lack of orthogonality in the D-optimal design table resulting from the considerable restrictions on the bounds of the feasible design space. Additional errors could arise if the SFC behaves in a more complex manner than a second-degree polynomial can capture. The core NPR and fan diameter RSEs boast good accuracy even though they also were created using non-orthogonal D-optimal DOEs; these RSEs may be more accurate because they are affected less by correlation in the estimates, or their behavior may less complex and easier to approximate with a quadratic

RSE. The approximation errors for takeoff field length appear to be due mostly to the lack of fit in the RSE, as evidenced by the fact that the RMS model-fitting error in Table 22 and the RMS approximation error in Table 23 are comparable. The landing field length and approach velocity RSEs show reasonable accuracy within the defined ranges of the design variables.

6.7 Analysis of uncertainty

An initial analysis of the uncertainty in the performance and noise metrics was performed for the baseline configuration. Each of the uncertain variables was sampled from a normal distribution with a mean equal to the midpoint of the defined variable range, and a standard deviation equal to one quarter of the variable range; with the exception that the turbine cooling mass flow was sampled from a triangular distribution with minimum and most-likely values of 0.25 and a maximum value of 0.30 (Figure 93). Monte Carlo analyses were performed using 10,000 simulations per metric and the resulting outputs from the RSEs were tabulated. Figure 94 shows the resulting empirical probability distributions for the three noise metrics; Figure 95 shows the empirical probability distributions for the various metrics and constraints. Even for the baseline configuration with no variation in the design variables there is considerable uncertainty in the engine SFC, aircraft performance constraints and the noise levels of the aircraft. The takeoff field length constraint, in particular, exhibits large variation due in large part to the poor fit of the RSE. The probability distributions for SFC and fan diameter are nearly triangular since they are influenced most by the variability in the turbine cooling mass flow. From Figure 95(b) it is apparent that the design core nozzle pressure ratio can vary quite a bit; in fact, there is a finite probability that the NPR would be less than unity, resulting in an infeasible baseline configuration altogether. There also is the risk that the baseline fan diameter would be larger than predicted, or that the baseline aircraft would not be able to meet its takeoff field length constraint.

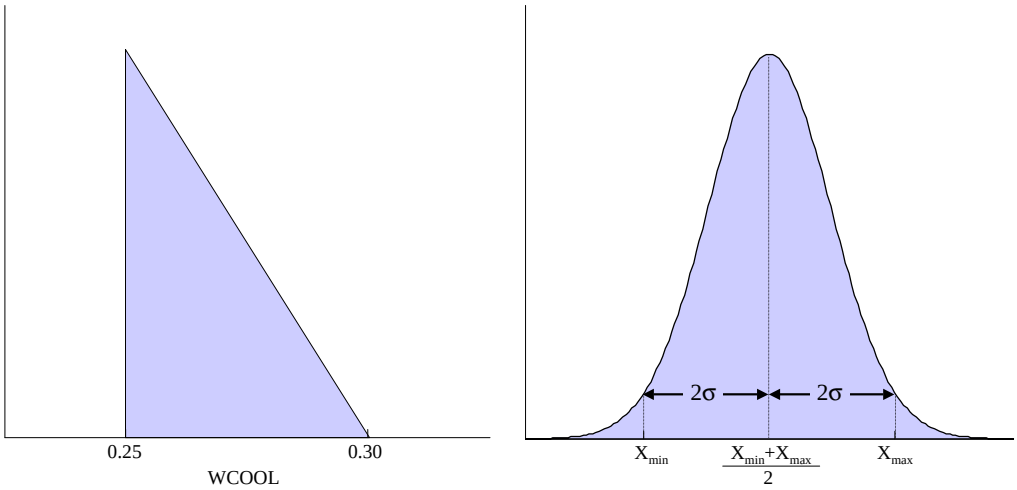

(a) turbine cooling distribution (b) all other uncertain variables

Figure 93: Defined probability distributions for uncertain variables.

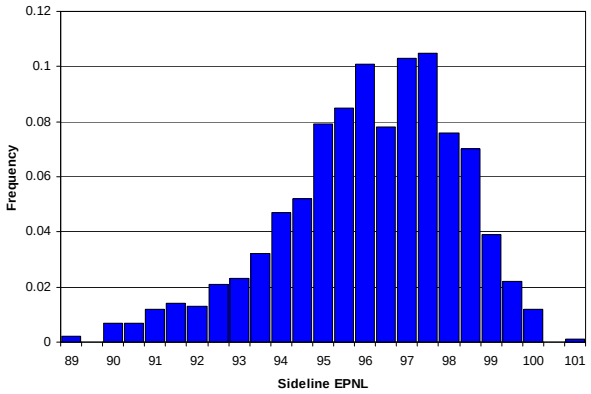

(a) sideline EPNL

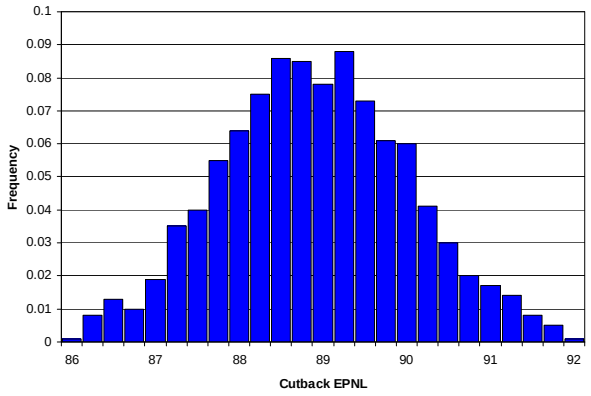

(b) cutback EPNL

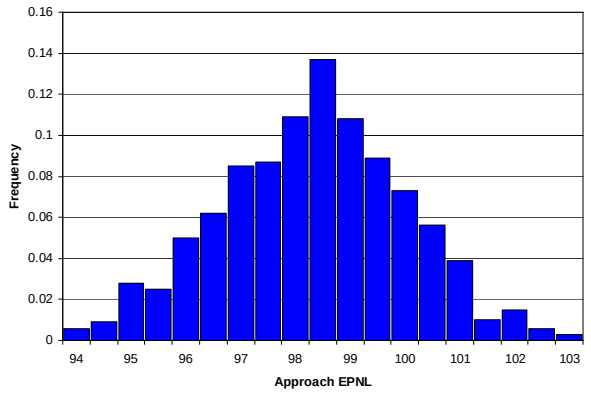

(c) approach EPNL

Figure 94: Empirical probability distributions for sideline, cutback and approach EPNLs using 10,000 Monte Carlo simulations.

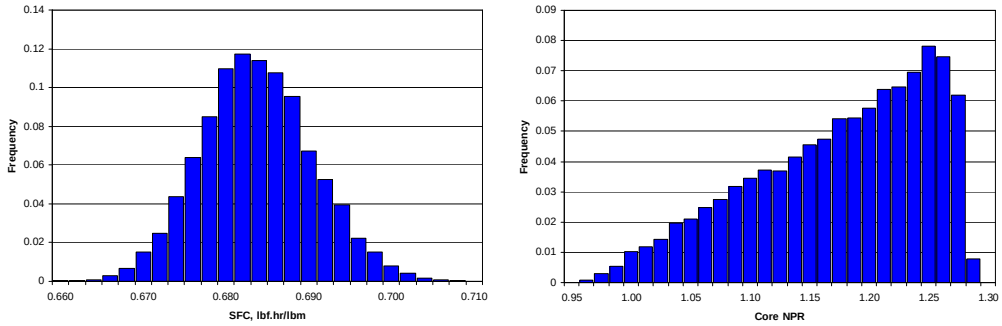

(a) cruise point SFC

(b) core NPR

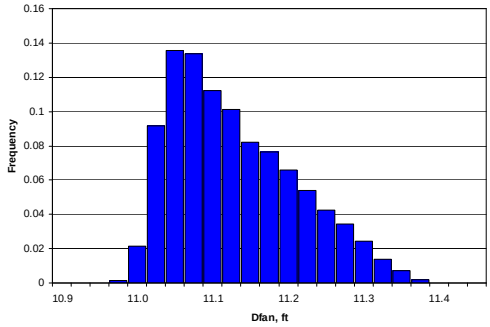

(c) fan diameter

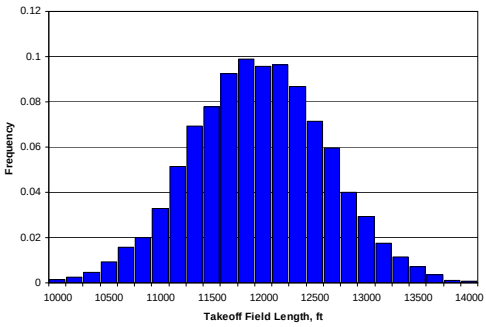

(d) takeoff field length

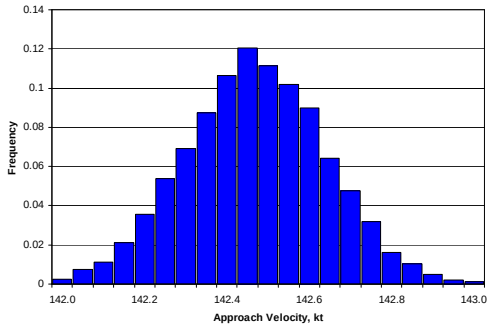

(e) approach velocity

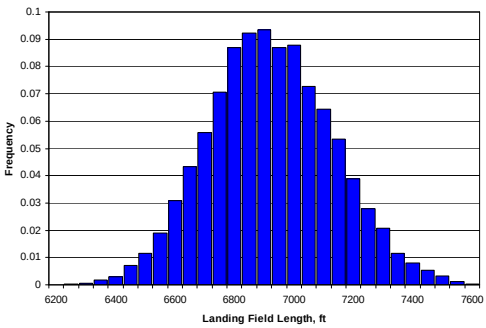

(f) landing field length

Figure 95: Empirical probability distributions for baseline constraints and performance metrics using 10,000 Monte Carlo simulations.

CHAPTER VII

ANALYSIS AND DISCUSSION

Once RSEs were created to give rapid estimates of the performance and noise metrics as functions of the design variables, design studies could be performed to study the tradeoffs between performance and noise considerations, to quantify the effects of uncertainty, and to assess the benefits of swept stators as a noise-reduction technology. Since the metamodels could be executed rapidly, design studies could be carried out which involved many thousands of analyses but could still be performed in a timely manner while still capturing the results of the physics-based analysis of the fan and jet noise levels.

7.1 SFC vs. noise

This section will examine the tradeoffs between minimizing the SFC and minimizing the noise levels when selecting an engine design cycle for use with the baseline airframe. If noise were not an issue, the engine would normally be designed to minimize the mission fuel while meeting all constraints such as engine dimensions, flight envelope, aeromechanical design limits, and engine and airframe airworthiness requirements. Since analysis of the full aircraft mission is outside the scope of the current analysis process, the cruise point SFC is used as a surrogate for the total mission fuel since the latter is normally minimized at or near the minimum for the former. The aircraft's noise levels are combined into a *cumulative noise level*, which is the sum of the sideline, cutback and approach EPNLs minus the sum of the FAR 36 Stage 3 sideline, cutback and approach noise limits, and gives a single metric with which to rate the noise produced by the aircraft; a cumulative noise level of -10 EPNdB corresponds to Chapter 4 noise limits, assuming that the other criteria are met (see Section 2.1).

Figure 96 shows carpet plots illustrating the effects of BPR, FPR and OPR on the cumulative noise level and cruise SFC through the entire design space. Other variables,

such as fan relative tip velocity, stator sweep, etc., were not varied because they affect either SFC or cumulative noise level, but not both. Several constraint lines are also shown for the core NPR and fan diameter. Within the limits of the design space, cumulative noise is always decreases when FPR is increased, but a minimum value of SFC is reached after which it begins to increase. Similarly, increasing BPR always reduces the SFC, but there is a minimum cumulative noise level which can be achieved. Increasing the OPR reduces both the SFC and the cumulative noise level, but the fan diameter increases and the core NPR decreases so the constraints become more restrictive. It is apparent from Figure 96, then, that the interactions between the cycle design variables are complex, and exploring the tradeoff between SFC and noise requires that multiple design variables be varied simultaneously.

Figure 97 illustrates the between cruise SFC and the cumulative noise level under various constraint scenarios. Each of the solid lines plots the locus of points having the minimum SFC for a given cumulative noise level. Individual points along each line were located by using an optimizer to find the optimum combination of BPR, FPR and OPR to minimize the SFC subject to various constraints, with an additional equality constraint used to force the cumulative noise level to the specific level. To improve the continuity of the tradeoff lines, the design space was expanded slightly to allow OPR to be as low as 25, and to allow BPR to be as high as 11.5. The accuracy of RSEs is degraded somewhat when they are used to extrapolate outside the usual design space, but this approach was acceptable because the actual optimum points proved to be within the original design space.

The first line in Figure 97 shows the trend line when the core NPR and fan diameter are unconstrained, and the engine cycle is constrained only by the boundaries of the design space. Not surprisingly, the minimum SFC lies along the edge of the design space at $BPR = 11.5$. Without constraints, there is no tradeoff between SFC and noise, and the two metrics decrease together without limit.

Realistically, though, the SFC and cumulative noise cannot continue to be reduced together because the amount of work required to drive the fan and compressors eventually exceeds the amount of work available from the turbines. The second line shows the trend

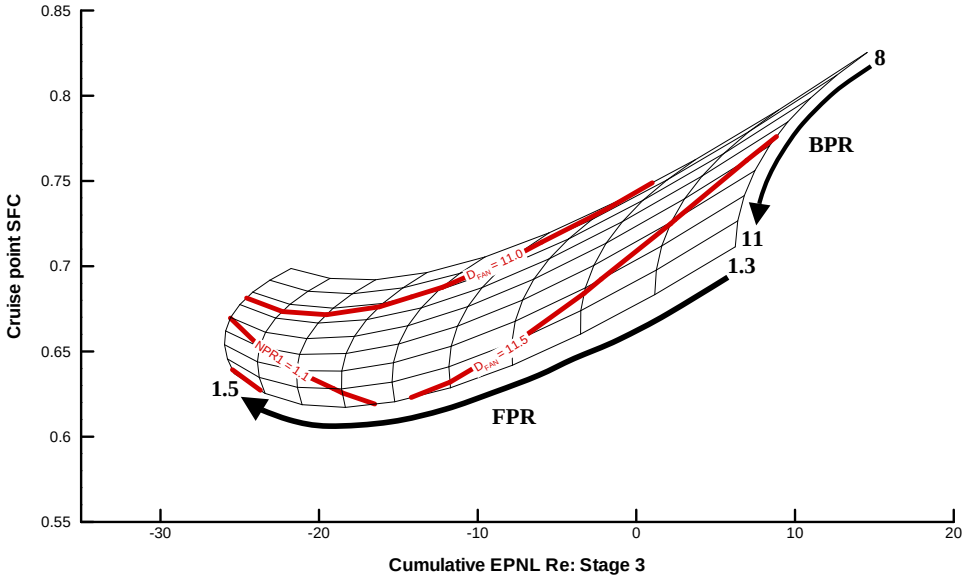

(a) OPR = 30

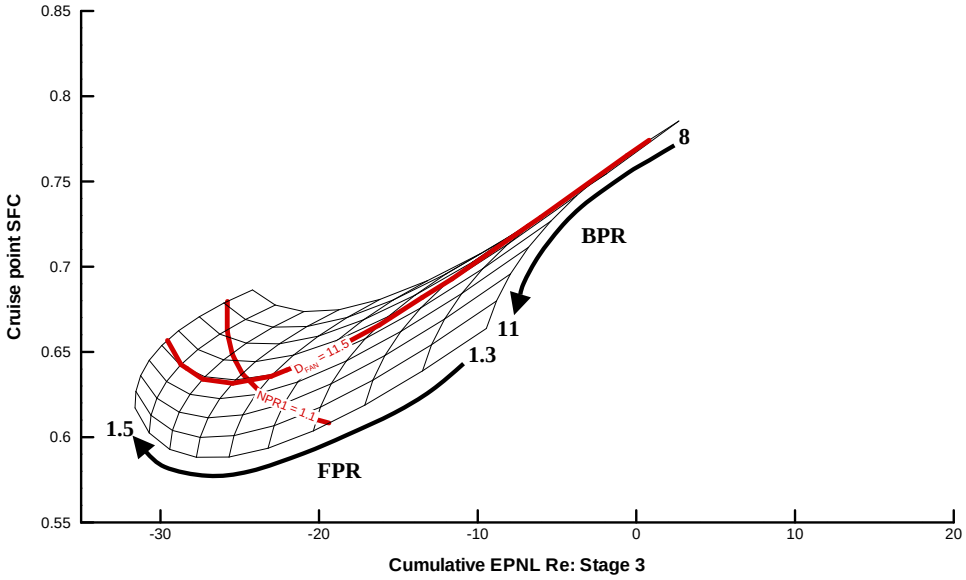

(b) OPR = 50

Figure 96: Carpet plots of SFC vs. cumulative noise level for varying BPR and FPR.

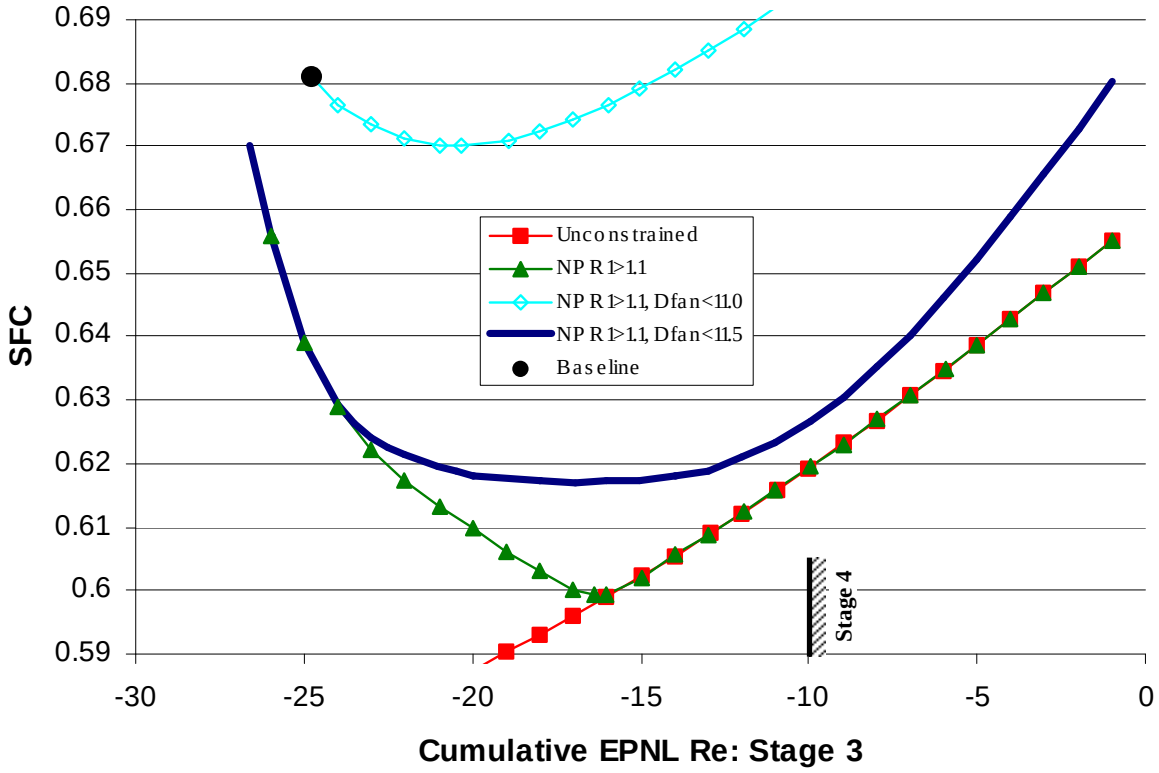

Figure 97: Minimum SFC vs. cumulative noise level.

line with the core nozzle pressure ratio constraint imposed, forcing the engine to adhere to the work constraints of the turbine. Activation of the constraint imposes a minimum on the SFC, and any additional reduction in noise can only be achieved by reducing the BPR and simultaneously increasing the FPR and OPR to avoid violating the constraint, resulting in an SFC penalty which grows larger as the noise level continues to decrease. The portion of this line to the left of the absolute minimum SFC represents a *Pareto set*, which is the set of all *Pareto optimal* points, i.e. points at which the cumulative noise margin cannot be reduced without increasing the SFC, or vice versa.

Near the absolute minimum of SFC, the fan diameter reaches a maximum which is much larger than the diameter of the baseline. With a limited space under the wing in which to integrate the engine, the designer must be conscious of the size of the engine and the maximum allowable engine size may be smaller than that of the optimum engine cycle. The third line in Figure 97 shows the trend line when the fan diameter is constrained to be no greater than that of the baseline (11.0 ft). Meeting the new diameter constraint requires

an increase in FPR and a decrease in BPR and OPR, which imposes an additional SFC penalty, although the cumulative noise level at the performance optimum is actually lower. All designs along this line lie against the fan diameter constraint.

As one follows the new Pareto set to the left of the minimum, the noise is reduced by simultaneously increasing the fan pressure ratio, slightly increasing the BPR and slightly reducing the OPR, which results in a modest increase in the cruise SFC. The dark single point indicates the SFC and cumulative noise level of the baseline engine. The location of this point along the Pareto set confirms that the baseline engine has been optimized for minimum cruise SFC and has likely been designed for reduced noise levels at the expense of a small increase in SFC. According to this analysis, the noise level has been reduced by 6.6 EPNdB at the expense of a 1.7% increase in SFC.

Finally, the fourth line in Figure 97 shows the trend line with the fan diameter constraint relaxed to 11.5 ft. Allowing a larger fan diameter allows the BPR to be increased and the FPR and OPR to be reduced, and the engine can be optimized at a lower SFC than the baseline. The optimum SFC is quite sensitive to the allowable fan diameter, as a 6-inch increase in diameter can give an 8% reduction in SFC. Although the new optimum has a higher cumulative noise level, the larger-diameter design can always be optimized to a lower SFC for a given noise level than the smaller-diameter design, or conversely, a lower cumulative noise level for a given SFC. Table 24 shows the optimum cycle parameters if the engine is optimized for minimum SFC using the three different constraints on D_{fan}.

From the preceding analysis, it is clear that there exists a tradeoff between minimizing the cruise fuel burn and minimizing the takeoff and landing noise levels. The performance-optimized engine cycle has fairly low noise levels to begin with, but any additional reduction in noise requires modifications to the cycle which negatively impact the cruise SFC. Table 25 shows the SFC penalty incurred by optimizing the engine cycle for lower cumulative noise levels under the three constraint scenarios. When the engine diameter is unconstrained, the SFC can grow rapidly for any reduction in cumulative noise level, but for diameter-constrained designs, the tradeoff is less severe and significant reductions in noise can be achieved for modest SFC penalties. For the $D_{fan} < 11.0'$ case, the cumulative noise cannot

Table 24: Minimum SFC design points.

Metric	D_{fan} unconstrained	$D_{fan} < 11.5'$	$D_{fan} < 11.0'$
BPR	11.50	11.08	8.74
FPR	1.366	1.418	1.457
OPR	43.53	31.34	33.75
Cruise SFC	0.599	0.617	0.670
Core NPR	1.10	1.10	1.46
D_{fan}	11.81	11.50	11.00
Sideline EPNL	92.9	96.5	100.5
Cutback EPNL	92.3	90.6	87.6
Approach EPNL	103.9	101.5	97.1
Cumulative EPNL	-16.4	-16.9	-20.3

Table 25: SFC penalty vs. cumulative noise level

SFC penalty	D_{fan} unconstrained	$D_{fan} < 11.0'$	$D_{fan} < 11.5'$
0%	-16.4	-20.3	-16.9
1%	-18.7	-24.0	-22.7
2%	-20.5	-25.2	-24.0
3%	-22.0		-24.7
4%	-23.2		-25.2

be reduced to less than -25.2 EPNdB without departing from the defined design space, so additional SFC penalties are not shown.

7.2 Swept stator benefits

Stator sweep is an axial shift of the stator vane that increases with radius so that the tip is farther downstream than the hub. Tests have shown that swept and stators can give significant reductions in both rotorstator interaction noise and broadband noise beyond what can be achieved through increased axial spacing alone[39][95][142]. Swept stator vanes can be employed to reduce the fan noise of an engine, producing a lower total noise level for a given engine design cycle, or conversely, allowing the engine to be optimized for a lower SFC at the same noise level. The effect of swept stator vanes cannot be modelled using the empirical methods in ANOPP, though, so their benefits must be obtained from external sources and incorporated as an adjustment to the predicted fan noise. In a traditional

design process, the benefits of swept stators might be analyzed using a physics-based noise analysis or a scale-model experiment for a single fan design, and the benefits assumed to be the same for other engines in the design space. In this study, however, the RSEs that were created could model the interactions between the stator sweep angle and the other engine design variables, so the analysis was able to discern different swept stator benefits to the sideline, cutback and approach noise, as well as showing how the swept stator benefit varies for different engine cycles. Only a partial benefit could be assessed, however, since the impact of stator sweep on the fan broadband noise could not be accounted for in the empirical methods; nevertheless, the advantages of using FPA to directly model the swept stators could still be demonstrated using the fan tone noise results.

The previously-created RSEs include stator sweep as one of the variables of which the noise levels are a function. To show how the benefits of stator sweep vary for different engine cycles, a DOE study was run for the engine cycle design variables which contribute to the cumulative noise levels—bypass ratio, fan pressure ratio, overall pressure ratio and fan rotor design tip speed, and the RSEs were used to calculate the noise levels. For each design point, the stator sweep angle was optimized to minimize the cumulative total noise level, and the stator sweep benefit was calculated as the difference between the cumulative noise level at zero sweep and the optimized level, with positive numbers indicating a reduction in noise. Figure 98 shows parametric sensitivity plots for the stator sweep benefit to the total aircraft cumulative noise level, as a function of the engine cycle design variables. Instead of being constant for all engines, the noise benefit of stator sweep is actually a function of the engine cycle to which it is applied, where the largest reduction in noise is achieved for lower bypass ratios, low fan pressure ratios and higher tip speeds where the fan noise is most dominant.

The SFC vs. noise tradeoff study from the previous section was revisited to assess the benefits of swept stators when selecting an optimum engine cycle. Figure 99 shows the difference between the previous trend line with unswept stators (SSWP=0), and a new line along which the stator sweep angle was allowed to vary to find the optimum value. Since the effect of swept stators on fan efficiency is not accounted for in the analysis, they do not change the global minimum SFC which can be achieved, but instead shift the entire

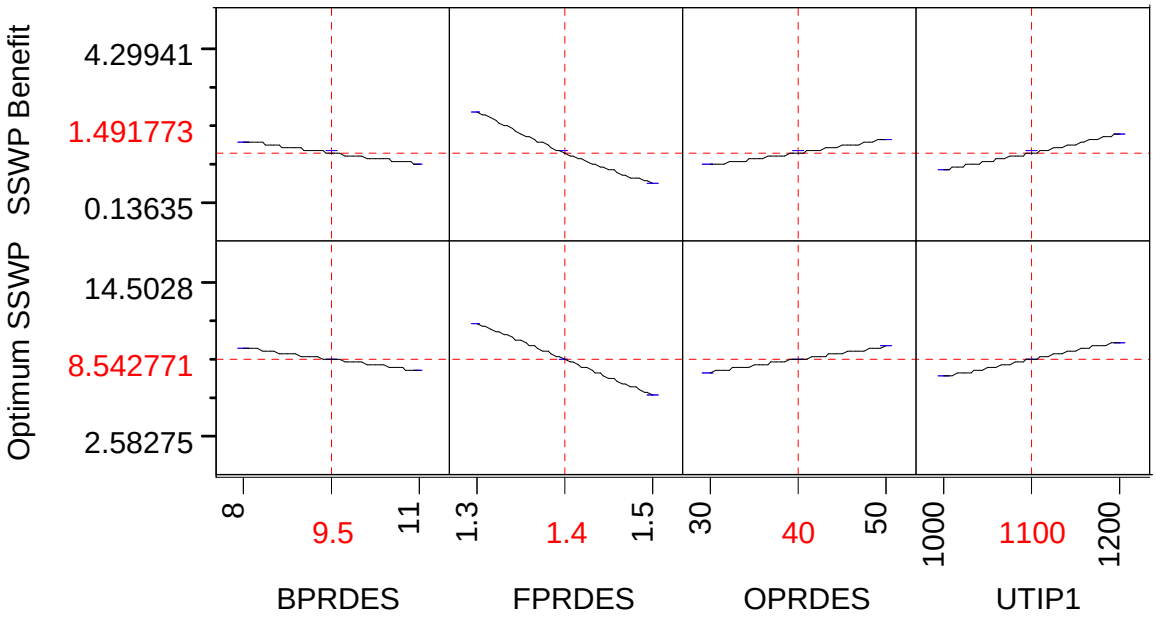

Figure 98: Benefits of stator sweep as a function of engine cycle design.

trend line toward lower noise levels. This means that the noise is lower for a given SFC, but also for a given target cumulative noise level the engine can be optimized to a lower cruise point SFC. For the optimum performance point, the cumulative noise level is reduced by approximately 1.8 EPNdB. If a swept stator fan efficiency penalty had been included in the engine cycle performance calculations, the line would also be shifted upward, but as long as the noise reduction were large enough the net result would still be a reduction in cumulative noise level for a given target SFC.

Table 26 shows how the SFC penalty required to achieve certain cumulative noise level targets can be reduced through the use of stator sweep. For example, if the engine were required to meet a target noise level of -25 EPNdB without swept stators, the cycle design would need to be adjusted significantly and would have a cruise SFC that is 4% higher than the performance-optimized cycle. With swept stators, however, the engine could be designed to the noise target with only a 1.4% SFC penalty.

7.3 Robust engine design

The analyses in the preceding sections all used deterministic values for the SFC, core NPR, fan diameter and cumulative noise levels, so the computed values for each of the metrics

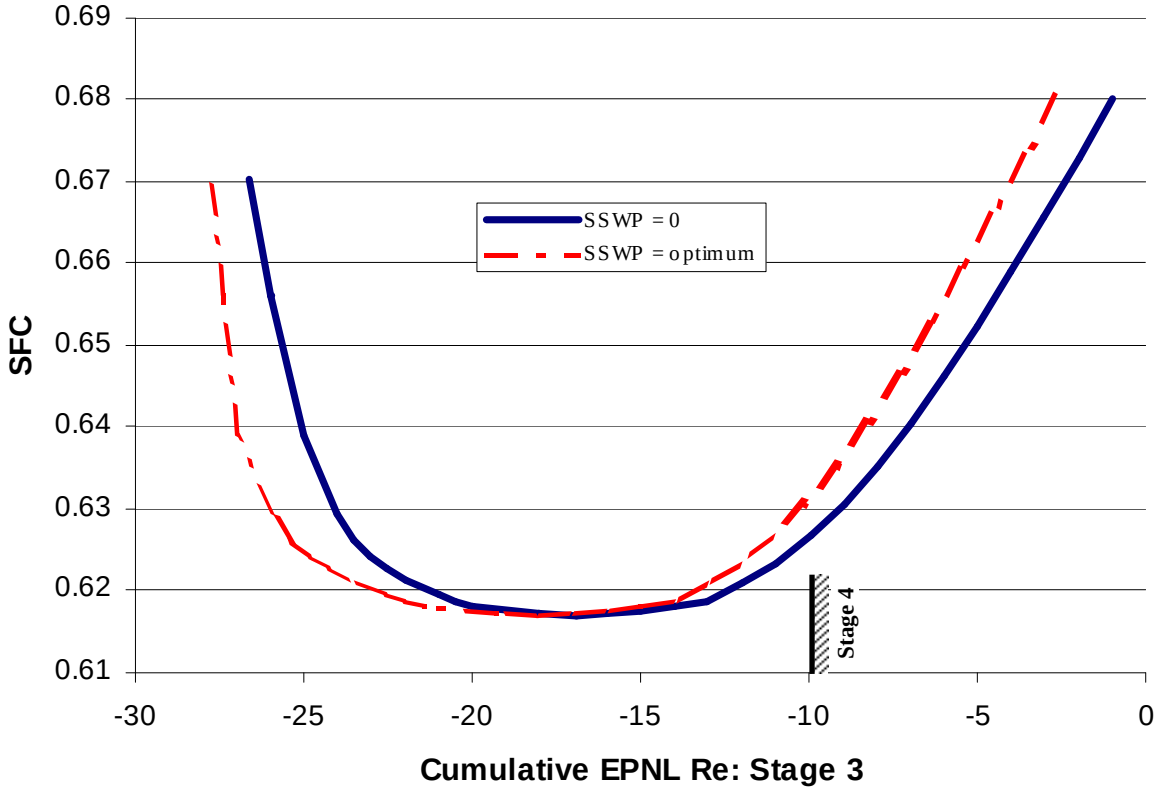

Figure 99: Minimum SFC vs. cumulative noise level with and without stator sweep.

Table 26: SFC penalty vs. cumulative noise level with and without swept stators.

Cumulative EPNL re: Stage 3	SSWP = 0	SSWP optimized
-16.9	1%	0%
-22.7	2%	0.44%
-24.0	3%	0.87%
-25.2	4%	1.4%

actually fall somewhere near the median in the distribution of possible values. As a result, there is only approximately a 50% chance that each metric will be as good as or better than predicted, and only a 50% chance that each constraint will not be violated, so the risk associated with failing to meet the prescribed design constraints or with failing to meet the promised performance and noise metrics could be much too large. It is desirable when designing the engine to allow for a margin of safety in each of the constraints to reduce the risk that the engine will fail to meet the constraints as predicted and force a costly redesign at a later stage in the design process. It also is desirable to allow for a margin of safety in the promised performance and noise levels to reduce the risk that design changes or costly corrections will need to be made to improve the performance or reduce the noise levels to the values that had been previously guaranteed.

7.3.1 Probabilistic RSEs, baseline airframe

Results of the analysis of uncertainty in the geometric, performance and noise metrics of the baseline engine and airframe were shown in Chapter 6. The probability distributions can be used to define "safety margins" for the different metrics, i.e. values which must be added to, or subtracted from, the deterministic values of the metrics to give an appropriate confidence level in the values. Without the ability to rapidly compute values of the metrics as functions of both design and uncertain variables, it might not be possible to conduct similar probabilistic analyses for a large number of engine cycles and airframes. If so, one would be forced to apply the baseline safety margins to any new design points while ignoring the real possibility that the margin of safety can change as a function of the engine cycle parameters, so either the true confidence level would not be as high as desired or the confidence level would be higher than desired and the penalties associated with meeting the confidence level would be unnecessarily high. Using RSEs, however, gives the designer the ability to rapidly compute values for the metrics which are functions of both design and uncertain variables, allowing the designer to perform the probabilistic analysis at a large number of different design points.

To extend the probabilistic analysis to all engine configurations in the design space, a

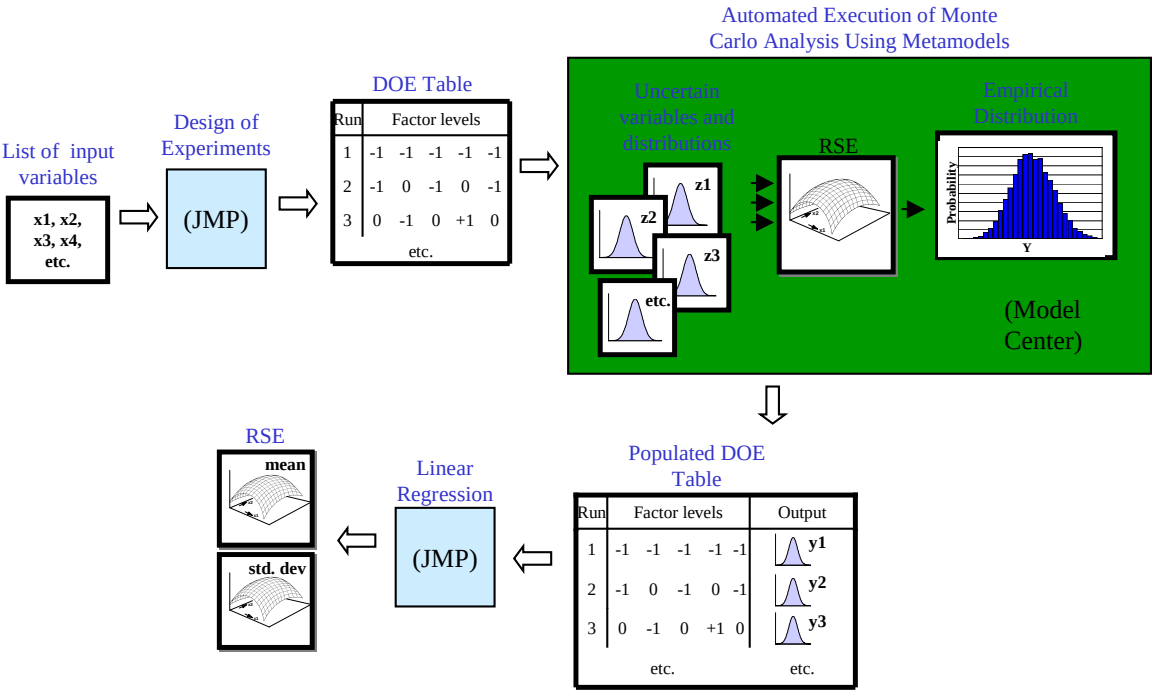

Figure 100: Process diagram for creation of probabilistic RSEs.

DOE study was performed in which the engine design variables were systematically varied, and for each design point a Monte Carlo analysis was performed in which all of the uncertain parameters were varied according to their defined distributions. This DOE study was similar to those conducted in Section 6.5, except in this case the responses were not deterministic values for the different metrics, but instead were probability distributions. Figure 100 shows a diagram illustrating the process of creating the new probabilistic RSEs; the portion of the process contained within the shaded box corresponds to the Monte Carlo analysis process from Figure 55 and was executed automatically within ModelCenter. For each design point the mean and standard deviation of the distribution were recorded, and used to calculate confidence margins on the metrics. For the cruise point SFC and the noise metrics, the 90% confidence values were calculated by approximating the empirical probability distributions as normal distributions and using the mean and standard deviation to determine the value:

$$X_{90\%} = \mu \pm 1.282\sigma \tag{59}$$

where $X_{90\%}$ is the level of the metric with 90% confidence, μ is the mean value of the empirical distribution for X, and σ is the standard deviation. The positive sign in Equation 59 is used for metrics for which smaller values are more desirable, and the negative sign is used for metrics for which larger values are desirable. The core NPR and fan diameter were approximated by triangular distributions, so the 90% confidence value was calculated as follows:

$$X_{90\%} = \mu - 1.487\sigma \tag{60}$$

for core NPR and

$$X_{90\%} = \mu + 2.6107\sigma \tag{61}$$

for fan diameter. Using the results of the new DOE studies, RSEs were created to give the mean, standard deviation and 90% confidence value as functions of the different engine design variables.

Figure 101 shows the parametric sensitivity plots for the engine performance and geometric metrics, and Figures 102 and 103 show the parametric sensitivity plots for the noise metrics. The mean values of SFC in Figure 101(a) are very similar to the deterministic values seen previously in Figure 90(a); this is to be expected, since as seen in the distribution for the baseline engine (Figure 95(a)) the probability distribution for SFC tends to be symmetrical. In contrast, the distributions for core NPR and fan diameter are not symmetrical, so the mean values for those metrics are higher and lower than their deterministic values, respectively. The 90% confidence values for core NPR are naturally lower than the mean values, and are higher for all other metrics; this reflects the margin of safety which must be included in the calculated metrics to increase the confidence that the values will be as good as, or better than, the values stated.

One important observation which can be made from Figures 101–103 is that by varying the design variables, not only is the mean value of each metric affected as seen previously, but the uncertainty in the values also changes. This means that it is possible to purposely choose values of design variables which reduce the uncertainty in the metrics and increase the confidence that the engine will satisfy the constraints and meet its performance and noise targets. For the most part, the 90% confidence values show the same sensitivities to

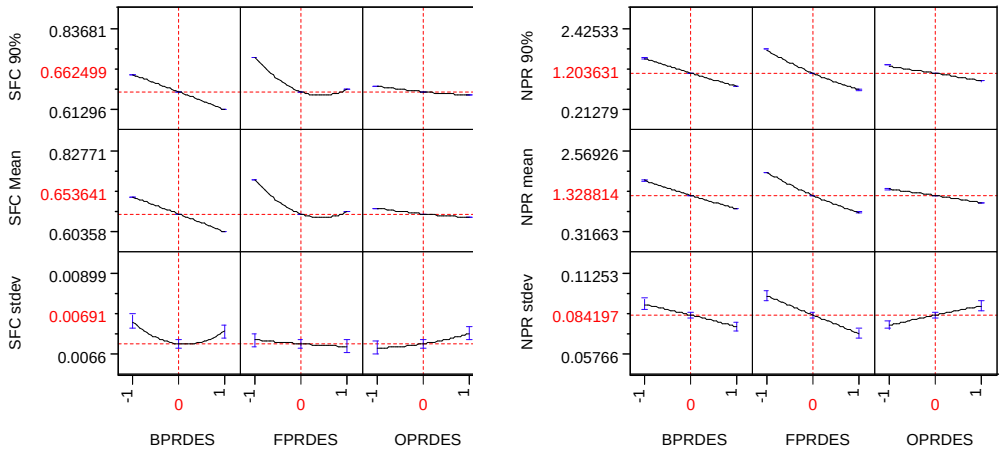

(a) SFC

(b) core NPR

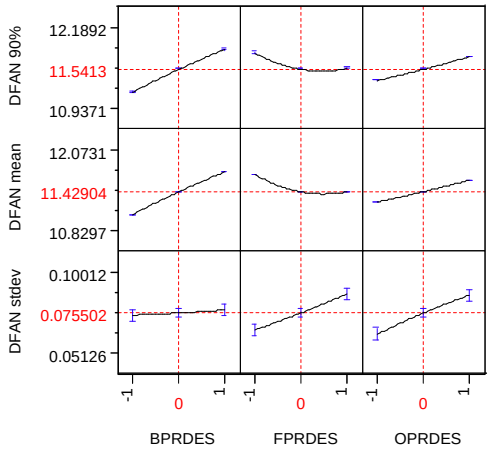

(c) fan diameter

Figure 101: Parametric sensitivity plots for mean, standard deviation and 90% confidence level of engine geometric and performance metrics.

the design variables as the mean values do, but there are subtle differences. For example, increasing the FPR serves to reduce the fan diameter, but also increases the standard deviation of the fan diameter, so that the 90% confidence value actually begins to increase slightly at the highest values of FPR.

A robust design cycle can be chosen which is a compromise between optimizing the mean values of the performance and noise levels and reducing the amount of uncertainty. These concepts will be explored in later sections, but first the probabilistic methods of this section will be extended to include all airframes in the design space.

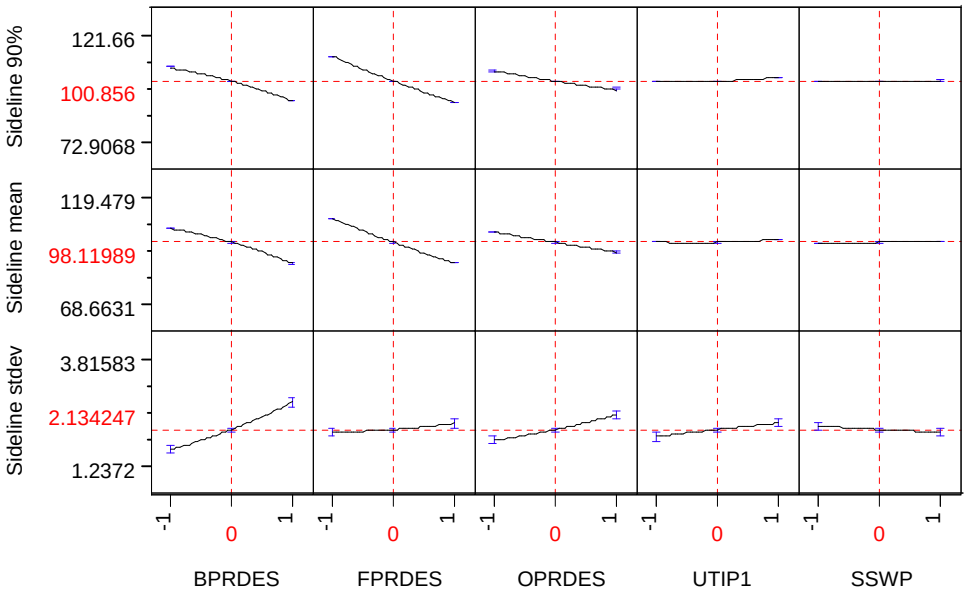

(a) sideline EPNL

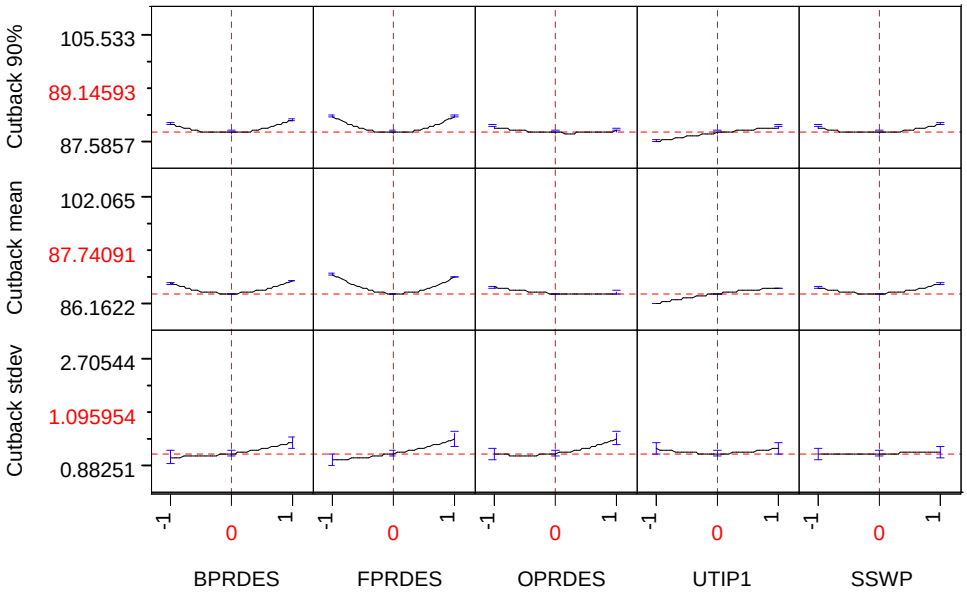

(b) cutback EPNL

Figure 102: Parametric sensitivity plots for mean, standard deviation and 90% confidence level of sideline and cutback EPNL, baseline airframe.

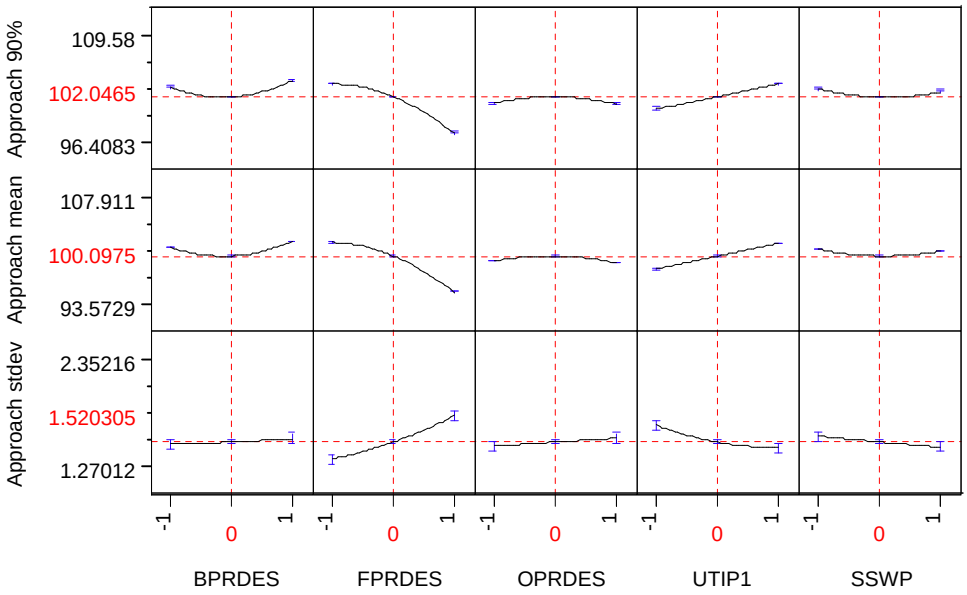

(a) approach EPNL

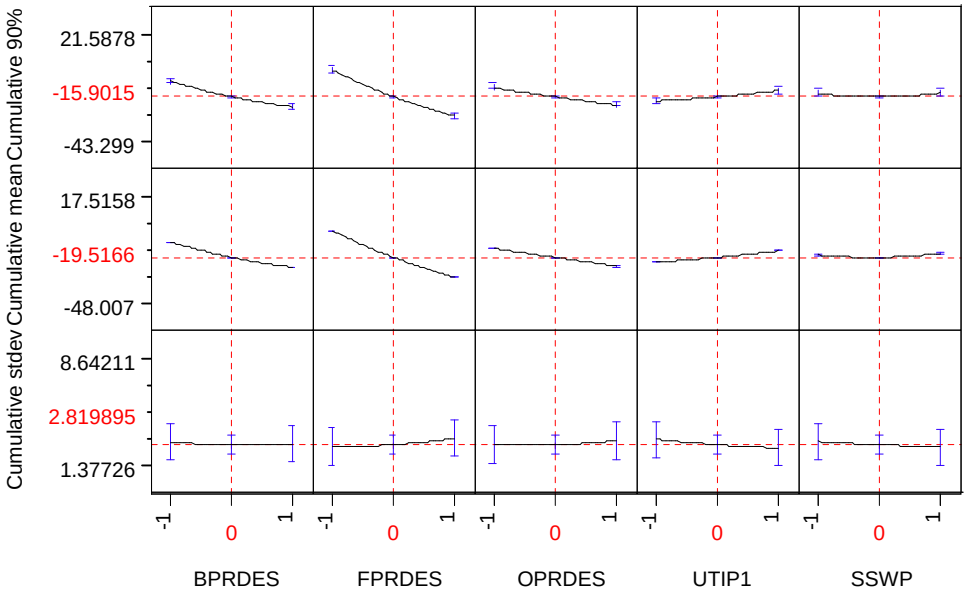

(b) cumulative EPNL, Re: Stage 3

Figure 103: Parametric sensitivity plots for mean, standard deviation and 90% confidence level of approach and cumulative EPNL, baseline airframe.

7.3.2 Probabilistic analysis for all airframes

Up to this point, all of the analyses shown, including the uncertainty analysis, were conducted for just the baseline airframe, which is the primary aircraft for which the engine would be expected to be used. There is an obvious economic benefit, however, to producing an engine design which can be used to efficiently and quietly power as large a number of different airframe designs as possible. If the engine is to be designed concurrently with an airframe for which it is meant to be compatible, assuring that the design is robust relative to changes in airframe design will allow for the design of the airframe to be modified without requiring large changes in the design of the engine. In addition, a robust engine design could effectively be used on a larger number of aircraft types, resulting in more of the engines being sold to a range of customers.

From the engine designer's perspective, the airframe design variables could be treated as uncertain variables because the engine designer has little actual control over their values. Representing the airframe variables as distributions of values, rather than deterministic values, allows the engine designer to examine how the engine will perform for a range of different airframe types, or under the influence of uncertainty in the final design choices or aerodynamic performance of a yet-to-be built airframe. To examine these concepts, further analyses were performed in which the airframe variables were treated as uncertain variables and given probability distributions. Uniform distributions were used for these variables to represent the idea that these their values are known for a given aircraft, but would vary over a range of values when dealing with a number of different airframe designs.

When the airframe design variables and aerodynamic coefficients are varied within their assumed ranges, the resulting aircraft size and performance metrics can vary dramatically, and metrics such as takeoff field length can take on values which would be considered unreasonably large. It is not in the interest of the designer to assess the noise levels on an aircraft which would not be able to meet certain realistic performance constraints. To overcome this issue, a logical check was used to examine the airframe performance metrics and reject the combinations of variables which resulted in invalid airframes, i.e. those that exceeded reasonable values for takeoff and landing field lengths or approach velocity.

To assess how variations in the airframe variables affect the aircraft performance metrics and noise levels, a probabilistic analysis was conducted for the baseline engine to determine the distribution of noise levels which can be expected over the design space of possible airframes which the engine might be used to power. The aircraft were constrained to those with takeoff and landing field lengths of less than 12,000 ft and an approach velocity of less than 150 kt. Figure 104 shows the empirical frequency distributions for the airframe performance metrics with and without rejection of the invalid airframe designs. The shaded area in each plot shows the portion of the distribution which was eliminated when the airframe performance constraints were enforced, and the solid line plots the proportion of designs which were rejected from each of the bins. For all three metrics the proportion of designs rejected increases as the metric increases. The vast majority of rejected airframes were eliminated because their takeoff field length was unacceptable, although a handful of the airframes were eliminated because they violated the approach velocity constraint alone. Not surprisingly, there is a clear correlation between the three metrics, as most of the designs rejected for violating the takeoff field length constraint also lie in the upper range of landing field length and approach velocity, and most of the designs rejected for violating the approach velocity constraint also lie in the upper range of takeoff field length and landing field length.

Figure 105 shows the empirical frequency distributions for the baseline engine noise metrics over all airframes, again with and without rejection of the invalid airframe designs. Since the sideline EPNL is largely unaffected by airframe variables, the rejection rate of designs is fairly uniform over the range of sideline noise levels. However, the rejected designs do tend to have the highest cutback noise levels since the rejected designs would tend to be the ones with the poorest climb performance. The rejection rate also appears to increase for higher approach EPNL, although the correlation is not as strong because approach noise is not a strong function of the airframe variables.

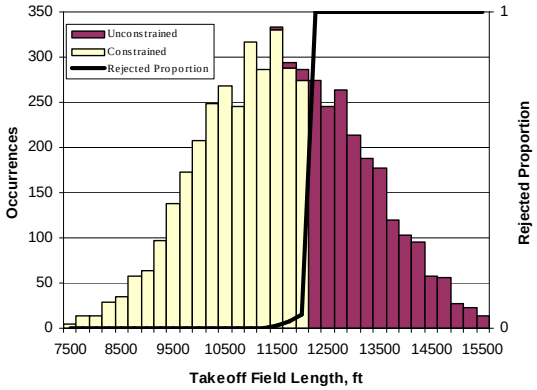

(a) takeoff field length

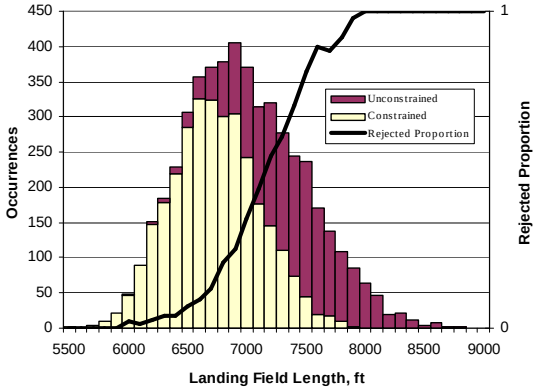

(b) landing field length

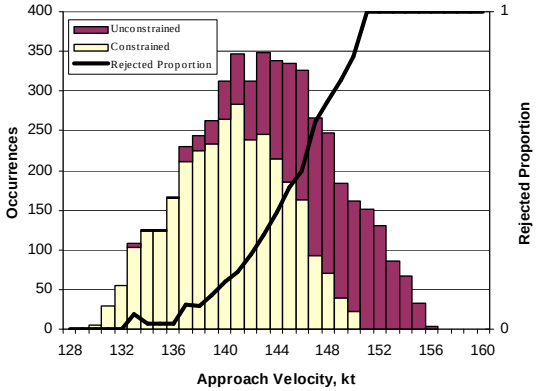

(c) approach velocity

Figure 104: Empirical frequency distributions for airframe performance metrics using 5000 Monte Carlo simulations.

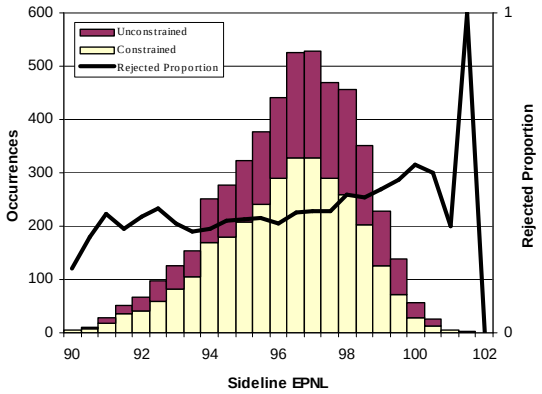

(a) sideline EPNL

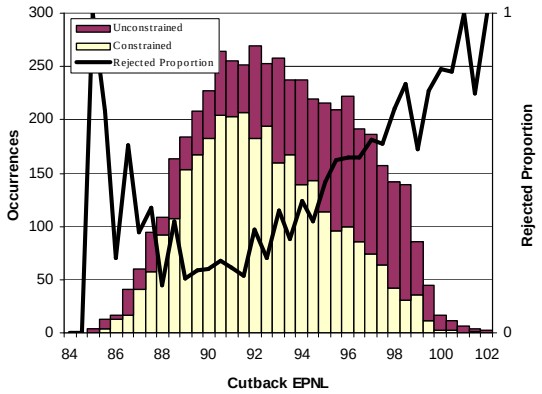

(b) cutback EPNL

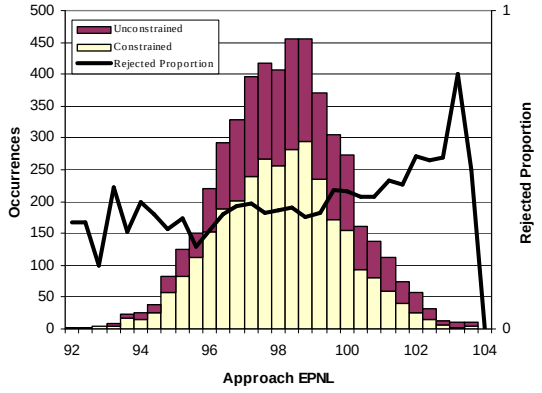

(c) approach EPNL

Figure 105: Empirical frequency distributions for baseline engine sideline, cutback and approach EPNLs for all airframes using 5000 Monte Carlo simulations.

7.3.3 Probabilistic RSEs, all airframes

A final DOE study was conducted to assess the effect of the engine design variables on the probability distributions of the different metrics; similarly to the DOE study in Section 7.3.1, a Monte Carlo analysis was performed at each design point to arrive at probability distributions for each of the metrics, except in this study the airframe variables were also varied uniformly within their assumed ranges. As discussed in the previous section, combinations of airframe variables which failed to meet reasonable performance metrics were rejected. Additional RSEs for the cruise SFC, core NPR and fan diameter were not required since these metrics are not a function of the airframe variables.

The parametric sensitivity plots for the new noise RSEs are shown in Figures 106 and 107. Since the sideline and approach noise are not strongly affected by the airframe variables, the sensitivity plots for sideline and approach EPNL for all airframes are very similar to the corresponding plots for just the baseline airframe. The cutback EPNL, however, is a stronger function of the airframe variables $C_{L,max}$ and thrust-to-weight ratio, so the standard deviations for cutback EPNL are higher for all airframes than for just the baseline.

7.3.4 SFC vs. noise with confidence

The new probabilistic RSEs were used to revisit the SFC vs. cumulative noise level trade study of Section 7.1, except that instead of deterministic values for the SFC, noise levels and constraints, the results of the probabilistic analyses were used to find the values with 90% confidence. In the first case, the means and standard deviations of the metrics for the baseline engine and airframe were used to define margins of safety for the metrics, i.e. a set of values which must be added to, or subtracted from, the metrics to give 90% confidence in their predicted values; these margins of safety were assumed constant for all engine cycles to illustrate a situation in which computational constraints limit the ability to perform probabilistic analyses for more configurations than just the baseline. In the second case, the new trend line was traced using the RSEs for the 90% confidence levels of the different metrics for the baseline airframe. The third case used the RSEs for the 90% confidence levels of the different metrics for *all* valid airframes in the design space. In each

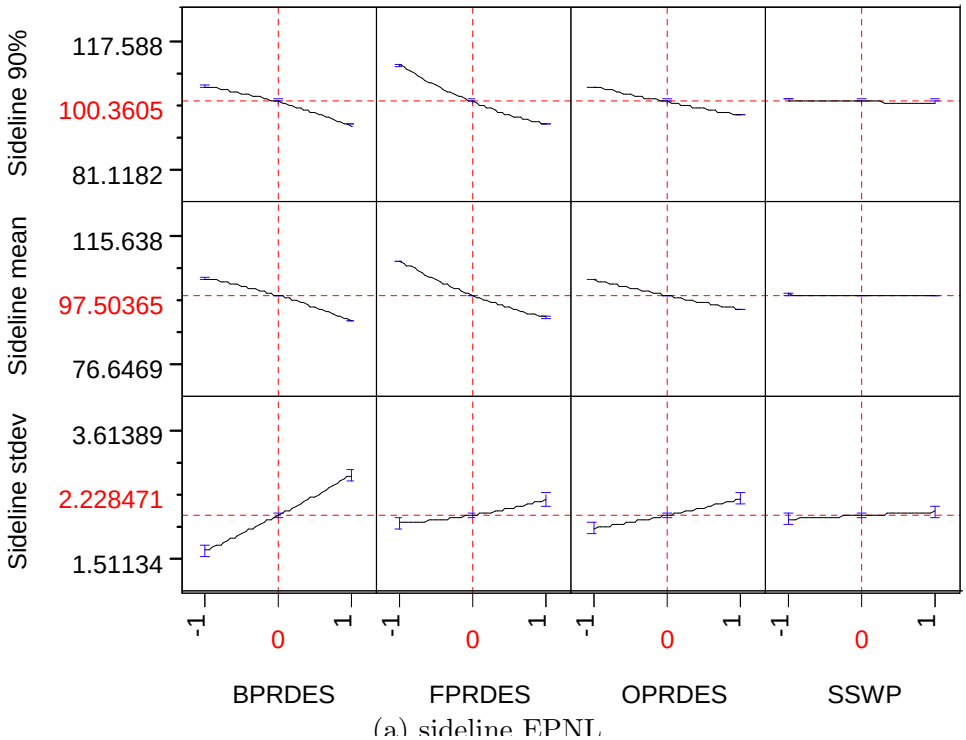

(a) sideline EPNL

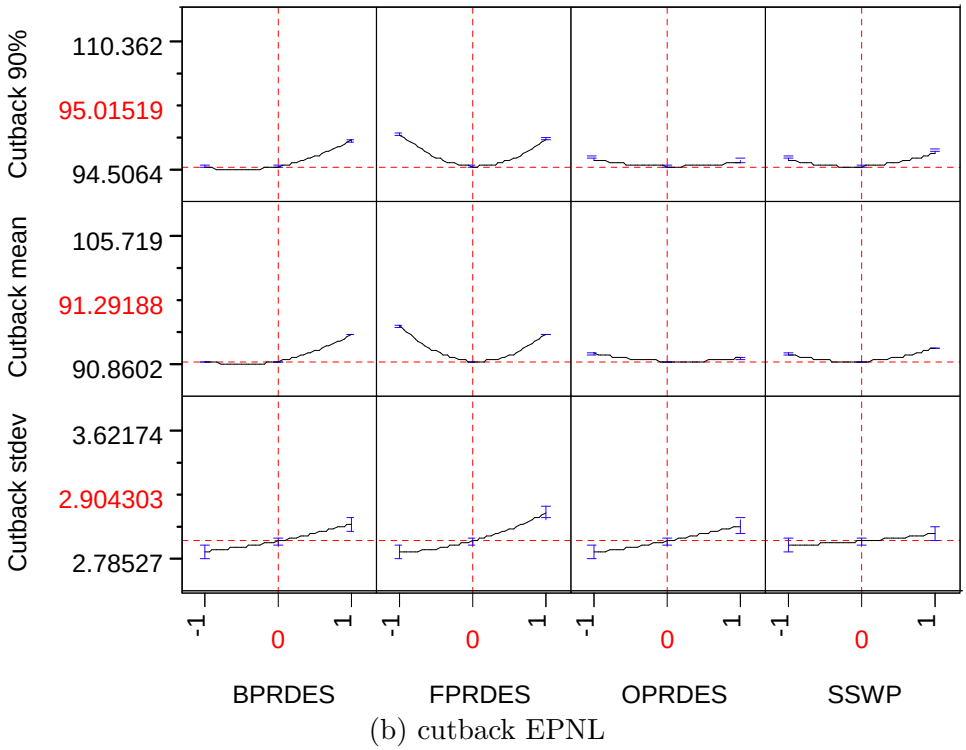

(b) cutback EPNL

Figure 106: Parametric sensitivity plots for mean, standard deviation and 90% confidence level of sideline and cutback EPNL, all airframes.

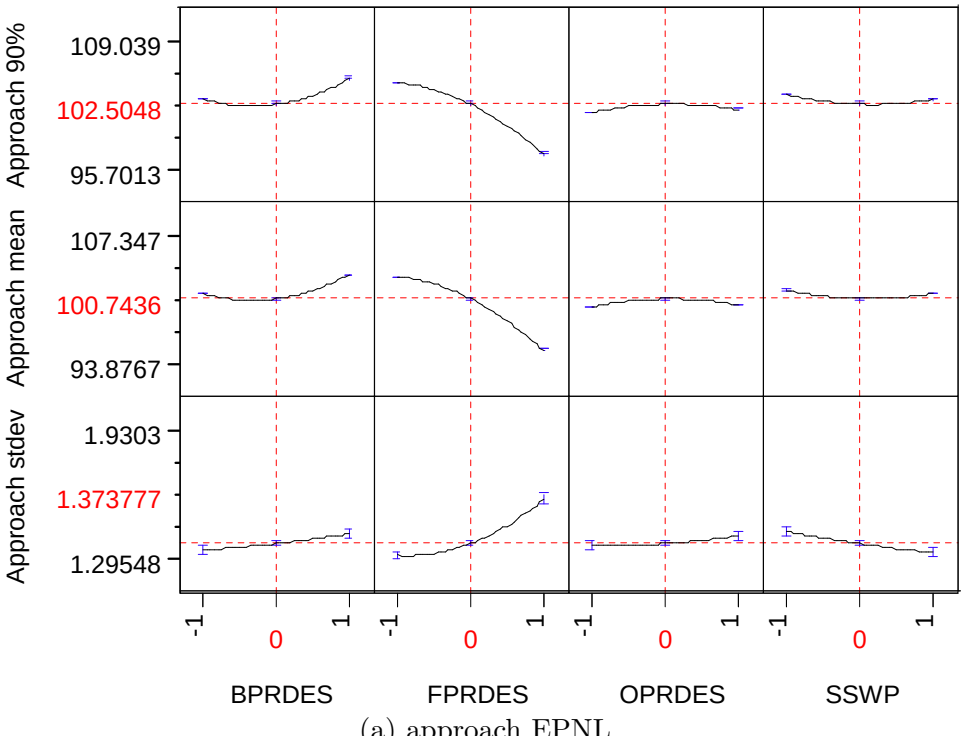

(a) approach EPNL

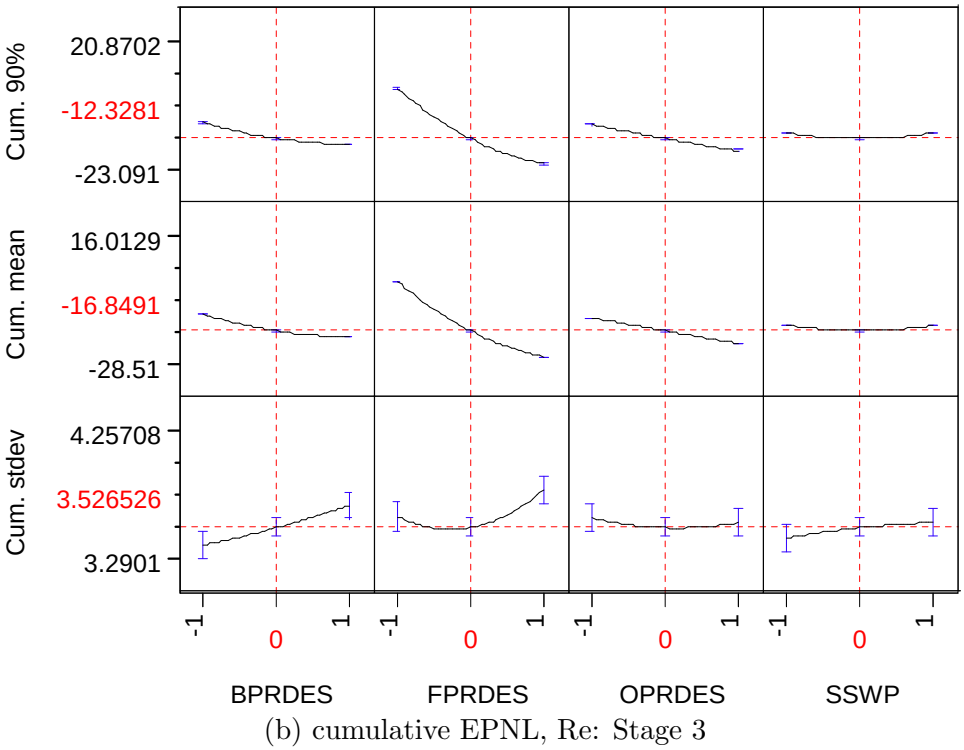

(b) cumulative EPNL, Re: Stage 3

Figure 107: Parametric sensitivity plots for mean, standard deviation and 90% confidence level of approach and cumulative EPNL, all airframes.

case, the trend line was traced by minimizing the 90% confidence value of SFC for each 90% confidence value of cumulative noise, with the requirement that the core NPR and fan diameter constraints be met with 90% confidence.

The results of the probabilistic SFC vs. cumulative noise trade study are shown in Figure 108. Figure 108(a) plots the 90% confidence values of SFC and cumulative noise margin, while Figure 108(b) shows the corresponding deterministic values. The first line in each plot shows the previous results of the deterministic trade study of Section 7.1, while the second and subsequent lines show the results of the new probabilistic trade studies under the three scenarios: using a constant margin of safety applied to the SFC, cumulative noise levels, fan diameter and core NPR; using the 90% confidence values for the metrics calculated by the RSEs for the baseline airframe; and using the 90% confidence values from the RSEs for all airframes. For the deterministic trend line, the 90% confidence values of SFC and cumulative noise level in Figure 108(a) were calculated using the new RSEs for the baseline airframe.

For each of the probabilistic trade studies the trend line is shifted significantly by the added requirement that the constraints be met with 90% confidence, instead of the approximately 50% confidence that they were met using the deterministic values. In order to increase the confidence that the constraints will be met, the engine must be designed with a lower BPR and a lower OPR, resulting in an SFC penalty . The cumulative noise level is not adversely affected by the increase in confidence, except that the noise will always be higher for a given target value of SFC.

There is a significant difference in the results when using constant margins of safety, as compared to using the RSEs to calculate the variation of standard deviation for each metric over the whole design space. Assuming a constant margin of safety can result in an inaccurate assessment of the confidence levels of the constraints and performance and noise targets, as Table 27 shows. The confidence levels for SFC and the fan diameter are higher than intended, and as a result the engine has been optimized with an SFC value 0.4% higher than was necessary to achieve the desired 90% confidence levels for the constraints. Even worse, the confidence levels for the core NPR and cumulative noise are lower than intended,

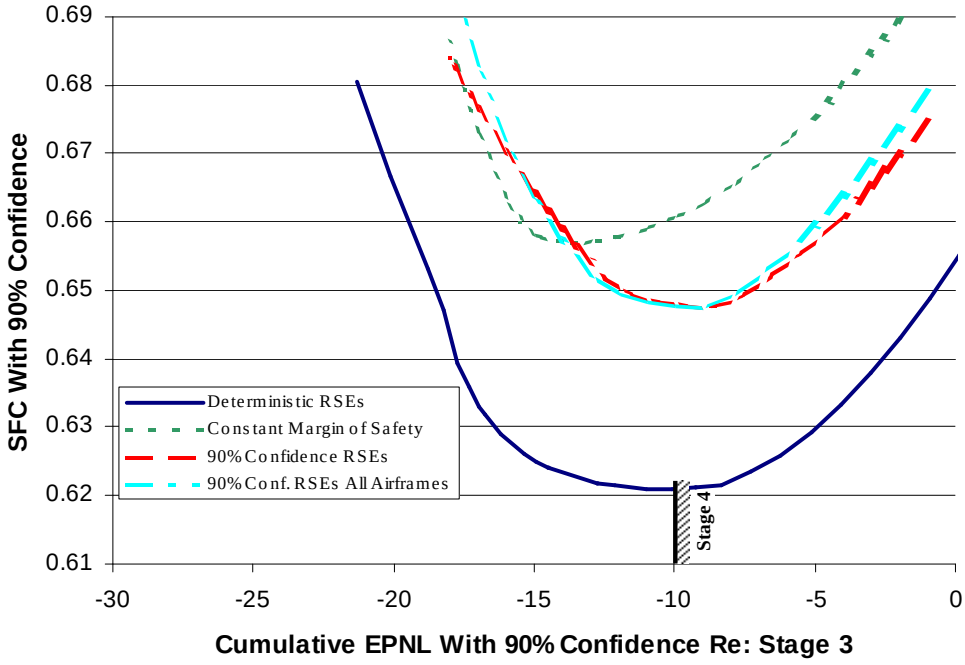

(a) 90% confidence values

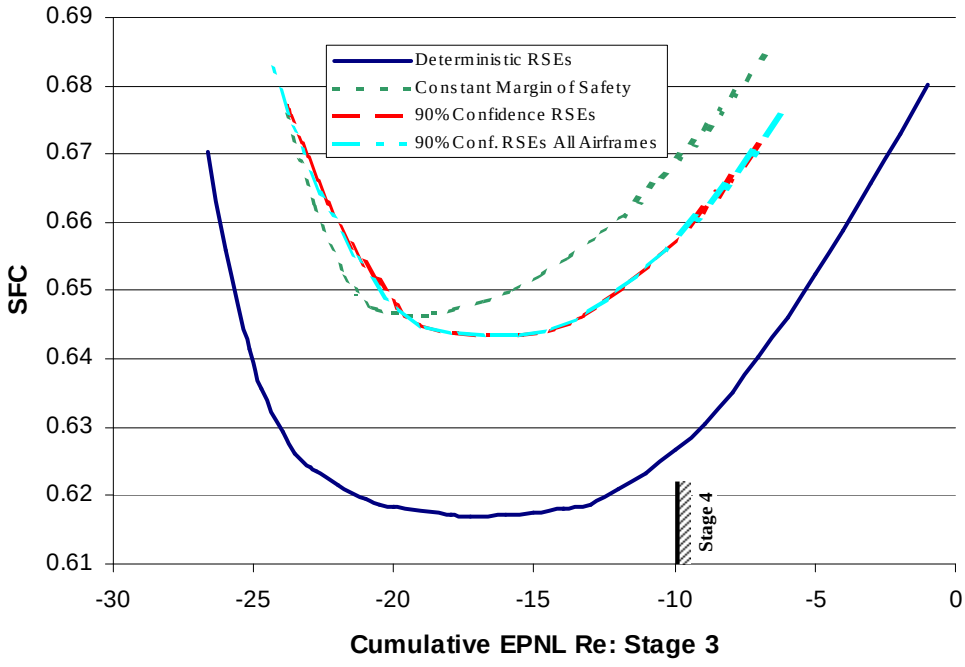

(b) deterministic values

Figure 108: Minimum SFC vs. cumulative noise level.

Table 27: Confidence levels for two methods of designing with confidence.

Metric	Constant margin of safety	90% confidence RSEs
Minimum SFC	0.6464	0.6439
SFC confidence	96.4%	90.0%
Core NPR confidence	89.5%	90.0%
Fan diameter conf.	100%	90.0%
Cumulative EPNL conf.	85.1%	90.0%

so the optimized design actually has higher risk than intended, with the added danger that the designer may not realize that the risk has been under-predicted.

On the other hand, there is almost no difference between the results for the baseline airframe and the results over all airframes. The 90% confidence value of the cumulative noise level for all airframes is higher than the corresponding value for just the baseline airframe, but the relationship between the engine design variables and the standard deviation of the cumulative noise follows the same pattern in each case. It is not necessary in this case to make modifications to the design of the engine to improve the robustness with respect to the type of airframe on which it is installed; it would appear that it is sufficient to use the baseline airframe as a platform for the optimization of the engine cycle. If the analysis process were to include an analysis of the full aircraft mission then it would be possible to use a more airframe-specific efficiency metric such as mission fuel, gross weight or direct operating cost, in which case a similar variation in airframes might actually prove to have an impact on the choice of the most robust engine.

Table 28 shows the new minimum-SFC design point as compared to the previous deterministic point. Note that the optimized point has the lowest 90% confidence SFC along the Pareto set, but it does not actually have the lowest deterministic SFC because the standard deviation of SFC varies with engine cycle. This is apparent when comparing the 90% confidence lines in Figure 108(a) with the corresponding lines in Figure 108(b), particularly in the bucket region surrounding the minimum-SFC point. If one starts at the performance optimum for the 90% confidence case in Figure 108(a) and traces the Pareto front to the left toward a lower noise level, the 90%-confidence value of SFC increases noticeably while

Table 28: Minimum SFC design points for differing confidence levels.

Metric	Deterministic	Baseline airf. 90% conf.
BPR	11.06	10.55
FPR	1.418	1.419
OPR	31.53	26.11
Predicted SFC	0.617	0.643
Predicted ΔEPNL	-15.1	-14.4
Predicted NPR	1.10	1.28
Predicted D_{fan}	11.50	11.34
90% conf. SFC	0.621	0.648
90% conf. ΔEPNL	-11.9	-8.9
90% conf. NPR	0.90	1.10
90% conf. D_{fan}	11.69	11.50

the deterministic value of SFC is nearly unchanged for the first few EPNdB of noise reduction. Therefore, even though the predicted SFC does not increase appreciably as the cumulative noise level is reduced, the engine becomes less robust as the risk of failing to meet a particular efficiency target increases.

CHAPTER VIII

CONCLUSIONS AND RECOMMENDATIONS

The use of physics-based analysis tools earlier in the design process, instead of the traditional empirical methods, can improve the process by making the analysis applicable to newer, revolutionary designs and by offering the ability to directly assess the benefits of new technologies. Because physics-based analysis methods require much longer execution times than empirical methods, they cannot be used directly to perform the rapid tradeoff and risk analysis studies needed at the conceptual design stage, so it was necessary to find additional techniques to enable their use.

In this research program, an approach was developed which allows for rapid conceptual-level tradeoff and risk analysis studies of commercial aircraft using physics-based noise analysis methods. The two key elements of the new design approach are (1) global approximation techniques and (2) probabilistic simulation methods. The approximation techniques are used to create metamodels that provide approximately the same functional relationships between the input variables and output metrics as the physics-based analysis method, but can be executed much more rapidly. The use of *global* approximation techniques, in particular, is valuable because the resulting metamodels can be used for all subsequent trade studies without the need to return to the full analysis process for more time-consuming analysis. Also, using the probabilistic simulation methods in combination with the previously-created metamodels is much more efficient than using probabilistic methods which access the analysis process directly.

In this study, response surface methodology was used to create metamodels consisting of polynomial response surface equations, although other global approximation techniques such as neural networks or Kriging could also be used in a similar manner. To create the response surface equations, Design of Experiments was used to specify the design variable values at a selection of points distributed through the feasible design space, and to determine the

values of the coefficients in the RSEs through linear regression. Monte Carlo analysis was used for probabilistic analysis, but other simulation methods such as importance sampling would also be suited to the approach.

A prototype integrated analysis process was created for computing the relationship between the engine and aircraft design and uncertain variables to the total aircraft EPNL at the FAR 36 certification measurement locations using several physics-based analysis methods. To account for the effects of the system-level variables on the noise, it was necessary to include methods for engine cycle design and analysis, engine cross-sectional geometry layout, fan blade preliminary design, aircraft takeoff and landing flight performance, and noise analysis in the integrated process. Rather than develop methods for each of these components, existing computer programs were used wherever possible. The physics-based portions of the noise analysis were validated using scale-model experimental results. The new analysis process was used to assess the performance and noise of the baseline aircraft, a 300-passenger, twin-engine commercial transport aircraft powered by two high-bypass ratio turbofan engines.

The analysis process was then used in combination with Design of Experiments to create response surface equations (RSEs) for the engine and aircraft performance metrics, geometric constraints and takeoff and landing noise levels. In addition, Monte Carlo analysis was used to assess the expected variability of the metrics under the influence of uncertainty, and to determine how the variability is affected by the choice of engine cycle.

Finally, the RSEs were used to conduct a series of proof-of-concept design studies: an examination of the compromises in engine cycle design that are needed to achieve lower noise levels, including a quantification of the resulting performance penalty; an assessment of the noise benefits of swept fan stators as a function of the engine cycle to which they are applied and calculation of the optimum sweep angle for any engine design point; a robust design study examining how the engine performance-versus-noise tradeoffs change when uncertainties in engine component efficiencies, operating environment and modelling errors are taken into account; and a final robust design study examining whether the engine cycle design point can be shifted to make the engine more robust relative to the type of aircraft

it is used to power.

8.1 Conclusions

The greatest difficulty in implementing FPA methods in a conceptual design process proved to be in the generation of a geometric definition of the engine components at sufficient detail to perform the computational aerodynamic analyses needed for calculation of the fan tone noise and jet mixing noise levels. During conceptual design, engine cycle performance is usually calculated with one-dimensional analysis methods which require very little knowledge of the actual geometry of the engine components, so additional methods had to be added to the analysis process for the purpose of developing the geometric definition at the required level of detail. Much of the development of the analysis process was focused on implementing a preliminary design method for the rotor blade geometry. In addition, much of the computational time required to calculate the noise levels of a given engine and airframe combination was devoted to the generation of the detailed geometry and not to the actual calculation of the noise itself.

To integrate the large number of analysis methods used in this process, the use of wrappers was vital. Since the complex computational analyses, particularly the computed fan rotor and jet plume flow fields, required large amounts of geometric and aerodynamic data to be passed from one analysis to the next, it also was important that the design data be organized in a coherent and non-contradictory manner. By assuring that the analysis process could execute without intervention by the designer for such tasks as data conversion, grid generation and adjusting of model input parameters, it was possible to execute larger numbers of analyses while reducing the chances of human error inherent in those tasks.

Even with physics-based analysis methods for only two of the noise sources—the fan rotor-stator interaction tones and jet mixing noise, both of which are models based on simplified physics and geometrical representations—the analysis process developed in this study requires approximately 30 hours to execute on an SGI Origin 2000 computer. To use a process such as this one, or an even more complex and computationally-intensive process, in earlier stages of the design process when larger numbers of functional evaluations are

required to explore the design space, it is necessary to resort to approximation methods.

With the ability of approximation methods to perform extremely rapid evaluations of the design metrics, it is possible to glean much more information out of design trade studies. Instead of running an optimizer and finding a few select points which define the tradeoff between SFC and cumulative noise level, it was possible to plot the trend line for the entire design space, for several different constraint scenarios. It was even possible to plot the complete trend line for probabilistic values of SFC, cumulative noise, fan diameter and core NPR. Being able to visualize results for the entire design space, rather than for a select number of optimized points, can greatly assist the designer in understanding the tradeoffs involved. Since the RSEs represent a global model of the design space, they can also be reused as much as needed without needing to return to the analysis process for additional time-consuming runs.

The use of an FPA process, combined with a method such as RSM which defines clear relationships between the design variables and the output metrics, is a powerful tool for assessing the benefits of technologies which cannot otherwise by accounted for using empirical methods. RSEs were used in this study to not only directly calculate the benefits of fan stator sweep to the cumulative noise level, but to examine how those benefits change for different engine cycles. Furthermore, the ability to rapidly evaluate the technology benefits allows the designer to optimize the engine and technology parameters simultaneously to achieve the most effective application of the new technology.

Theoretically, the use of high-fidelity, first-principles analysis methods should have the benefit of improving the accuracy of the analysis relative to empirical methods, particularly when analyzing configurations which are outside of the empirical database. When analyzing configurations which are not too different than those used to form the empirical database, however, the use of FPA in the manner outlined in this study may not actually produce a more accurate analysis, because its use necessitates the application of approximation methods which naturally degrade the accuracy of the results. In this study the accuracy of the noise metamodels suffered from the necessity of severely limiting the number of analysis runs which could be performed, as well as the lack of orthogonality of the DOEs due to

restrictions in the design space. Even if all of the accuracy gains were completely offset by the use of approximation methods, however, FPA would still retain a significant advantage due to the ability to directly assess the effects of design variables and technologies which are not part of the empirical method, rather than relying on experimental or computational results for a limited range of engine cycles and operating conditions.

Finally, the use of metamodels in combination with a simulation-based probabilistic analysis method proved to be very valuable in performing technical risk analysis throughout the entire design space. The analyses in this study demonstrated that the robust design of an aircraft engine is a more complex problem than simply adding a margin of safety to the computed metrics to reduce the risk. This approach was shown to result in a different choice of design point than a more rigorous analysis which accounts for the effects of engine cycle on the variability of the metrics. Choosing the design cycle based on the simpler margin of safety approach can result in a cycle that has been over-designed relative to certain design requirements and under-designed relative to others. Additional risk analysis at the new design point would likely reveal that the risk levels were higher or lower than expected, requiring additional optimization studies with the new estimates for the required margins of safety. As before, this approach lacks the benefit of being able to visualize the trend lines throughout the entire design space.

In Chapter 1, a set of research questions was asked, and three hypothesis were proposed. These hypotheses will now be reexamined, and conclusions will be drawn from the research in support of, or in opposition to, the hypotheses:

Hypothesis 1: It is possible to use first-principles noise analysis at the conceptual design stage to predict the noise levels of an aircraft concept while still retaining the ability to evaluate a large design space.

Due to lack of available noise analysis methods for some sources, and a lack of resources for creating the type of comprehensive analysis process a design organization might use, the prototype noise analysis process used in this research was not created with physics-based methods for every component. Nevertheless, including the two physics-based methods

resulted in an analysis process which required approximately a day to execute, making it impossible to use with gradient-based optimizers or evolutionary algorithms no matter how well automated. Through the use of approximation methods and probabilistic methods, however, it was demonstrated in this research that the analysis process could be used in the same manner as faster empirical methods have been.

It should not be overlooked, however, that in order to use the physics-based analysis process in conceptual design studies, it was first necessary to conduct a series of analyses in support of the variable screening studies and then for development of the RSEs eventually used in the trade studies. This meant that the use of the higher-fidelity analysis was not without cost; several months were required for execution of these runs, during which trade studies were put on hold until the metamodels were available for use. If empirical methods had been used instead, multiple studies could have been performed during this time, so the use of the physics-based methods reduced the volume of the trade studies which could be performed. Offsetting this fact, however, is the fact that the higher-fidelity methods represent the type of analysis which might normally be performed during preliminary design, so the argument can be made that these analyses might have been performed anyway and were merely shifted to an earlier stage in the design process. Since these analyses were performed at a time when the design freedom was much greater than it would be at the beginning of preliminary design, the net result is that the acquisition of design knowledge was likely accelerated without severely impacting the design cycle time.

Traditionally there is a point in the design cycle where conceptual design studies are complete and the preferred vehicle concept is "thrown over the wall" to one or more other organizations to begin preliminary design studies. Since the geometric representation of a design is usually very simple even by the end of the conceptual phase, the interface to the preliminary design phase necessarily involves significant work to increase the complexity of the geometry definition prior to employing the preliminary-level analysis methods. The use of higher-fidelity analysis methods earlier in the design, however, serves to encourage a more detailed definition of the geometry from the earliest stages of concept definition and should serve to smooth the transition to the discipline experts at the next stages of the

process.

Hypothesis 2: It is possible to quantify the effect of uncertainty in analysis, manufacture, and operation of an aircraft on the variation of the certification noise levels.

As seen in the literature search, the use of probabilistic analysis methods to quantify uncertainty in a design is not a new concept. One of the contributions of this study was to demonstrate techniques for using probabilistic analysis which incorporates the advantages of physics-based analysis.

Although the technique was not used for this research, probabilistic analysis could also be used to quantify the benefits of using physics-based analysis by accounting for the reduction in the modelling error which can be achieved by improving the fidelity of the analysis. For the design space examined here, the prototype analysis process was not more accurate, especially when taking into account the shortcomings of the high-fidelity analysis methods used. One would not necessarily expect the physics-based analysis to be more accurate for conventional engine and aircraft configurations, but for revolutionary configurations the accuracy could be greatly improved relative to empirical methods, and probabilistic analysis could quantify the reduction in the variance of the predicted noise levels and show how the performance penalties are reduced.

Hypothesis 3: It is possible—through reduction in absolute noise levels, variance due to uncertainty, or both—to develop a strategy for multidisciplinary optimization of a conceptual aircraft to reduce the risk of exceeding a set of targeted noise levels.

The use of probabilistic simulation methods in conjunction with metamodels allowed for not only an estimation of the uncertainty in the performance, geometric and noise metrics of the baseline engine and aircraft, or of the optimized design, but of any design in the design space. Through the creation of metamodels which relate both the mean and standard deviation of the metrics to the values of the design variables, it was demonstrated that it is possible to conduct robust trade studies in the same manner as deterministic ones. It was shown that the most robust engine cycle design is not necessarily the one for which the

mean value of a metric such as SFC or cumulative noise level has been minimized, but may involve minimizing a combination of both the mean and standard deviations of the metric. It also was shown that it can be important to account for the effects of the cycle design on the uncertainty, rather than assuming that the required safety margins are invariant throughout the design space.

8.2 Recommendations

The RSEs that were developed suffered in accuracy due to the non-orthogonality of the design space resulting from the removal of large infeasible regions. It would be beneficial in future work to explore methods of improving the accuracy of the approximation methods under such conditions. One simple method would be to use relative, rather than absolute, ranges for several of the engine design variables, and defining a reference value which is a function of other design variables. For example, as seen in Section 6.3.4 the combination of high BPR, high OPR and low FPR results in an infeasible design because the required fan power exceeds the available power from the core; as a countermeasure, the fan pressure ratio could be expressed in the following form:

$$FPR = f(BPR, OPR) + \Delta FPR \tag{62}$$

where $f(BPR, OPR)$ is a function which decreases with BPR and OPR. The actual variable used in the RSE would be the ΔFPR, the relative FPR; the absolute FPRs would be higher when the BPR and OPR are at their minimums, and lower when the BPR and OPR are at their maximums.

The use of neural networks as an alternate to RSM could also improve the accuracy of the approximations. As stated previously, RSM was used in this study because of its ready availability for use in the ModelCenter® software and because of its ease of use and the large body of previous work using it engineering design applications. Using NN to perform the trade studies and to create the model approximations within the ModelCenter® would require a certain amount of programming effort to implement, but could serve as a useful alternative global approximation method when RSEs prove unable to provide an accurate metamodel.

The analyses of Chapter 7 demonstrated the utility of using metamodels in the conceptual design process in place of computationally intensive analysis methods. Although this study was focused on the prediction of noise levels for conceptual engine and aircraft designs, the same concepts can be applied to a full range of design problems in many disciplines. The advantage of these techniques is clear for high-fidelity analysis methods that take hours or days to run, but the combination of metamodelling combined with risk analysis is useful even when the analysis method is fairly fast, since a robust design optimization process based on finding the optimum design at a given confidence level will inevitably require tens of thousands of runs. For an analysis method that takes just 30 seconds to complete, this would require a week or more to run the optimization, whereas the use of spreadsheet-based RSEs could cut the optimization time to a matter of hours.

Finally, the integrated analysis process used in this research represents just a starting point in the type of integrated design methodology which could be assembled. The low-speed aerodynamic polars for the aircraft could be computed using an aerodynamic analysis method rather than being used as input. The detailed fan blade geometric definition could be used with Swift to compute fan performance maps to be fed back into the engine cycle analysis for refinement of the design. The modularity of the methodology is a key advantage to simplifying the amount of effort required to implement additional methods.

APPENDIX A

NOISE METRICS

For those unfamiliar with the many different methods for expressing the relative loudness or annoyance of a sound source, this appendix provides a more detailed description of the metrics which are specifically relevant to this thesis.

A.1 Sound pressure level

Sound-pressure amplitude or RMS pressure can be measured directly and expressed in pascals (Pa) or any other unit of pressure. Sound pressures of interest occur over a very wide range—the threshold of hearing occurs at approximately 20 μPa while the threshold of pain is approximately 20 Pa[109]—so it is more useful to use a logarithmic scale when reporting sound levels. The sound pressure level, L_p, is given as

$$L_p = 10 \log_{10} \frac{(p'_{rms})^2}{p^2_{ref}}$$

where p'_{rms} is the RMS acoustic pressure and p_{ref} is a reference pressure, which for airborne sound is usually set to 20 μPa[140]. It follows from the definition of L_p that a doubling of sound intensity is reflected by a change of 3 dB. Table 29 shows the sound pressure level (SPL) for some common sounds.

A.2 One-third octave bands

Not only can the human hearing system tolerate a very large range of sound pressures, but it also is able to perceive a wide range of frequencies. Pressure fluctuations at frequencies as low as 20 Hertz (Hz) can be sensed as sound, and in young people the audible range extends to approximately 20,000 Hz (20 kHz)[123]. It is impractical to report measured sound levels at such a wide range of frequencies, so it becomes desirable to subdivide the range into a number of manageable pieces, or *bands*. Although constant bandwidths are sometimes used,

Table 29: Examples of sound pressure and SPL for common sounds[109][140].

Description	**Sound pressure (Pa)**	**SPL (dB) re 20 μPa**
Jet engine at 3 m	200.	140
Permanent hearing damage	63.	130
Threshold of pain	20.	120
Accelerating motorcycle at 5 m	6.3	110
Pneumatic hammer at 2 m	2.	100
Noisy factory	0.63	90
Vacuum cleaner	0.2	80
Busy traffic	0.063	70
Loud conversation	0.02	60
Quiet restaurant	0.0063	50
Public park	0.002	40
Library	0.00063	30
Rustling of leaves	0.0002	20
Human breathing at 3 m	0.00006	10
Threshold of hearing	0.00002	0

it is more common to use bands which are one *octave*, or a fraction of an octave, in width. An octave represents a doubling of frequency, and to the human ear represents the same perceived change in frequency anywhere in the audible range. For example, a one-octave frequency change from 40 to 80 Hz is heard with approximately the same ease as a frequency change from 4000 to 8000 Hz, while smaller changes may not be perceptible[140].

In aircraft noise problems, one-third octave bands are usually used when quantifying sound levels at different frequencies. The one-third octave bands are defined by dividing octave bands into three parts. First, the center frequency of the lowest band, f_1 is assigned, and the center frequency of each successive band, f_{b+1} is related to the previous center frequency, f_b, according to the formula

$$f_{b+1} = 2^{1/3} f_b$$

The upper and lower frequencies of each band, f_U and f_L, respectively, are related to the band's center frequency, f_C, as follows:

$$f_U = 2^{1/6} f_C$$

$$f_L = \frac{f_C}{2^{1/6}}$$

Since round numbers are more convenient, the center frequencies have been standardized

into a set of preferred one-third octave bands, which are listed in Table 30 for frequencies in the audible range.

A.3 Overall sound pressure level

If sound levels are measured as SPL values, reporting the results requires the specification of values at up to several dozen frequencies even when one-third octave bands are used. It is useful to integrate the measured sound levels at multiple frequencies into a single value, and several metrics exist which represent single-value measure of the sound level. The simplest of these metrics is the overall sound pressure level (OASPL), which is a simple integration of the mean-square pressure over the frequency spectrum:

$$L_{OA} = 10 \log_{10} \sum_{b} 10^{\frac{L_{p,b}}{10}}$$

where $L_{p,b}$ is the SPL for the b^{th} frequency band.

A.4 A-weighted sound level

Human perception of loudness varies with the frequency of sound. Sound occurring near the middle of the audible range, near 1 kHz, is perceived as louder than sound with equal energy occurring at low or hight frequencies. When describing a sound sample with multiple frequencies as a single number, a frequency weighting function can be used to account for the different perceived loudness of the different frequencies. The most common weighting function is A-weighting, which is intended to adjust the spectrum such that sounds with the same adjusted level but different frequencies will be equally loud, regardless of their actual sound pressures[109]. The A-weighted sound level is calculated by adding the weighting functions to the measured SPL at each frequency, then integrating the mean-square pressure over the frequency spectrum:

$$L_A = 10 \log_{10} \sum_{b} 10^{\frac{L_{p,b}+W_A(f_b)}{10}}$$

where W_A is the A-weighting relative response function for frequency f_b. Values for W_A for the standard one-third octave bands are given in Table 31 and plotted in Figure 109.

Table 30: Standard one-third octave band frequencies[3].

Lower frequency, f_L (Hz)	**Center frequency, f_C (Hz)**	**Upper frequency, f_U (Hz)**
22.4	25.	28.
28.	31.5	35.5
36.	40.	45.
45.	50.	56.
56.	63.	71.
71.	80.	90.
90.	100.	112.
112.	125.	140.
140.	160.	180.
180.	200.	224.
224.	250.	280.
280.	315.	355.
355.	400.	450.
450.	500.	560.
560.	630.	710.
710.	800.	900.
900.	1000.	1120.
1120.	1250.	1400.
1400.	1600.	1800.
1800.	2000.	2240.
2240.	2500.	2800.
2800.	3150.	3550.
3550.	4000.	4500.
4500.	5000.	5600.
5600.	6300.	7100.
7100.	8000.	9000.
9000.	10,000.	11,200.
11,200.	12,500.	14,000.
14,000.	16,000.	18,000.
18,000.	20,000.	22,400.

Table 31: A-weighting relative response function[140].

Frequency (Hz)	**A-weighting relative response (dB)**
25.	-44.7
31.5	-39.4
40.	-34.6
50.	-30.2
63.	-26.2
80.	-22.5
100.	-19.1
125.	-16.1
160.	-13.4
200.	-10.9
250.	-8.6
315.	-6.6
400.	-4.8
500.	-3.2
630.	-1.9
800.	-0.8
1000.	0.
1250.	0.6
1600.	1.0
2000.	1.2
2500.	1.3
3150.	1.2
4000.	1.0
5000.	0.5
6300.	-0.1
8000.	-1.1
10,000.	-2.5
12,500.	-4.3
16,000.	-6.6
20,000.	-9.3

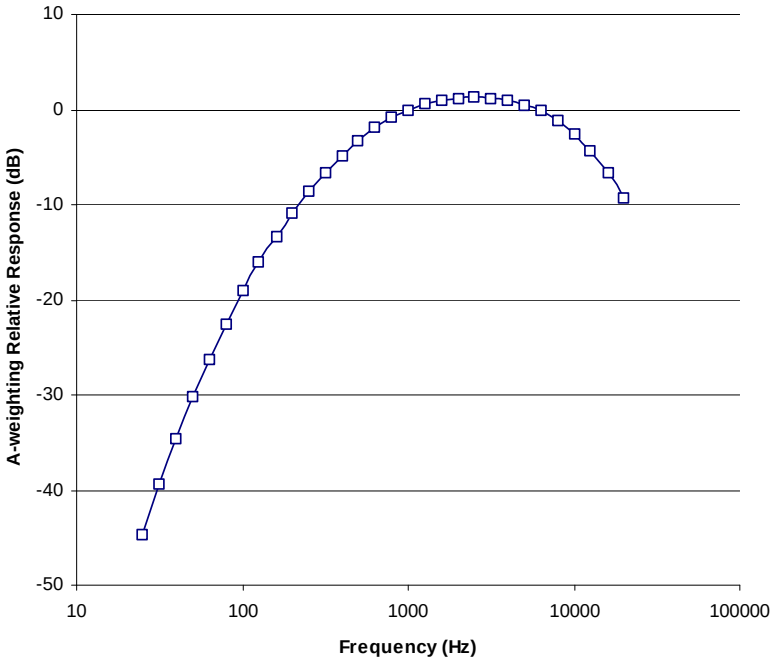

Figure 109: A-weighting relative response function.

A.5 Sound power level

Sound power level (PWL) provides a measure of the total sound produced by the source at a given frequency. For a specific frequency band, the average power, $\mathcal{P}_{b,av}$, produced by a sound source is the integral over any surface completely surrounding the source, S, of the time-averaged acoustic intensity, $\mathbf{I}_{b,av}$:

$$\mathcal{P}_{b,av} = \iint_S \mathbf{I}_{b,av} \cdot \mathbf{n} dS$$

where $\mathbf{n}$ is the unit normal to S. The value of $\mathcal{P}_{b,av}$ is independent of the size and shape of S. The sound power level, $L_{\mathcal{P}}$, is the sound power expressed in decibels:

$$L_{\mathcal{P}} = 10 \log_{10} \frac{\mathcal{P}_{b,av}}{\mathcal{P}_{ref}}$$

where $\mathcal{P}_{ref} = 10^{-12}$ W is the reference power.

A.6 Equivalent sound level

Equivalent sound level is a time average of sound energy, usually based on A-weighted SPL, which provides a single-number descriptor of a time-varying sound level for use in

environmental impact statements and other documents[140]. Equivalent sound level, L_{eq}, is calculated by averaging the mean-square pressure over a specified time interval, T, and expressing the result in decibels:

$$L_{eq} = 10 \log_{10} \left(\frac{1}{T} \int_0^T 10^{L_A/10} dt \right)$$

The value of the averaging time interval depends on the application, and should be stated; common values include one hour, one day, or one year. Equivalent sound level will generally differ from the arithmetic mean and median levels of the A-weighted sound pressure levels, and tends to be dominated by readings near the maximum.

A.7 Day-night noise level

The day-night noise level (DNL) is similar to equivalent sound level with a 24-hour averaging time interval, with the addition of a 10-dBA penalty for any sound measured between the hours of 10 p.m. and 7 a.m. to account for the additional annoyance of aircraft at nighttime, when urban background noise levels are low[123]:

$$L_{DN} = 10 \log_{10} \left[\frac{1}{24} \left(\int_{7a.m.}^{10p.m.} 10^{L_A/10} dt + \int_{10p.m.}^{7a.m.} 10^{(L_A+10)/10} dt \right) \right]$$

where L_{DN} is the day-night noise level and the time, t, is measured in hours[140]. DNL is used exclusively in the United States for describing the impact of airport community noise. Under the requirements of FAR Part 150[1], each public airport in the U.S. is required to develop a noise exposure map which shows predicted DNL contours for the area surrounding the airport; such a noise exposure map is used for land use planning and for government-funded residential sound insulation programs.

A.8 Perceived noise level

Unlike the A-weighted noise level, which applies a weighting function based on the perceived loudness of sound at different frequencies, the perceived noise level (PNL) applies a weighting function to measure the "annoyance" of a frequency spectrum. The response curves were developed by means of audiometric tests in the 1950s which covered a range of

discrete and broadband sound sources, including real aircraft noise[123]. The PNL calculation uses only those SPL values in the 24 one-third octave bands between 50 Hz and 10 kHz. For measured data, the sound levels are corrected for any deviation from the standard test conditions:

1. Sea level pressure (1.013×10^5 Pa)
2. Standard day temperature (25 ^{o}C)
3. 70% relative humidity
4. Zero wind velocity

The corrected SPL values are then used in the calculation of PNL.

For each frequency band, the SPL is converted to perceived noisiness as follows:

$$\begin{aligned} n_b &= 10^{M_1[L_p - L_1]} \quad f < 400\text{Hz or } f > 6300\text{Hz and } L_1 \leq L_p \leq L_2 \\ n_b &= 10^{M_0[L_p - L_0]} \quad f < 400\text{Hz or } f > 6300\text{Hz and } L_p \geq L_2 \\ n_b &= 10^{M_0[L_p - L_0]} \quad 400\text{Hz} \leq f \leq 6300\text{Hz and } L_p \geq L_0 \end{aligned}$$

where n_b is the perceived noisiness in noys for frequency band b and L_0, L_1, L_2, M_0 and M_1 are constants for each frequency band (Table 32). If L_p is less than L_0 or greater than L_2, the value of n_b must be looked up from a table of perceived noisiness versus frequency and SPL in a reference such as FAR 36[100]. Figure 110 shows how perceived noisiness varies with frequency and SPL. The noisiness values for the individual frequencies are combined to calculate the total perceived noisiness, N, according to the formula

$$N = 0.85 n_{max} + 0.15 \sum_{b=1}^{24} n_b$$

where n_{max} is the maximum value of n_b, $b = 1 \ldots 24$. Finally, the perceived noise level, L_{PN}, in PNdB is computed as follows:

$$L_{PN} = 40 + 33.32 \log_{10} N$$

Table 32: Constants for noy calculations[140].

Band, b	f (Hz)	M_1	L_1 (dB)	L_2 (dB)	M_0	L_0 (dB)
1	50	0.043478	64	91.0	0.030103	52
2	63	0.040570	60	85.9	0.030103	51
3	80	0.036831	56	87.3	0.030103	49
4	100	0.036831	53	79.9	0.030103	47
5	125	0.035336	51	79.8	0.030103	46
6	160	0.033333	48	76.0	0.030103	45
7	200	0.033333	46	74.0	0.030103	43
8	250	0.032051	44	74.9	0.030103	42
9	315	0.030675	42	94.6	0.030103	41
10	400	—	—	—	0.030103	40
11	500	—	—	—	0.030103	40
12	630	—	—	—	0.030103	40
13	800	—	—	—	0.030103	40
14	1000	—	—	—	0.030103	40
15	1250	—	—	—	0.030103	38
16	1600	—	—	—	0.029960	34
17	2000	—	—	—	0.029960	32
18	2500	—	—	—	0.029960	30
19	3150	—	—	—	0.029960	29
20	4000	—	—	—	0.029960	29
21	5000	—	—	—	0.029960	30
22	6300	—	—	—	0.029960	31
23	8000	0.042285	37	44.3	0.029960	34
24	10,000	0.042285	41	50.7	0.029960	37

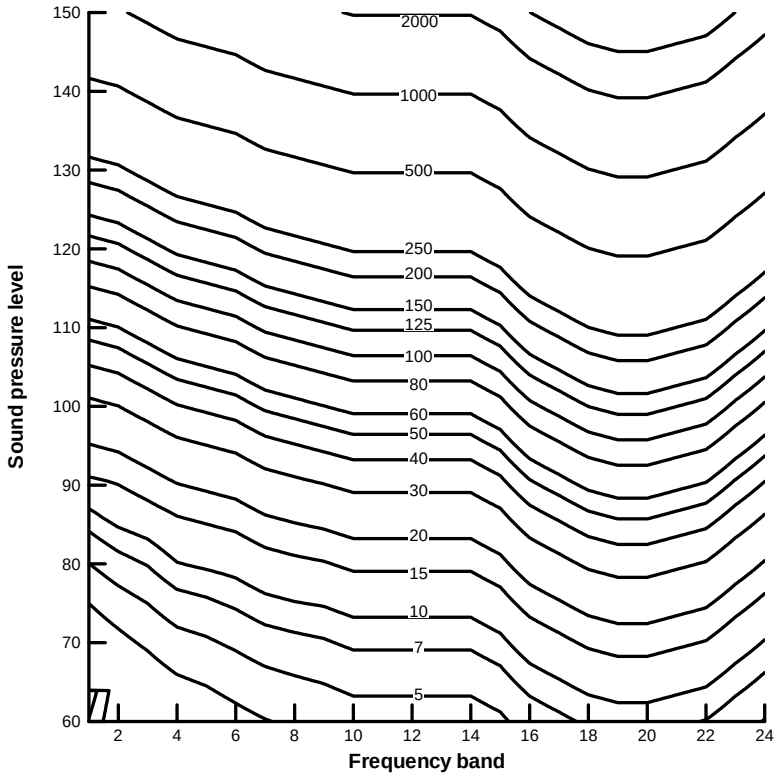

Figure 110: Contours of equal noisiness.

A.9 Tone-corrected perceived noise level

The tone-corrected perceived noise level (PNLT) adds an additional tone correction factor to the PNL to account for the additional annoyance of distinct tones which protrude above the rest of the spectrum. For each frequency band in which a tone is identified, the amount by which the tone exceeds the the surrounding bands, F_b, is calculated as

$$F_b = L_p - L_p^{''}$$

where $L_p^{''}$ is the background sound pressure level, which is determined by adjusting the original SPL through a complex procedure described in detail in Far 36[100]. For each non-zero value of F_b, the tone correction factor, C_b, is calculated as shown in Table 33. The tone correction factor functions are plotted in Figure 111 for the three frequency different ranges.

Once the correction factors have been found for each of the tones, the total tone correction factor, C, is set equal to the maximum value of C_b, $b = 1 \ldots 24$, and is added to the

Table 33: Formulas for tone correction factor[100].

Frequency f, Hz	**Level difference F, dB**	**Tone correction C_b, dB**
$50 \leq f < 500$	$3/2 \leq F < 3$	$F/3 - 1/2$
	$3 \leq F < 20$	$F/6$
	$20 \leq F$	$10/3$
$500 \leq f < 5000$	$3/2 \leq F < 3$	$2F/3 - 1$
	$3 \leq F < 20$	$F/3$
	$20 \leq F$	$20/3$
$5000 \leq f < 10,000$	$3/2 \leq F < 3$	$F/3 - 1/2$
	$3 \leq F < 20$	$F/6$
	$20 \leq F$	$10/3$

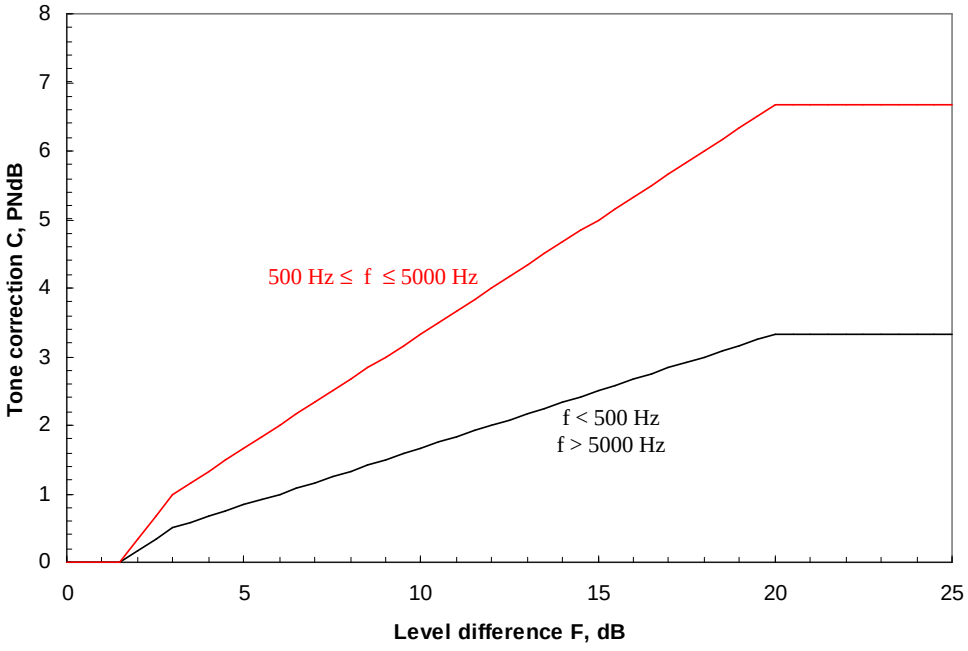

Figure 111: Tone correction factors.

PNL to arrive at the tone-corrected perceived noise level, L_{PNT}:

$$L_{PNT} = L_{PN} + C$$

Subjective evaluation also allows C to be adjusted if it is believed that the most significant tone is divided between two frequency bands or if the correction factor is suspected to be the result of an effect other than an actual tone.

A.10 Effective perceived noise level

The unit of measurement for certification noise is the effective perceived noise level (EPNL), which integrates the time history of the PNLT to account for the additional effect of the duration of a noise event on the annoyance. The PNLT time history, $L_{PNT}(t)$, is integrated as follows:

$$L_{EPN} = 10 \log_{10} \left[\left(\frac{1}{T} \right) \int_{t_1}^{t_2} 10^{\frac{L_{PNT}(t)}{10}} \right] dt$$

where T is a normalizing time constant and t_1 and t_2 are the beginning and ending of the time period during which the PNLT is within 10 PNdB of its maximum value, respectively, as shown in Figure 112. For FAR 36 certification, a value of $T = 10$ s is used. PNLT is generally calculated from SPL values measured or calculated at discrete time intervals, so the EPNL calculation can be rewritten as a summation:

$$L_{EPN} = 10 \log_{10} \left[\left(\frac{1}{T} \right) \sum_{k=k_1}^{k=k_2} \Delta t 10^{\frac{L_{PNT,k}}{10}} \right]$$

where $L_{PNT,k}$ is the PNLT at the k^{th} time interval, k_1 and k_2 are the beginning and ending time intervals during which the PNLT is within 10 PNdB of its maximum value, and Δt is the length of the equal increments of time for which the sound is measured or calculated. For FAR 36 certification, Δt must be no greater than 0.5 s.

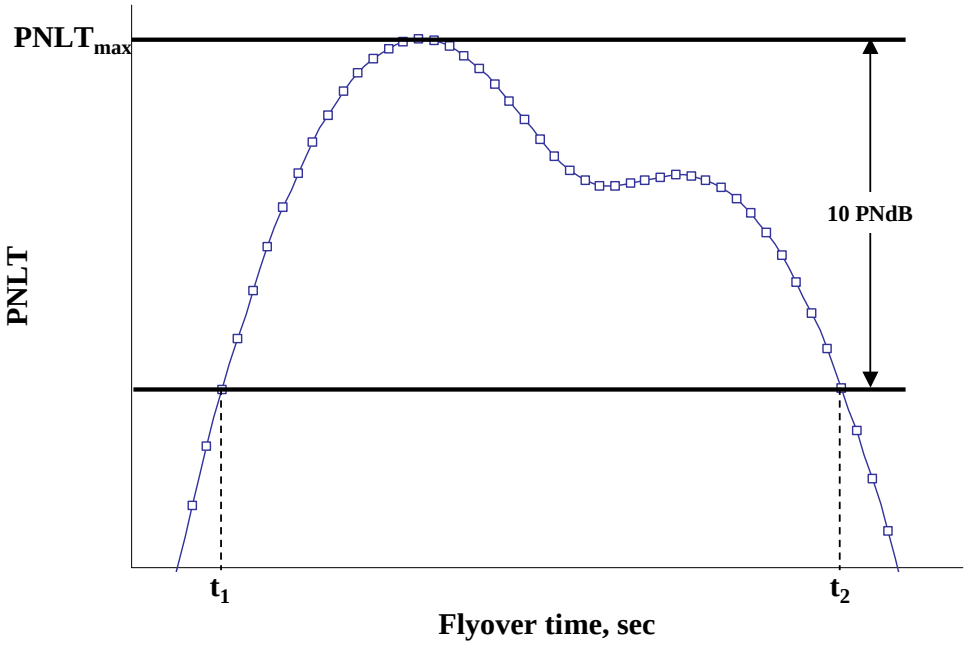

Figure 112: Example PNLT time history for EPNL integration.

APPENDIX B

LIST OF COMPUTER PROGRAMS

This appendix lists the FORTRAN routines which make up the wrappers and geometry utilities in the integrated performance and noise analysis process. This list excludes the off-the-shelf analysis methods themselves. The first section lists general routines which are used by all, or nearly all, of the wrappers and geometry utilities. Subsequent sections list the routines which are more specific to the individual components.

B.1 All components

Routine	**Description**
ARGUMENTS	Parses command-line arguments
AT62	Returns standard atmospheric conditions at a given altitude
BRACKET	Finds the index of an axial location within an array of duct wall axial values
CFIT	Compute coefficients for a one-dimensional polynomical curve fit
CCSPLN	Computes clamped cubic spline coefficients
CONSOLIDATE	Transfer all case data to the host processor when executing multiple cases with MPI
DISTRDATA	Transfer all necessary data from the host processor to all other processors when executing multiple cases with MPI
ENGDECK	Looks up engine thrust for a given flight condition
ENGFIT	Fills in missing full-power data in the engine parameters data
ENGSORT	Sorts engine parameters by increasing thrust, altitude and Mach number
EQPARA	Used by ENGSORT to re-order engine data

FIFACT	Finds interpolation factors
INTERPP	Interpolates from 3-dimensional engine arrays
LSQPOL	Determines coefficients for a least-squares polynomial
MPISETUP	Makes calls to MPI initialization routines
NCSPLN	Computes natural cubic spline coefficients
PARAMS	Looks up engine component thermodynamic data for a given flight condition
NMLFORMS	A collection of subroutines to write an output variable or array in namelist format
QXZ037	Provides single-precision machine numbers
READCASE	Loads input data for the current analysis case from the input arrays
READNAMS	Reads namelist input data
SPLININT	Interpolates an array using a natural cubic spline fit
SPLININTC	Interpolates an array using a clamped cubic spline fit
SWITCH	Interchanges two values in an array
SYMPDS	Solves the matrix equation Ax=b
THERM	Calculates thermodynamic properties of air
WRITECASE	Transfers output data for the current analysis case to output arrays
WRITENAMS	Writes output data for every namelist
ZMNOZ	Computes thermodynamic properties of a fully-expanded jet
ZM1D	Computes compressible flow properties of a quasi-one-dimensional flow

B.2 ENGGENWRAP

Routine	**Description**

ENGGENPOST	Post-processor for ENGGEN
ENGGENPRE	Pre-processor for ENGGEN
ENGGENRUN	Execution control for ENGGEN
ENGGENWRAP	Main wrapper routine for ENGGENWRAP
ENGGENWRIT	Writes output data specific to ENGGENWRAP
ENJOMIN	Extracts engine geometry from an ENGGEN plot file
TABMOD	Modifies an ENGGEN component map file based on changes to design variables

B.3 MODGEOM

Routine	**Description**
CRVTO	Draws a curve between two points using a cubic polynomial
MODGEOM	Main routine for MODGEOM
MODGEOMWRIT	Writes output data specific to MODGEOM
STRETCH	Stretch the engine between two points to add a new component

B.4 MERIDWRAP

Routine	**Description**
BLADESURF	Fits rotor and stator blade surfaces
CONMIN	Free off-the-shelf optimization routine
INTBLADE	Find the intersection of a horizontal mesh line or streamline with the leading- or trailing-edge of a blade (or some other radially-oriented line).
INTSECT	Called by INTBLADE to find the intersection of two lines
MERIDOBJ	Calculates the objective function for the optimization

MERIDOPT	Fan velocity triangle optimization routine
MERIDPOST	Post-processor for MERIDLN
MERIDPRE	Pre-processor for MERIDLN
MERIDRUN	Execution control for MERIDLN
MERIDSETUP	Sets up MERIDLN input data that will not change during optimization
MERIDWRAP	Main wrapper routine for MERIDWRAP
MERIDWRIT	Writes output data specific to MERIDWRAP
PLOSS	Computes blade section total pressure loss based on inlet Mach number and flow turning
ZMSL	Compute flow properties along a streamline

B.5 BLADEWRAP

Routine	**Description**
BLADEOPT	Rotor blade inverse design routine
BLADESURF	Fits rotor and stator blade surfaces
BLADEWRAP	Main wrapper routine for BLADEWRAP
BLADEWRIT	Writes output data specific to BLADEWRAP
CUMNOR	Computes the cumulative of the normal distribution
GAUSS	Perform Gaussian elimination on a matrix
INVERSE	Finds the inverse of a matrix
INVDES	Integrate for the rotor camber line which produces a prescribed tangential velocity field
IPMPAR	Provides integer machine constants
POLYFIT	Compute a one-dimensional polynomial fit
SPMPAR	Provides single-precision machine constants
SWIFTPOST	Post-processor for Swift

SWIFTPRE	Pre-processor for Swift
SWIFTRUN	Execution control for Swift
TCGRIDPOST	Post-processor for TCGRID
TCGRIDPRE	Pre-processor for TCGRID
TCGRIDRUN	Execution control for TCGRID
XNORMFCT	

B.6 PLOTGEOM

Routine	**Description**
PLOTGEOM	Main routine for PLOTGEOM

B.7 FLOPSWRAP

Routine	**Description**
FLOPSPOST	Post-processor for FLOPS
FLOPSPRE	Pre-processor for FLOPS
FLOPSRUN	Execution control for FLOPS
FLOPSWRAP	Main wrapper routine for FLOPSWRAP
FLOPSWRIT	Writes output data specific to FLOPSWRAP

B.8 CASEPICK

Routine	**Description**
CASEPICK	Main wrapper routine for CASEPICK
CASESWRIT	Writes output data specific to CASEPICK

B.9 SWIFTWRAP

Routine	Description
INTBLADE	Find the intersection of a horizontal mesh line or streamline with the leading- or trailing-edge of a blade (or some other radially-oriented line).
INTSECT	Called by INTBLADE to find the intersection of two lines
SWIFTCONV	Monitors Swift pre-processing, execution, and post-processing to assure convergence of the numerical algorithm and enforces the required rotor pressure ratio or mass flow
SWIFTPOST	Post-processor for Swift
SWIFTPRE	Pre-processor for Swift
SWIFTRUN	Execution control for Swift
SWIFTWRAP	Main wrapper routine for SWIFTWRAP
SWIFTWRIT	Writes output data specific to SWIFTWRAP
TCGRIDPOST	Post-processor for TCGRID
TCGRIDPRE	Pre-processor for TCGRID
TCGRIDRUN	Execution control for TCGRID

B.10 TFANSWRAP

Routine	Description
ARCLEN	Computes arc length along a segment of engine duct
AWAKENPRE	Pre-processor for AWAKEN
AWAKENRUN	Execution control for AWAKEN
CUP3DPOST	Post-processor for CUP3D

CUP3DPRE	Pre-processor for CUP3D
CUP3DRUN	Execution control for CUP3D
EVERSPOST	Post-processor for Eversman radiation codes
EVERSPRE	Pre-processor for Eversman radiation codes
EVERSRUN	Execution control for Eversman radiation codes
FANTABLE	Write fan tone noise to a table of SPL vs. throttle setting, frequency and directivity angle
FINDTHETA	Finds the point along a duct surface which is at a given directivity angle from the origin
SRC3DPOST	Post-processor for SOURCE3D
SRC3DRUN	Execution control for SOURCE3D
SRC3DSETUP	Sets up SOURCE3D input data prior to running AWAKEN
TFANSWRAP	Main wrapper routine for TFANSWRAP
TFANSWRIT	Writes output data specific to SWIFTWRAP
XNORM	Shifts axial coordinates to the origin and normalize by duct diameter
YNORM	Normalizes radial coordinates by duct diameter

B.11 WINDWRAP

Routine	**Description**
GRDSTRCH	Finds the width of the smallest cells in a stretched grid
WINDGRID	Generates a grid for running Wind
WINDPOST	Post-processor for Wind
WINDPRE	Pre-processor for Wind
WINDRUN	Execution control for Wind
WINDWRAP	Main wrapper routine for WINDWRAP
WINDWRIT	Writes output data specific to WINDWRAP

XLINFCT	Finds the width of a given cell in a stretched grid
ZBALANCE	Finds the proper way to divide up gridlines between adjacent blocks to even out the grid spacing across the interface

B.12 MGBWRAP

Routine	**Description**
ISWITCH	Interchanges two values in an integer array
MGBPOST	Post-processor for MGBK
MGBPRE	Pre-processor for MGBK
MGBRUN	Execution control for MGBK
MGBTABLE	Write jet mixing noise to a table of SPL vs. throttle setting, frequency and directivity angle
MGBWRAP	Main wrapper routine for MGBWRAP
MGBWRIT	Writes output data specific to MGBWRAP

B.13 ANOPPWRAP

Routine	**Description**
ANOPPPOST	Post-processor for ANOPP
ANOPPPRE	Pre-processor for ANOPP
ANOPPRUN	Execution control for ANOPP
ANOPPWRAP	Main wrapper routine for ANOPP
ANOPPWRIT	Writes output data specific to ANOPPWRAP

APPENDIX C

DESCRIPTION OF DESIGN DATABASE

C.1 Namelist OPT

DESID	=	ID for this design (Default = 'Design')
ENGDEF	=	Name of base ENGGEN input file (Default = 'ENGGEN.BASE')
FLPDEF	=	Name of base FLOPS input file (Default = 'FLOPS.BASE')
FILBASE	=	Base name for creation of input, output, and data file names (Default = 'default'). Default names for each of the following file names are created using FILBASE.
ENGBASE	=	Base name for ENGGEN input and output files
FLPBASE	=	Base name for FLOPS input and output files
NOFILE	=	Name of FLOPS takeoff noise profile file
APFILE	=	Name of FLOPS approach noise profile file
ENGDEK	=	Name of engine performance deck to be created by ENGGEN
ANOPFIL	=	Name of engine thermodynamic data file (renamed from "ANOPP" after FLOPS executes)
DUCTGEOM	=	File in which duct geometry will be written, instead of the output file
FANFLOW	=	File in which flow data will be written, instead of the output file
FANGEOM	=	File in which fan detailed geometry data will be written, instead of the output file
BLADFIL	=	Name of TECPLOT® plotting file for fan blade stacking
MERIDBASE	=	Base name for MERIDLN input and output files
TCGRDBASE	=	Base name for TCGRID input and output files
SWIFTBASE	=	Base name for SWIFT input and output files

TFNBASE	=	Base name for TFANS input and output files
WINDBASE	=	Base name for WIND input and output files
MGBBASE	=	Base name for MGB input and output files
MGBXFIL	=	Name of 2-D grid file for MGB input
FNINAM	=	Name of file to which fan inlet source noise table is written
FNENAM	=	Name of file to which fan exhaust source noise table is written
JETNAM	=	Name of file to which jet source noise table is written
ANOPBASE	=	Base name for ANOPP input and output files
ANOPNAMO	=	Name of file to which ANOPP OASPL data are written
ANOPNAMS	=	Name of file to which ANOPP SPL data are written
AIRINM	=	Aircraft identifier for use in INM data files (character*6)
ENGINM	=	Engine identifier for use in INM data files (character*6)
IFWRIT	=	0, Only output data which have been changed by the current wrapper.
	=	1, Output all data (Default)
IPSWIFT	=	0, Don't create plot files for Swift computational results in BLADEWRAP and SWIFTWRAP
	=	1, Create plot files for convergence and inlet and outlet conditions only
	=	2, Create all plot files (Default)

C.2 Namelist DESIGN

GW	=	Aircraft gross weight, lb. If GW = 0, GW is calculated from THRUST and TWRAT.
TWRAT	=	Aircraft thrust-to-weight ratio, only used if GW = 0
XNAC	=	Nacelle length, ft
DNAC	=	Nacelle diameter, ft

WRATIO	=	Ratio of landing weight to gross weight
WLDG	=	Aircraft landing weight, lb (only used if WRATIO=-1)
WINL	=	Inlet weight, lb
WNOZ	=	Nozzle weight, lb
WENG	=	Engine weight, lb
SW	=	Wing area, sq. ft, or wing loading if WSR=-1 in FLPDEF
WSR	=	0, SW is wing area
	=	-1, SW is wing loading
	>	0, WSR is wing loading and SW is calculated
TR	=	Wing taper ratio, sq. ft
FLAPR	=	Ratio of flap area to wing area
AR	=	Wing aspect ratio
DIH	=	Wing dihedral, deg
SWEEP	=	Wing sweep, deg
SHT	=	Horizontal tail area, sq. ft.
ARHT	=	Horizontal tail aspect ratio
SWPHT	=	Horizontal tail sweep, deg
SVT	=	Vertical tail area, sq. ft.
ARVT	=	Vertical tail aspect ratio
SWPVT	=	Vertical tail sweep, deg
CRMACH	=	Mach number at which engine cruise performance will be calculated (Default=0.85)
CRALT	=	Altitude at which engine cruise performance will be calculated, ft. (Default=35000)
BPRDES	=	Design bypass ratio
FPRDES	=	Design fan pressure ratio
UTIP1	=	Design rotor tip speed
OPRDES	=	Design overall pressure ratio
TETDES	=	Design turbine inlet temperature, R

TTRDES	=	Design throttle ratio
XMEFF	=	Design fan inlet axial Mach number
IPCPR	=	Design intermediate-pressure compressor pressure ratio. If input, the high-pressure compressor pressure ratio is computed from HPCPR = OPRDES / FPRDES / IPCPR.
HPCPR	$\geq$	1, Design high pressure compressor pressure ratio (IPCPR = 0)
	$<$	1, Ratio of design high pressure compressor pressure ratio to OPRDES (IPCPR = 0).
THRUST	$\geq$	1, Thrust per engine, lb
	$<$	1, Thrust/weight ratio. GW must be greater than zero.
THRSO	=	Baseline engine thrust, lb., corresponding to WENG, etc
NEWI	=	Number of engines on the wing
NEFU	=	Number of engines on the fuselage
XENG	=	Logitudinal location of engine inlet relative to wing root leading edge, ft. (positive aft)
YENG	=	Spanwise location of engine inlet relative to wing root leading edge, ft. (positive outboard)
ZENG	=	Vertical location of engine inlet relative to wing root leading edge, ft. (positive up)
DEFFFAN	=	Delta for fan efficiency (Default=0)
DEFFHPC	=	Delta for high-pressure compressor efficiency (Default=0)
DEFFIPC	=	Delta for intermediate-pressure compressor efficiency (Default=0) (Not currently used)
DEFFTUR	=	Delta for turbine efficiency (Default=0)
DEFFSHAFT	=	Delta for shaft efficiency (Default=0) (Not currently used)
DEFFNOZ1	=	Delta for core nozzle thrust coefficient (Default=0)
DEFFNOZ2	=	Delta for fan nozzle thrust coefficient (Default=0)
DEFFINL	=	Delta for inlet efficiency (Default=0) (Not currently used)
DEFFBURN	=	Delta for burner efficiency (Default=0) (Not currently used)

COSTBL	=	Customer bleed, lb/sec
WCOOL	=	Turbine cooling flow as a fraction of high pressure compressor mass flow.
HPEXT	=	Customer power extraction, hp
VANGL	=	Aircraft pitch rate, deg/sec
SPRATE	=	Engine spool rate (fractional change in thrust per second)
TIBRAK	=	Time between touchdown and brake application during landing, sec
PILOTT	=	Time between engine failure and pilot recognition during takeoff, sec
ARGEF	=	Aspect ratio factor for ground effects
BRAKMU	=	Coefficient of friction during braking
ROLLMU	=	Coefficient of friction during roll
TINC	=	Thrust incidence on the ground, deg
ALPRUN	=	Angle of attack on the ground, deg

C.3 Namelist AERO

CL0T	=	Takeoff $C_{L,0}$
CLALFT	=	Takeoff $C_{L,\alpha}$
CLTOM	=	Takeoff $C_{L,max}$
CL0L	=	Landing $C_{L,0}$
CLALFL	=	Landing $C_{L,\alpha}$
CLLDM	=	Landing $C_{L,max}$
CD0T	=	Takeoff $C_{D,0}$
ZK1T	=	Takeoff K_1
ZK2T	=	Takeoff K_2
CD0L	=	Landing $C_{D,0}$
ZK1L	=	Landing K_1

ZK2L	=	Landing K_2
DCL0	=	Addtional increment to $C_{L,0}$ for both takeoff and landing
DCLALF	=	Additional increment to $C_{L,\alpha}$ for both takeoff and landing
DCLMAX	=	Additional increment to $C_{L,max}$ for both takeoff and landing
DCD0	=	Additional increment to $C_{D,0}$ for both takeoff and landing
DZK1	=	Additional increment to K_1 for both takeoff and landing
DZK2	=	Additional increment to K_2 for both takeoff and landing
CDGEAR	=	Gear drag coefficient, both takeoff and landing
CDEOUT	=	Engine out drag coefficient increment, both takeoff and landing

C.4 Namelist GEOM

NSTGC1	=	Number of stages for LP compressor
NSTGC2	=	Number of stages for HP compressor
NSTGT1	=	Number of stages for HP turbine
NSTGT2	=	Number of stages for LP turbine
NBCT2	=	Number of blades for the last stage of the LP turbine
NZ	=	Number of engine duct geometry zones Z = 1 is the inlet cone, fan hub, inside edge of the core and core nozzle. Z = 2 is the outside of the core and core nozzle. Z = 3 is the inside edge of the bypass duct. Z = 4 is the outside edge of the bypass duct (inside of the nacelle). Z = 5 is the exterior of the nacelle.
NP(Z)	=	Number of points in duct geometry zone Z (Z = 1, NZ)
XG(P,Z)	=	X-coordinate of point P in duct geometry zone Z (P = 1, NP(Z))
RG(P,Z)	=	R-coordinate of point P in duct geometry zone Z
RH2T1	=	Fan hub-tip ratio

GRATIO	=	Fan gear ratio
NB	=	Number of fan rotor blades
NV	=	Number of stator vanes. If NV=0, an appropriate value will be computed to cut off the BPF tone. Variable ITCASE in Namelist FANNOIS specifies from which case to use the flight conditions in calculating NV.
FANAR	=	Rotor aspect ratio
FANAS	=	Stator aspect ratio
FANAC	=	Core stator aspect ratio
XITHR	=	Inlet throat axial location, ft
RITHR	=	Inlet throat radius, ft
TMAXRH	=	Fan rotor thickness-to-chord ratio at the hub
TMAXRT	=	Fan rotor thickness-to-chord ratio at the tip
TMAXSH	=	Fan stator thickness-to-chord ratio at the hub
TMAXST	=	Fan stator thickness-to-chord ratio at the tip
XFHUB1	=	Axial location of fan hub leading edge, ft
XFHUB2	=	Axial location of fan hub trailing edge, ft
RFHUB1	=	Radial location fan hub leading edge, ft
RFHUB2	=	Radial location fan hub trailing edge, ft
XFTIP1	=	Axial location of rotor leading edge, ft
XFTIP2	=	Axial location of rotor trailing edge, ft
RFTIP1	=	Radial location of rotor leading edge, ft
RFTIP2	=	Radial location of rotor trailing edge, ft
XRSTK	=	rotor stack axis axial location, ft
XSHUB1	=	Axial location of fan stator hub leading edge, ft
XSHUB2	=	Axial location of fan stator hub trailing edge, ft
XSTIP1	=	Axial location of fan stator leading edge, ft
XSTIP2	=	Axial location of fan stator trailing edge, ft
RSHUB1	=	Radial location of fan stator hub leading edge, ft

RSHUB2	=	Radial location of fan stator hub trailing edge, ft
RSTIP1	=	Radial location of fan stator leading edge, ft
RSTIP2	=	Radial location of fan stator trailing edge, ft
XSSTKH	=	fan stator stack axis hub axial location, ft
XSSTKT	=	fan stator stack axis tip axial location, ft
XCHUB1	=	Core stator hub leading-edge axial location, ft
XCHUB2	=	Core stator hub trailing-edge axial location, ft
XCTIP1	=	Core stator leading-edge axial location, ft
XCTIP2	=	Core stator trailing-edge axial location, ft
RCHUB1	=	Core stator hub leading-edge radius, ft
RCHUB2	=	Core stator hub trailing-edge radius, ft
RCTIP1	=	Core stator leading-edge radius, ft
RCTIP2	=	Core stator trailing-edge radius, ft
CROTIP	=	Rotor blade tip chord, in
CSTATIP	=	Stator vane tip chord, in
CCSTATIP	=	Core stator vane tip chord, in
RSSF	=	Rotor-fan stator spacing re: fan mean blade chord
RSS2	=	Rotor-core stator spacing re: fan mean blade chord
AVDR	=	Fan rotor area contraction ratio, leading edge/trailing edge
AFSPLIT	=	Ratio of core inlet area to total area at the splitter. The default is calculated from the design bypass ratio.
SSWP	=	Stator sweep, deg
SLEAN	=	Stator lean, deg
XNLOD	=	Core nozzle length to diameter ratio
XNLD2	=	Fan nozzle length to diameter ratio
X1R	=	Inlet cowl length to radius ratio
X1RC	=	Inlet cone length to radius ratio
ICOPLN	=	0, Use XNLD2 to set the length of the fan nozzle

= 1, Make the fan and core nozzles coplanar. XNLD2 will be recomputed. If accurate nacelle weights are desired, ENGGEN should be re-run with the new value of XNLD2 (Default).

XP1HUB1 = IP compressor hub leading-edge axial location, ft

XP1HUB2 = IP compressor hub trailing-edge axial location, ft

XP1TIP1 = IP compressor tip leading-edge axial location, ft

XP1TIP2 = IP compressor tip trailing-edge axial location, ft

RP1HUB1 = IP compressor hub leading-edge radius, ft

RP1HUB2 = IP compressor hub trailing-edge radius, ft

RP1TIP1 = IP compressor tip leading-edge radius, ft

RP1TIP2 = IP compressor tip trailing-edge radius, ft

XP2HUB1 = LP compressor hub leading-edge axial location, ft

XP2HUB2 = LP compressor hub trailing-edge axial location, ft

XP2TIP1 = LP compressor tip leading-edge axial location, ft

XP2TIP2 = LP compressor tip trailing-edge axial location, ft

RP2HUB1 = LP compressor hub leading-edge radius, ft

RP2HUB2 = LP compressor hub trailing-edge radius, ft

RP2TIP1 = LP compressor tip leading-edge radius, ft

RP2TIP2 = LP compressor tip trailing-edge radius, ft

XT1HUB1 = HP turbine hub leading-edge axial location, ft

XT1HUB2 = HP turbine hub trailing-edge axial location, ft

XT1TIP1 = HP turbine tip leading-edge axial location, ft

XT1TIP2 = HP turbine tip trailing-edge axial location, ft

RT1HUB1 = HP turbine hub leading-edge radius, ft

RT1HUB2 = HP turbine hub trailing-edge radius, ft

RT1TIP1 = HP turbine tip leading-edge radius, ft

RT1TIP2 = HP turbine tip trailing-edge radius, ft

XT2HUB1 = LP turbine hub leading-edge axial location, ft

XT2HUB2 = LP turbine hub trailing-edge axial location, ft

XT2TIP1	=	LP turbine tip leading-edge axial location, ft
XT2TIP2	=	LP turbine tip trailing-edge axial location, ft
RT2HUB1	=	LP turbine hub leading-edge radius, ft
RT2HUB2	=	LP turbine hub trailing-edge radius, ft
RT2TIP1	=	LP turbine tip leading-edge radius, ft
RT2TIP2	=	LP turbine tip trailing-edge radius, ft
LMG	=	Length of main gear, ft
LNG	=	Length of nose gear, ft
AFAN	=	Fan inlet cross-sectional area, sq. ft
LENGIN	=	Inlet duct outer wall treated length
LENGAF	=	Aft duct treated length
HITEIN	=	Inlet duct average height, ft
AREAIN	=	Inlet cross-sectional area, sq. ft
HITEAF	=	Aft duct average height, ft
AREAAF	=	Aft cross-sectional area, sq. ft
RPLUG	=	Plug radius, ft
ACORE	=	Burner inlet area, sq. ft
ATURBT2	=	LP Turbine inlet area, sq. ft
DTURBT2	=	LP Turbine diameter, ft
CTURBT2	=	LP Turbine last-stage chord, ft

C.5 Namelist FANDES

DRTMAX	=	Maximum rotor diffusion factor for rotor velocity triangle optimization
DSHMAX	=	Maximum stator diffusion factor for rotor velocity triangle optimization

SMACHMX = Maximum stator leading-edge Mach number for rotor velocity triangle optimization

RMACHMX = Maximum rotor outlet Mach number for rotor velocity triangle optimization

DBETAMX = Maximum rotor turning for rotor velocity triangle optimization, deg

ITMER = Maximum number of iterations for rotor velocity triangle optimization

NVP = Number of points used to define the rotor exit tangentia velocity distribution. More points may improve the results, especially for severely constrained designs, but will increase computation time (Default = 6).

RFXVP(N) = Spanwise fractional locations of control points at which the tangential velocities will be defined (N = 1, NVP). RFXVP(1) must equal 0 and RFXVP(NVP) must equal 1. The default is NVP evenly-spaced points.

TIPPR = Factor for adjusting the initial tangential velocity distribution in cases where the initial values cause MERIDLN to crash. The default will usually work, but TIPPR may need to be increased by 0.01 at a time if the final stage pressure ratio is too low, or decreased if the stage pressure ratio is too high (Default = 1.98).

CTOPT = Initial constraint thickness (must be negative). The default value is usually acceptable, but if CONMIN fails to find a feasible solution, especially if some of the calculated step sizes are unusually small or large, then the absolute value of CTOPT may need to be reduced (Default=-0.1).

NDES = Number of radial points for case J.

ZDES(R) = Axial location at radial station R, ft (R = 1, NDES)

RDES(R) = Radius at radial station R, ft

VTHDES(R)	=	Design tangential velocity at radial station R, ft/sec (positive in the direction opposite rotor rotation)
VTHDESI(R)	=	Design tangential velocity at radial station R for inviscid blade design, ft/sec
NLOSR	=	Number of radial points (Default = 0)
FLOSR(P)	=	Fractional span at point P (P = 1, NLOSR)
PLOSR(P)	=	Fractional pressure loss at point P

The following three variables define regression coefficients for estimating the rotor fractional pressure loss in MERIDLN as a function of leading-edge relative Mach number and flow turning. These are ignored if NLOSR > 0. Default values are defined.

DELTA-P	=	CLOSS(1) + CLOSS(2) * ZMT + CLOSS(3) * VTT + CLOSS(4) * ZMT**2 + CLOSS(5) * ZMT * VTT + CLOSS(6) * VTT**2 + CLOSS(7) * ZMT**3 + CLOSS(8) * ZMT**2 * VTT
Where ZMT	=	[MLR - ZLOSS(1)] / [ZLOSS(2) - ZLOSS(1)]
VTT	=	[VTH - VLOSS(1)] / [VLOSS(2) - VLOSS(1)]
MLR	=	Rotor leading-edge relative Mach number
VTH	=	Rotor exit absolute tangential velocity, ft/sec
ZLOSS(1:2)	=	Minimum and maximum Mach numbers for normalization (Default = [0.61323, 1.25467])
VLOSS(1:2)	=	Minimum and maximum rotor exit absolute tangential velocities for normalization, ft/sec (Default = [239.74, 576.90])
CLOSS(1:8)	=	Regression coefficients (Default = [0.02071, -0.04778, -0.03097, 0.05649, 0.05532, 0.01679, 0., 0.])
PLEND	=	Total end-wall pressure losses as a fraction of inlet total pressure.

XBRKMX = Maximum value for axial break point in the design swirl distribution, relative to axial chord. For transonic and supersonic blade sections, the blade is designed with a swirl distribution which is intended to produce a flat-top pressure distribution in the forward portion of the blade up to the break point, after which the pressure gradually increases to the trailing edge. A lower XBRKMX moves the upper-surface shock forward (Default=0.6).

OMEGV = Relaxation factor for updating the circumferentially- averaged axial and radial velocity distributions across the rotor blade from values used during the previous iteration (Default = 0.1)

OMEGVP = Relaxation factor for correcting the prescribed tangential velocity to account for deviations between the design and actual tangential velocity distributions (Default = 0.1)

CONVV = Convergence criterion for the RMS tangential velocity distribution, ft/sec (Default = 10)

CONVD = Convergence criterion for the RMS design tangential velocity error, ft/sec (Default = 15)

MAXI = Maximum number of iterations (Default = 40, Maximum 100)

NSECR(B) = Number of radial locations at which blade sections will be defined for blade B (B = 1 is the rotor, B = 2 is the stator) (Default = 4)

NCAMX = Number of chordwise points at which the camber lines will be defined, not including the points at the leading and trailing edges where the camber is by definition zero

NTHKX = Number of chordwise points at which the thickness distribution will be defined, not including the points at the leading and trailing edges where the thickness is by definition zero

RSECTC(R,B) = Fractional radial location of blade section R (R = 1, NSECR) of blade B. The first value should be equal to zero and the last equal to one [Default = (R-1)/(NSECR-1)].

CHORDC(R,B) = Chord of blade section R of blade B, divided by the tip chord (Default = 1 for all sections)

THETAC(R,B) = Setting angle of section R of blade B. The setting angle is the angle of the chord relative to the meridional direction, and should be positive for most rotor sections and negative for the stator (Default is computed from design velocity triangles).

AINCC(R,B) = Incidence angle of section R of blade B, relative to the design (not necessarily actual) velocity triangles. Incidence angle is the relative tangential flow angle minus the leading-edge blade angle (Default is computed during blade design).

ADEVC(R,B) = Deviation angle of section R of blade B, relative to the design (not necessarily actual) velocity triangles. Deviation angle is the relative tangential flow angle minus the trailing-edge blade angle (Default is computed during blade design).

TCLMPLC(R,B) = Spline slope at the leading edge for the thickness distribution of section R of blade B (Default is computed from TTHIKC values)

RADLEC(R,B) = Leading-edge half-thickness-to-chord ratio for section R of blade B (Default computed from leading-edge Mach number)

RADTEC(R,B) = Trailing-edge half-thickness-to-chord ratio for section R of blade B (Default = 0.002)

XCAMBC(C,R,B) = Axial location, relative to chord, of camber control point C (C = 1, NCAMX) for section R of blade B. All values must be greater than zero and less than one and monotonically increasing [Default = C / (NCAMX+1)].

YCAMBC(C,R,B) = Camber, relative to chord, of camber control point C for section R of blade B. (Default computed from design velocity triangles)

XTHIKC(T,R,B)	=	Axial location, relative to chord, of thickness control point T (T = 1, NTHKX) for section R of blade B. All values must be greater than zero and less than one and monotonically increasing [Default = T / (NCAMX+1)].
TTHIKC(T,R,B)	=	Thickness-to-chord ratio of thickness control point T for section R of blade B. (Default computed from leading-edge Mach number). TTHIKC is the FULL thickness, unlike RADLEC and RADTEC which are HALF thicknesses.
NRRSTA	=	Number of rotor radial geometry stations
NRXSTA	=	Number of rotor axial stations
FFROT(R)	=	Fractional span at rotor radial station R (R = 1, NRRSTA)
CROTOR(R)	=	Rotor blade chord at radial station R
RLROT(R)	=	Rotor leading-edge radius / chord at radial station R
RTROT(R)	=	Rotor trailing-edge radius / chord at radial station R
B1ROT(R)	=	Rotor leading-edge blade angle at radial station R
B2ROT(R)	=	Rotor trailing-edge blade angle at radial station R
RROTOR(R,X)	=	Blade radius at radial station R, axial station X (X = 1, NRXSTA), ft
XROTC(R,X)	=	Blade centerline axial coordinate at radial station R, axial station X, ft
YROTC(R,X)	=	Blade centerline circumferential coordinate (R*THETA) at radial station R, axial station X, ft
LBLADE	=	0, Use TNROT (below) to define the blade thicknesses (Default).
	=	1, Use THTROT (below) to define the blade thicknesses
THTROT(R,X)	=	Blade tangential (circumferential) thickness/chord at radial station R, axial station X
TNROT(R,X)	=	Blade normal thickness/chord at radial station R, axial station X
NSRSTA	=	Number of stator radial geometry stations

NSXSTA	=	Number of stator axial stations
FFSTA(R)	=	Fractional span at stator radial station R
CSTATR(R)	=	Stator blade chord at radial station R (R = 1, NSRSTA)
RLSTA(R)	=	Stator leading-edge radius at radial station R
RTSTA(R)	=	Stator trailing-edge radius at radial station R
B1STA(R)	=	Stator leading-edge blade angle at radial station R
B2STA(R)	=	Stator trailing-edge blade angle at radial station R
XSTAC(R,X)	=	Stator centerline axial coordinate at radial station R, axial station X (X = 1, NSXSTA)
YSTAC(R,X)	=	Stator centerline circumferential coordinate (R*THETA) at radial station R, axial station X
THTSTA(R,X)	=	Stator tangential (circumferential) thickness/chord at radial station R, axial station X
TNSTA(R,X)	=	Stator normal thickness/chord at radial station R, axial station X
RSTATR(R,X)	=	Stator radius at radial station R, axial station X
NRRSEC	=	Number of radial sections defining the rotor surface
NRXSEC	=	Number of points defining each rotor section, including both upper and lower surfaces
IRLE(R)	=	Axial index of the leading-edge point at radial station R
IRTE(R)	=	Axial index of the trailing-edge point at radial station R
XRSEC(R,X)	=	Axial coordinate of rotor surface at radial station R, point X
RRSEC(R,X)	=	Radial coordinate of rotor surface at radial station R, point X
YRSEC(R,X)	=	Circumferential coordinate (R*THETA) of rotor surface at radial station R, point X
NSRSEC	=	Number of radial sections defining the stator surface
NSXSEC	=	Number of axial sections defining each stator section, including both upper and lower surfaces
ISTE	=	Axial index of the trailing edge point

XSSEC(R,X)	=	Axial coordinate of stator surface at radial station R, point X
RSSEC(R,X)	=	Radial coordinate of stator surface at radial station R, point X
YSSEC(R,X)	=	Circumferential coordinate (R*THETA) of stator surface at radial station R, point X
NLEG	=	Number of cells used to define the leading edge of the rotor blade (Default = 15)
NTEG	=	Number of cells used to define the trailing edge of the rotor blade (Default = 10)
FACKV	=	Grid spacing away from the rotor surface relative to blade chord. Smaller values give better resolution but result in more points in the J direction (Default = 1.e-04).
FACKW	=	Grid spacing away from the duct surface relative to blade span. Smaller values give better resolution but result in more points in the K direction (Default = 1.e-04).
TIPCL	=	Rotor tip clearance relative to span (Default = 0.)
IWAKEP	=	1, Locate the outlet plane of the grid at the leading edge of the stator. If the stator is swept then the outlet plane will be also (Default).
	=	2, Locate the outlet plane of the grid DXEX chord lengths downstream of the rotor hub trailing edge, perpendicular to the engine axis. The rotor wake decay will be extrapolated to the stator leading edge. This option may be needed if the grid becomes too sheared at the outlet when IWAKEP = 1.
DXEX	=	Axial location of rotor grid outlet plan, in chord lengths downstream of the rotor hub trailing edge, when IWAKEP = 2 (Default = 0.5)
CMUTM	=	Ratio of turbulent to laminar viscosity at which boundary layer transition occurs (Default = 14)

TINTENS = Free stream normalized turbulence intensity for the k-omega turbulence model (Default = 0.02)

TLENFAC = Free stream turbulence length scale relative to tip inlet boundary-layer height (Default = 0.03)

HROUGH = Surface roughness height in turbulent wall units (Default = 5). Used during blade design, but not analysis.

CONVM = Convergence criterion for mass flow error (Default = 0.005)

CONVR = Convergence criterion for RMS residual (Default = 1e-07)

CONVP = Convergence criterion for rotor pressure ratio within a Swift run. The pressure is considered to have converged if the difference between the maximum pressure ratio and the minimum pressure ratio in the last 100 iterations is less than CONVP (Default = 5e-04).

CONVPR = Convergence criterion for the rotor pressure ratio boundary condition. The exit static pressure boundary condition is iterated until either the calculated pressure ratio is within CONVPR of the required rotor pressure ratio (Default = 0.01).

ITINT = Initial number of iterations to compute the flow solution before starting to check for convergence

CONVMI = Convergence criterion for mass flow error during fan blade inverse design (Default = 0.005)

CONVRI = Convergence criterion for RMS residual during fan blade inverse design (Default = 1e-07)

CONVPI = Convergence criterion for rotor pressure ratio during fan blade inverse design (Default = 5e-04)

CONVPRI = Convergence criterion for the rotor pressure ratio boundary condition during fan blade inverse design

C.6 Namelist FANNOIS

IFTTAB	=	0, Use ANOPP to compute fan tone noise
	=	1, Fan tone noise is tabulated in FNINAM and FNENAM
IPRED	=	1, Compute rotor/stator interaction noise
	=	0, Rotor wake calculations only
IRMETH	=	1, Use Eversman codes for duct propagation and radiation (Default)
	=	2, Use Rice codes for radiation approximation
INAFT	=	3, Both inlet- and aft-radiated noise (Default)
	=	2, Aft-radiated noise only
	=	1, Inlet-radiated noise only
	=	0, Do not compute inlet or exhaust radiation
NHMAX	=	Maximum BPF harmonic to include in radiation calculations
IWAKE	=	0, Use CFD results for wake velocity deficits (Default)
	=	1, Loaded fan wake profile
	=	2, Linear rational function
	=	3, GE 1995 wake model
ICUP	=	1, Compute coupling of rotor and stator upstream/downstream acoustic and vorticity waves in CUP3D (Default).
	=	0, No coupling
LTYPI	=	Inlet liner type (Not currently used)
	=	1, single-degree-of-freedom liner
	=	2, two-degrees-of-freedom liner
	=	3, bulk absorber
LTYPE	=	Exhaust liner type (see LTYPI for options) (Not currently used)
NPOST	=	Type of plotting output from Eversman radiation codes
	=	1, Postscript file of normalized acoustic pressure contours

= 2, Both a Postscript file and a TEPLOT file of normalized acoustic pressure contours (Default)

ITCASE = Case to use for determining the tuning frequency of the fan inlet and aft treatment, and for setting the number of stator vanes to cut off the BPF tone. The tuning frequency will be set to 2*BPF for the specified CASE namelist.

C.7 Namelist JETDES

DMACH = Primary nozzle design Mach number

The following variables are used for creation of a grid for CFD computations of the jet flow field. The number of vertical grid lines is controlled by XSPACE and STRFX, while the number of horizontal grid lines is controlled by YPLUS and STRFY. There are three axial break points: the plug tip, the core nozzle exit, and the fan nozzle exit. There are six grid blocks (see dissertation for definition of grid blocks). The primary grid block is downstream of all break points, and the other grid blocks are within and around the plug and nozzles. The "shear region" is the portion of the overall grid that is inside the axial grid line that extends downstream from the fan nacelle trailing edge.

JGRID = Case number for the flow properties which are used to estimate the required grid density (Default = JDESIGN)

GLOD = Length of primary grid block / duct diameter (Default = 20)

GWOD = Width of primary grid block / duct diameter (Default = 4)

XFSH2 = Number of fan nozzle diameters downstream of the fan nozzle exit at which the shear region reaches minimum width, after which the width remains constant (or increases if STRFZX > 1) (Default = 1). A cubic polynomial is used to created a smooth transition of the shear region from the nacelle trailing edge to the point defined by variables XFSH2 and YFSH2. XFSH2 and YFSH2 can be used to adjust the shape of the shear region to keep the highest grid density within the actual shear layer when WIND is executed.

YFSH2 = Shear region width XFSH2 fan nozzle diameters downstream of the fan nozzle exit, relative to the shear region width at the fan nozzle exit (Default = 0.97)

STRFZX = Factor on shear region width downstream of the minimum. If STRFZX > 1, the shear region width will increase downstream at the rate X * (STRFZX - 1) (Default = 1).

XSPACE = Required minimum axial grid spacing at the left side of the primary grid block, relative to the fan nozzle exit diameter (Default = 1.5e-03). This sets the axial grid density for all blocks. The number of axial grid points is increased by 32 until the grid spacing is less than XSPACE, so small changes in XSPACE won't change the grid density.

STRFX(N) = Axial stretching factor for grid block N, N = 1, 6. (Default = 1.04, 5*1.1). The axial grid spacing is smallest at interfaces with other grid blocks and the grid stretched toward the other edge (or the middle).

YPLUS = Required grid spacing away from the wall at each nozzle exit, relative to the estimated non-dimensional boundary layer coefficient at that point (Default = 5). This sets the radial grid density for all blocks. The number of radial grid points is increased by 8 until the grid spacing is less than the maximum computed from YPLUS, so small changes in YPLUS won't change the grid density. Also, grid points might be shifted above and below the shear layers to maintain reasonable stretching, so the effects of changing YPLUS may be uneven.

STRFY = Grid stretching in the radial direction (Default = 1.2). The radial grid spacing is smallest in shear and boundary layers, and increases toward the middle of the block (or toward the freestream edge).

FACTN0 = Rate at which the radial stretching becomes uniform downstream of each nozzle in the shear region (Default = 1.0). The radial stretching varies as

STRFX(X) = 1 + (STRFX - 1) * EXP(-FACTN0 * DELTX)

where DELTX is the distance from the nozzle exit relative to the fan nozzle diameter.

MBLOK = Number of zones into which to attempt subdividing the grid for parallel processing (Default = 12). The actual number of zones may end up being less than MBLOK but the program will run fine.

CHEMFIL = WIND chemistry file name (Default='air-5sp-std-06k.chm')

The following variables are used to control convergence of WIND flow field computations.

CFLMAX(N)	=	Maximum CFL number for the Nth level of grid sequencing (N = 0, 3). The actual CFL number starts at CFLMAX/2 and is increased to CFLMAX as the solution progresses (Default = 1.2, 2.0, 2.0, 2.0).
CFLMX1	=	Maximum CFL number for the primary grid block. The CFL number for each zone in the primary grid block will be the lesser of CFLMAX(N) and CFLMX1 (Default = 1.2).
NCYCLE(N)	=	Number of cycles at the Nth level of grid sequencing. There are 5 iterations per cycle. (Default = 1800, 1200, 800, 400)
TVD	=	Factor for TVD flux limiting (Default = 3). Values less than the default may improve convergence.
FCROSS	=	Cross-flow CFL factor. This is the ratio of the time step in boundary and shear layers perpendicular to the flow direction, relative to the time step parallel to the flow. Values less than 1 may improve convergence if the shear layers develop instabilities (Default = 1).
ITLNS	=	1, Solve the thin-layer Navier-Stokes equations (Default)
	=	0, Solve the full Reynolds-Averaged Navier-Stokes equations
DQ	=	0, No DQ limiting
	>	0, Enable DQ limiting for the second and subsequent grid levels and set the DQ limiter to DQ for both density and temperature (Default = 0.01).

The following variables are used in MGB jet noise computations. They are computed in the WIND wrapper routine.

LREF	=	Reference length used for non-dimensionalization of grid and flow variables

KLIP	=	Radial count for the grid at the lip line
JEXIT	=	Axial count for the grid at the nozzle exit

C.8 Namelist JETNOIS

IJTAB	=	0, Use ANOPP to compute jet noise
	=	1, jet noise is tabulated in JETNAM
ALPHMC	=	Convection constant (Default = 0.5)
BETAMC	=	Convection constant (Default = 0.25)
ALFA	=	Proportionality factor for finding the characteristic time delay of correlation based on k and ϵ (Default = 2.0)
ALPHT(P)	=	Convection amplification factor constant for polar directivity angle number P (P = 1, 15) (Default = 15*0.5)

C.9 Namelist PROPA

RS	=	Reference distance for noise source tables, ft (Default = 40)
SUPPLI	=	Uniform suppression to be applied to ANOPP-computed fan inlet noise, dB (Default = 0)
SUPPLE	=	Uniform suppression to be applied to ANOPP-computed fan exhaust noise, dB (Default = 0)
SUPPLC	=	Uniform suppression to be applied to core noise, dB (Default = 0)
SUPPLT	=	Uniform suppression to be applied to turbine noise, dB (Default = 0)
SUPPLJ	=	Uniform suppression to be applied to ANOPP-computed jet mixing noise, dB (Default = 0)

SUPPLK	=	Uniform suppression to be applied to shock noise, dB (Default = 0)
SUPPLR	=	Uniform suppression to be applied to airframe noise, dB (Default = 0)
TDDELT	=	Design turbine temperature extraction, R
MD	=	Design rotor relative tip Mach number
IFAN	=	1, Compute fan noise within ANOPP (Default). The fan tone computation will be overridden if IFTTAB=1 in Namelist FANNOIS
	=	0, No fan noise computations within ANOPP
ITREAT	=	1, Compute fan treatment effects within ANOPP (Default).
	=	0, No fan treatment effects within ANOPP
ICORE	=	1, Compute core noise within ANOPP (Default).
	=	0, No core noise within ANOPP
ITURB	=	3, Compute turbine noise within ANOPP using TUR.
	=	2, Compute turbine noise within ANOPP using SMBTUR (Default).
	=	1, Compute turbine noise within ANOPP using GETUR.
	=	0, No turbine noise within ANOPP
IJET	=	3, Compute jet noise within ANOPP using STNJET (Default). This option will be overridden if IJTAB=1 in Namelist JETDES.
	=	2, Compute jet noise within ANOPP using CNLJET.
	=	1, Compute jet noise within ANOPP using SGLJET.
	=	0, No jet noise within ANOPP
ISHOCK	=	1, Compute shock noise within ANOPP (Default).
	=	0, No shock noise within ANOPP
IAIRF	=	1, Compute airframe noise within ANOPP (Default).
	=	0, No airframe noise within ANOPP
IWING	=	1, Compute wing reflection/shielding within ANOPP.

	=	0, No wing reflection/shielding within ANOPP (Default)
NPD	=	1, Generate NPD tables for INM
	=	0, No NPD tables

Uncertainty parameters

DMG	=	Main gear tire diameter, ft (Default = 3)
DNG	=	Main gear tire diameter, ft (Default = 3)
NMG	=	Number of main gear trucks (Default = 4)
NNG	=	Number of nose gear trucks (Default = 2)
NWMG	=	Number of wheels per main gear truck (Default = 4)
NWNG	=	Number of wheels per nose gear truck (Default = 1)
NSA	=	Number of slots in flap system (Default = 1)
SIGMA	=	Specific flow resistance of the ground (Default=485.08)

C.10 Namelist CASE

NCASE	=	Number of cases
JDESIGN	=	Case number for the design case
IC2RUN	=	Array of up to five case numbers at which analysis is to be performed (Default = All cases)

The following arrays specify flight conditions for each case.

ACASID(J)	=	Description of flight condition for case J (J = 1, NCASE)

NAIFLI(J)	=	0, The flight condition is defined by variables AVEL(J), AALT(J) and ATOT(J), below (Default).
	>	0, FLOPSWRAP will look up AVEL(J), AALT(J) and ATOT(J) from the takeoff flight path (NAIFLI(J) = 1) or the approach flight condition (NAIFLI(J)=2) at the point where the aircraft passes through altitude AHCOND(J) or where the aircraft passes through distance AXCOND(J). Either AHCOND(J) or AXCOND(J) must be input, but not both.
AXCOND(J)	=	Distance from brake release (for takeoff) or relative to the threshold (for approach) at which the flight condition will be looked up, ft (NAIFLI(J) > 0)
AHCOND(J)	=	Altitude at which the flight condition will be looked up, ft (NAIFLI(J) > 0)
AVEL(J)	=	Flight velocity, ft/sec (NAIFLI(J) = 0)
AALT(J)	=	Altitude, ft (NAIFLI(J) = 0)
ATOT(J)	=	Thrust / thrust available (NAIFLI(J) = 0)

Fan blade/stator streamline data

NANSL(J)	=	Number of streamlines
NANMSP(J)	=	Number of meridional points for streamline geometry definition
AMRSP(M,S,J)	=	Meridional coordinates along streamline S, (M = 1, NANMSP(J)).
AXMSP(M,S,J)	=	Axial coordinates along streamline S
ARMSP(M,S,J)	=	Radial coordinates along S
ABESP(M,S,J)	=	Stream sheet thickness values along S

APTSP(M,S,J)	=	Total pressure along streamline S
APSP(M,S,J)	=	Static pressure along streamline S
AZMSP(M,S,J)	=	Absolute Mach number along streamline S
ABSP(M,S,J)	=	Absolute flow angle along streamline S
ATTSP(M,S,J)	=	Total temperature along streamline S
AVMSP(M,S,J)	=	Meridional velocity along streamline S
AVTHSP(M,S,J)	=	Absolute tangential velocity along streamline S
AASP(M,S,J)	=	Meridional flow angle along streamline S

Fan blade/stator inlet and exit conditions along streamlines:

M = 1 is located at the rotor leading edge

M = 2 is located at the rotor trailing edge

M = 3 is located at the stator leading edge

M = 4 is located at the stator trailing edge

"Relative" quantities are relative to the rotor when M = 1 or 2 and relative to the stator when M = 3 or 4.

AFLTB(S,M,J)	=	Stream function of streamline S [0-1] (M = 1, 4; S = 1, NANSL(J))
AXLTB(S,M,J)	=	Axial location of intersection of streamline S with meridional station M, ft
ARLTB(S,M,J)	=	Radial location of intersection of streamline S with meridional station M, ft
AZLTB(S,M,J)	=	Meridional location of intersection of streamline S with meridional station M, ft
AVMLTB(S,M,J)	=	Meridional velocity at intersection of streamline S with meridional station M, ft/sec
AVTHLTB(S,M,J)	=	Absolute tangential velocity at intersection of streamline S with meridional station M, ft/sec

AVTRLTB(S,M,J) = Relative tangential velocity at intersection of streamline S with meridional station M, ft/sec

AVLTB(S,M,J) = Absolute velocity at intersection of streamline S with meridional station M, ft/sec

AVRLTB(S,M,J) = Relative velocity at intersection of streamline S with meridional station M, ft/sec

AZMLTB(S,M,J) = Absolute Mach number at intersection of streamline S with meridional station M

AZMRLTB(S,M,J) = Relative Mach number at intersection of streamline S with meridional station M

AALTB(S,M,J) = Meridional flow angle at intersection of streamline S with meridional station M, deg

ABLTB(S,M,J) = Absolute flow angle at intersection of streamline S with meridional station M, deg

ABRLTB(S,M,J) = Relative flow angle at intersection of streamline S with meridional station M, deg

APLTB(S,M,J) = Static pressure at intersection of streamline S with meridional station M, psf

ATLTB(S,M,J) = Static temperature at intersection of streamline S with meridional station M, R

APTLTB(S,M,J) = Total pressure at intersection of streamline S with meridional station M, psf

ATTLTB(S,M,J) = Total temperature at intersection of streamline S with meridional station M, R

APTRLTB(S,M,J) = Relative total pressure at intersection of streamline S with meridional station M, psf

ATTRLTB(S,M,J) = Relative total temperature at intersection of streamline S with meridional station M, R

Parameters for fan CFD calculations

APRRAT(J)	=	Ratio of the hub exit static pressure to the reference total pressure. If not given, PRRAT will be found through iteration so that the fan pressure ratio equals the design value.
ACFLFAN(J)	=	CFL number for Swift CFD computations
NAIRESTI(J)	=	0, Start a new Swift computation (Default). IRESTI will be reset to 1 in SWIFTWRAP after Swift is run.
	=	1, Restart from a previous computation

Fan wake velocity profiles

NANRWAKE(J)	=	Number of radial locations at which the rotor exit velocity profile will be given
NANWAKE(J)	=	Number of circumferential points along which the rotor exit velocity profile is defined
AXWAKE(R,J)	=	Meridional coordinate at which the rotor exit velocity profile is given for radial location R
ARWAKE(R,J)	=	Radius for radial location R at Z = AXWAKE(R,J), ft
APTWAKE(R,J)	=	Circumferentially-averaged total pressure for radial location R at Z = AXWAKE(R,J), psf
ATTWAKE(R,J)	=	Circumferentially-averaged total temperature for radial location R at Z = AXWAKE(R,J), R
ATHWAKE(R,T,J)	=	Circumferential coordinate, at point T, radial location R, radians (T = 1, NANWAKE(J))
AVXWAKE(R,T,J)	=	Axial velocity at point T, radial location R, ft/sec

AVRWAKE(R,T,J) = Radial velocity at point T, radial location R, ft/sec

AVTHWAKE(R,T,J) = Tangential velocity, at point T, radial location R, ft/sec

ATKEWAKE(R,T,J) = Turbulent kinetic energy at point T, radial location R, ft**2/sec**2

Fan noise calculations

ASUPFI(J) = Fan inlet tone noise level adjustment. All fan inlet tone noise levels will be reduced by ASUPFI(J).

ASUPFA(J) = Fan aft tone noise level adjustment. All fan aft tone noise levels will be reduced by ASUPFI(J).

Jet operating conditions:

ATREF(J) = Jet reference temperature for CFD calculations, R

APREF(J) = Jet reference pressure for CFD calculations, psf

AMGBQFIL(J) = Name of 2-D Q file for MGB input for this case

AMGBTFIL(J) = Name of 2-D k-e file for MGB input for this case

The following variables define how the noise data for the current case are to be used in creation of INM data files by ANOPPWRAP:

AOPMODE(J) = 'D', This is a departure (takeoff) flight condition (Default if NAIFLI(J)=1)

= 'A', This is an approach flight condition (Default if NAIFLI(J)=2)

= '-', Do not include noise data for this case in the INM data files (Default if NAIFLI(J)=0)

C.11 Namelist METRICS

FAROFF	=	Takeoff field length
FARLDG	=	Landing field length
SFC	=	Cruise SFC (Calculated at CRMACH and CRALT)
EPNLS	=	Sideline total EPNL, EPNdB
EPNLT	=	Takeoff total EPNL
EPNLA	=	Approach total EPNL
EPNLFIS	=	Fan inlet EPNL at sideline
EPNLFES	=	Fan exhaust EPNL at sideline
EPNLFS	=	Fan total EPNL at sideline
EPNLCS	=	Core EPNL at sideline
EPNLTS	=	Turbine EPNL at sideline
EPNLJS	=	Jet mixing EPNL at sideline
EPNLKS	=	Shock EPNL at sideline
EPNLRS	=	Shock EPNL at sideline
EPNLFIT	=	Fan inlet EPNL at takeoff
EPNLFET	=	Fan exhaust EPNL at takeoff
EPNLFT	=	Fan total EPNL at takeoff
EPNLCT	=	Core EPNL at takeoff
EPNLTT	=	Turbine EPNL at takeoff
EPNLJT	=	Jet mixing EPNL at takeoff
EPNLKT	=	Shock EPNL at takeoff
EPNLRT	=	Shock EPNL at takeoff
EPNLFIA	=	Fan inlet EPNL at approach

EPNLFEA	=	Fan exhaust EPNL at approach
EPNLFA	=	Fan total EPNL at approach
EPNLCA	=	Core EPNL at approach
EPNLTA	=	Turbine EPNL at approach
EPNLJA	=	Jet mixing EPNL at approach
EPNLKA	=	Shock EPNL at approach
EPNLRA	=	Shock EPNL at approach

REFERENCES

[1] Airport noise compatibility planning. Code of Federal Regulations Title 14, Part 150, Federal Aviation Administration, Department of Transportation, January 1985.

[2] Airworthiness standards: Transport category airplanes. Code of Federal Regulations Title 14, Part 25, Federal Aviation Administration, Department of Transportation, 26 December 2002.

[3] American national standard preferred frequencies and band numbers for acoustical measurements. American National Standards Institute, 1976.

[4] Janis Auzins. Direct optimization of experimental designs. In *Proceedings of the 10th AIAA/ISSMO Multidisciplinary Analysis and Optimization Conference*. American Institute of Aeronautics and Astronautics, 30 August–1 September 2004.

[5] Vladimir Balabanov, Raphael T. Haftkat, Bernard Grossman, William H. Mason, and Layne T. Watson. Multifidelity response surface model for HSCT wing bending material weight. AIAA Paper 1998-4804, American Institute of Aeronautics and Astronautics, 1998.

[6] Thomas F. Balsa and Philip R. Gliebe. Aerodynamics and noise of coaxial jets. *AIAA Journal*, 15(11):1550–1558, November 1977.

[7] Steven L. Baughcum, Donald J. Sutkus, and Stephen C. Henderson. Year 2015 aircraft emission scenario for scheduled air traffic. NASA CR 1998-207638, National Aeronautics and Space Administration, March 1998.

[8] Steven L. Baughcum, Donald J. Sutkus, and Stephen C. Henderson. Source methodology for turbofan noise prediction (SOURCE3D technical documentation). NASA CR 1999-208877, National Aeronautics and Space Administration, March 1999.

[9] E. D. Bediako and K. Yamamoto. Aerodynamic design and analysis for shock-cell noise reduction system. GE Report R81AEG543, General Electric Company, September 1981.

[10] Robert T. Biedron, Christopher L. Rumsey, Gary G. Podboy, and M. H. Dunn. Predicting the rotor-stator interaction acoustics of a ducted fan engine. AIAA Paper 2001-0664, American Institute of Aeronautics and Astronautics, 2001.

[11] G. E. P. Box, W. G. Hunter, and J. S. Hunter. *Statistics for Experimenters, An Introduction to Design, Analysis, and Model Building*. John Wiley & Sons, New York, 1978.

[12] Kenan Bozkaya, Bülent Sümer, Bayýndýr Kuran, and Mehmet Ali Ak. Reliability analysis of a solid rocket motor based on response surface method and monte carlo simulation. In *Proceedings of the 41st AIAA/ASME/SAE/ASEE Joint Propulsion Conference & Exhibit*, Tucson, AZ, 10–13 July 2005. American Institute of Aeronautics and Astronautics.

[13] Carl Burleson and Lourdes Maurice. Aviation and the environment: Challenges and opportunities. In *AIAA/ICAS International Air and Space Symposium and Exposition: The Next 100 Years*. American Institute of Aeronautics and Astronautics, 14–17 July 2003.

[14] R. H. Bush, G. D. Power, and C. E. Towne. WIND: The production flow solver of the NPARC alliance. In *Proceedings of the 36th Aerospace Sciences Meeting and Exhibit*. American Institute of Aeronautics and Astronautics, 12–15 January 1998.

[15] Michael J. Caddy and Stanley R. Shapiro. NEPCOMP—the Navy engine performance computer program, version 1. NADC 74045-30, Naval Air Development Center, April 1975.

[16] Aircraft noise. International Civil Aviation Organization (ICAO) Annex 16, Environmental Protection, volume I, Amendment 7 effective 21 March 2002.

[17] Wei Chen and Sriram Varadarajan. Integration of design of experiments and artificial neural networks for achieving affordable concurrent design. AIAA Paper 1997-1230, American Institute of Aeronautics and Astronautics, 1997.

[18] K. J. Chilcot. Application of risk assessment techniques in optimizing future space missions. In *Proceedings of the AIAA Space Programs and Technologies Conference*, Houston, TX, 21–24 June 1988.

[19] R. V. Chima. Viscous three-dimensional calculations of transonic fan performance. In *CFD Techniques for Propulsion Appliations, AGARD Conference Proceedings No. CP-510*, pages 21–1 to 21–19. Advisory Group for Aerospace Research and Development, February 1992. Also NASA TM-103800.

[20] R. V. Chima. *TCGRID 3-D Grid Generator for Turbomachinery, User's Manual and Documentation, Version 206*. NASA Glenn Research Center, Cleveland, OH, December 1999.

[21] R. V. Chima, P. W. Giel, and R. J. Boyle. An algebraic turbulence model for three-dimensional viscous flows. AIAA Paper 93-0083, American Institute of Aeronautics and Astronautics, January 1993. Also NASA TM-105931.

[22] R. V. Chima and J. W. Yokota. Numerical analysis of three-dimensional viscous flows in turbomachinery. *AIAA Journal*, 28(5):798–806, May 1990.

[23] Rodrick V. Chima. Calculation of multistage turbomachinery using steady characteristic boundary conditions. AIAA Paper 98-0968, American Institute of Aeronautics and Astronautics, January 1998. Also NASA TM-1998-206613.

[24] Rodrick V. Chima. Calculation of tip clearance effects in a transonic compressor rotor. *Journal of Turbomachinery*, 120(1):131–140, January 1998.

[25] Rodrick V. Chima. Computational modeling of vortex generators for turbomachinery. ASME Paper GT-2002-30677, American Society of Mechanical Engineers, April 2002. Also NASA TM-2002-211551.

[26] Rodrick V. Chima. Comparison of the AUSM+ and H-cusp schemes for turbomachinery applications. AIAA Paper 2003-4120, American Institute of Aeronautics and Astronautics, June 2003. Also NASA TM-2003-212457.

[27] Paul Collopy. Balancing risk and value in system development. In *Space 2003*, Long Beach, CA, 23–25 September 2003.

[28] David G. Crighton. Airframe noise. In Hubbard [62], pages 391–448.

[29] Paul Crisafulli, Matthew Kaufman, Anthony A. Giunta, William H. Mason, Bernard Grossman, Layne T. Watson, and Raphael T. Haftka. Response surface approximations for pitching moment including pitch-up in the MDO design of an HSCT. In *6th AIAA, NASA, and ISSMO Symposium on Multidisciplinary Analysis and Optimization*, pages 1308–1322, Bellevue, WA, 4–6 September 1996. American Institute of Aeronautics and Astronautics.

[30] Debora D. Daberkow and Dimitri N. Mavris. An investigation of metamodeling techniques for complex systems design. In *Proceedings of the 9th AIAA/ISSMO Symposium on Multidisciplinary Analysis and Optimization*. American Institute of Aeronautics and Astronautics, 4–6 September 2002.

[31] S. V. Damle. Throughflow method for turbomachines using Euler solvers. AIAA Paper 96-0010, American Institute of Aeronautics and Astronautics, January 1996.

[32] Benoit de Gouville, Michel Roger, and Jean Marc Cailleau. Prediction of fan broadband noise. AIAA Paper 98-2317, American Institute of Aeronautics and Astronautics, 1998.

[33] Daniel A. DeLaurentis and Dimitri N. Mavris. Uncertainty modeling and management in multidisciplinary analysis and synthesis. AIAA Paper 2000-0422, American Institute of Aeronautics and Astronautics, 2000.

[34] Robert P. Dougherty. A wave-splitting technique for nacelle acoustic propagation. In *Proceedings of the 3rd AIAA/CEAS Aeroacoustics Conference*, Atlanta, GA, 12-14 May 1997.

[35] Alain Dravet, Jacques Julliard, Michel Ah-Fa, and Gilles Rollin. Computation of jet mixing noise for confluent flow nozzles using k-ϵ turbulence model. (98-2257), May 1998.

[36] M. C. Duta, A. Laird, and M. B. Giles. Aeroacoustic analysis using a hybrid finite element method. In *6th European Conference on Turbomachinery, Fluid Dynamics and Thermodynamics*, Lille, France, 7–11 March 2005.

[37] M. S. Eldred, A. A. Giunta, and S. S. Collis. Second-order corrections for surrogate-based optimization with model hierarchies. In *10th AIAA/ISSMO Multidisciplinary Analysis and Optimization Conference*. American Institute of Aeronautics and Astronautics, 30 August–1 September 2004.

[38] Walter C. Engelund, Douglas O. Stanley, Roger A. Lepsch, Mark M. McMillian, and Resit Unal. Aerodynamic configuration design using response surface methodology analysis. In *Proceedings of the AlAA Aircraft Design, Systems and Operations*

Meeting, Monterey, CA, 11–13 August 1993. American Institute of Aeronautics and Astronautics.

[39] E. Envia, D. L. Huff, and C. R. Morrison. Analytical assessment of stator sweep and lean in reducing rotor-stator tone noise. AIAA Paper 96-1791, American Institute of Aeronautics and Astronautics, 1996.

[40] Edmane Envia. Fan noise source diagnostic test—vane unsteady pressure results. In *8th AIAA/CEAS Aeroacoustics Conference & Exhibit*, Breckenridge, Colorado, 17–19 June 2002.

[41] W. Eversman, A. V. Parrett, J. S. Presser, and R. J. Silcox. Contributions to the finite element solution of the fan noise radiation problem. *ASME Journal of Vibration, Acoustics, Stress, Reliability in Design*, 107:216–223, 1985.

[42] Fereidoun Farassat. Sound propagation in a duct and interaction tones. Lecture Notes, NASA Langley Research Center, 1998.

[43] Ulrich Ganz, Stewart A. L. Glegg, and Paul Joppa. Measurement and prediction of broadband fan noise. AIAA Paper 98-2316, American Institute of Aeronautics and Astronautics, 1998.

[44] Victor E. Garzon and David L. Darmofal. Using computational fluid dynamics in probabilistic engineering design. In *Proceedings of the 15th Computational Fluid Dynamics Conference*, Anaheim, CA, 11–14 June 2001. American Institute of Aeronautics and Astronautics.

[45] Karl A. Geiselhart. *Engine Cycle Analysis Program User's Guide, Version 4.0.*

[46] Karl A. Geiselhart. A technique for integrating engine cycle and aircraft configuration optimization. NASA CR 191602, National Aeronautics and Space Administration, February 1994.

[47] Karl A. Geiselhart, Michael J. Caddy, and Shelby J. Morris, Jr. Computer program for estimating performance of air-breathing aircraft engines. NASA TM 4254, National Aeronautics and Space Administration, May 1991.

[48] Ghader Ghorbaniasl and Charles Hirsch. Validation and application of a far-field time domain formulation for fan noise prediction. In *Proceedings of the 11th AIAA/CEAS Aeroacoustics Conference*, Monterey, CA, 23-25 May 2005.

[49] Ronnie E. Gillian. Aircraft noise prediction program user's manual. NASA TM 84486, National Aeronautics and Space Administration, January 1983.

[50] Anthony A. Giunta, Robert Narducci, Susan Burgee, Bernard Grossman, William H. Mason, Layne T Watson, and Raphael T. Haftka. Variable-complexity response surface aerodynamic design of an HSCT wing. AIAA Paper 1995-1886, American Institute of Aeronautics and Astronautics, 1995.

[51] P. Gliebe, R. Mani, H. Shin, B. Mitchell, G. Ashford, S. Salamah, and S. Connell. Aeroacoustic prediction codes. NASA CR 2000-210244, National Aeronautics and Space Administration, August 2000.

[52] P. R. Gliebe, J. F. Brausch, R. K. Majjigi, and R. Lee. Jet noise suppression. In Hubbard [63], pages 207–270.

[53] P. R. Gliebe, R. E. Motsinger, and A. Sieckman. High velocity jet noise source location and reduction, task 6 supplement—computer programs: Engineering correlation (M*S), jet noise prediction method and unified aeroacoustic prediction model (M*G*B) for nozzles of arbitrary shape. FAA RD 76-79, VIa, Federal Aviation Administration, March 1979.

[54] Philip R. Gliebe. The GE90: Quiet by design: Quieter aircraft engines through leveraging new technologies. Presentation for 2003 Berkeley Airport Noise Symposium, Doing The Wright Stuff: 100 years of Aviation and the Environment, 11 March 2003.

[55] John F. Groeneweg, Thomas G. Sofrin, Edward J. Rice, and Phillip R. Gliebe. Turbomachinery noise. In Hubbard [62], pages 151–210.

[56] E. Groeschel, M. Meinke, and W. Schroederd. Noise prediction for a turbulent jet using an LES/CAA method. In *Proceedings of the 11th AIAA/CEAS Aeroacoustics Conference*, Monterey, CA, 23-25 May 2005.

[57] William Gropp and Ewing Lusk. Dynamic process management in an MPI setting. In *Proceedings of the 7th IEEE Symposium on Parallel and Distributed Processing*, pages 530–534. Institute of Electrical and Electronics Engineers, 25–28 October 1995.

[58] Laurence J. Heidelberg. Fan noise source diagnostic test—tone modal structure results. In *8th AIAA/CEAS Aeroacoustics Conference & Exhibit*, Breckenridge, Colorado, 17–19 June 2002.

[59] M. F. Heidmann. Interim prediction method for fan and compressor source noise. NASA CR X-71763, National Aeronautics and Space Administration, June 1979.

[60] D. E. Hobbs and H. D. Weingold. Development of controlled diffusion airfoils for multistage compressor applications. *Journal of Engineering for Gas Turbines and Power*, 106(4):271–278, April 1984.

[61] Charles G. Hodge. Quiet aircraft design and operational characteristics. In Hubbard [63], pages 383–414.

[62] Harvey H. Hubbard, editor. *Aeroacoustics of Flight Vehicles: Theory and Practice*, volume 1. NASA RP-1258, August 1991.

[63] Harvey H. Hubbard, editor. *Aeroacoustics of Flight Vehicles: Theory and Practice*, volume 2. NASA RP-1258, August 1991.

[64] Christopher E. Hughes, Robert J. Jeracki, Richard P. Woodward, and Christopher J. Miller. Fan noise source diagnostic test—rotor alone aerodynamic performance results. In *8th AIAA/CEAS Aeroacoustics Conference & Exhibit*, Breckenridge, Colorado, 17–19 June 2002.

[65] Craig A. Hunter. *An Approximate Jet Noise Prediction Method Based on Reynolds-Averaged Navier-Stokes Computational Fluid Dynamics Simulation.* PhD dissertation, The George Washington University, January 2002.

[66] Kwon-Su Jeon, Jae-Woo Lee, and Joo-Ho Choi. Efficient system optimization techniques through subspace decomposition and response surface refinement. In *Proceedings of the 40th AIAA Aerospace Sciences Meeting & Exhibit*, Reno, NV, 14–17January 2002. American Institute of Aeronautics and Astronautics.

[67] Phillip Joseph and Anthony Parry. Rotor / wall boundary-layer interaction broadband noise in turbofan engines. In *Proceedings of the 7th AIAA/CEAS Aeroacoustics Conference*, Maastricht, Netherlands, 28–30 May 2001.

[68] Sagar M. Kale, Pankaj Joshi, and Rajkumar S. Pant. A generic methodology for determination of drag coefficient of an aerostat envelope using CFD. In *Proceedings of the 5th Aviation, Technology, Integration, and Operations (ATIO) Conference*, Arlington, VA, 26–28 September 2005. American Institute of Aeronautics and Astronautics.

[69] Theodore Katsanis and W. D. McNally. Revised FORTRAN program for calculating velocities and streamlines on the hub-shroud midchannel stream surface of an axial-, radial-, or mixed-flow turbomachine or annular duct, i–user's manual. Nasa tn, National Aeronautics and Space Administration, March 1977.

[70] Matthew Kaufman, Vladimir Balabanov, Susan L. Burgee, Anthony A. Giunta, Bernard Grossman, William H. Mason, Layne T. Watson, and Raphael T. Haftka. Variable-complexity response surface approximations for wing structural weight in HSCT design. In *Proceedings of the 34th Aerospace Sciences Meeting & Exhibit*, Reno, NV, 15–18 January 1996. American Institute of Aeronautics and Astronautics.

[71] Mohammad R. Khalessi and Hong-Zon Lin. Practical implementatation of probabilistic technology. Short Course Notes, PredictionProbe, Inc., 3 May 2002.

[72] Abbas Khavaran, Eugene A. Krejsa, and Chan M. Kim. Computation of supersonic jet mixing noise for an axisymmetric convergent-divergent nozzle. *Journal of Aircraft*, 31(3):603–609, 1994.

[73] A. J. Khuri and J. A. Cornel. *Response Surface Methodology.* Virginia Commonwealth University, Boston, 1971.

[74] Aaron King and Sanford Fleeter. 3-d linearized Euler simulation and evaluation of rotor-IGV interactions. In *36th AIAA/ASME/SAE/ASEE Joint Propulsion Conference and Exhibit*, Huntsville, Alabama, 16–19 2000.

[75] Aaron King and Sanford Fleeter. Numerical simulation of sound propagation and radiation from aero-engine intakes. In *3rd Aeroacoustics Workshop SWING*, Stuttgardt, Germany, 26–27 October 2002.

[76] Duane L. Knill, Anthony A. Giunta, Chuck A. Baker, Bernard Grossman, William H. Mason, Raphael T. Haftka, and Layne T. Watson. Hsct configuration design using response surface approximations of supersonic euler aerodynamics. AIAA Paper 1998-905, American Institute of Aeronautics and Astronautics, 1998.

[77] L. Danielle Koch. Evaluation of the tone fan noise design/prediction system (tfans) at the nasa glenn research center. NASA TM 1999, National Aeronautics and Space Administration, 1999.

[78] Srinivas Kodiyalam, Jian Su Lin, and Brett A. Wujek. Design of experiments based response surface models for design optimization. AIAA Paper 1998-2030, American Institute of Aeronautics and Astronautics, 1998.

[79] Justin H. Lan. Turbofan duct propagation model. NASA CR 2001-211245, National Aeronautics and Space Administration, December 2001.

[80] M. J. Lighthill. On sound generated aerodynamically. I general theory. *Proceedings of the Royal Society of London*, A211:564–587, 1952.

[81] M. J. Lighthill. On sound generated aerodynamically. II turbulence as a source of sound. *Proceedings of the Royal Society of London*, A222:1–32, 1954.

[82] G. M. Lilley. Jet noise classical theory and experiments. In Hubbard [62], pages 211–290.

[83] G. M. Lilley, P. Morris, and B. J. Tester. On the theory of jet noise and its applications. AIAA Paper 73-987, American Institute of Aeronautics and Astronautics, October 1973.

[84] M. G. Macaraeg. Fundamental investigations of airframe noise. In *Proceedings of the 4th AIAA/CEAS Aeroacoustics Conference*, Toulouse, France, 2-4 June 1998.

[85] Sankaran Mahadevan and Natasha L. Smith. System risk assessment and allocation in conceptual design. NASA CR 2003-212162, National Aeronautics and Space Administration, May 2003.

[86] J. Robert Mahan and Allen Karchmer. Combustion and core noise. In Hubbard [62], pages 483–518.

[87] S. J. Majumdar and N. Peake. A theoretical model for the prediction of unsteady distortion noise. In *Proceedings of the 2nd AIAA/CEAS Aeroacoustics Conference*, State College, PA, 6-8 May 1996.

[88] Jack D. Mattingly, William H. Heiser, and Daniel H. Daley. *Aircraft Engine Design*. American Institute of Aeronautics and Astronautics, New York, 1987.

[89] Dimitri N. Mavris, Daniel A. DeLaurentis, Oliver Bandte, and Mark A. Hale. A stochastic approach to multi-disciplinary aircraft analysis and design. In *Proceedings of the 36th Aerospace Sciences Meeting and Exhibit*. American Institute of Aeronautics and Astronautics, 12–15 January 1998.

[90] Dimitri N. Mavris and William T. Hayden. Probabilistic analysis of an hsct modeled with an equivalent laminated plate wing. AIAA Paper 1997-5571, American Institute of Aeronautics and Astronautics, 1997.

[91] Dimitri N. Mavris, Noel I. Macsotai, and Bryce Roth. A probabilistic design methodology for commercial aircraft engine cycle selection. AIAA Paper 1998-5510, American Institute of Aeronautics and Astronautics, 1998.

[92] A. McAlpine and M. J. Fisher. On the prediction of "buzz-saw" noise generated by an aero-engine. In *Proceedings of the 6th AIAA/CEAS Aeroacoustics Conference*, Lahaina, HI, 12–14 June 2000.

[93] L. A. McCullers. *FLOPS User's Guide, Version 6.02.* NASA Langley Research Center, Hampton, VA, 11 March 2003.

[94] P. J. Morris, Q. Wang, L. N. Long, and D. P. Lockard. Numerical predictions of high speed jet noise. In *Proceedings of the 3rd AIAA/CEAS Aeroacoustics Conference*, Atlanta, GA, 12-14 May 1997.

[95] M. Nallasamy and E. Envia. Computation of far-field tone noise levels for radial and swept & leaned stators. AIAA Paper 99-1865, American Institute of Aeronautics and Astronautics, 1999.

[96] D. M. Nark, F. Farassat, D. S. Pope, and V. Vatsa. The development of the ducted fan noise propagation and radiation code CDUCT-LARC. AIAA Paper 2003-3243, American Institute of Aeronautics and Astronautics, 2003.

[97] National research and development plan for aviation safety, security, efficiency, and environmental compatibility. National Science and Technology Council Subcommittee on Transportation Research and Development, November 1999.

[98] A. C. Nerurkar, T. Q. Dang, E. S. Reddy, and D. R. Reddy. Design study of turbomachine blades by optimization and inverse techniques. AIAA Paper 96-2555, American Institute of Aeronautics and Astronautics, July 1996.

[99] John Neter, Michael H. Kutner, Christopher J. Nachtsheim, and William Wasserman. *Applied Linear Statistical Models.* Irwin, Chicago, IL.

[100] Noise standards: Aircraft type and airworthiness certification. Code of Federal Regulations Title 14, Part 36, Federal Aviation Administration, Department of Transportation, 1 January 1990.

[101] Gordon C. Oates. *Aerothermodynamics of Gas Turbine and Rocket Propulsion.* American Institute of Aeronautics and Astronautics Education Series, Washington, DC, 1984.

[102] R. E. Owens. Energy efficient engine propulsion system–aircraft integration evaluation. NASA CR-159488, 1979.

[103] Y. Özyörük and L. N. Long. Computation of sound radiating from engine inlets. *AIAA Journal*, 34(5):894–901, May 1996.

[104] Nilay Papild, Wei Shyyt, Norman Fitz-Coy, and Raphael T. Haftkao. Assessment of neural net and polynomial-based techniques for aerodynamic applications. AIAA Paper 99-3167, American Institute of Aeronautics and Astronautics, 1999.

[105] A. V. Parrett and W. Eversman. Wave envelope and finite element approximations for turbofan noise radiation in flight. *AIAA Journal*, 24(5):753–760, May 1986.

[106] A. B. Parry. Modular prediction scheme for blade row interaction noise. *Journal of Propulsion and Power*, 13(3):334–341, 1997.

[107] Surya N. Patnaik, Rula M. Coroneos, James D. Guptill, Dale A. Hopkins, and William J. Haller. A subsonic aircraft design optimization with neural network and regression approximators. In *Proceedings of the 10th AIAA/ISSMO Multidisciplinary*

Analysis and Optimization Conference, Albany, NY, 30 August–1 September 2004. American Institute of Aeronautics and Astronautics.

[108] Surya N. Patnaik, James D. Guptill, Dale A. Hopkins, and Thomas M. Lavelle. Neural network and regression approximations in high-speed civil aircraft design optimization. *Journal of Aircraft*, 35(6):839–850, 1998.

[109] Allan D. Pierce. *Acoustics: An Introduction to Its Physical Principles and Applications*. The Acoustical Society of American, Woodbury, NY.

[110] Gary G. Podboy, Martin J. Krupar, Christopher E. Hughes, and Richard P. Woodward. Fan noise source diagnostic test—LDV measured flow field results. In *8th AIAA/CEAS Aeroacoustics Conference & Exhibit*, Breckenridge, Colorado, 17–19 June 2002.

[111] Carl C. Poteet and Max L. Blosser. Improving metallic thermal protection system hypervelocity impact resistance through design of experiments approach. In *Proceedings of the 40th Aerospace Sciences Meeting & Exhibit*, Reno, NV, 14–17 January 2002. American Institute of Aeronautics and Astronautics.

[112] John Premo and Paul Joppa. Fan noise source diagnostic test—wall measured circumferential array mode results. In *8th AIAA/CEAS Aeroacoustics Conference & Exhibit*, Breckenridge, Colorado, 17–19 June 2002.

[113] Daniel P. Raymer. *Aircraft Design: A Conceptual Approach*. American Institute of Aeronautics and Astronautics, Washington, DC, 1989.

[114] Michael Richman and Sanford Fleeter. Navier-Stokes simulation of igv-rotor-stator interactions in a transonic compressor. AIAA Paper 2000-3379, American Institute of Aeronautics and Astronautics, 2000.

[115] I. D. Roy and W. Eversman. Improved finite element modeling of the turbofan engine inlet radiation problem. *Journal of Vibration and Acoustics*, 117(1):109–115, January 1995.

[116] I. D. Roy and W. Eversman. Development of the inlet and aft fan duct acoustic radiation codes. Informal Report to NASA Lewis under NASA grant NAG3 1678, April 1996.

[117] Indranil Danda Roy and Walter Eversman. Far-field calculations for turbofan noise. *AIAA Journal*, 39(12):2255–2261, December 2001.

[118] C. L. Rumsey, R. T. Biedron, F. Farassat, and P. L. Spence. Ducted-fan engine acoustic predictions using a Navier-Stokes code. *Journal of Sound and Vibration*, 213(4):643–664, June 1998.

[119] Julien Scharl and Dimitri Mavris. Building parametric and probabilistic dynamic vehicle models using neural networks. AIAA Paper 2001-4373, American Institute of Aeronautics and Astronautics, 2001.

[120] T. E. Shaw. An overview of risk management techniques, methods and application. In *Proceedings of the AIAA Space Programs and Technologies Conference*, Huntsville, AL, 25–28 September 1990. American Institute of Aeronautics and Astronautics.

[121] Bart A. Singer, Kenneth S. Brentner, David P. Lockard, and Geoffrey M. Lilley. Simulation of acoustic scattering from a trailing edge. In *Proceedings of the 37th Aerospace Sciences Meeting & Exhibit*, Reno, NV, 11–14 January 1999.

[122] Bart A. Singer, David P. Lockard, Kenneth S. Brentner, Mehdi R. Khorrami, Mert E. Berkman, and Meelan Choudhari. Computational aeroacoustic analysis of slat trailing-edge flow. In *Proceedings of the 5th AIAA/CEAS Aeroacoustics Conference*, Seattle, WA, 10–12 May 1999.

[123] Michael J. T. Smith. *Aircraft Noise*. Cambridge University Press, Cambridge, England, 1989.

[124] P. L. Spence. Ducted fan noise prediction using wave envelope analysis and the kirchhoff formula. AIAA Paper 97-1651, American Institute of Aeronautics and Astronautics, 1997.

[125] D. Stanescu, D. Ait-Ali-Yahia, W. G. Habashi, and M. B. Robichaud. Multidomain spectral computation of sound radiation from ducted fans. *AIAA Journal*, 37(3):296–302, March 1999.

[126] Christopher K. W. Tam. Jet noise generated by large-scale coherent motion. In Hubbard [62], pages 311–390.

[127] C.S. Thomas, K.I. Hume, and P.D. Hooper. Aircraft noise, airport growth and regional development. AIAA Paper 2004-2806, American Institute of Aeronautics and Astronautics, May 2004.

[128] Russell H. Thomas, Meelan M. Choudhari, and Ronald D. Joslin. Flow and noise control: Toward a closer linkage. In *ICAS 2002 Congress*, Toronto, CA, 8–13 September 2002.

[129] David A. Topol. Development and evaluation of a coupled fan noise design system. In *Proceedings of the 3rd AIAA/CEAS Aeroacoustics Conference*. American Institute of Aeronautics and Astronautics, 12–14 May 1997.

[130] David A. Topol. TFaNS tone fan noise design/prediction system, volume I: System description, CUP3D technical documentation and manual for code developers. NASA CR 1999-208882, National Aeronautics and Space Administration, March 1999.

[131] David A. Topol. TFaNS tone fan noise design/prediction system, volume III: Evaluation of system codes. NASA CR 1999-208884, National Aeronautics and Space Administration, March 1999.

[132] Naoki Tsuchiya, Yoshiya Nakamura, Akihiro Yamagata, Hidekazu Kodama, Osamu Nozaki, Toshio Nishizawa, and Kazuomi Yamamoto. Fan noise prediction using unsteady cfd analysis. In *Proceedings of the 8th AIAA/CEAS Aeroacoustics Conference*, Breckenridge, CO, 17–19 June 2002.

[133] Naoki Tsuchiya, Yoshiya Nakamura, Akihiro Yamagata, Hidekazu Kodama, Osamu Nozaki, Toshio Nishizawa, and Kazuomi Yamamoto. Investigation of acoustic modes generated by rotor-stator interaction. In *Proceedings of the 9th AIAA/CEAS Aeroacoustics Conference*, Hilton Head, SC, 12–14 May 2003.

[134] D. L. Tweedt, R. V. Chima, and E. Turkel. Preconditioning for numerical simulation of low Mach number three-dimensional viscous turbomachinery flows. AIAA Paper 97-1828, American Institute of Aeronautics and Astronautics, June 1997.

[135] Stefan Uellenberg. Buzzsaw noise predictions for modern turbofans. In *Proceedings of the 10th AIAA/CEAS Aeroacoustics Conference*, Manchester, UK, 10–12 May 2004.

[136] Resit Unal, Roger A. Lepsch, Walter C. Engelund, and Douglas O. Stanley. Approximation model building and multidisciplinary design optimization using response surface methods. In *6th AIAA, NASA, and ISSMO Symposium on Multidisciplinary Analysis and Optimization*, pages 592–598, Bellevue, WA, 4–6 September 1996. American Institute of Aeronautics and Astronautics.

[137] Garret N. Vanderplaats. CONMIN - a FORTRAN program for constrained function minimization: User's manual. NASA TM X-62282, National Aeronautics and Space Administration, August 1973.

[138] Joseph M. Verdon. Linearized unsteady aerodynamic analysis of the acoustic response to wake/blade-row interaction. NASA CR 2001-210713, National Aeronautics and Space Administration, January 2001.

[139] William L. Willshire, Jr and David G. Stephens. Aircraft noise technology for the 21st century. In *NOISE-CON 98*, pages 7–22. Institute of Noise Control Engineering of the USA, 5–8 April 1998.

[140] Charles E. Wilson. *Noise Control: Measurement, Analysis, and Control of Sound and Vibration*. Krieger, Malabar, FL.

[141] David Gordon Wilson and Theodosios Korakianitis. *The Design of High-Efficiency Turbomachinery and Gas Turbines*. Prentice Hall, Upper Saddle River, NJ, 1998.

[142] Richard P. Woodward, David M. Elliott, Christopher E. Hughes, and Jeffrey J. Berton. Benefits of swept-and-leaned stators for fan noise reduction. *Journal of Aircraft*, 38(6):1130–1138, 2001.

[143] Richard P. Woodward, Christopher E. Hughes, Robert J. Jeracki, and Christopher J. Miller. Fan noise source diagnostic test—far-field acoustic results. In *8th AIAA/CEAS Aeroacoustics Conference & Exhibit*, Breckenridge, Colorado, 17–19 June 2002.

[144] K. Yamamoto, J. F. Brausch, B. A. Janardan, D. J. Hoerat, A. O. Price, and P. R. Knott. Experimenal investigation of shock-cell noise reduction for single-stream nozzles in simulated flight. NASA CR 168234, National Aeronautics and Space Administration, May 1984. Comprehensive Data Report.

[145] William E. Zorumski. Aircraft noise prediction program theoretical manual. NASA TM 83199, National Aeronautics and Space Administration, February 1982.

VITA

Erik Olson received a Bachelor of Science Degree in Aerospace Engineering from the University of Missouri at Rolla in 1989, and a Master of Science Degree in Aerospace Engineering from the Georgia Institute of Technology in 1997. He is a member of the Tau Beta Pi engineering fraternity, the Sigma Gamma Tau aerospace engineering fraternity, and the American Institute of Aeronautics and Astronautics. He has been employed since 1989 by the National Aeronautics and Space Administration (NASA) at Langley Research Center in Hampton, Virginia. During his professional career, he has studied aircraft systems noise level prediction methods, noise abatement takeoff procedures, and noise reduction technology integration in support of NASA's Advanced Subsonic Transport, High Speed Civil Transport, Quiet Aircraft Technology, Revolutionary Aerospace Systems Concepts, and Efficient Aerodynamic Shapes and Integration programs.